THE SPECTROSCOPY OF DA WHITE DWARFS AT HIGH RESOLUTION

Nigel P Bannister

Thesis submitted to the University of Leicester for the degree of Doctor of Philosophy.

25th July 2001

X-ray Astronomy Group
Department of Physics and Astronomy
University of Leicester
UK.

Declaration

I hereby declare that no part of this thesis has been previously submitted to this or any other University as part of the requirement for a higher degree. The work described herein was conducted by the undersigned except for contributions from colleagues as acknowledged in the text.

Nigel P Bannister
25th July 2001

THE SPECTROSCOPY OF DA WHITE DWARFS AT HIGH RESOLUTION

Nigel P Bannister

Abstract

This thesis is concerned with the spectroscopy of hot, hydrogen-rich white dwarfs, and the development of instrumentation with which to further their study. It begins with a review of white dwarf research, and a summary of results from some notable Extreme-Ultraviolet (EUV) missions. The absence of helium in hot hydrogen-rich white dwarfs is introduced, and the need to precisely determine their composition is explained.

These issues provide motivation for the *Joint Astrophysical Plasmadynamic Experiment* (*J-PEX*). Using normal incidence, multilayer coated optics and a high resolution focal plane detector, this spectrometer offers a substantial improvement in effective area and spectral resolution over current instrumentation. The design and development of a microchannel plate (MCP) detector for *J-PEX* is discussed, and a study of MCP sensitivity enhancement processes presented. A CsI photocathode is found to offer superior performance in the 225 - 245 Å band covered by *J-PEX*. The low quantum efficiencies recently measured for MCPs are also discussed.

A preliminary analysis of data from the first successful flight of *J-PEX*, on board a sounding rocket, is described. Techniques are devised to overcome uncertainties in wavelength calibration, leading to production of the highest resolution EUV spectrum currently available for an astronomical object. These data reveal the presence of helium along the line of sight to the white dwarf G191-B2B, and prove the value of the *J-PEX* design.

Data from the Hubble Space Telescope and the International Ultraviolet Explorer are used to search for white dwarfs with highly ionised, non-photospheric absorption features. Three new identifications are made, in the white dwarfs REJ 1738+665, REJ 0558+165 and WD 2218+706. Possible explanations, including absorption by planetary nebulæ, are suggested. The spectra are of longer wavelength, but higher resolution than currently obtainable by *J-PEX*, and complement the latter instrument by resolving multiple velocity components along the line-of-sight. The importance of these measurements in the context of *J-PEX* results, is demonstrated.

List of Publications

Some of the results reported in this thesis have been incorporated into the following papers. The chapters to which these papers are relevant are indicated in parentheses.

1. *The Joint Astrophysical Plasmadynamic Experiment (J-PEX)*,
   N.P. Bannister, M.A. Barstow, G.W. Fraser, J.E. Spragg, R.G. Cruddace, M.P. Kowalski, G. Fritz, D. Yentis, J.S. Lapington, B.S. Sanderson, T. Barbee, W.H. Goldstein and J.F. Cordas,
   in *11th European Workshop on White Dwarfs*, eds. J.-E. Solheim, & E.G. Meištas, ASP Conf. Series **169**, 188, 1999.
   (Chapters 2 and 4.)

2. *STIS observations of five hot DA white dwarfs*,
   N.P. Bannister, M.A. Barstow, J.B. Holberg and F.C. Bruhweiler,
   in *Proceedings of the 12th European White Dwarf Workshop*, eds. H.L. Shipman and J.L. Provencal, ASP Conf. Series, 105-110, 2001.
   (Chapter 5.)

3. *A high resolution imaging microchannel plate detector for EUV spectrometry*,
   N.P.Bannister, J.S.Lapington, M.A. Barstow, G.W. Fraser, B.S. Sanderson, J.A. Tandy, J.F. Pearson and J.E. Spragg,
   in *X-ray, and Gamma-Ray Instrumentation for Astronomy XI*, Proc.SPIE, **4140**, 199-210, 2000.
   (Chapter 4.)

4. *Heavy Elements in DA White Dwarfs*,
   M.A. Barstow, M.R. Burleigh, N.P. Bannister, J.B. Holberg, I. Hubeny, F.C. Bruhweiler and R. Napiwotzki,
   in *Proceedings of the 12th European White Dwarf Workshop*, eds. H.L. Shipman and J.L. Provencal, ASP Conf. Series, 128-134, 2001.
   (Chapter 5.)

5. *Far-UV spectroscopy of the hot DA white dwarf WD 2218+706 (DeHt5) with STIS*,
   M.A. Barstow, N.P. Bannister, J.B. Holberg, I. Hubeny, F.C. Bruhweiler and R. Napiwotzki,
   in Mon. Not. R. Astron. Soc., **325**, 1149-1156, 2001.
   (Chapter 5.)

6. *High-Resolution Spectroscopy of G191-B2B in the Extreme Ultraviolet*,
   R.G. Cruddace, M.P. Kowalski, D. Yentis, G.G. Fritz, H. Gursky, M.A. Barstow, N.P. Bannister, G.W. Fraser, J.E. Spragg, J.S. Lapington, J.A. Tandy, B.S. Sanderson, J.L. Culhane, T.W. Barbee, J.F. Kordas and W. Goldstein,
   in ApJ, 2001 (in press).
   (Chapters 2, 4 and 6.)

ACKNOWLEDGEMENTS

My decision to embark on a PhD came about as a result of involvement in two undergraduate research projects, run by Martin Barstow, and concerned with white dwarf stars. During these projects, Martin provided as clear a demonstration as is possible, that astronomical objects do not need a high redshift to be interesting and worthy of study. I have many reasons to be grateful to Martin: for giving me the opportunity to work with a team of world-class astronomers; for entrusting me with freedom and responsibility during the J-PEX development program - an extraordinary experience which has left me with many memorable moments and images - and for giving me the chance to work and experience life abroad. Most of all, thank you, Martin, for giving me the chance of pursuing the career to which I aspired, more years ago than I care to remember.

I owe a great debt of thanks to George Fraser, not only for numerous crash courses and discussions on various aspects of physics and detectors, but also for his ceaseless encouragement and advice; for supplying large doses of perspective and humour when nature, schedules, and microchannel plates seemed to conspire against us, and for a listening ear which turned mountains into mole-hills on more than one occasion.

Jim Pearson and John Lees have borne much of the un-enviable task of turning me from a liability in the lab, into someone who, I hope, can now be left alone with a NIM rack, with minimal risk of explosion or other undesirable incident. Without their considerable knowledge and experience, I doubt that the project would have had such a successful outcome. Thanks for your help, for showing me one end of a detector from the other, and explaining all the fiddly bits which go on in-between! And for four enjoyable years in the Space Research Centre, evenings investigating the local ale house, and large amounts of help whenever required, I'd like to thank all at SRC - particularly Adam Brunton, Gareth Price, Jason ("Zap") Page, Fletch, David Bassford, Rob Rideout and Adrian Martin (now in Berkeley - thanks for a great stay in San Fransisco, Adrian!).

Thanks to Matt Burleigh for useful discussions, memorable days and nights at observatories in South Africa and La Palma, several wooly heads, and an incident on the hotel roof in Santa Cruz; and Paul Dobbie, for numerous explanations, suggestions, and company while sampling the local offerings in Tromsø and Delaware. I've also received a tremendous amount of help and advice from Jay Holberg at the Lunar & Planetary Laboratory, University of Tucson - thanks for supplying codes, know-how and suggestions, Jay.

A considerable amount of design and engineering work was involved in construction of the flight detector, and this would have been impossible without the amazing efforts of people in the Physics workshop, and the Spaceflight Engineering experts at the Space Research Centre. Specifically, John Spragg and Dave Watson, for distilling wisdom on many occasions; Harold Chapman, Baden Favill, and Barry Towell, and the people in the Physics department workshop - for designing and making the impossible, on timescales which were improbable. I'm also grateful to Duncan Ross and John Holt, who designed and built the electronics components under the same conditions. All made the difference between success and failure. (Thanks also to John H. for introducing me to some interesting - and unusual - venues in Leicester!)

To my colleagues at MSSL - Jon Lapington, Ben Sanderson and Jason Tandy, and their families, thanks not only for the serious *J-PEX* work and your magnificent anode, but being great fun to work with and making the whole experience generally more pleasant. The nights I remember in Alexandria were great, those I can't, presumably more so. Oh yes, and thanks for almost finishing me off up a mountain in New Mexico...

Through *J-PEX* I've made many friends in the United States. So "thank you", Ray Cruddace, Mike Kowalski (Mike, I'll have those numbers next week...), Daryl Yentis, Bill Hunter and their colleagues the US Naval Research Laboratory; Gregg Clifford and Janet Baciak at Silver Engineering (hope we get to do it again!), Don Woods, and the people at NSROC and the Physical Sciences Laboratory for bringing it all together at White Sands.

And of course, thanks to Janice, for everything.

This research has made extensive use of the NASA ADS system, and the White Dwarf Database at the Lunar & Planetary Laboratory, University of Tucson, Arizona, USA.

To Mum & Dad

for a lifetime of love and support

and

Audrey & Matt

my grandparents

who already know the answers

CONTENTS

List of Figures

LIST OF TABLES

CHAPTER 1

INTRODUCTION

1.1 White dwarf stars

1.1.1 History

THROUGHOUT HISTORY, a special status has been awarded to the star Sirius. Its name is derived from the Greek for "scorching", appropriate for this, the brightest of all stars in the night sky. Sirius was of great symbolic and practical importance; the ancient Egyptians called it the "Nile star" and recognized its first appearance in the year as a sign that the flood season was approaching, bringing with it the most fertile period in the calendar for the Nile valley region. Lying at a distance of 8.8 light years, Sirius is a relatively close neighbour to the Sun and owes much of its apparent brilliance to this proximity. It is a fairly ordinary main sequence star of spectral type A1 V, with an effective temperature of around 10,000K and a diameter approximately twice that of the Sun.

In 1808 the Prussian government began work on a new observatory in the city of Königsberg (now Kaliningrad), and upon its completion in 1810, the astronomer Friedrich Wilhelm Bessel was appointed as its first director. A brilliant and meticulous observer, Bessel set himself the task of measuring the positions and distances to the closest stars[1], and as part of this work he made careful measurements of the position of Sirius. Already known as a high proper motion star at 1.32" yr^{-1}, Bessel noticed that this proper motion was not uniform as expected, but that instead the star appeared to "weave" as it traversed the sky. Suggesting that this was the result of oscillations superimposed on the proper motion of Sirius, Bessel deduced that the star was part of a binary system; however, all attempts to detect the companion object were unsuccessful. Twenty eight years later, in January 1862, the American telescope maker Alvan G. Clark was at work evaluating a new $18\frac{1}{2}$ inch refractor, which was eventually to be housed in the Dearborn Observatory (built by the Chicago Astronomical Society and the University of Chicago, Illinois). While testing the optics by observing Sirius, he detected a faint (magnitude 8.3) companion in the overpowering glare of the primary star, thereby confirming Bessel's work (Moore, 1989). Using Kepler's third law and knowledge of the distance to the Sirius system, the mass of the companion was found to be around 0.9 $\mathrm{M}_{\odot}$.

[1] Bessel succeeded in this task, announcing the distance to 61 Cygni in 1838.

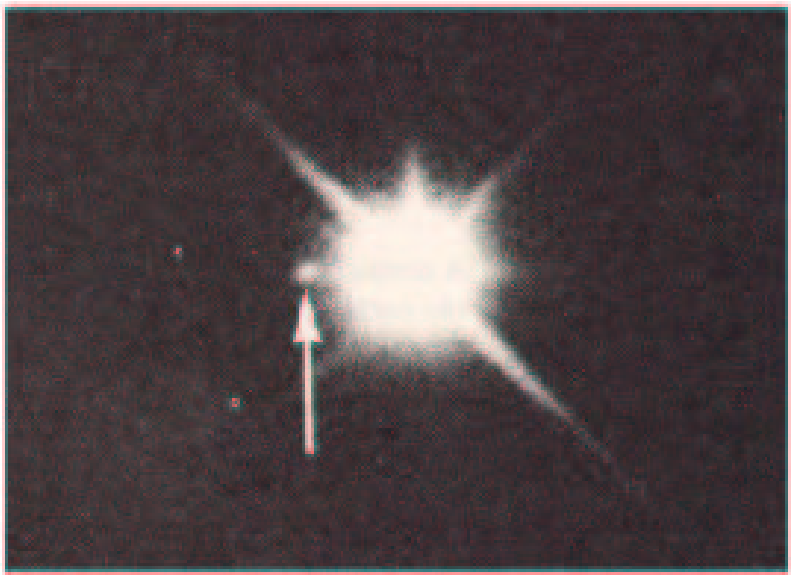

Figure 1.1: The first white dwarf to be discovered, Sirius B (arrowed) is faintly visible in the glare of the primary star. Image courtesy of the Lick observatory.

Figure 1.1 shows the two stars, illustrating the difficulty in detecting the white dwarf companion to the brilliant primary star.

Sirius B, as the companion was named, was believed to be a cool object, since it was very faint for a $1\,\mathrm{M}_{\odot}$ star at that distance. This was a natural assumption to make; according to classical physics, the more mass the star had, the greater its size. Assuming a blackbody spectrum, the luminosity L of a star with effective temperature T and radius R is given by the simple relation

$$L = 4\pi R^2 \sigma T^4 \ \text{(Watts)}, \tag{1.1}$$

where σ is the Stefan-Boltzmann constant. From this relation, it is clear that if a star with large radius has low luminosity, the effective temperature must also be low.

The unusual nature of Sirius B was deduced by Otto Struve, who made careful measurements of the Sirius A-B binary system over several years[2]. From his observations, Struve estimated that the mass of Sirius B was approximately half that of its brilliant companion, and recognised that, if the two objects were of the same constitution, Sirius B ought to be a 1^{st} magnitude star with a diameter only 20% smaller than that of Sirius A (Struve, 1865). Struve had placed Sirius B around 8^{th} magnitude, and concluded:

> *Hence it follows that, to maintain the identity* [between the observed star and that responsible for perturbing Sirius A], *we must admit that both bodies are of a very different physical constitution.*

Further evidence of the unusual nature of Sirius B came in 1915, when the astronomer Walter S. Adams, working at the Mount Wilson observatory in the United States, was able to obtain a spectrum of the star. He found that although it had a luminosity comparable to that of a cool main sequence star (around $3 \times 10^{-3}\ \mathrm{L}_{\odot}$), the effective temperature was an incredible 29,500K – much hotter than Sirius A. This result placed observation in direct conflict

[2]The author is grateful to Jay Holberg for bringing these often-overlooked observations to light

with theory, indicating that Sirius B contained a mass equivalent to the Sun inside a radius comparable to that of the Earth. The implied density of 3×10^9 kg m^{-3} was little short of a crisis for classical physics, which could provide no mechanism for the existence of matter in such an extreme state, and this prompted many astronomers including some of the most eminent names of the period, to doubt the validity of the observations. However, with the subsequent discovery of similar "anomalous" companions orbiting Procyon, 40 Eridani and several other stars, the reality of these objects became inescapable, and the search for answers marked the beginning of the study of white dwarf stars.

1.1.2 Foundations of understanding

In order to understand these objects, science had to wait until the twentieth century, for one of the most outstanding successes of modern physics - the development of quantum mechanics. Describing the behaviour of particles and matter on very small scales, it was not until this comparatively new branch of physics was established that inroads could be made in the study of white dwarfs. Of particular importance is a theorem developed by the Austrian physicist Wolfgang Pauli, who proposed that each atomic electron can be completely characterized by four "quantum numbers": the principal, orbital, magnetic and spin numbers describing respectively the quantization of energy, angular momentum, magnetic moment and spin direction of each electron. Pauli's exclusion principle essentially states that in a multi electron atom, no two electrons can occupy the same state, or alternatively, each electron in an atom must have a unique combination of quantum numbers. It is this restriction which prevents all of the electrons in an atom from occupying the lowest energy state (the 1*s* subshell); the greatest number of electrons which can occupy a given atomic orbital characterized by the principal, orbital and magnetic quantum numbers, is therefore two due to the two possible spin directions which an electron may assume ($s = \pm\frac{1}{2}$). A system in which this maximum occupancy is reached is referred to as *degenerate*, and further compression, implying greater occupancy of levels, is countered by an outward reactive force known as electron degeneracy pressure. The role of degeneracy pressure in supporting white dwarf stars against gravitational collapse (the very problem to which classical physics could provide no solution) was demonstrated by Sir Ralph Fowler in 1926 (Fowler, 1926).

One of the true luminaries in the field of white dwarf research was Subrahmanyan Chandrasekhar (figure 1.2). Chandrasekhar was born in Lahore on October 19$^{\text{th}}$ 1910, into an educated family. His father, Chandrasekhara Subrahmanya Ayyar, was Deputy Auditor General of the Northwestern Railways, and the elder brother of scientist and Nobel Laureate Chandrasekhara Venkata Raman (who won the 1930 Nobel Prize for Physics for his work on the scattering of light, and for the discovery of the effect named after him). His mother was also a scholar, motivating Chandrasekhar with stories of the great Indian mathematician Srinivasa Ramanujan. In 1918, Chandrasekhar's father was transferred to Madras, and it was here that Chandrasekhar attended high school, and eventually college. He obtained his Bachelor of Science degree in 1930, at the top of his class.

Chandrasekhar was awarded a scholarship by the Indian government to attend Trinity College Cambridge, where he became the research student of Sir Ralph Fowler. During this work, Chandrasekhar studied "The Internal Constitution of Stars" by Sir Arthur Eddington, in which the author described his belief that all stars, irrespective of mass, end their lives as white dwarfs. Chandrasekhar realized that Eddington had neglected to include the effects

Figure 1.2: Subrahmanyan Chandrasekhar in later life (courtesy of the University of Chicago Press).

of special relativity and quantum mechanics, and succeeded in showing that once these effects were accounted for, a fundamental limit was placed on the maximum mass that a white dwarf star can contain (Chandrasekhar, 1931). Beyond this limit ($1.44\,\mathrm{M}_{\odot}$, now known as the *Chandrasekhar Limit*), electron degeneracy pressure is no longer sufficient to support the star; gravity wins the battle, and inverse beta decay occurs ($p^{+} + e^{-} \rightarrow n + \nu$), so that electrons are forced into the atomic nucleus to combine with protons and form a neutron star. During this time he also derived the mass-radius relationship for white dwarf stars, a relationship which reflects the extraordinary nature of degenerate material, showing the inverse dependence of radius on mass (Chandrasekhar, 1935). The relationship between radius, R, and mass, M, in a degenerate object may be stated simply as

$$R \propto M^{-1/3}. \tag{1.2}$$

Extending his work to its natural conclusion, Chandrasekhar suggested that there should exist yet more extreme examples of stars, with densities so great that even photons were unable to escape the gravitational field. Much of this work would later form the basis of Chandrasekhar's "The Mathematical Theory of Black Holes" (Chandrasekhar, 1983). His theories on stellar evolution, and suggestion that the path of evolution at all stages must be a function of a star's mass, brought Chandrasekhar into an acrimonious dispute with Eddington, and following completion of his doctorate in 1933 he moved to the University of Chicago, where he remained for the rest of his career. Chandrasekhar was awarded the Nobel prize for physics in 1983; he died in 1995.

Today, the work started by scientists such as Adams and Chandrasekhar continues throughout the world in research groups who apply the latest techniques in computer modeling, and the most advanced ground and space-based instrumentation, in an effort to improve our understanding of these faint stellar embers. The consequences of this research extend far beyond the immediate field of white dwarfs; as members of the class of objects which include neutron stars and black holes, these stars provide us with environments impossible to recreate in the laboratory, in which theories of atomic and nuclear physics, and of relativity, may be tested and refined. A comprehensive

appreciation of the final stages in a star's life leads to a more accurate description of the phases which have preceded, and thus our knowledge of stellar evolution including its very earliest moments, is advanced.

White dwarfs have recently played a central role in one of the most intriguing developments in cosmological research. Type 1a supernovæ have been observed over a wide range of redshifts, and the results suggest that those with redshift $z > 0.5$ are fainter than expected for a non-accelerating universe (Riess *et al.*, 1998, Perlmutter *et al.*, 1999), assuming that such supernovæ may be regarded as standard candles[3]. These results have been used to support the idea that the expansion of the universe is accelerating - i.e. the Cosmological Constant Λ is non-zero and positive. It must be clearly stated, however, that *the precise nature of Type 1a supernovæ is not yet understood* (see, for example, Livio, 2000) and therefore, their validity as standard candles remains open to debate. The progenitors of Type 1a supernovæ are widely believed to be C-O core white dwarf stars, which are accreting material from a binary companion - but until recently, no direct identification of a likely progenitor system had been made. Maxted *et al.* (2000) published observations of the short period (2h 17m) white dwarf + sdB binary system KPD 1930+2752, which will merge within approximately 200 million years due to evolutionary expansion of the subdwarf, and loss of energy in the form of gravitational wave radiation. The total mass of this system is at least $1.47 \pm 0.01\ \mathrm{M}_{\odot}$, in excess of the 1.4 $\mathrm{M}_{\odot}$ Chandrasekhar limit. Accretion of helium and other heavy elements from the subdwarf onto the unseen white dwarf star will ultimately push the white dwarf over this limit, and therefore KPD 1930+2752 is the first good candidate for the progenitor of a Type 1a supernova in which accretion of heavy elements causes the white dwarf to exceed this mass limit. Given the importance of the high redshift supernova survey results, and the uncertainty which surrounds the precise origin of these spectacular events, cosmologists and stellar astronomers alike must ensure that white dwarf stars are paid the attention which they merit.

The benefits of white dwarf research are far reaching indeed. Theories describing the evolution of galaxies are unlikely to be complete without sufficient understanding of the lives of the stars which populate them. White dwarf stars can be used as indicators for the age of the galactic disk, and white dwarf research has a role to play in pinning down some of the most sought after parameters in cosmology. But justification for the study of these faint, distant glows can be found closer to home, seeking to understand the final fate of our own Sun, the star upon which all life on Earth currently depends.

1.1.3 Formation

The main sequence is that part of a stars life in which it generates energy in nuclear reactions which convert hydrogen into helium. The amount of time a star spends on the main sequence depends on its mass, with stars of 30 $\mathrm{M}_{\odot}$ exhausting the majority of their hydrogen in less than 6 million years, and stars like the Sun lasting nearer 10 billion years; very low mass stars use their fuel more frugally, and can live to twice this age. However, eventually every star exhausts its hydrogen supplies, and at this stage dramatic structural changes move the object off the main sequence. These changes are mass-dependent. High mass stars use a sequence of nuclear reactions to create

[3]The peak optical brightness of Type 1a supernovæ varies by about 1 magnitude, and is related to the form of the light curve. Therefore, their use as "standard candles" requires adequate observation of this curve.

a range of atomic elements in the core, before ending their lives in the transient brilliance of a supernova explosion, and leaving as their epitaph a rapidly expanding cloud of gas which may contain a neutron star. In contrast, stars below approximately seven solar masses are less destructive, and proceed into the white dwarf phase (Weidemann, 1987, Vennes, 2000).

While on the main sequence, energy produced inside a star provides enough outward radiation pressure to support the overlying layers of the star against collapse due to gravity. However, with the depletion of fuel comes a reduction in energy output, and this balance is destroyed; gravity now dominates, and the helium-rich core begins to contract, raising the temperature until hydrogen can be burned in a shell surrounding the core. The resultant radiation pressure over compensates for gravity, and the outer layers expand and cool; the star has entered its Red Giant phase. Convection becomes an important mechanism in energy transport from the central regions to the outside. During this period, the star may lose a substantial amount of mass in a wind ($< 2 \times 10^{-6}$ $\mathrm{M}_{\odot}$ yr^{-1}, Dupree, 1986), possibly produced by radiation pressure exerted on the loosely bound dust grains which form in the distended atmosphere. The Sun will enter this phase in around 5 billion years time, expanding to around 100 times its current radius, and producing 1000 times its present luminosity.

The helium produced by the hydrogen burning shell falls into the core, increasing the temperature and pressure until new nuclear reactions convert helium into carbon. This process starts explosively due to the high thermal conductivity of the degenerate core, but eventually settles down to a steady controlled burning of helium, which becomes the main source of energy. However, just as core hydrogen depletion was followed by hydrogen shell burning, so the exhausting of helium in the centre of the star leads to the burning of helium in a shell surrounding the carbon/oxygen core, with an associated expansion of the outer envelope. The star is said to have entered the Asymptotic Giant Branch (AGB), and it develops an electron-degenerate core of C and O (for initial masses less than 8 $\mathrm{M}_{\odot}$) or O and N (between 8 and 10.5 $\mathrm{M}_{\odot}$) (Iben & MacDonald, 1995). The increase in temperature brought about by He-shell burning ignites an adjacent shell of H, which then provides much of the stars luminosity, while enriching the He-content beneath. The star burns shells of He and H alternately, but though H burns quiescently, each He burning episode is preceded by a thermonuclear runaway. Twin-shell burning is thus unstable, and the He shell undergoes periodic (every $\sim$ 100,000 years) phases of explosive burning, extinguishing the H shell and increasing stellar luminosity for ~ 500 years. After approximately 20,000 years, stability is restored; the H shell re-ignites, and the cycle starts again. This period is referred to as the “thermal pulsing phase”, and over 30 such phases may be experienced by the star (Bloecker, 1993, Dobbie, 1999). The pulses grow in severity until mass loss rates reach rates of $\sim 10^{-4}$ $\mathrm{M}_{\odot}$ yr^{-1}, and the star sheds its outer atmosphere to leave the small degenerate core behind. This is the process responsible for the formation of planetary nebulae , shells of ex-stellar gas expanding into space at velocities upwards of 10 kilometres per second. The naked core left in the centre of the nebula is known as a “planetary nebula nucleus” (PNN), and is the immediate progenitor of the white dwarf. The gas in the nebula is illuminated by the PNN which has a surface temperature in excess of 100,000K. The rapid expansion into surrounding space means that in just 100,000 years the nebula diffuses into the interstellar medium, and the central star collapses and cools into a hot, young, degenerate white dwarf.

All nuclear reactions have shut down, and further gravitational contraction is prevented by electron degeneracy

pressure. The star shines using the energy that was stored up in the material during the collapse of the core of the progenitor - energy known as the “heat of formation”. With no means of replacing the energy radiated into space, all that lies ahead of the star is a slow, inexorable fade into the obscurity of a cold, black dwarf. More than 10^{10} years may elapse between the cessation of major energy generation, and cooling to a point where $\mathrm{L}/\mathrm{L}_{\odot} \simeq 10^{-6}$ (see, for example, Hansen, 1999).

1.1.4 White Dwarf Classification & Evolution

Just as normal stars are divided into the familiar classes of the Harvard spectral system, there exists a classification system for white dwarfs, also based upon spectral characteristics (Sion *et al.*, 1983). Due to their great densities, white dwarfs have high gravitational fields (typically 10 million times that of the Earth), and since they lack any major energy production mechanisms, we observe a wide range of temperatures, from a few thousand Kelvin for cool, old stars, to comparatively young stars at more than 100,000K (e.g. Hambly *et al.*, 1997, Dreizler & Werner, 1996). The white dwarf’s gravitational field exerts an influence on the atomic constituents in its atmosphere; heavier elements sink below the photosphere, leaving an outer gaseous atmosphere a few kilometres thick which is made up chiefly of hydrogen and helium. However, the initially simple picture is complicated by other factors such as convection in the inner regions, in which hot material in the core rises into the upper, cooler layers and is mixed in with lighter elements. At temperatures above 40,000K, radiation pressure can push heavier elements into the outer atmosphere, where they contaminate the otherwise pure H / He spectrum (Chayer *et al.*, 1994). Because of these temperature-related effects, the resulting spectral classes may be divided into hot and cool objects, with some overlap between the temperature groupings (Finley *et al.*, 1997, Barstow *et al.*, 1998).

White dwarfs may be broadly classified as either hydrogen-rich, or helium-rich stars. The origin of these two main populations is believed to be related to the amount of H and He removed through successive episodes of mass loss while the star is on the AGB, and the point at which the star leaves the AGB (Iben & MacDonald, 1995). In particular, when the envelope mass falls below a critical value, there occurs an abrupt drop in the rate at which H burns, and so the envelope contracts. In certain circumstances, the He shell can be heated sufficiently during this contraction for a final He shell flash to take place, leading to a so-called “born again AGB star”. The precise way in which a star leaves the AGB, and whether it undergoes a late He flash, is a complicated function of stellar mass and composition (Iben & MacDonald, 1995). However, the dichotomy between the H and He rich objects is believed to arise from this phase of evolution, and from the point in the thermal pulse cycle when departure from the AGB occurs. Recent work by Lawlor & MacDonald (2001) suggests a direct link between the occurrence of a late He flash and the formation of highly evolved H-deficient objects, including the H-poor white dwarf population.

The hottest of the H-rich objects are given the label “DA”, and these account for 75% of all white dwarfs. DA’s are observed over a wide range of temperatures, from 6000K upwards. A second type of H-rich white dwarf, the hybrid “DAO” shows a spectrum also dominated by H, but with some additional weak He II features. Once thought to indicate a direct link between the H and He-rich evolutionary channels, these rare objects (less than 1% of known white dwarfs) are now thought to be related primarily to binary systems, with interactions between the two components adding helium to the atmosphere of the degenerate object.

The main population of He-rich white dwarfs begins with the DO stars, having temperatures between 45,000K and 100,000K, showing strong He II absorption features, along with some He I lines. Significantly, no He-rich objects are observed with temperatures between 30,000K and 45,000K (the so-called "DO-DB gap") but below this barren region come the DB stars, between 12,000K and 30,000K, with their spectra dominated by He I. Hybrid objects also exist: DBA stars have temperatures between 12,000K and 30,000K, and exhibit lines of He I and the H I Balmer series. Several theories have been advanced to explain these observations, including accretion of H from the ISM (Aannestad & Sion, 1985), or convective mixing of residual H into the upper atmosphere of a pure DB star as it enters the low temperature regime.

Cool white dwarfs carry the designations DQ (atomic or molecular C lines) , DZ (spectra dominated by metal lines only), and DC (showing an almost featureless continuum). As in the case of their hotter relatives, these designations may be combined to describe objects with hybrid spectra. Convective mixing of He and heavier elements in the atmospheres of cooler stars may cause some H-rich objects to assume the appearance of a He-rich star (of type DB), while accretion from the ISM may also enrich the atmosphere with heavy elements, producing stars of type DQ or DZ.

Direct links between the central stars of planetary nebulæ (CSPN), the progenitors of white dwarf stars, and both the H and He dominated white dwarfs are observed. An apparent gap in the high temperature end of the DA sequence is now understood to be a selection effect, as discussed by Napiwotzki (1999), but a remaining problem in white dwarf research is the difference between the ratio of the hottest DA to DO stars (7:1, Fleming *et al.*, 1986) and that of the H to He-rich CSPN (4:1, Napiwotzki, 1999). The DO white dwarfs are linked to their PNN progenitors *via* the PG 1159 stars (named after the discovery object, PG 1159-035), rich in He, C and O. The hottest of these stars is H1504+65, with a temperature of $\simeq 170,000$K (Werner, 1991). Approximately 50% of PG 1159 objects are central stars of planetary nebulæ (Dreizler & Werner, 1996). However, complications abound in the He-rich white dwarf channel. As Dreizler & Werner (1996) explain, a coherent evolutionary path, from PNN, through the PG 1159 stars, to the DO white dwarfs, is not evident; they confirm the gap between 30,000 and 45,000K where none are found. This may indicate that as the white dwarf evolves, it can undergo changes which alter the spectral type, causing the object to change class. It has been suggested that as the He-rich (DO) white dwarf drops below 45,000K, any traces of H in the bulk of the atmosphere float up to the surface to form a very thin layer which effectively shrouds the He from observation, and causes the star to take on the appearance of a DA type. Below 30,000K, processes such as convection may dredge up the atmosphere to reveal He again, producing the spectrum of a DB star (Dreizler & Werner, 1996). However, there is, at best, circumstantial evidence to support this explanation, and the suggested mechanisms behind these changes are poorly understood. Part of current research attempts to identify white dwarfs which have made this temporary move into the hydrogen group. Recently, Wolff *et al.* (2000) described observations of a DAB white dwarf in this gap, with a temperature of 35,000K and a helium abundance of $\sim$ 1%, proposing that the star is accreting helium and metals from an interstellar cloud.

Also relevant to white dwarf evolution are the subdwarf stars, which form from progenitors which have insufficient mass to sustain a He-shell burning phase, so that they never reach the AGB. Evolving off the horizontal branch,

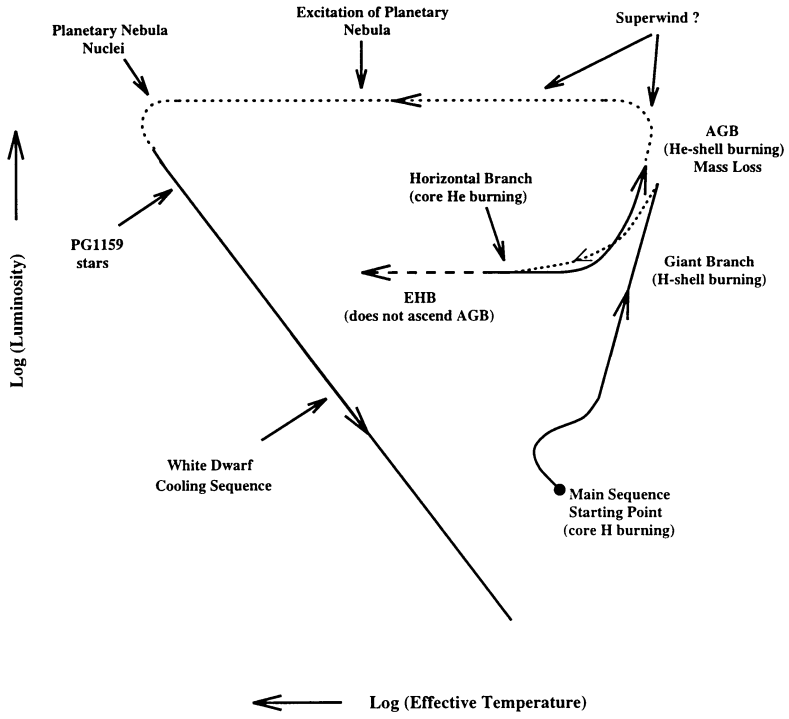

Figure 1.3: Hertzsprung-Russell diagram showing the evolutionary paths of stars from the main sequence to the white dwarf stage. (AGB = Asymptotic Giant Branch, EHB = Extended Horizontal Branch). (Marsh, 1995).

these objects contract at constant luminosity along the Extended Horizontal Branch (EHB) until their cores become degenerate and the star becomes a white dwarf. The star therefore avoids passing through the planetary nebula phase, and so subdwarf stars constitute an alternative route to the formation of a white dwarf. Examples of hot subdwarfs are found with hydrogen-rich atmospheres (sdB), helium-rich atmospheres (sdO), and also with "hybrid" envelopes (sdOB). These stars are thought to be the progenitors for $\simeq 2\%$ of white dwarf stars (Drilling & Schoenberner, 1985, Sansom *et al.*, 1992). Figure 1.3 shows the Hertzsprung-Russell diagram outlining the path taken by stars evolving off the main sequence into their white dwarf stage.

In the white dwarf classification system suggested by Sion *et al.* (1983), "D" signifies a degenerate object, while the composition dependent symbols were chosen for a variety of historical and practical reasons. Additional labels may also be assigned to particular stars, e.g. "P" indicates a magnetic star showing polarization, "H" for magnetic stars with no detectable polarization, "X" for a peculiar spectrum, and "V" for a variable degenerate. The main classes of white dwarf are summarized in table 1.1.

1.2 Thermal evolution: determining the age of the galaxy

In his seminal 1952 paper, Mestel recognized that the evolution of white dwarf stars was essentially a cooling problem (Mestel, 1952). Since they have no internal energy source of their own, white dwarfs cool steadily, and it becomes possible to find a star's age by determining its temperature. Mestel used the basic laws of thermodynamics and stellar structure to determine the behaviour of a white dwarfs' luminosity and temperature with time. Modern

HOT WHITE DWARFS	
DA	Objects with atmospheres rich in H, with only traces of He and other elements. This class contains stars encompassing a broad temperature range, from around 6,000K to over 80,000K.
DO	He rich objects with temperatures in excess of 45,000K. The spectrum is dominated by the signature of He II, although H and higher elements may be observed in smaller amounts.
DB	This class may be regarded as an extension of the DO group into lower temperature regions (below around 30,000K). The cooler temperatures are insufficient to ionise helium, and so the spectrum is dominated by He I, with only trace amounts of H (only 1/10000th of the observed He abundance).
COOL WHITE DWARFS (Temperatures less than 11,000K)	
DQ	Stars with predominantly He atmospheres, showing lines of molecular or atomic carbon in any part of the spectrum. These stars are cool enough so that H atoms can join together into molecules, and so the signature of molecular H may also be observed.
DZ	Stars exhibiting only metal lines from species such as Ca and Fe. No H or He present.
DC	Stars showing relatively featureless spectra, because the temperatures are insufficient to excite the atomic H and He into a state where they produce emission/absorption.

Table 1.1: Principal white dwarf classes as defined by Sion *et al.* (1983).

research has developed Mestel's theories to include the complex structural changes and subtle quantum mechanical effects which occur as the star ages, but the results of his work still compare well with the refined values.

Characteristic timescales for cooling to low luminosities are of the order of billions of years, and it is here that the strength of the technique for galactic dating lies; given that the length of time taken by a white dwarf to fade below detection limits is longer than the age of the galaxy (or even the Hubble time), we expect to see an abrupt cutoff in the luminosity function at low luminosities. This point can then be used to determine the age of the oldest white dwarf stars, and hence the age of the galactic disk. Surveys show that low-brightness white dwarfs significantly outnumber their more luminous counterparts, but that there is indeed a minimum luminosity below which no more are found, despite detection techniques which are capable of revealing fainter objects. To obtain usefully accurate age estimates, processes not incorporated into Mestel's theory must be accounted for. Some of these effects are briefly outlined below.

1. NEUTRINO COOLING. Neutrinos are a powerful "sink" of energy in the cores of giant stars, and the mechanism also plays an important role in the behaviour of evolving white dwarfs (D'Antona & Mazzitelli, 1990), with neutrinos removing up to three times as much energy as the flux from the surface luminosity at certain points in the evolution of the star.

2. FLUID COOLING. When the stellar temperature falls below a critical value, the separation of constituent ions reduces enough for the interior to liquefy. The effect of this phase change in a core of C and O ions is to double the ionic heat capacity (Shaviv & Kovetz, 1976, Iben & Tutukov, 1984), reducing the rate of cooling in the star. It is during the fluid-cooling phase that we find the ZZ-Ceti instability strip, and by using asteroseismological studies of these pulsating stars, more accurate information on the composition of the core and atmospheric layers may be obtained. This in turn should enable an improvement in the cooling models (Iben & Tutukov, 1984).

3. CRYSTALLIZATION. When the core temperature is sufficiently low, the white dwarf experiences a phase change from liquid to solid state. Crystallization releases latent heat, increasing cooling times by between 5 and 30% (Shaviv & Kovetz, 1976). The increase in specific heat capacity of the core causes an additional reduction in the cooling rate. Various atomic species crystallize at different times; the subsequent release of gravitational potential energy as the material diffuses out of the atmosphere further prolongs cooling in the star. Heavier elements exist in smaller quantities, and Segretain *et al.* (1994) found that the energy released through chemical differentiation of these trace elements was comparable to that produced by the most abundant constituents, prolonging the fading of these stars by several billion years.

4. THE EFFECTS OF CONVECTION. In the context of thermal evolution, the main consequence of convection in the outer layers of the star is to modify the opacity, which regulates energy loss rates (e.g. Iben & Tutukov (1984)).

5. MASS DEPENDENCE. Massive white dwarfs exhibit longer cooling periods, since these stars have a higher thermal energy content, and a smaller surface area over which to radiate this energy. However, higher densities in the cores of these stars bring about the phase transition from liquid to solid state at earlier times. As a consequence, the increase in heat capacity which comes with crystallization accelerates the evolution of massive white dwarfs with respect to their "lighter" counterparts, for $L \leq 10^{-3.9}\ \mathrm{L}_{\odot}$. This results in massive stars reaching low luminosities ($10^{-5}\ \mathrm{L}_{\odot}$, well below the observed cutoff point) as much as 5×10^{9} years earlier than a $0.6\,\mathrm{M}_{\odot}$ object.

1.2.1 The white dwarf luminosity function

Central to the use of white dwarf stars as age indicators is the luminosity function, usually presented as a plot of the "space density" of objects with increasing luminosity (Fleming *et al.*, 1986). The luminosity function of Liebert *et al.* (1988) is shown in figure 1.4. In common with other similar studies, the results show an abrupt cutoff at low luminosities, within the interval $-4.2 \leq \log(\mathrm{L}/\mathrm{L}_{\odot}) \leq -4.6$. Efforts to explain this feature suggest that it is real and not a selection effect. Searches of binary systems have been conducted in an attempt to locate fainter white dwarfs, but all stars discovered in these surveys (sensitive to separations from the primary of little more than 1 AU) possess luminosities above the cutoff. The "tail" observed beyond the cutoff has been cited by some researchers (e.g. Winget *et al.*, 1987) as evidence for the release of gravitational energy during crystallization.

This abrupt termination of the luminosity function is attributed to the finite age of the galactic disk, which can be approximated as being equal to the white dwarf cooling age. To estimate the age, Winget *et al.* (1987) produce a synthetic luminosity function using a number of models covering a range of white dwarf mass and composition, accounting for the effects of convection and crystallization. By matching the theoretical cutoff to the observed feature, the resulting age of the white dwarf population is found to be $9\ \pm 1.8 \times 10^{9}$ years. The age of the galactic disk must be approximately equal to that of the oldest white dwarfs, plus the main sequence lifetime of the progenitor. Adding on this time, and accounting for the effects of crystallization (Hernanz *et al.*, 1994), the age of the galactic disk is estimated at $\tau_{disk} = 11.4\ \pm 0.9 \times 10^{9}$ years.

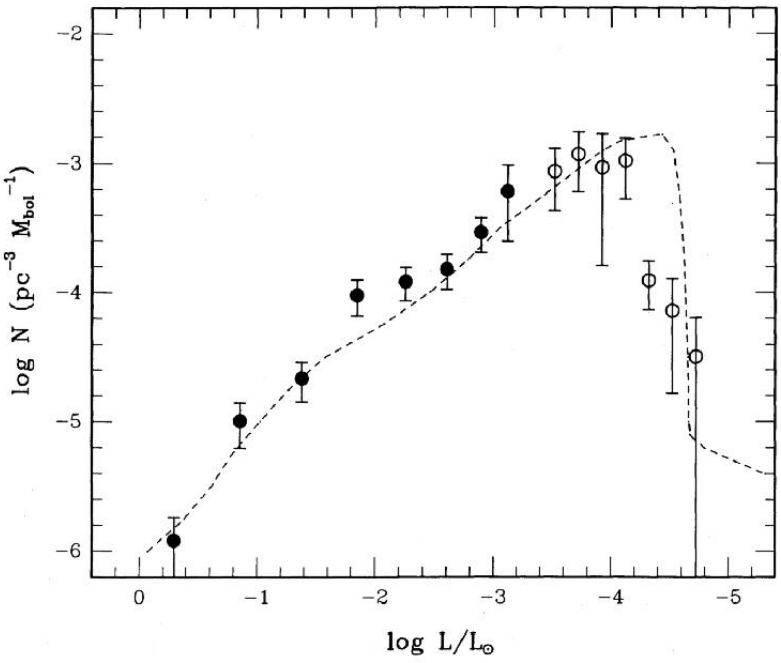

Figure 1.4: The observed white dwarf luminosity function (data points) with a theoretical function superimposed. Note (a) the cutoff at low luminosity due to the finite age of the population, and (b) the change of slope at $\log(L/L_\odot) \simeq -1.5$ due to cessation of the neutrino-loss dominated era. (Liebert *et al.*, 1988).

If we can estimate the time between the era of recombination and the onset of star formation, then the age of the universe can be determined. The pre-stellar time must be calculated using cosmological models, but is generally believed to be far shorter than the age of the galactic disk (Winget *et al.*, 1987), at around 10^9 years. An age of the universe of $\tau_u = 11.7 \pm 2.2 \times 10^9$ years is obtained, agreeing with results from other researchers working independently but also using models of thermal evolution.

It is a widely held view that using white dwarfs to estimate population ages is significantly more accurate than competing schemes, and in their work on determining the distance and age of the globular cluster NGC 6752, Renzini *et al.* (1996) cite this as the principal strength of their method. The thermal evolution of white dwarfs is one of the best understood processes in stellar astrophysics, and ages determined in this manner can be regarded with some confidence. Barstow *et al.* (1997b) used Hipparcos parallax measurements of the star V471 Tauri to obtain accurate estimates of the star's radius, and hence its mass. From these observations, Barstow *et al.* were able to confirm the accuracy of the white dwarf mass-radius relationship, which is central to the evolutionary models used to calculate the theoretical luminosity function.

1.3 A history of spaceborne observation

Until the early 1970's, white dwarf research was limited to studies in the optical region of the electromagnetic spectrum. While much valuable information about the stars can be determined using optical data (e.g. estimates of temperature, mass and gravity) the restriction is severe since the majority of important absorption features are only found at higher energies: the far ultraviolet (FUV, 1000 – 2000 Å), extreme ultraviolet (EUV, 100 – 1000 Å), and soft X-ray (SXR, 10 – 100 Å). Photons at these wavelengths are blocked by the Earth's atmosphere, and so

instrumentation must be placed above the atmosphere on spaceborne platforms (Barstow, 1996). Cruddace *et al.* (1974) presented a detailed study of the composition and structure of the ISM, in which they produced evidence that the attenuation of photons in the SXR and EUV region might be significantly lower than previously believed. Their conclusion was that, contrary to earlier findings, the inhomogeneous and anisotropic nature of the ISM might allow the detection of galactic EUV and SXR sources, possibly in excess of 1000 parsecs distance in preferential directions.

Several preliminary surveys at soft X-ray wavelengths were carried out in the mid 1970s, using instrumentation flown on sounding rockets. Margon *et al.* (1976) describe a 1974 sounding rocket flight in which an intense ultrasoft X-ray source was observed, with a spectral distribution unlike that of any previously observed class of object. Hearn *et al.* (1976) independently detected a source in the same region of sky using the *Small Astronomy Satellite* SAS-3, (a proportional-counter based X-ray observatory launched in 1975), suggesting the DA white dwarf HZ 43 as the optical counterpart. Six weeks after the SAS-3 observations, during the closing days of the *Apollo* manned spaceflight project, came the Apollo-Soyuz rendezvous mission. On board the Apollo spacecraft was an EUV telescope, consisting of a 37cm diameter grazing incidence mirror, several filters producing a (non-contiguous) observational bandwidth spanning 55 to 1540 Å, and two channel electron-multiplier (CEM) photon detectors. Observations confirmed that HZ 43 was an extremely intense source in the EUV, and so it became the first non–solar source to be positively detected in the EUV (Lampton *et al.*, 1976). It was originally assumed that such high energy photons must be produced by accretion or hot coronal emission in these stars; however, around this time, Shipman (1976) demonstrated that the soft X-ray flux from white dwarfs could be explained by thermal emission from the underlying layers of a metal-poor atmosphere passing through the optically thin ionised outer regions. The HZ 43 observations demonstrated that white dwarf stars are powerful emitters of EUV radiation, and confirmed the work of Cruddace *et al.* (1974) by showing that the density of the local interstellar gas was indeed low enough to allow objects to be observed and studied at such wavelengths, provided that the targets were close enough, or lay in directions of preferentially low column density.

Early instrumentation provided the first glimpses of conditions inside these stars. The visible and EUV observations of HZ 43 were successfully reproduced by Auer & Shipman (1977) using a pure H model atmosphere, and this well studied object remains as one of the comparatively few DA white dwarf stars which can be modeled so simply (see figure 1.5). Despite their poor sensitivity compared to modern standards, instruments flown on sub-orbital sounding rockets and short duration missions such as the Apollo-Soyuz flight not only returned valuable results in their own right, but also provided conclusive proof that there was a wealth of data waiting to be discovered at soft X-ray and EUV wavelengths. Clearly, a comprehensive understanding of white dwarf stars could not be achieved without considering these regions. The need for increased sensitivity and longer missions was obvious, and resulted in a new generation of major orbiting observatories. Many EUV and X-ray satellites have contributed valuable data to the study of white dwarfs, including the first High Energy Astronomy Observatory (*HEAO-1*, operational between 1977 and 1979) and the US/UK *Copernicus* mission (1972 - 1981). The following section is not intended as an exhaustive review of orbiting observatories, but concentrates on four missions, some of the results from which are of particular relevance to the work which follows.

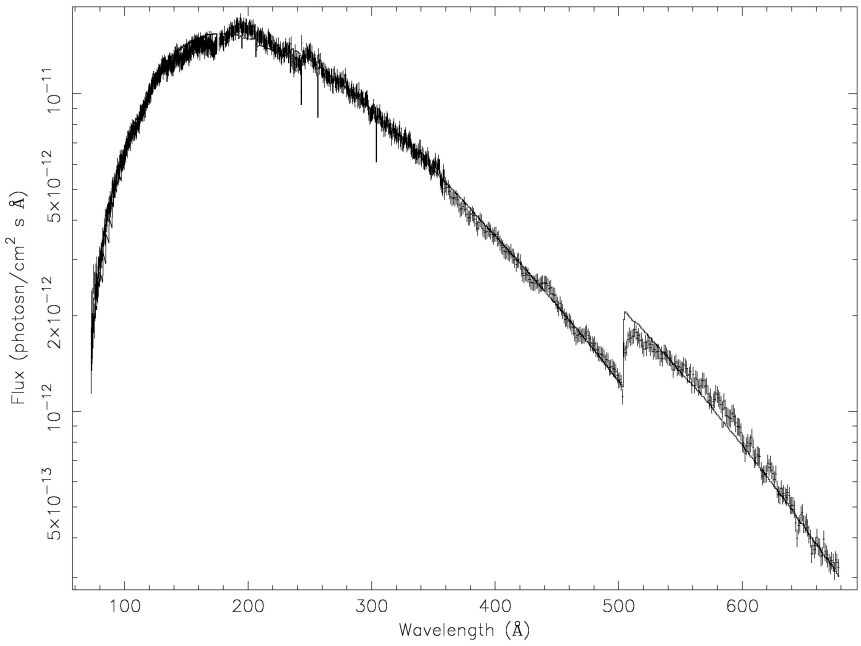

Figure 1.5: Flux corrected *EUVE* spectrum of the pure H DA white dwarf HZ 43. The data points are represented by error bars and the solid histogram is the prediction of the best-fit H model spectrum for a star of the same temperature and gravity. Note the absorption from interstellar He I at 500 Å. (See Barstow *et al.*, 1995, Barstow, 1996).

1.3.1 The International Ultraviolet Explorer

The International Ultraviolet Explorer (*IUE*) was the result of a collaboration between NASA, ESA and the UK Science and Engineering Research Council. Launched on 26$^{\text{th}}$ January 1978 from Cape Kennedy, the spacecraft was placed into a geosynchronous orbit above the Atlantic, with a perigee of 27,600 km and an apogee of 43,950 km. Spectrometers on board *IUE* covered the range of wavelengths from 1200 to 3350 Å. *IUE* was in every sense a remarkable mission; its expected lifetime was 3 years; the final shut down on 30$^{\text{th}}$ September 1996 brought to an end 18 years and 9 months of continuous operation.

It was initially believed that heavy elements would sink out of the stellar atmosphere as a result of the large gravitational field, leaving white dwarfs with smooth continuum fluxes. Consequently it was thought that nearby white dwarfs could be used as "cosmic beacons", backlighting material in the LISM, which would appear as absorption features in the otherwise bland stellar spectrum. *IUE* observed such features, including the lines of neutral and low ionisation[4] stages of C, N, O and Si. However, additional absorption due to highly ionised species was also detected in several stars, amongst them G191-B2B (Bruhweiler & Kondo, 1981) and Feige 24 (Dupree & Raymond, 1982, Wesemael *et al.*, 1984). Such lines, including those of C IV, N V and Si IV, could not be from material native to the cool tenuous interstellar medium, but were characteristic of the conditions found in a white dwarf photosphere, or circumstellar environment (e.g. Dupree & Raymond, 1982, Holberg *et al.*, 1995a).

[4]Although white dwarfs do ionise the ISM, the ionisation state of Z>2 ions in the ISM is maintained principally by the flux from O and B stars for $\lambda > 900$ Å.

1.3.2 Einstein and EXOSAT

Einstein was the first satellite to employ grazing incidence focusing X-ray mirrors. The spacecraft was launched into low Earth orbit on 13th November 1978, and remained operational until April 1981. The scientific payload achieved a sensitivity several hundred times greater than that of any previous X-ray instrumentation, but was outperformed by detectors onboard the later *EXOSAT*. Launched on 26th May 1983 into a highly eccentric 90.6 hour orbit, *EXOSAT* remained operational until 9th April 1986 when the attitude control system failed, resulting in the re-entry of the spacecraft on 6th May 1986. *EXOSAT* carried three instruments: a pair of Wolter type I grazing incidence imaging telescopes operating from 0.05 to 2.5 keV, with microchannel plates as the detection elements; a medium energy array of eight proportional counters operating from 1 to 20 keV and 5 to 50 keV, and a gas scintillation proportional counter (GSPC) covering the range from 2.0 to 64 keV. With this impressive array of instrumentation, *EXOSAT* was capable of imaging, photometry and medium resolution spectroscopy. *EXOSAT* detected 34 white dwarfs using broadband photometry, and for three of these stars (HZ 43, Feige 24 and Sirius B), spectroscopic data was obtained (Paerels & Heise, 1989).

Since the energy emitted by a white dwarf is almost exclusively due to thermal radiation from the atmosphere, models make it possible to predict the flux and overall spectral shape in one wavelength region by using observations in another. Comparison between optical measurements and broadband photometric observations of hot DA white dwarfs made by *EXOSAT* and *Einstein* showed a flux deficit at EUV wavelengths, suggesting that an extra source of opacity existed in the stellar atmosphere. This source was originally assumed to be He, being the most abundant element after H. It was proposed that He might be accreted from the interstellar medium, or may be suspended in the atmosphere by radiation pressure (Kahn *et al.*, 1984).

EXOSAT revealed that the He 228 Å absorption edge was absent in the spectrum of HZ 43, placing limits on the abundance of He in the atmosphere and casting doubt on its role as the principal source of opacity. *EXOSAT* was able to show that Sirius B also had a H-rich atmosphere, with He/H $\leq 2 \times 10^{-5}$ (Paerels *et al.*, 1988). Spectra for these white dwarfs were used to estimate the density of the interstellar H I column to the stars, by including the value as a free parameter in models used to reproduce the spectra. However, observations of Feige 24 could not be explained using the H or H+He models which had been successful in matching the FUV observations from *IUE*. It was subsequently found that by incorporating He along with trace amounts of heavy species such as C, N, O, Si, Ar and Ca, greater agreement could be found between theory and observation.

Feige 24 was thus identified as a peculiar type of DA white dwarf for which simple H or H+He atmospheres provided no adequate explanation of the EUV spectrum. Some comfort could be found in the binary nature of the star; perhaps interactions with its red dwarf companion might explain the presence of such heavy elements in the spectrum. However, as the *EXOSAT* mission drew to a close, astronomers were left asking whether the pure H atmosphere of HZ 43, or the metal-laden atmosphere of Feige 24, was most representative of DA white dwarfs.

1.3.3 ROSAT

Launched on June 1st 1990, and operational until February 12th 1999, the first six months of the mission were devoted to an all-sky survey at 0.1 – 2.5 keV, using the satellite's 2.4m focal length Wolter Type-I telescope and Position Sensitive Proportional Counter (*PSPC*) detector, and at 60 – 200 Å, using the Wide Field Camera (*WFC*). Also using Wolter type I grazing incidence mirrors, but employing microchannel plate detectors, and two filters defining wavebands covering 60 – 140 Å and 112 – 200 Å, the *WFC* was an EUV imaging telescope built by a collaboration of British institutes under the direction of Leicester University. Two catalogues were produced as a result of the *WFC* all-sky survey; the Bright Source Catalogue (BSC) of Pounds *et al.* (1993) containing 383 sources, and the later 2RE catalogue, which selected objects from the observations using more sensitive search criteria, and contains 479 sources (Pye *et al.*, 1995).

Prior to the launch of *ROSAT*, Barstow (1989) estimated the number of white dwarf detections which could be expected in the survey, suggesting that approximately 2000 objects should be revealed, the majority being new discoveries (approximately 20 stars had been detected in the X-ray and EUV bands at that time). In reality, the number of white dwarfs harvested from the *WFC* survey amounted to only 10% of the expected quantity. Barstow *et al.* (1993) performed a detailed study of the EUV and soft X-ray emission of 30 DA white dwarfs detected in the 2RE catalogue, noting that none of the stars with $T_{\rm eff} \geq 60,000$K listed in previous surveys, were detected by *ROSAT*, yet the detection rate for objects with $25,000\text{K} \leq T_{\rm eff} \leq 40,000$K was almost 100%. Barstow *et al.* (1993) showed that the anomalously low *ROSAT* count rates for DAs hotter than 40,000K could only be explained by invoking a source of opacity in addition to He. Observed fluxes are shown compared to predictions for pure H atmospheres in figure 1.6. Furthermore, 9 of the 30 stars in their sample could not be explained by H+He models; instead, heavy element opacity was necessary to model the stars accurately. In fitting *ROSAT* fluxes with model spectra, He was shown to contribute very little to the overall opacity in the stellar atmosphere, and this also frustrated attempts to link the H-rich DAs and He-rich DO and DB stars. However, the authors maintained that the apparent lack of He absorption could be due simply to the inability of *ROSAT*'s broadband photometry to separate the effects of He and heavier element opacity. Clearly, higher resolution spectroscopic data of these stars was required, and this would be supplied by the next orbiting observatory: *EUVE*.

1.3.4 The Extreme Ultraviolet Explorer

The Extreme Ultraviolet Explorer (*EUVE*) was launched on June 7th 1992, carrying three grazing incidence scanning telescopes and an EUV spectrometer. The instruments covered a range of wavelengths between 70 – 760 Å, in four bandpasses, with a resolving power of ~ 400, or approximately 0.5 Å at 200 Å. The first phase of *EUVE* observations took the form of a six month all-sky survey and simultaneous deep EUV survey along the ecliptic, followed by a phase of pointed observations with targets selected by guest observers. *EUVE* science operations ended on January 26th, 2001.

One of the most remarkable results obtained by *EUVE* is the surprising lack of He in any of the spectra of DA white dwarfs observed. For example, theories predicted that the pressure of radiation from within the star would suspend

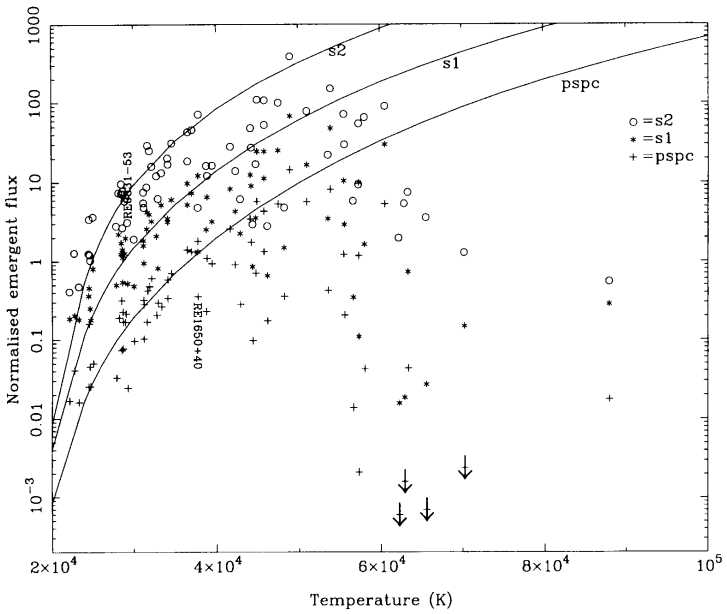

Figure 1.6: Normalized emergent EUV/X-ray fluxes vs. temperature for a range of white dwarfs detected in the *ROSAT* S1 and S2 *WFC* bands, and also the PSPC. Lines correspond to predicted fluxes for a pure-H atmosphere and H I column of 5×10^{18} cm^{-2}. (Marsh *et al.*, 1997a).

He in the atmosphere, countering the influence of gravity which would otherwise cause helium to diffuse out of the upper regions of the atmosphere. Radiative levitation theories suggested that for a star with the temperature and mass of HZ 43, the ratio of He:H is 3×10^{-6}, far below the detection limits of previous instruments, but an order of magnitude higher than the limit of *EUVE* - yet the spacecraft failed to detect He (Barstow *et al.*, 1995), consistent with the indications from *ROSAT* that He contributes little to the opacity of DA white dwarfs. However, of particular relevance to the work which follows are the observations of the bright DA star G191-B2B.

G191-B2B is one of the most intensively studied white dwarfs, due in part to its brightness, which offers a chance to provide photon-starved white dwarf researchers with relatively high signal-to-noise data. Earlier observations by *IUE* showed that in common with many other DA white dwarfs, its atmosphere is rich in heavy elements (though He was not detected). The addition of high quality *EUVE* data at shorter wavelengths allowed Lanz *et al.* (1996) to place constraints on the composition of G191-B2B, using data spanning the optical, UV and EUV regions of the spectrum, bringing astronomers a step closer to understanding the link between the two evolutionary channels of white dwarfs.

1.4 Modeling white dwarf spectra

Much of the information extracted from white dwarf spectra, such as those acquired by the spacecraft listed in the preceding section, is obtained by fitting synthetic spectra generated by model atmosphere codes, to the observations. The physical parameters determined for a star are those which, when used as input to the relevant model, produce the most faithful reproduction of the observations. Although the precise techniques used in the modeling of white dwarf spectra vary, it is instructive to consider the basic principles, and the following section summarises the essential stages in such an analysis, as described by Lanz *et al.* (1996) in their analysis of G191-B2B.

Values for T_{eff} and log g may be obtained by modeling the observed Balmer line profiles, which occur in the optical region (e.g. 6562.75 Å for H_α). In common with all photospheric spectral features, these lines are sensitive to temperature and pressure. As temperature increases, more H atoms become ionised, leaving fewer with electrons in the lower energy state (n=2 for the Balmer series), so that the strength of the absorption line decreases. Furthermore, line broadening occurs in conditions of high pressure or density, since the atomic energy levels of an atom are affected by neighboring particles, particularly ions and electrons. Perturbations by these particles are random, leading to broadening of the spectral feature; increased pressure or density produces more collisions, and broadens the line profile.

These effects are essential diagnostics in determining the physical conditions which exist inside any stellar envelope. A "grid" of synthetic spectra is constructed over a range of values for T_{eff} and log g. Each spectrum is then fitted to the optical observations, with the closest match between synthetic and observed spectra indicating the most probable description of gravity and temperature. Although the values of two free parameters are sought, the wide variety of processes which can affect line profiles make it necessary to use at least four absorption lines in order to find a unique solution; the lines of H_β H_γ, H_δ and H_ϵ are convenient for this purpose.

The value of log g can then be fixed, and a second grid of models calculated, in which heavy element abundances, and T_{eff}, are varied. This is an essential step since these abundances may affect the quality of fit between model and observation. A further complication is introduced when considering hot white dwarfs, where conditions are such that the assumption of local thermodynamic equilibrium (LTE) in the atmosphere is no longer appropriate. Local thermodynamic equilibrium is assumed in the case of relatively cool stars, where the number density of particles in the atmosphere is high enough so that collisions between particles occur frequently. Under these conditions, the average number of atoms in a given excitation state is dependent only on temperature, and the distribution of states is given by Boltzmann's equation, which can be stated as

$$n_{\rm i} = g_{\rm i} n_0 \exp\left(\frac{-E_{\rm i}}{k_{\rm B}T}\right), \tag{1.3}$$

where $n_{\rm i}$ is the number of particles in a state with energy $E_{\rm i}$ above the ground state energy, n_0 is the number of particles in the ground state, $g_{\rm i}$ is the statistical weight of the system (the number of states with the same energy), $k_{\rm B}$ is the Boltzmann constant, and T is the temperature of the system.

Local thermodynamic equilibrium also implies *ionisation equilibrium*, in which the rate of ionisation equals the rate of recombination. The number density N of atoms in an ionisation state i+1 is related to the number in the next lowest state by the Saha equation,

$$\left(\frac{N_{\rm i+1}}{N_{\rm i}}\right) = \left[\frac{A(k_{\rm B}T)^{3/2}}{N_e}\right] \exp\left(\frac{-\chi_{\rm i}}{k_{\rm B}T}\right), \tag{1.4}$$

where A is constant for a given atomic species, $\chi_{\rm i}$ is the ionisation potential for stage i, N_e is the electron density, and the other symbols have their usual meaning.

However, for high temperatures, radiative atomic transitions may dominate over collisional rates, leading to non-LTE (NLTE) effects such as emission in the cores of lines like H_α (Lanz & Hubeny, 1995). In a study considering the differences between LTE and NLTE models for a range of hot white dwarf and subdwarf stars, Napiwotzki (1997) showed that pure H models calculated for log *g* = 7.5 exhibited moderate NLTE effects for $T_{\rm eff} > 80,000$K, with perfect agreement between LTE and NLTE for $T_{\rm eff} < 70,000$K. The addition of trace quantities of He was found to have a significant effect, with departures from the LTE model (particularly in the Balmer lines) being observed at $T_{\rm eff} > 40,000$K. The choice of LTE or NLTE model therefore has a significant effect on the accuracy with which basic parameters are determined, and on the results of subsequent analysis. Originally, the majority of models assumed LTE conditions, but as computing power has increased and codes have become more sophisticated, non-LTE models have been developed, and with them an associated improvement in the quality of fit between model and observation gained. In the study of G191-B2B by Lanz *et al.* (1996), both LTE and non-LTE models were considered. The most significant influence on the estimated value of $T_{\rm eff}$ was found to be the choice of LTE or non-LTE code, with heavy element abundance being of lesser importance.

Following determination of $T_{\rm eff}$ and log *g*, attention can be turned to FUV and EUV wavelengths, where the majority of spectral features from heavy elements are found, and where the choice of metal abundance in the model becomes critical. An iterative procedure is adopted, in which an initial model produces a spectrum which is then refined by modification of abundances. He is incorporated as an atmospheric constituent, and also as a component in the ISM column. The interstellar He I, He II and H can be varied as free parameters in order to achieve the best fit. The column densities thus derived can then be compared with independently obtained values. Ionisation fractions (the ratio of He I to He II) are also useful diagnostics in estimating the accuracy of these fitted quantities.

1.5 Helium and heavy element abundances in white dwarf atmospheres

1.5.1 The presence of heavy elements in white dwarf spectra

As discussed in the preceding sections, models can only reproduce the spectra of certain white dwarfs if the effects of absorption from heavy elements are included. Given the powerful gravitational fields possessed by white dwarf stars, it was logical to suppose, in the early days of research, that the spectra of these objects would appear to be mono-elemental. This supposition was founded on the belief that heavy elements present in the star would diffuse out of the atmosphere under the influence of gravity, resulting in a spectrum devoid of heavy elements. White dwarf stars would then make ideal tools for studying the composition of the ISM, since interstellar material would produce conspicuous lines in the otherwise relatively featureless spectrum. However, beginning with the *IUE* observation of G191-B2B by Bruhweiler & Kondo (1981), highly ionised species incompatible with temperatures expected in the ISM, were observed in the spectra of many white dwarf stars. Observations in the soft X-ray and EUV revealed that the fluxes of white dwarfs in these wavelength ranges were lower than expected (e.g. Kahn *et al.*, 1984, Koester, 1989). Vennes *et al.* (1988) also showed that the shape of the Feige 24 EUV spectrum obtained by *EXOSAT* could only be explained by including heavy elements in the models. Results from the *ROSAT* all-sky survey suggested

that most white dwarfs with $T_{eff} \geq$ 40,000 K possessed atmospheres containing heavy elements (Barstow *et al.*, 1997c).

The presence of heavy element opacity in white dwarf spectra is generally explained in terms of radiative levitation theory, in which radiation pressure balances the diffusion of metals out of the atmosphere under the influence of gravity; model atmospheres must incorporate this theory in order to predict the form of individual features in white dwarf spectra, and to reproduce the modification of flux levels due to the overall opacity. Radiative levitation theory has succeeded in predicting which species should be present in the stellar spectra (Chayer *et al.*, 1994, 1995a,b), but obtaining accurate *quantitative* results has proved considerably more difficult, as described by Chayer *et al.* (1995b), and encountered in studies of specific objects (Barstow *et al.*, 1996, Lanz *et al.*, 1996). Radically different abundances are also observed in apparently similar stars, as demonstrated by the comparison between the cool DA GD 394, in which Si appears over-abundant compared to theoretically predicted values (Barstow *et al.*, 1996), and REJ 1614-085, a star of similar temperature and gravity with an unremarkable Si abundance, but with a large over-abundance of N (Holberg *et al.*, 1997c,b).

Lanz *et al.* (1996) produced the first successful model for the optical, FUV and EUV spectrum of G191-B2B using *EUVE* data. An accurate match to observation was achieved by including the effects of "line blanketing" to account for absorption by more than 9 million atomic transitions, the majority from Fe and Ni. These transitions absorb significant amounts of the energy emitted by the star, and explain the deficit in flux from hotter stars illustrated in figure 1.6. The resulting model is shown compared to the observational data in figure 1.7. However, the excellent agreement between observation and theory achieved in this work was only possible by including opacity from a large quantity of (unobserved) He II to suppress a flux excess below 228 Å. The material was initially assumed to be interstellar, yet while the value for the interstellar H I column was in agreement with independent estimates, the numbers suggested for He II appeared less reasonable, indicating a He ionisation fraction of 80%, over twice the value measured for other stars in the LISM. Such a high degree of ionisation in the cool ISM was difficult to explain. There was no evidence of material existing in a circumstellar shell, unlike the case of the star REJ 0457-281, a similar object in many respects (Barstow *et al.*, 1997c), and the suggestion was made that the He was photospheric. The absence of He II features could then be explained by blending with the many heavy element absorption features at the limited resolution of *EUVE* and *IUE*. This hypothesis was tested by computing new models in which the ratio of He to H (originally fixed) was allowed to vary; however, Lanz *et al.* (1996) found that the best-fit model also produced a He II line at 1640 Å, at a strength above *IUE* detection limits.

The substantial differences between observed and predicted abundances were, for some time, thought to be due to physical processes such as mass loss, or accretion of material around a star - for example, from the ISM or a circumstellar cloud (Holberg *et al.*, 1997a). Such processes would invalidate the assumption of equilibrium between gravity and radiation pressure in the stellar atmosphere - an assumption upon which model atmosphere calculations were based. Evidence for the possible presence of non-equilibrium processes is observed in comparatively few hot DA white dwarfs, and is a subject discussed in detail in Chapter 5. However, over the past few years, a promising alternative explanation for the differences between measured and predicted abundances has emerged, and relates to the fundamental structure of the atmosphere.

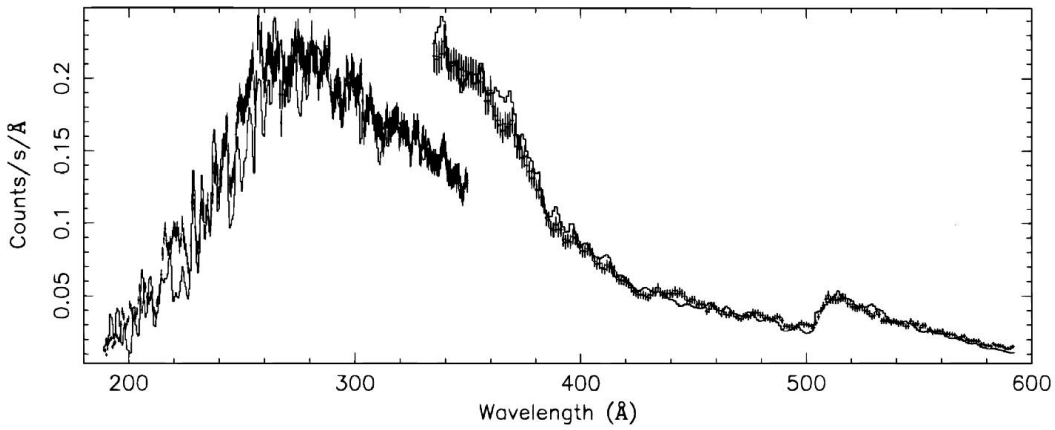

Figure 1.7: The EUV count spectrum of G191-B2B. Data points (error bars) are compared to the predictions of a best-fit model atmosphere calculated by Lanz *et al.* (1996). The discontinuity near 320 Å is a result of an overlap in spectrometer bandpasses, with differing effective areas. (Lanz *et al.*, 1996).

1.5.2 Stratification in white dwarf atmospheres

Early models made the simplifying assumption that white dwarf atmospheres were homogeneous mixtures of atomic species. In the late 1990's this premise was brought into question, and the possibility of a *stratified* distribution of material was raised. As Vennes *et al.* (1988) had shown, radiative levitation can support heavy elements such as C, N, O, Si, Fe and Ni in the upper atmosphere, but is less effective for He which has fewer atomic transitions, and therefore a smaller radiative cross section for levitation. As a result, He rapidly sinks out under the influence of gravity, leaving a thin layer of absorbing H overlying a He envelope, thus weakening the 1640 Å line. However, stratification is not only important for the distribution of He; quantities such as ionisation and radiation field intensity make the radiative cross sections of each element depth dependent (Dreizler & Wolff, 1999), and lead to an overall abundance stratification within the envelope.

In the investigation by Barstow & Hubeny (1998), a stratified H upon He atmosphere and a homogeneous mix of heavier elements was shown to reduce the strength of the 1640 Å line, providing an improved match to observational data. This model also brought the interstellar He ionisation fraction into line with values more typical of the local interstellar medium. However, He II Lyman line strengths were increased above the observational limit, and this situation could not be resolved without increasing the H-layer thickness, which in turn destroyed the overall match to the EUV continuum.

As the sophistication of stratified models has increased, so the results of these investigations have improved. At the 11^{th} European Workshop on White Dwarfs in June 1998, Barstow *et al.* (1999a) described the results of models in which the Fe abundance was stratified. The stellar atmosphere was divided into two or three discrete regions; the Fe abundance was fixed within each region, but levels were allowed to vary from one region to another (initial abundances being obtained from best-fit models to *EUVE* data). By increasing the quantity of Fe with depth, in contradiction to radiative levitation calculations, this "slab model" removed the excess flux shortward of 190 Å, the authors proposing a mechanism such as radiatively driven mass loss to explain depletion of Fe in the outer layers of the star. At the same time, this work demonstrated that a good match to the optical, FUV and EUV spectrum of G191-B2B could be obtained without recourse to excessive helium opacity.

Further credence was given to heavy element stratification by Dreizler & Wolff (1999), who used models in which gravitational settling and radiative levitation were calculated explicitly, relaxing the assumptions of homogeneously mixed trace elements and fixed flux distribution through the envelope. Again, the need for photospheric or interstellar helium to remove the short wavelength flux excess was diminished, and mass loss mechanisms also became unnecessary. Most recently, Dreizler & Schuh (2001) and Schuh & Dreizler (2001) reported the results of new models in which stratified abundances are established self-consistently, using an iterative approach which begins with a homogeneous atmosphere from which the temperature, density, radiation field and level populations are determined. These values are then used to calculate opacities which, when coupled with the radiation field, provide a quantification of the depth-dependent radiative forces. The results from this calculation then lead to abundance estimates, assuming balance between gravity and radiative acceleration, and are used as input to the next cycle of calculation. The process is repeated until changes between successive emergent spectra fall to a pre-defined level.

The results of this work have been successful in reproducing the soft X-ray, EUV and FUV spectra of a sample of DA stars including G191-B2B, and can explain the widely varying levels of metallicity in hot DA white dwarfs[5]. Agreement with observation is not complete, however. For example, lines of C, N and O are not reproduced as accurately as those of Fe and Ni, while no explanation was found for the compositional differences between stars with similar $\log g$ and $T_{\rm eff}$. Nevertheless, such stratified models, which are still in the relatively early stages of development, appear to offer a solution to the problem of inaccurate abundance predictions, and can remove the need for excess He II opacity to suppress the flux emitted below 228 Å in stars such as G191-B2B.

1.6 Motivation: where is the Helium in DA white dwarfs ?

Model atmospheres incorporating the stratification of heavy elements appear to provide at least partial solutions to some of the problems encountered in studies of hot DA white dwarfs. Specifically, the failure of equilibrium radiative levitation theories (such as those presented by Chayer *et al.*, 1995a) to quantitatively predict observed abundances appears to arise from the assumption that the heavy element content is mixed uniformly throughout the white dwarf atmosphere. Further, the stratification of Fe discussed by Barstow *et al.* (1999b) modifies the continuum profile of G191-B2B (and by inference, that of other stars) such that the flux at short EUV wavelengths (< 228 Å) is lower than predicted by earlier models. This obviates the need for excessive quantities of opacity from He II, bringing the line of sight He II column density and ionisation fraction into closer agreement with values more typical of the local ISM. These successes are particularly encouraging given that the introduction of stratified models to white dwarf research is a comparatively recent advance, and much work lies ahead in the testing and refinement of these codes.

Despite these improvements, problems relating to the helium content of DA white dwarfs remain. Although the division of the white dwarf population into H-rich and He-rich groups is beginning to be understood on the basis of the late- and post-AGB evolution of the progenitor stars (discussed briefly in section 1.1.4) the absence of He-rich white dwarfs with temperatures between $\sim 30,000 - 45,000$K (the DO/DB gap) is still a mystery. Direct

[5] Application of this same theory to the He-rich DO group shows much poorer agreement with observation, suggesting that DO stars do not possess stratified atmospheres (Dreizler & Schuh, 2001).

measurement of the abundance of photospheric He provides important information on the prior evolutionary history of the star. In progenitor stars with masses less than 8 $M_{\odot}$, helium is produced by core H-burning on the main sequence, and consumed again during the core He-burning phase, leading to a C/O core white dwarf progenitor on the AGB. Mass loss, and the creation of a planetary nebula, removes the outer layers of the star so that only the exposed core remains. The composition of the envelope, including the He abundance, is then determined by the results of core nucleosynthesis, shell-burning processes, and mass loss. Gravitational settling subsequently modifies the photospheric composition, allowing He to sink out of the atmosphere, resulting in the build up of an overlying layer of H. The He can only be detected if this H layer is sufficiently thin for the line-forming region to extend into the He layer.

In the H-rich CSPN, the immediate precursors of the H-rich DA white dwarfs, significant quantities of He are visible in the optical and UV spectra, with abundances (He/H) in the range $10^{-3} - 10^{-1}$. However, a serious problem for studies of white dwarf evolution is the non-detection of He in the atmospheres of isolated DA white dwarfs, which are the direct descendants of the H-rich CSPN. Helium can only be detected in the optical and far-UV wavebands if the homogeneous abundance exceeds a few times 10^{-5}. EUV spectroscopy provides a potentially more sensitive method of detection in the crucial region of the He II Lyman absorption series between 304 Å and the limit at 228 Å. Barstow *et al.* (1994a) use *EUVE* observations of the DA stars Feige 24, G191-B2B, GD 71 and GD 246 to place lower limits on the mass of the overlying H-strata of 2.4×10^{-13}, 2.6×10^{-13}, 3.0×10^{-12} and 9.7×10^{-14} $M_{\odot}$ respectively, and suggest an H-layer mass of $\approx 10^{-12}$ $M_{\odot}$ is required to prevent He lines from being observed in the EUV spectrum.

EUV spectroscopic studies of He in DA white dwarfs provide an important test of ideas about mass-loss on the AGB (which is difficult to observe) and subsequent diffusion and mixing in the atmosphere. Some evolutionary calculations predict that DA white dwarfs should be formed with comparatively massive H layers ($\sim 10^{-4}$ $M_{\odot}$, e.g. Iben & Tutukov, 1984). In this case the diffusion of He out of the atmosphere should render it undetectable in the EUV. The detection of He in an individual star would indicate that there is much less residual H than predicted or that there is unexpected mixing. Comparative abundance measurements in EUV, FUV and optical bands can determine the H/He structure (stratified H upon He or homogeneous H/He mixture) and distinguish between the two situations

One possible explanation for the lack of He in the spectra of stars such as G191-B2B is that the resolution of current instrumentation cannot resolve the He features from the forest of lines from heavy elements. Alternatively, the stratification of heavy elements in the atmosphere, as described in section 1.5, removes the signature of He from the stellar spectrum. These two ideas are not always presented as being mutually exclusive; although the model of Dreizler & Wolff (1999) does not require excessive quantities of He to reproduce the spectrum of G191-B2B, other work (Barstow & Hubeny, 1998, Barstow *et al.*, 1999b) combines these effects to produce similar results (though admittedly, this may be due to the less precise nature of the stratification and radiative levitation calculations included in these earlier studies). Many objects have proved similarly difficult to model; are both of these explanations correct, and at work in different stars?

1.7 Structure of the thesis

There exists a pressing need to determine whether or not significant quantities of He are present in white dwarf atmospheres. Finding He in a typical, isolated DA object would finally provide the link between the DA and DO/DB channels. Direct measurement of He abundances would also assist in the verification and development of stratification theories. Alternatively, the measurement of large abundances of He would support earlier models which required opacity from He II to suppress the flux from DA stars such as G191-B2B at shorter wavelengths. However, the current generation of instrumentation is incapable of resolving He lines from the vast numbers of heavy element features.

Determining whether or not He is really present and, if so, its location, requires an instrument with an EUV resolving power $\lambda/\Delta\lambda = 5000$, exceeding the capability of currently available facilities (i.e. $\lambda/\Delta\lambda \sim 235$ at 235 Å with *EUVE*). The design for such an instrument exists: *J-PEX*, a near-normal incidence EUV spectrometer, is an ideal instrument for this application, and the first flight of this device, on board a sounding rocket, is devoted to the study of G191-B2B. *J-PEX* is discussed in Chapter 2. Much of the material in this thesis is concerned with the development of *J-PEX*, with particular emphasis on the focal plane detector, built and developed in a collaboration between the University of Leicester and Mullard Space Science Laboratory (MSSL), London. With the limited exposure time available on sounding rocket flights, maximum efficiency is required from the detector in order to achieve an adequate signal-to-noise ratio (S/N) in the stellar spectrum obtained by the instrument. Chapter 3 is devoted to an investigation into methods of increasing the sensitivity of microchannel plates, and the selection of a suitable process for application to the MCPs installed in the *J-PEX* detector. Development and calibration of the detector itself is discussed in Chapter 4.

The apparent success of stratification theories presents an interesting problem relating to the highly ionised features at non-photospheric velocities observed in many He-rich white dwarfs, and a small number of DA objects. One suggestion for the failure of earlier radiative levitation models to quantitatively predict heavy element abundances in white dwarf envelopes, was the presence of processes such as mass loss and accretion, which modified the equilibrium abundances in certain stars. The circumstellar features observed in some white dwarfs could then be qualitatively understood as the signature of such processes. Heavy element stratification may eventually provide an alternative explanation for the observed abundances, but highly ionised circumstellar features remain. In Chapter 5, a sample of white dwarf spectra at UV wavelengths, acquired from the *STIS* spectrometer on the Hubble Space Telescope (HST), from a previous HST instrument (*GHRS*), and from *IUE*, are examined for signs of these features; possible explanations for their presence in some objects, and absence in others, are discussed. This work is also important for the interpretation of data returned from *J-PEX*, which operates at shorter wavelengths. Since the resolution of *STIS* is significantly higher than that of *J-PEX* (which is still in the early stages of development), the data are more sensitive to the presence of multiple velocity components in absorption features. The *STIS* study therefore provides important information on the distribution of material along the line of sight, and can assist in determining the location (stellar or interstellar) of material detected by *J-PEX*.

The culmination of work on the *J-PEX* spectrometer is presented in Chapter 6, in which the reduction and analysis

of data from the first successful flight is presented. At the time of writing, this work is still "in progress", but the preliminary results already demonstrate the significant contribution which *J-PEX* can make to the study of white dwarf stars (and many other fields of astrophysics), and provide new information about the nature of G191-B2B and the DA white dwarfs.

1.8 Summary

- White dwarf stars represent the evolutionary endpoints for the majority of stars, including the Sun. A comprehensive understanding of their formation and the physical processes which govern their appearance, is essential if we are to understand stellar evolution (and, by implication, galactic evolution) in a broader sense. Lack of any major energy generation mechanism makes the white dwarf a useful tool in determining cosmological ages.

- As degenerate objects, white dwarfs belong to the same family as neutron stars and black holes. The exotic conditions within these objects make them ideal laboratories in which to study fields such as nuclear physics, testing theories using the extreme temperatures and densities which are impossible to recreate in terrestrial laboratories.

- Helium is a primordial element, and the product of nucleosynthesis. He is detected in significant quantities in the H-rich central stars of planetary nebulæ, which are the precursors of the H-rich DA white dwarfs. Nevertheless, all attempts to detect He in typical, isolated DA objects have failed. Theories also suggest that the stars "missing" from the He-rich sequence between 28,000K and 45,000K may reside in the DA channel. Only above 45,000K is radiation pressure sufficient to suspend significant quantities of He in the upper atmosphere; below 28,000K, convective mixing dredges up He from the lower regions of the gaseous envelope to restore the He-rich appearance of the star. Thus, appreciable quantities of He should be present in some DA white dwarfs within this temperature range; none has yet been found.

- Recent models which include heavy element stratification can explain some of the features in white dwarf atmospheres. The quantitative predictions of heavy element abundances are an improvement on those produced by earlier theories which assumed a homogeneous mixture of material in the atmosphere, and short wavelength flux levels are in much closer agreement with observations. The precise measurement of He abundances and location (interstellar, circumstellar or photospheric) would assist in confirming the validity of stratification theories, as well as contributing to their ongoing development.

- Failure to detect He in DA white dwarf stars might be attributed to the inability of current instrumentation to resolve He absorption lines. At the resolution of currently available instruments, these lines may be blended with the large number of heavy element features present as a result of radiative levitation in the atmosphere. New, high resolution instrumentation is therefore required to provide the first direct measurement of He abundance in the atmosphere of an isolated DA white dwarf.

CHAPTER 2

THE JOINT ASTROPHYSICAL PLASMADYNAMIC EXPERIMENT

2.1 Introduction

THE JOINT ASTROPHYSICAL PLASMADYNAMIC EXPERIMENT (*J-PEX*) is a project designed to provide answers to the questions posed in Chapter 1: is there helium in the atmosphere of G191-B2B and, by implication, in other isolated hot DA white dwarf stars? These answers are to be found through the development and flight of a new class of spectrometer, producing a resolution surpassing that of any currently available instrument. *J-PEX* is a project run as a collaboration between the University of Leicester (UL), the U.S.Naval Research Laboratory (NRL), Lawrence Livermore National Laboratory (LLNL) and Mullard Space Science Laboratory (MSSL). The *J-PEX* sounding rocket payload represents one of the first in a new generation of instruments employing multilayer optics operating at near-normal incidence. The payload design is shown in figure 2.1, and in this chapter, the individual components which make up the spectrometer will be discussed in more detail. Development work on the microchannel plate (MCP) detector, the specific responsibility of the University of Leicester, will be covered in Chapter 3.

2.2 Instrument design

Instruments flown on earlier spacecraft such as *EUVE* used traditional Wolter mirrors and separate dispersion elements. Operating at grazing incidence dramatically reduces the geometric area for a given aperture, and nests of mirrors give relatively poor returns for a large investment in mass and total area. Separate dispersion gratings are also not ideal, since they introduce an extra reflection in the light path, and hence a further reduction in throughput.

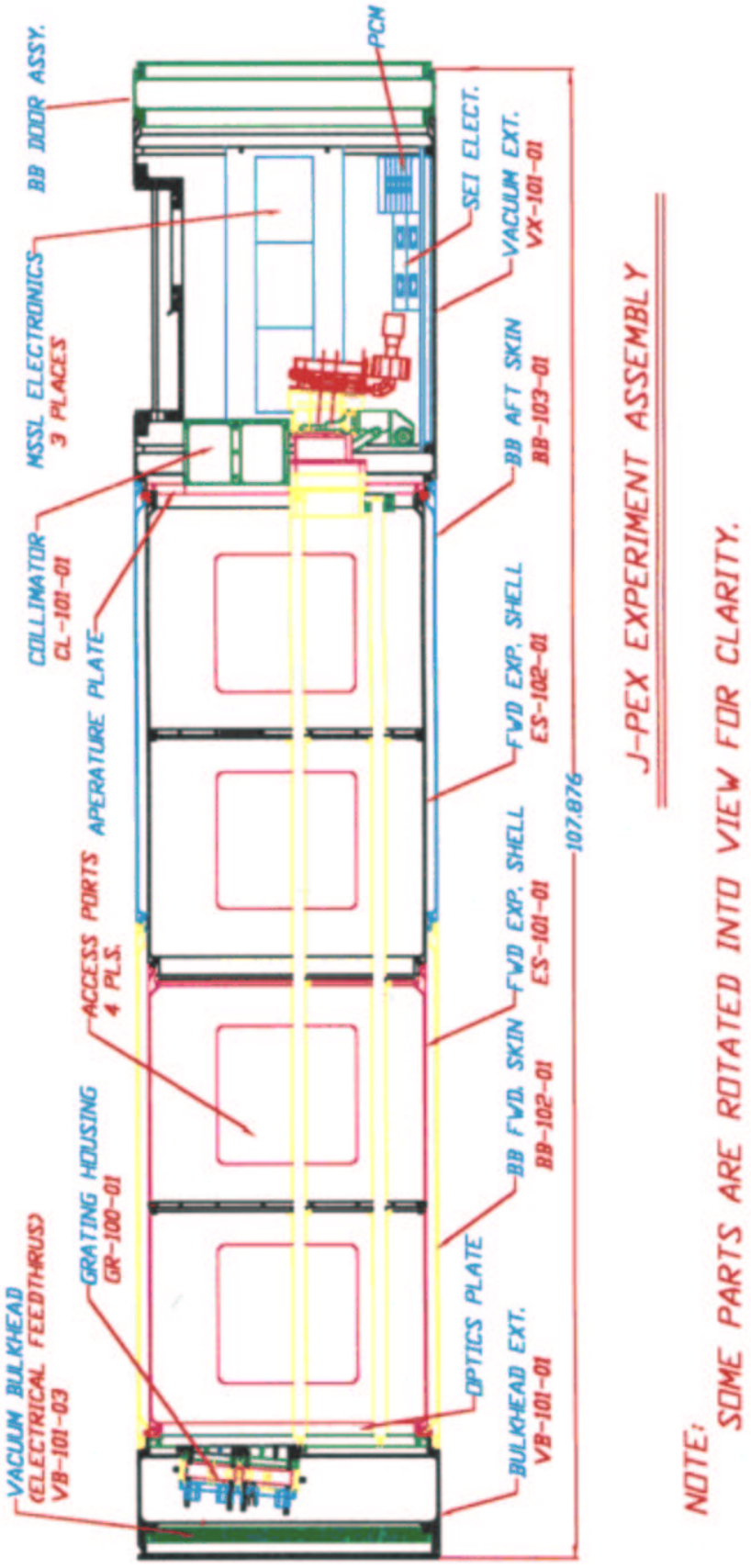

Figure 2.1: Schematic view of *J-PEX*

These problems are neatly addressed in *J-PEX* through the use of multilayer coated gratings which perform the tasks of light collection *and* dispersion. The design is a slitless Wadsworth mount, which is a derivation of a similar instrument used in NRL's Skylab S082A spectroheliograph. At the heart of this spectrometer lies a set of reflection gratings manufactured by Carl Zeiss. The four gratings have identical multilayer coatings which were developed at NRL and LLNL, are ion etched to achieve a highly precise, reproducible laminar profile with 3600 lines mm^{-1}, and are spherically figured with a 2m focal length. The design enables *J-PEX* to achieve an effective area of $\sim$5 cm^2 and a resolving power of 4700 at 235 Å (more than ten times that of *EUVE*). Four gratings are used, each of area 8 x 16 cm (the largest size which can currently be manufactured). They produce four individual spectra which are co-added *post facto*, to produce a spectrum equivalent to that from a single element with a total geometrical area of 512 cm^2.

Figure 2.1 illustrates the optical path of the spectrometer. Light from the target passes through a collimator which minimizes the geocoronal EUV background flux entering the system. It is then collected by the gratings, which disperse the beam and focus the spectrum onto an MCP detector, mounted along the grating optical axis to minimize aberrations. The detector contains two microchannel plates mounted in a chevron configuration. The front MCP is coated with a photocathode to enhance detection efficiency, and an aluminium filter is mounted in front of the detector to absorb any residual EUV background radiation scattered by the gratings. Imaging is by means of a progressive geometry Vernier conductive anode readout which, along with the electronics and HV supply, has been developed and supplied by MSSL. The entire detector assembly is mounted in its own vacuum chamber with an integral ion pump and a motorized door. The spatial resolution of the detector is better than 18 μm, and much of the work presented in the following chapters concerns development of this detector at the University of Leicester.

The sounding rocket attitude control system (ACS) permits highly precise pointing and target tracking. However, there are residual drifts in pointing which, if unchecked, would smear the spectrum and reduce resolution. *J-PEX* is therefore equipped with an optical telescope, consisting of a spherical mirror of 12.5 cm diameter and 2m focal length, and a CCD detector adapted from a design flown on the *Clementine* lunar mission. By imaging the target throughout the period of observation, this telescope provides the means to reconstruct a fine aspect solution. Also included in the design is an EUV mirror which forms an image of the target star on the MCP detector, providing redundancy and cross-checking of aspect reconstruction. The optical path is shown in figure 2.2, and in the sections which follow, each component is examined in closer detail.

2.2.1 Multilayer coated gratings

At the heart of *J-PEX* are four gratings configured for use in the EUV. These gratings collect and disperse light from the target star, focusing four separate spectra onto the MCP detector, which is positioned near the entrance aperture. The four tracks are combined post-flight to produce a single, high signal-to-noise spectrum. Several authors have described the design and operation of multilayer coated gratings in some detail (Barbee, 1989, Kowalski *et al.*, 1996), but since the innovative nature of the *J-PEX* spectrometer owes much to these devices, it is appropriate to provide an overview of the basic principles underlying such gratings here.

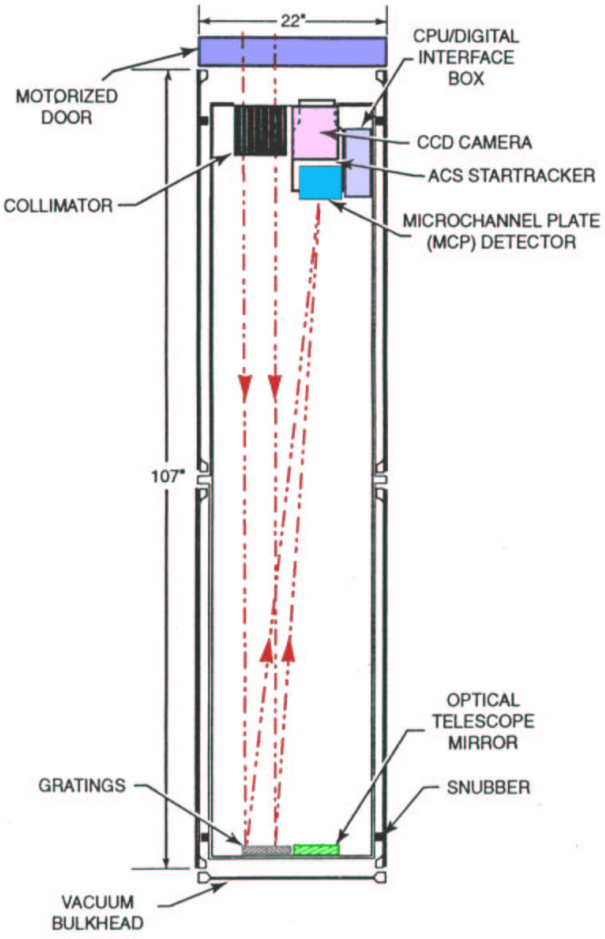

Figure 2.2: Cutaway of the *J-PEX* spectrometer, showing the optical path of the near-normal incidence optics.

Development of the first diffraction grating for astronomical use is attributed to the American astronomer David Rittenhouse, around the year 1785 (Hecht, 1987). However, it was the German physicist Joseph von Fraunhofer who, having independently rediscovered the principle some years later, made some of the first significant spectroscopic observations by using a grating spectrometer to map absorption lines in the solar photospheric continuum - lines which now bear Fraunhofer's name.

Several varieties of diffraction grating exist. Some are used in transmission, while others (including those onboard *J-PEX*) are reflection gratings. All rely on the modulation of either amplitude or phase (as in the case of *J-PEX*) of the incident radiation. Until relatively recently, most gratings were produced by ruling a periodic pattern of lines into a thin film of aluminium, evaporated onto the surface of an optically flat glass blank. Light reflected from these periodic structures arrives at the imaging plane with a definite phase relationship, as shown in figure 2.3.

The type of device shown in figure 2.3 is known as a *laminar* grating, referring to the flat profile of the diffracting structures; the gratings employed by *J-PEX* are of this type. By considering the difference in path length between the two incident rays, the generalized grating equation can be derived; from the figure, this is simply

$$\overrightarrow{ab} - \overrightarrow{cd} = s \times n \times (cos\ \beta - cos\ \alpha), \tag{2.1}$$

where *s* is the grating line spacing, α is the angle of incidence, β is the angle of the refracted ray (both measured with respect to the plane of the grating surface), and n is the *average* refractive index of the grating medium. These angles are related to the angles in vacuum by Snell's law,

$$n\cos\beta = \cos\beta_v,$$
$$n\cos\alpha = \cos\alpha_v,$$

where the v subscript indicates an angle *in vacuum*. For constructive interference, the path difference must be equal to an integer multiple of the wavelength of interest (λ), and so the grating equation may be stated as

$$m\frac{\lambda}{n} = s(\cos\ \beta - \cos\ \alpha), \tag{2.2}$$

where *m* specifies the *order* of the various principal maxima in the diffraction pattern.

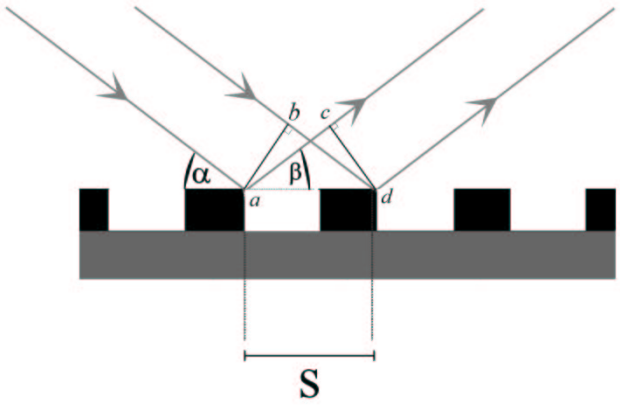

Figure 2.3: Operation of a laminar grating

2.2.1.1 Multilayer coatings

The extreme ultraviolet region of the electromagnetic spectrum has proved to be one of the more challenging areas in which to conduct studies. At wavelengths below approximately 20 Å, X-ray spectroscopy can be achieved using Bragg diffraction in appropriately chosen crystals; above $\simeq$300 Å, normal incidence optics become useful (Ridgeley, 1992). Occupying the region in which neither of these methods are suitable, EUV studies have traditionally exploited optical designs based upon grazing incidence geometry, and have thus suffered from the disadvantages which accompany such instruments (for instance, limited collecting area, the need for cumbersome systems of nested mirrors, and complex manufacturing procedures). Gratings are themselves reliant upon reflection of photons from the facet surfaces, and have therefore seen little use in the EUV. However, the relatively recent development of multilayer coatings with high normal incidence reflectance in the EUV has transformed this field, and through the application of such multilayers to diffraction gratings, high performance normal-incidence

instrumentation in the extreme ultraviolet is now possible. By incorporating these developments, *J-PEX* represents a milestone in the evolution of high energy space instrumentation.

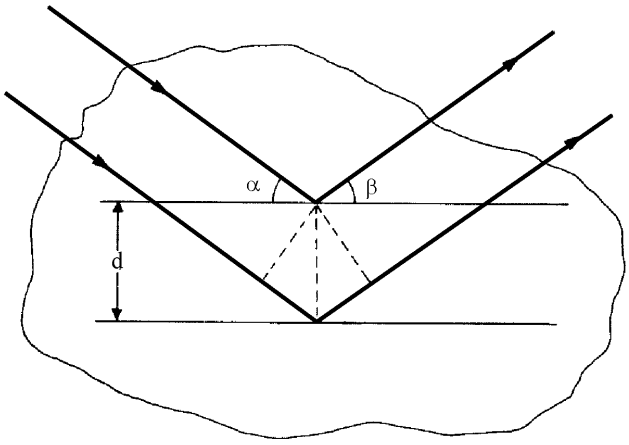

Figure 2.4: Bragg reflection

A search of the current literature reveals much information on the use of multilayers in the EUV. Explanations of the theory and application of such systems are given in varying levels of detail by Barbee (1989), Rife *et al.* (1989), Keski-Kuha *et al.* (1990) and André *et al.* (1992), while the efficiencies of multilayer gratings are addressed by Thomas *et al.* (1991), Seely *et al.* (1995) and Kowalski *et al.* (1997) amongst others.

The primary purpose of applying multilayers to a diffraction grating is the enhancement in reflectivity, through Bragg reflection from the surface coating. Figure 2.4 shows two adjacent layers in a crystalline structure (or multilayer). The angles α and β are again the angles of incidence and refraction respectively, and it is clear that the condition for constructive interference in such a structure (the *Bragg condition*) is

$$p\frac{\lambda}{n} = d(\sin\ \beta + \sin\ \alpha), \tag{2.3}$$

where p is the diffraction order. The Bragg equation is typically given for the most common case where the angles of incidence and reflection are equal, i.e.

$$p\frac{\lambda}{n} = 2d\sin\alpha. \tag{2.4}$$

Following the derivation given by André *et al.* (1992), combining equations 2.2 and 2.3, the condition for constructive interference in a laminar, multilayer grating is found to be

$$p\frac{\lambda}{n} = d\sin\alpha\left[1 + \sqrt{1 - 2\frac{\cos\alpha}{\sin^2\alpha}\frac{\lambda m}{ns} - \frac{1}{\sin^2\alpha}\left(\frac{\lambda m}{ns}\right)^2}\right]. \tag{2.5}$$

Equation 2.5 is particularly important, illustrating as it does the interdependence of the grating line density and the multilayer period. A further important property of multilayer gratings can be appreciated by considering the

analogy with a simple symmetric transmission grating, as suggested by Barbee (1989) and illustrated in figure 2.5. Here the angle of the m^{th} order refracted ray is expressed in terms of the angle of the zeroth order (which is simply equal to the angle of incidence in a laminar grating), and an additional angle, ϕ_m, which represents the angle between the zeroth order refracted ray and the m^{th} order diffracted ray.

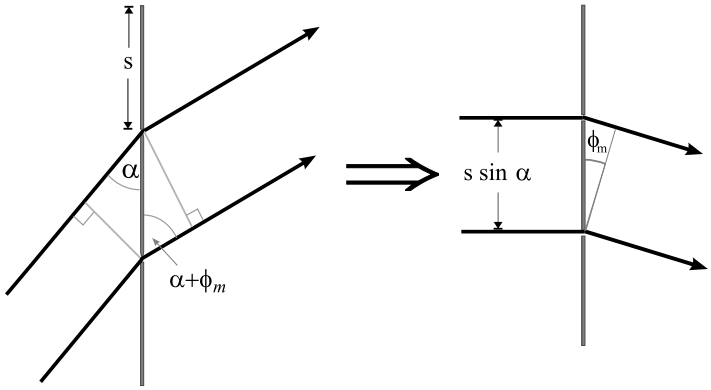

Figure 2.5: An alternative treatment of the multilayer laminar grating, after Barbee (1989).

Following the treatment given by Barbee (1989), a grating in which light is incident at angle α is equivalent to one in which the incident light is at normal incidence, but in which the grating period is reduced by a factor $\sin\alpha$. The grating equation expressed in these terms becomes

$$m\frac{\lambda}{n} = s\sin\alpha\sin\phi_m, \tag{2.6}$$

and combining this expression with the Bragg condition (2.4) yields

$$\sin\phi_m = \frac{2dm}{sp}, \tag{2.7}$$

demonstrating that, as a result of combining the periodicity of the multilayer and the grating, the dispersion angle of the m^{th} order is independent of the angle of incidence, and the wavelength, of the incoming beam. As Barbee (1989) states, it is this property which makes multilayer gratings such a powerful tool in EUV and X-ray instrumentation, not least because of the simplicity which this independence introduces into the optical design.

2.2.1.2 J-PEX Grating manufacture

As described by Kowalski *et al.* (1999), each of the four flight gratings was manufactured by Carl Zeiss using fused silica substrates with dimensions 160mm x 90mm x 20mm. A spherical figure was ground onto one of the 160mm x 90mm faces of each substrate, to produce a 2.2m focal length. Grooves were etched into the substrate using a two-stage process, in which the figured surface was first coated with a 1000 Å thick layer of photoresistive material. The grooves were then holographically recorded onto this layer by shining two monochromatic plane waves with $\lambda = 4880$ Å onto the surface, such that an interference pattern was produced with a period equal to the

desired line density (3599 lines mm^{-1}), and yielding a positional accuracy better than 5×10^{-6} of that density[1].

The photoresistive layer was developed, revealing the silica surface wherever an interference maximum had occurred. A collimated Ar-ion beam with an energy of 300 eV was then used to etch away the lines of exposed silica, producing grooves with an average depth of 62 Å. After etching, the residual photoresist stripes were removed in a series of chemical cleaning steps. The entire surface was then cleaned in order to permit maximum adhesion of the multilayer coating when applied. Figure 2.6 shows the surface profile of one of the completed (but not coated) flight gratings.

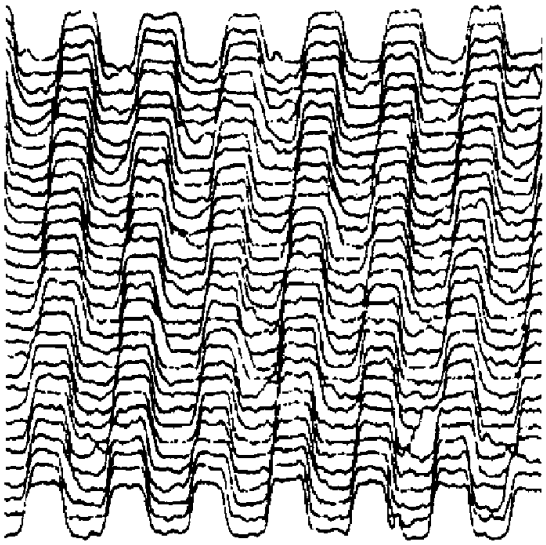

Figure 2.6: Surface profile of one of the *J-PEX* flight gratings prior to multilayer coating. The image size is 2μm square, and the average groove depth is 73 Å. (From Kowalski *et al.*, 1999.)

A molybdenum + silicon multilayer coating was applied to the gratings by sputter deposition in a vacuum facility at the Lawrence Livermore National Laboratory. Each grating was fitted to a rotating turntable inside the chamber, offset from the turntable rotation axis with the figured surface facing Mo and Si sources. At appropriate points during each orbit, shutters were opened to expose the grating surface to the sources, producing eight Mo + Si layers with a period of 125.8 Å, each Molybdenum stratum being 35 Å in depth. Since any oxidation of the coating would result in a dramatic loss of efficiency, the surface was finally sealed with a 10 Å thick layer of carbon.

Grating efficiency was measured using a synchrotron beam at the Brookhaven National laboratory, using a transfer-standard GaAsP photodiode as a reference counter; the results of these measurements are shown in figure 2.7. Kowalski *et al.* (1999) report the maximum efficiency as 11.7% at 234 Å, which at the time of publishing was the highest efficiency obtained from any grating at that wavelength. A useful figure of merit for multilayer gratings is the *grating groove efficiency*, defined as the ratio of the measured grating efficiency to the multilayer reflectance. For flight grating N$^{o.}$ 1, this efficiency is between 33.0% and 39.2%, impressively close to the theoretical maximum of 40.5% (Kowalski *et al.*, 1997).

Six gratings were manufactured, from which four were selected as flight units. The average reflectance of these

[1] A 10mm x 154mm region of lower ruling density (154.83 lines mm^{-1}) was also included along one edge of each grating as an alignment aid.

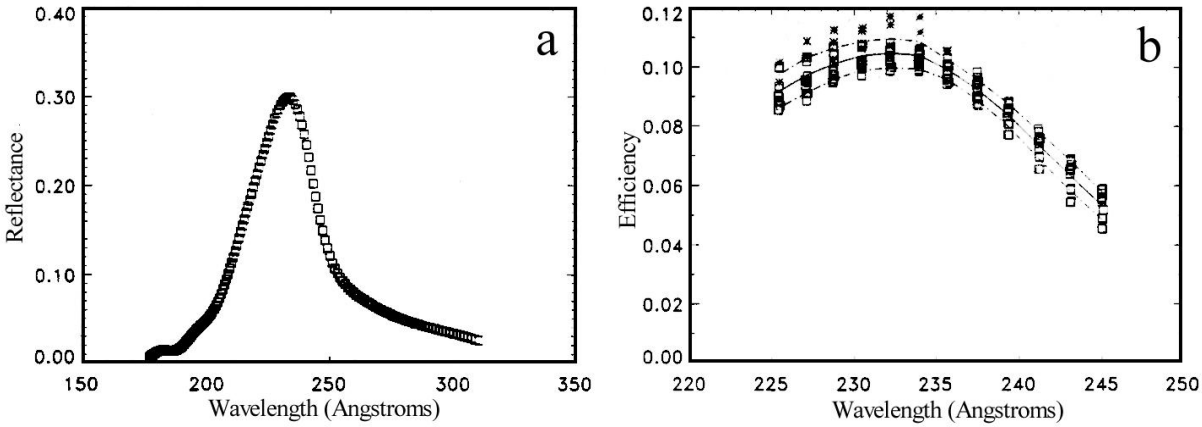

Figure 2.7: (a) Reflectance profile of the multilayer applied to each grating, measured from a witness flat coated in an identical procedure. (b) Efficiency of a grating measured at the angle to be used in flight (first inside order at 5° incidence angle). The curve shows efficiency measured at 17 positions across the grating; crosses correspond to locations near the alignment rulings. (From Kowalski *et al.*, 1999.)

gratings was measured at the central wavelength of 235 Å, and was found to be 10%, 7%, 9% and 8% for gratings 1, 3, 4 and 6 respectively.

2.2.2 Collimators

Judicious design of components such as the gratings and microchannel plate detector, ensures maximum sensitivity of the instrument to radiation in the wavelength region of interest. However, the background sky is not perfectly black at EUV wavelengths; instead there exists a bright, diffuse glow due to scattered sunlight. This radiation is dominated by solar photons scattered by neutral H and He atoms in the interplanetary medium, producing lines at 1216 Å (Ly-α) and 584 Å respectively, and also from geocoronal He II, introducing an emission line at 304 Å (Adams & Frisch, 1977, Labov & Bowyer, 1991). Admission of this radiation into the instrument is undesirable, since background flux falling onto the detector degrades the signal-to-noise ratio of an accumulated spectrum. The EUV background flux into the instrument is considerably reduced by limiting the field of view, using a collimator fitted over the grating aperture, and also over the entrance to the EUV telescope (figure 2.8). A detailed account of the collimator manufacture is given by Golembiewski *et al.* (1998), and is summarized here.

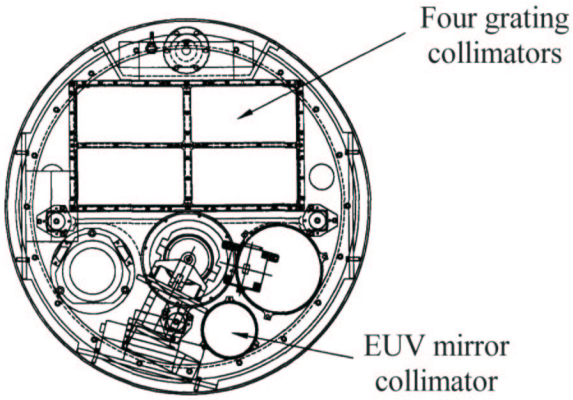

Figure 2.8: Location of the four grating collimators and EUV collimator in *J-PEX*

All collimator elements were custom-fabricated from a series of 25.4 μm thick copper sheets, each of which was corrugated with a half-hexagon profile using a pair of metal rollers with the appropriate surface relief. Collimators were built up by taking pairs of these corrugated sheets and aligning them in precisely formed aluminium mandrels, then joining together with an epoxy resin to form hollow wafers with hexagonal cross-sections. Large numbers of these wafers were then stacked on top of each other to produce the basic honeycomb collimator structure.

Since the reflectance of copper is relatively high at EUV wavelengths, the collimator walls are coated with an absorbtive material to inhibit background photons entering the instrument by successive reflections down the cell walls. EUV reflectivity of the collimator was reduced by a factor of 100 using a commercially available coating process.

The four rectangular collimators serving each of the four diffraction gratings were assembled into a frame and thence into the spectrometer, without further processing. However, due to the paucity of free space around the instrument aperture plate, a cylindrical collimator was required for the EUV telescope such that it could be installed *inside* the telescope tube. The extreme fragility of the assembled collimators prevented cutting the element to the required shape without crushing or deformation. This problem was solved by filling the collimator with wax to provide mechanical stability. The resulting rigid block was then cut to the required shape before being heated to melt and remove the wax, leaving behind the finished, circular collimator.

The basic steps in collimator manufacture are illustrated in figure 2.9. Each completed collimator consists of a honeycomb structure, with cells 0.254 cm in diameter and 11.43 cm in length producing a field of view of 1.2° full width at half maximum (FWHM).

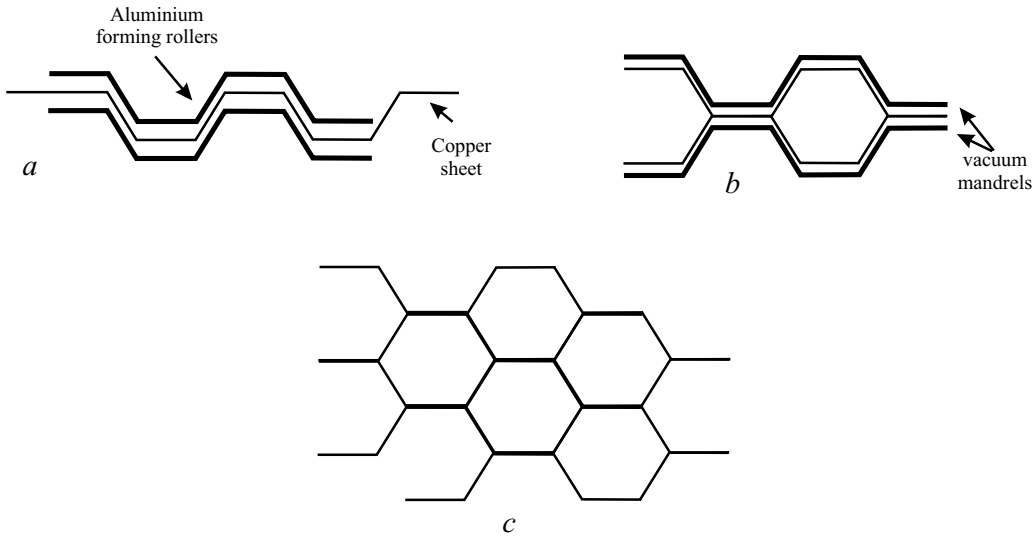

Figure 2.9: Principle steps in the manufacture of a *J-PEX* collimator. (a) Copper sheets pressed into shape between metal rollers. (b) Formed sheets held onto positioning mandrels by vacuum, and epoxied together. (c) Single honeycomb wafers epoxied to form complete collimator structure.

2.2.3 Optical telescope

The purpose of the optical telescope is to track "jitter" produced by the limitations of the rocket's attitude control system (ACS). These small scale random motions, of order 1 arcsecond per second, cause smearing of the spectrum which would lead to unacceptable degradation in spectral resolution if neglected. By recording the movement of the stellar image in the focal plane, post-flight aspect reconstruction is possible, effectively deconvolving this motion from the data, and shifting events displaced by jitter into their correct location.

The telescope is a prime focus system consisting of a 125mm diameter, 2000mm focal length mirror of fused silica, treated with a coating of Al/MgF to enhance UV reflectance. The mirror is used off-axis, allowing the imaging CCD detector to be placed off-centre in the telescope aperture, reducing loss in effective area by keeping obstructions such as mounting hardware, to a minimum.

The CCD detector is a modified form of units flown on the *Clementine* lunar mapping mission. Prepared at the Lawrence Livermore National Laboratory, the detector uses a Thompson 384 x 288 pixel CCD coated with a 10,000 Å thick phosphor layer to enhance sensitivity at FUV wavelengths. Each pixel measures 23 μm on a side, resulting in an array 8.8 x 6.6mm in size. The nominal CCD operating temperature is -25° C, and so the device is attached via a braided copper strap, to a cold-block fitted to the payload skin. Liquid CO_2 is flowed for several hours to cool the block, adopting a regulated flow/no flow duty cycle to prevent over-cooling. The time taken for the cold block + CCD to return to ambient temperature is long enough to allow continuous camera operation throughout the flight without the need for in-flight cooling.

The accuracy of aspect reconstruction is determined fundamentally by the size of a single CCD pixel. Neglecting grating aberrations, and summing the CCD pixel size in quadrature with the spatial resolution of the MCP detector (approximately 18 μm) produces an effective resolution of $\sqrt{18^2 + 23^2} = 29.2$ μm, or approximately 0.041 Å given the nominal dispersion at the spectrometer focal plane (1.389 Å μm^{-1}). Each CCD pixel subtends an angle of 2.4 arcseconds (f = 2.0m), so that given the estimated ACS drift rate of 2 arcsec sec^{-1}, CCD integrations of 1 second duration are required for optimum aspect reconstruction. The true frame rate is 0.998 Hz, accounting for the finite time required to perform frame shift and image readout.

2.2.4 EUV mirror

The demands of high resolution spectroscopy mean that mission success depends on the availability of adequate data for aspect reconstruction. Although the optical telescope described above is the primary source of these data, provision of a backup system is clearly a prudent measure, and this is available in the form of a second spherical mirror with a multilayer coating identical to that applied to the gratings. The EUV mirror specifications are presented in table 2.1.

The EUV mirror entrance aperture is fitted with a collimator identical to that serving the four gratings. Light incident on the mirror from the target star is reflected to the focal point, which falls within the active area of the main MCP detector, and places the stellar image near one corner of the region occupied by the four spectral tracks.

ITEM	DESCRIPTION
Spherical mirror	Fused silica
Focal length	2015.5mm
Diameter	80.0mm
Accuracy	1/4 wave
Coating	Mo + Si multilayer

Table 2.1: Specifications of the EUV mirror.

The optics are mounted on a common rigid plate, with the MCP detector and CCD camera attached to each other. Therefore the stellar image formed by the EUV mirror is subject to the same motion as the spectra, and hence may also be used to deconvolve the effects of spacecraft jitter from the data.

2.2.5 Attitude Control System

Although not strictly part of the *J-PEX* instrument, belonging instead to the set of systems serving the launch vehicle, the attitude control system (ACS) controls the fine pointing of the instrument, and therefore warrants brief description.

The ACS is a mark VI version of the unit produced by Aerojet Corporation of Sacramento, California. The system provides pointing control to the payload via cold gas thrusters, which use high pressure (≥ 7000 psi) Argon as the reaction material. Two sets of thrusters are installed in the vehicle, providing fine and course pitch, yaw and roll manoeuvrability. These thrusters are activated according to data sent back to the ACS by attitude sensors.

Attitude sensing is provided by gyroscopes and a star tracker. Two groups of twin-axis gyroscopes pass attitude information to the system from the moment of launch. Following separation of the second stage booster (the Black Brant sustainer), they rotate the instrument approximately 180° in pitch, to point in the direction of the first reference star (Sirius, or α CMa), approximately 111 seconds into the flight. Control is then passed from gyros to the star tracker. This device consists of a focusing lens coupled to a photomultiplier tube, the output of which is raster-scanned by a video camera-like device which sends positional information about the stellar image back to the ACS. The star tracker attempts to position the stellar image in the centre of the field of view by appropriate use of the gas thrusters in a closed-loop system, before moving on to acquire and center the second star (Capella, or α Aur).

Acquisition of the two reference stars provides a new 3-axis inertial reference frame for the ACS. Control is then passed back to the gyros, the positional resolution of which considerably exceeds that of the star tracker (the latter also being of limited use in sensing faint stars such as G191-B2B). The ACS then uses inertial information to acquire the target, positioning the star in the centre of the field of view inside a 2 arcminute diameter error circle. The expected drift rate once on-target, due to gyro limitations, is approximately 1 arcsec s^{-1}.

Continuous pointing information is available throughout the observation via the CCD camera and MCP detector images, which are displayed at the ground station in real time. Should these images reveal that the instrument is off-target (e.g. due to excessive gyro drift or an error in the initial pointing phase), uplink commands may be sent

to control the ACS manually, and attempts made to steer the instrument back on-target.

Also related to attitude control are two further systems. The boost-guidance system ("S-19") positioned behind the ACS module uses four canard winglets to provide fine-steering for the first 18 seconds of the flight, at which point the winglets are decoupled and provide no further guidance. This system reduces the error in estimates of the uprange payload impact position, and can thus extend the range of conditions in which a launch can take place.

Finally, despin of the payload to 0.0 Hz is achieved through the use of two "yo-yo's", metal weights attached to wires and fixed to opposite sides of the Black Brant booster near the joint with the payload. These weights are deployed using pyrotechnic devices at T+62 seconds into the flight. Centripetal force then carries the weights away from the vehicle, absorbing its angular momentum. Residual spin is then corrected by the ACS.

2.2.6 Microchannel plate detector

The tasks of EUV photon detection and imagery are performed by the combination of a microchannel plate (MCP) detector and Vernier anode readout system. The MCP detector was designed and built at the University of Leicester, while the anode and readout electronics were developed at MSSL. The genesis of the detector is related in Chapter 4, and a simplified schematic of the instrument design is shown in figure 2.10.

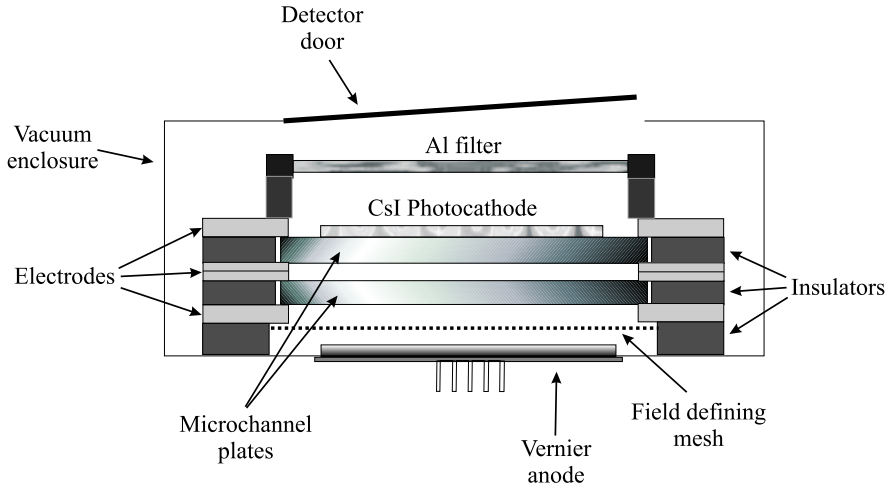

Figure 2.10: Schematic of the *J-PEX* MCP detector design (ion pump and high voltage connections omitted for clarity).

The detector consists of a pair of microchannel plates arranged in the conventional chevron configuration. The upper face of the front MCP is coated with a layer of Caesium Iodide (CsI) to a depth of 10,000 Å, acting as a photocathode to enhance the sensitivity of the detector at EUV wavelengths. A thin ($\simeq 1100$ Å) aluminium filter is installed above the MCP stack to absorb EUV background radiation scattered into the detector by the gratings; the transmission of this filter is approximately 50% in the 225 – 245 Å band covered by *J-PEX*, while it effectively blocks wavelengths longer than ~ 800 Å. A more detailed discussion of this filter, including a transmission curve, is reserved for Chapter 4.

The Vernier anode sits behind the rear MCP, forming part of the vacuum enclosure. This anode, with its associated electronics, converts events amplified by the MCP stack into the positional information which will ultimately be

interpreted as the stellar spectrum or image. In between the anode and the rear MCP is a fine metal grid, which serves to establish an electric field used to "tune" the trajectory of electrons in the rear of the detector - an important step in achieving the best possible spatial resolution from the system.

The entire detector sits in its own vacuum chamber, equipped with an integral ion pump (not shown in figure 2.10), allowing a high quality vacuum to be established prior to launch. This reduces the possibility of detector failure from electrical breakdown in a partial pressure environment during flight, and also allows detector operations to continue during the integration phase of the program, whether or not the spectrometer assembly is under vacuum. Maintenance of a vacuum inside the detector is also crucial for preservation of the CsI photocathode, which is hygroscopic, and is destroyed if exposed to air.

Light is admitted into the detector by means of an electrically operated, hermetically sealed door fitted to the front of the detector vacuum enclosure. This door opens after launch, when the pressure in the main spectrometer chamber is low enough to present negligible risk of back-filling the detector resulting in coronal discharge. The door is closed once again following the observations, to protect the detector during its reentry. The door mechanism was originally designed for SSULI (*Special Sensor Ultraviolet Limb Imager*), an optical remote sensing mission run by the U.S. Naval Research Laboratory, also using MCP technology. For more information on SSULI, see e.g. Thonnard *et al.* (1994).

2.2.7 Instrument structure

As illustrated in figure 2.2, the spectrometer is housed in a cylindrical shell of aluminium alloy, which slides inside the payload skin of the sounding rocket. All joints in this shell are fitted with O-ring vacuum seals, and "snubbers" at each end of the shell prevent lateral oscillations of the spectrometer during the flight. The interior of the aluminium shell is fitted with baffles to absorb any scattered light, as well as the diffracted beams of airglow, within the spectrometer.

The demands of high resolution spectroscopy make it particularly important that the separation between gratings and detector remain constant to preserve focus. However, during the flight, thermal and mechanical stresses threaten to change this separation, and so the instrument is fitted with Invar tubes linking the grating and detector mounting plates, the latter being free to slide on bearings along the major axis of the instrument. These tubes have an extremely low coefficient of thermal expansion, and so by effectively suspending the detector on a structure which does not share the expansion of the rocket skins, the focus of the instrument is preserved.

Electronics and power supplies for the instrument are housed in the "vacuum extension", a single-walled aluminium skin fitted over the front of the spectrometer. These components are mounted on two plates fixed to, but thermally isolated from, the side of the extension, and carefully positioned to ensure that optical fields of view remain clear of obstruction. This arrangement is illustrated in figure 2.11, which shows the location of all major optical and electronic structures mounted on the aperture plate at the front of the spectrometer.

The vacuum extension is equipped with feedthroughs providing essential connections between the instrument and

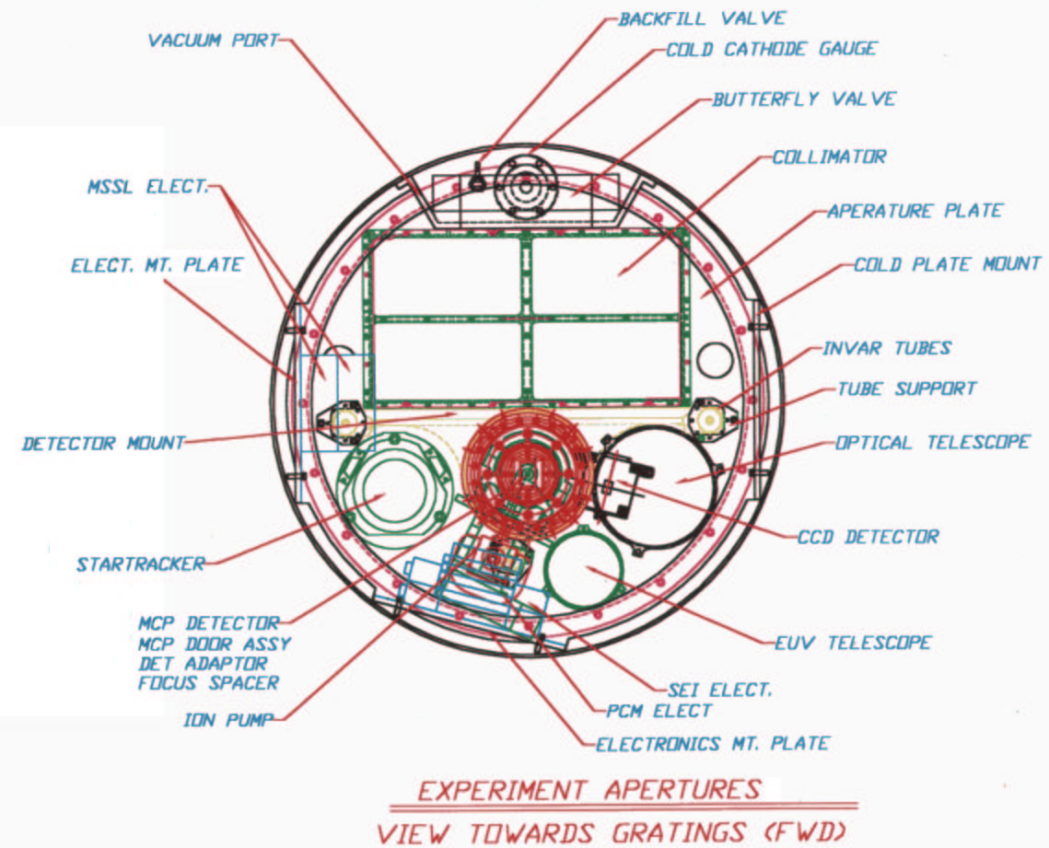

Figure 2.11: The *J-PEX* aperture plate, housing the MCP detector, collimators, optical CCD and ACS startracker. Electronics plates are shown mounted around the interior of the vacuum extension. (After Cruddace *et al.*, 1997.)

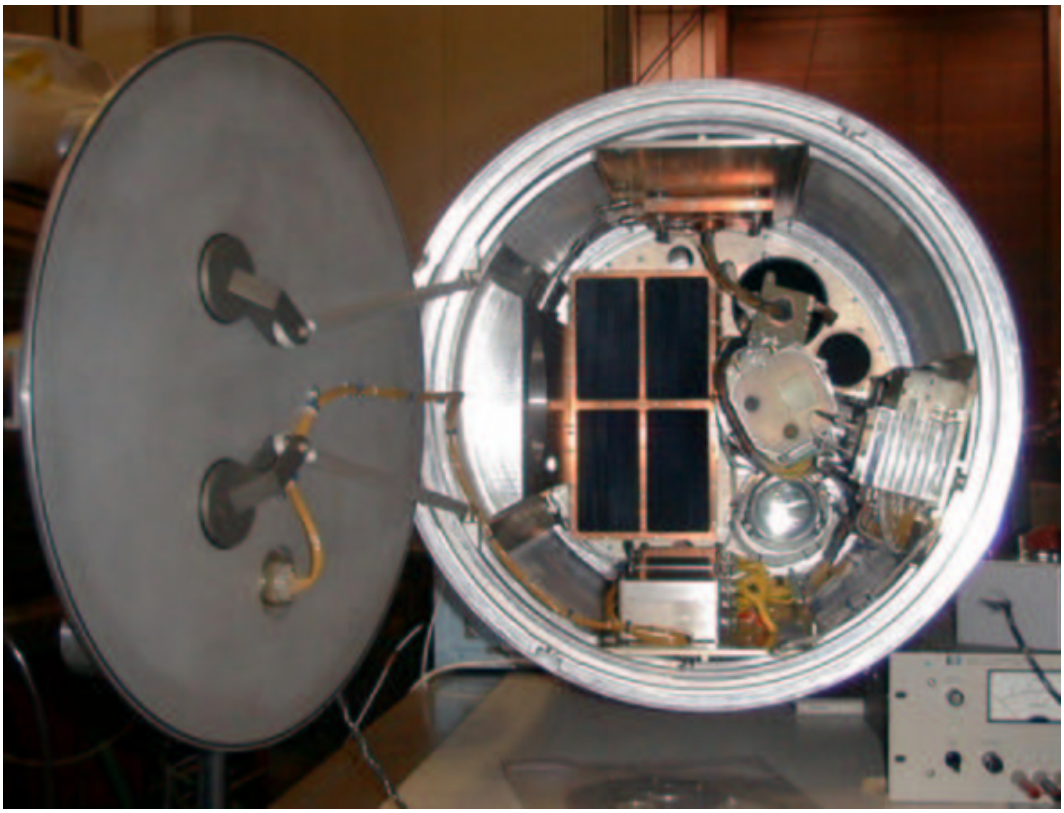

Figure 2.12: A view inside the aperture of *J-PEX*, taken 5 days before launch. (Refer to figure 2.11 to identify components.)

ground support hardware. The connections provide power for the MCP detector ion pump (which is not active during flight), coolant for the CCD camera, vacuum pumping lines, connections for monitoring equipment, and a supply of dry nitrogen gas to be used should back-filling of the payload become necessary. All of these connections are removed prior to launch.

A one-piece motorized door completes the spectrometer assembly. Fitted to the open end of the vacuum extension, this door provides the final hermetic seal for the instrument, and is closed immediately before and after the observational phase of the flight. The MCP detector door is timed to open *after* the shutter door, so that the main payload volume is under vacuum before the detector is exposed. Figure 2.12 provides a view inside the spectrometer aperture, clearly showing the external shutter door. This image was taken during final integration shortly before the first flight (36.162) at White Sands, New Mexico in February 2000.

The orientation of the spectrometer inside the sounding rocket is shown in the centre portion of figure 2.13. The spectrometer faces the base of the rocket, sitting immediately above the second stage booster. Following separation of this final stage, the ACS moves the spectrometer into position for observations, and the instrument doors are opened.

2.3 Science goals

The primary target for *J-PEX* is G191-B2B, described in some depth in Chapter 1. The star produces an observed flux of 0.4 photons $cm^{-2}s^{-1}$ $Å^{-1}$ in the instrument bandpass (225 Å to 245 Å), as determined by earlier *EUVE* observations. The primary science goal of *J-PEX* is to acquire an EUV spectrum of sufficient resolution to separate lines of He II, if present, from the large numbers of features produced by heavier elements such as C, N, O, Fe and Ni. The predicted resolution of the instrument surpasses that required for this task (see figure 2.14).

By modeling the width and depth of any He II features, the location of the material (photospheric or circumstellar / interstellar) can be determined. Furthermore, the data products acquired by *J-PEX* have potential applications in other related areas of study. For example, the precise heavy element abundances which can be determined from such high resolution data will enable testing of radiative levitation theory with much greater levels of precision than was previously possible.

2.4 First flight: 36.162

J-PEX was flown on a Black Brant VC sounding rocket, with a Terrier first-stage booster, on 25^{th} February 2000, from the White Sands Missile Range in New Mexico, USA. The nominal sequence of events for this flight is presented in table 2.2.

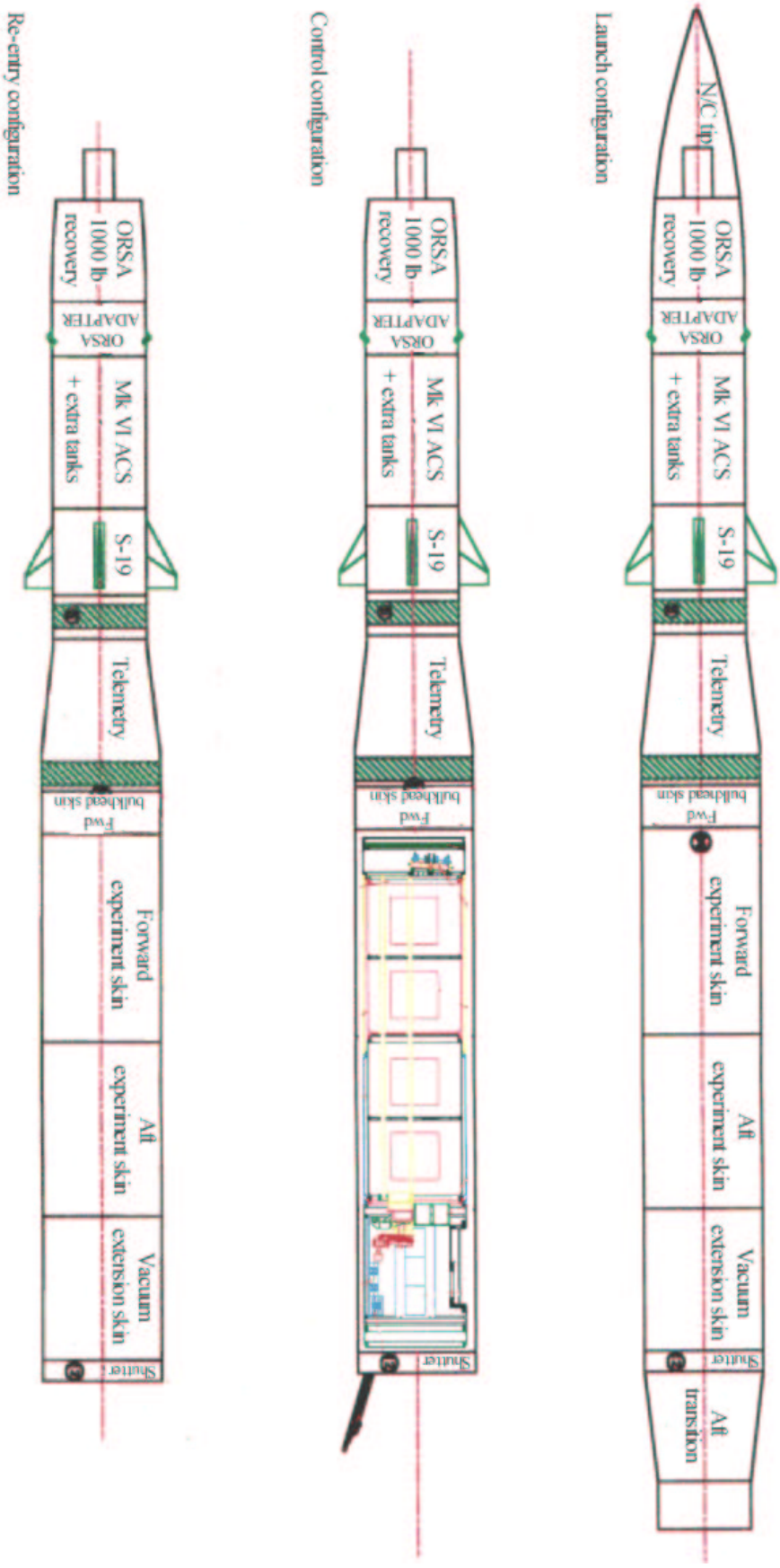

Figure 2.13: Configuration of the experiment during launch, observation, and re-entry phases of the flight. The position of the spectrometer is shown in the central diagram. Note the external shutter in the central diagram, open during the period of observation.

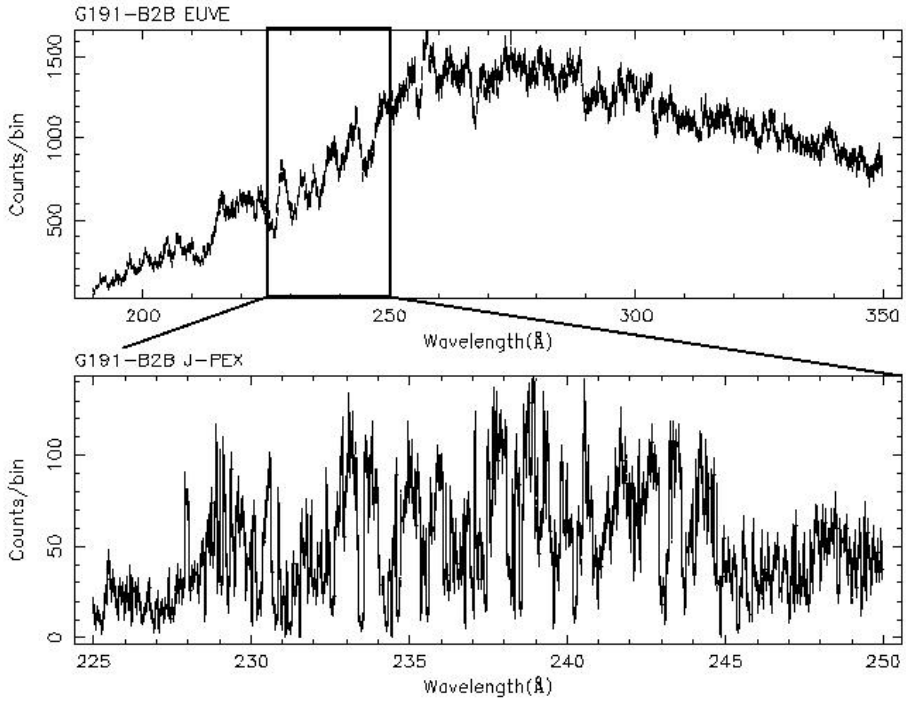

Figure 2.14: The spectrum of G191-B2B obtained by *EUVE* (top), and a simulated spectrum at the resolution of *J-PEX* (bottom) in which He II absorption features at 232.7, 234.5, 237.5 and 243.3 Å are revealed, along with the 228 Å Lyman limit.

T (Secs)	ALT. (Km)	DESCRIPTION
0.0	0.0	Terrier 1st stage ignition
6.2	3.1	Terrier burnout
12.0	6.1	Black Brant VC ignition
18.0	9.4	S-19 Canard decouple
44.0	45.1	BBVC burnout
62.0	77.8	Despin to 0.0 Hz
66.0	85.7	Payload separation
70.0	97.3	Shutter door OPEN
77.0	110.4	Nose tip eject
90.0	133.5	Payload power ON
95.0	142.0	Detector test signal on
123.7	186.0	Detector door OPEN [ACS capture of Sirius]
133.7	199.0	Detector power ON
134.0	200.0	[ACS capture of Capella]
137.4	204.0	Detector test signal OFF. OBSERVATION BEGINS
278.7	294.2	Apogee
457.0	151.0	Detector door CLOSED
460.0	146.0	Detector test signal ON
465.0	138.0	Detector power OFF
469.0	131.0	Detector test signal OFF
472.0	126.0	Payload power OFF
466.0	125.7	Shutter door CLOSED
478.0	122.3	Spin-up START
598.0	9.1	ACS power OFF
603.5	4.9	Parachute deployment
861.4	1.2	Payload impact

Table 2.2: Flight event sequence.

2.4.0.1 Results of the first flight

Unfortunately, data pertaining to high altitude winds above the launch site, and used to determine the positioning of the launch rail, appear to have been incorrect. During a sounding rocket flight, the initial trajectory is set *into* the wind, effectively canceling out its effect. However, investigations showed that in the case of *J-PEX*, these winds were not present, contrary to data reported by high altitude balloons released shortly before launch. As a result the vehicle flew beyond the range boundary. Safety precautions then dictated that the booster be destroyed, and this procedure was carried out at around T+43 seconds, effectively removing the despin mechanism, and also causing the payload to tumble.

The instrument ultimately achieved an apogee only slightly short of the intended value (289 km), and appears to have functioned precisely as designed, with stars being observed in the CCD image briefly as the spectrometer tumbled, although this motion resulted in the MCP detector accumulating only background counts. Instrument shutdown occurred as planned, though at a lower altitude, resulting in suspected coronal discharge within the MCP detector in the final seconds before power was turned off. Parachutes were deployed at the appropriate time, and the instrument was recovered in excellent condition, allowing the possibility of a reflight to be considered, after some minor refurbishment of the detector. This reflight is the subject of Chapter 6.

2.5 Summary

- *J-PEX* represents the first in a new generation of instruments designed to observe astronomical objects in the Extreme Ultraviolet region of the electromagnetic spectrum – an area which has traditionally proved challenging for conventional instrument designs to explore efficiently.
- The key concept which distinguishes *J-PEX* from earlier EUV hardware such as *EUVE* is its use of *normal incidence optics*. By applying multilayer coatings to spherically figured, precisely etched reflection gratings, the tasks of light collection and dispersion can be performed by a single element. This reduces to one the number of reflections in the system, and also removes the need for wasteful grazing incidence elements in the design. As a consequence, optical throughput is dramatically increased, and higher degrees of wavelength dispersion become possible.
- The microchannel plate detector incorporated in *J-PEX* was designed and built at the University of Leicester, using a high resolution readout anode developed at MSSL. Making use of transmission photocathodes and recently developed small pore microchannel plates, construction of the imaging detector formed a major element of the author's research project, and this work is discussed in the following chapters.
- The first flight of *J-PEX* is a "proof of concept" flight, and aims to answer a long standing question in white dwarf research: is there He in the atmosphere of G191-B2B and, by implication, in other isolated hot DA white dwarf stars? By unambiguously determining the presence or absence of He, a successful flight of *J-PEX* will prove the validity of a design which has the potential to be the instrument of choice for the next generation of EUV observatories, with applications in many fields of astrophysical research.

CHAPTER 3

ENHANCEMENT OF MICROCHANNEL PLATE QUANTUM EFFICIENCY

3.1 Introduction

THE SUCCESS OF *J-PEX* relies on obtaining spectra with a signal-to-noise ratio high enough to permit unambiguous identification of helium in the spectrum of the white dwarf G191-B2B. The predicted count flux from this star between 225 and 245 Å has been estimated as 0.4 photons s^{-1} cm^{-2} $Å^{-1}$, and with an on-target exposure time limited to approximately 5 minutes, the fraction of photons detected by the system must be as high as possible. This fraction is known as the *Quantum Efficiency* (QE) of the detector. QE values for MCPs subjected to no post-manufacture processing are typically around 18 – 20% at 304 Å (such plates are referred to as "bare glass" MCPs, although an electrode layer is deposited on the surface). However, a variety of surface depositions and chemical treatments can produce substantial increases in efficiency. To obtain maximum QE from the *J-PEX* detector, a program of laboratory trials was conducted to determine the most appropriate technique for the 225 – 245 Å bandpass.

Four processes were investigated: coating with a caesium iodide (CsI) photocathode, a potassium bromide (KBr) photocathode, thermal annealing of the CsI, and nitric acid etching. In this chapter, each technique is described, and its effect on MCP efficiency evaluated by measuring the QE of an MCP detector, unrelated to the *J-PEX* design, at EUV wavelengths between 161.7 and 584 Å.

The operating characteristics of MCPs are of considerable significance in this work, and so the discussion begins in section 3.2 with an overview of their manufacture and operation. The enhancement techniques under consideration are introduced in section 3.3. Experimental procedures and equipment are described in section 3.4, followed in section 3.5 by the QE enhancement study. Results from the study are discussed in section 3.6.

3.2 The manufacture and operation of Microchannel Plates

Detailed discussions of the history and manufacture of MCPs are provided by Fraser (1989) and Martin (2000). The relatively brief summary which follows, is extracted from these sources.

3.2.1 History

MCPs have their roots in military technology, being developed to provide a solution to the problem of high resolution imaging in low light conditions. They represent the evolution of discrete-dynode photomultiplier tubes, in which each dynode provides a gain multiplication stage. An MCP may be thought of as a large array of small, *continuous*-dynode photomultiplier tubes, with the very large number of virtual gain stages in each channel resulting in high gain ($10^6 - 10^8$) as illustrated in figure 3.1. As the first incarnation of the continuous dynode, Channel Electron Multipliers, or CEMs, represent an intermediate stage in the development of MCPs. Not only were they used on several successful space missions (including Copernicus and Apollo-Soyuz), but when stacked together, CEMs constituted the first continuous dynode arrays, the true forerunners of the MCP. CEMs are still in much demand, and were used in the following study as reference counters.

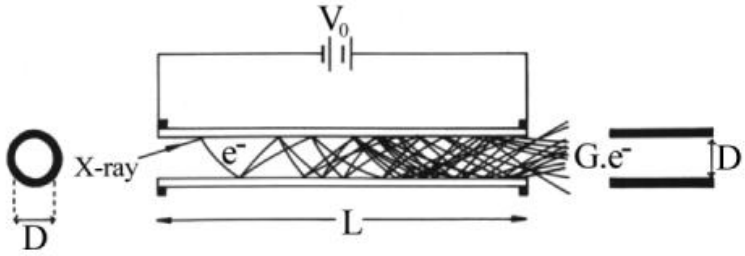

Figure 3.1: Operation of a continuous dynode electron multiplier (or an individual MCP channel), of channel diameter D and length L, with a potential V_0 across the front and rear surfaces, resulting in a gain of G (Fraser, 1989).

3.2.2 Manufacture

In common with their CEM predecessors, MCPs are made from glass, the principal constituents of which are PbO and SiO_2. Production begins with a hollow tube of high Pb content cladding glass a few mm thick, and of order 1m in length. Into this tube is inserted the softer and more soluble core glass. The assembled couple is hung from a tower and heated until the glass becomes soft enough to draw out using a pair of gripping wheels near the base of the tower. After the first draw, the fibres are $\sim$ 1mm wide, and are cut into lengths of $\sim$ 500mm. These fibres are stacked into multifibre bundles, and drawn again before being assembled into a solid glass envelope to produce a *boule*. The boules are fused under high pressure and temperature, and cut into slices, with the cutting angle determining the channel bias angle. Each slice is ground and polished, prior to being etched for several hours in hydrochloric acid to remove the core glass. The solid envelope of the boule may be cut away if soft edge MCPs are required.

The etched MCPs are fired in a hydrogen atmosphere to produce a semiconducting surface layer, the secondary

electron yield of which determines the MCP gain. Finally, the MCP is coated on both faces with a conductive layer such as nichrome ($Ni_7Cr_2Fe_3$), which allows a potential difference to be applied across the MCP. The principal stages in manufacture are illustrated in figure 3.2.

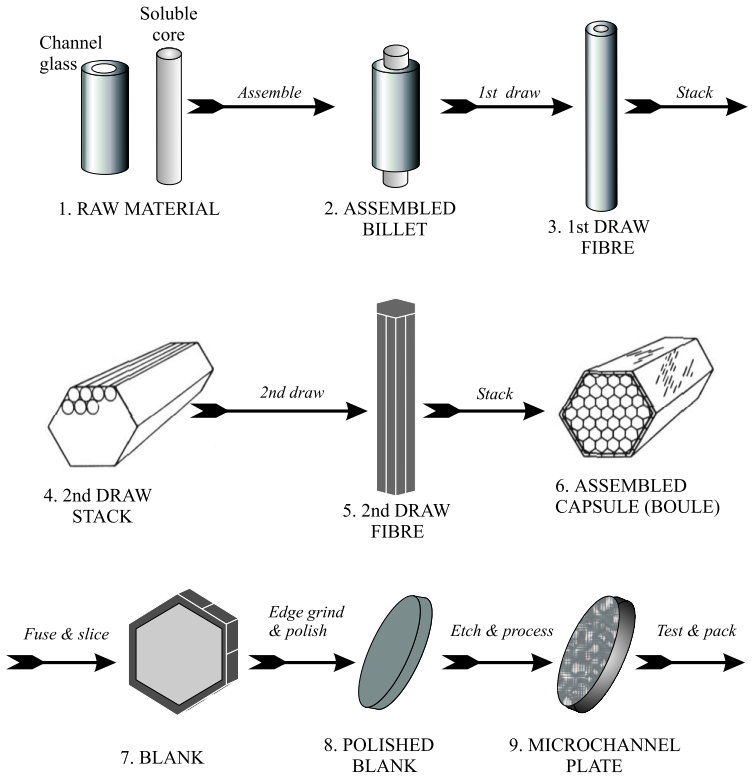

Figure 3.2: Principal stages in the manufacture of microchannel plates (see text for details). After Fraser (1989).

3.2.3 Operation of MCP detectors

3.2.3.1 Gain mechanisms in MCPs

Photon detection occurs in MCPs via the photoelectric effect. At EUV energies, photons incident on an MCP have insufficient energy to penetrate through the channel walls into adjacent channels, and so detection is a "single channel" process.

MCPs can be operated in *saturated* or *linear* modes. In the linear case, low voltage applied to the plate allows a large number of possible electron trajectories down the channel, leading to a wide range of electron energies and secondary electron yields during collisions with the channel wall. The gain is then dependent on the level of stimulation at the input, and the pulse height distribution[1] (PHD) has a negative-exponential form. However, photon counting MCP detectors are operated in *saturated* mode, producing the characteristic peaked PHD with high modal gain. The narrow full-width-half-maximum (FWHM) PHD maximises the electronic signal-to-noise ratio and limits the dynamic range which must be handled by the imaging electronics (Pearson, 1984). This mode is achieved by applying a large $\underline{E}$ field ($\geq 10^6$ V m^{-1}) across the MCP. The collisional energy, and hence secondary yield,

[1] A *pulse height distribution* is a histogram showing the number of events detected in a given interval of gain. In the case of a microchannel plate detector, an "event" in this context is the pulse of electrons received at the readout anode, produced by an incident X-ray or EUV photon. The "gain" of the event then refers to the number of electrons in this pulse (or equivalently, the charge deposited on the anode).

of electrons, is high, and gain becomes limited by *positive wall charging*. As the electron avalanche progresses down a channel, it depletes the walls of charge, which must be replaced by electron redistribution in the material over some finite timescale τ. In saturated mode, this timescale is longer than the transit time of the avalanche, and hence the wall charges up. Ejected secondaries are gradually retarded, reducing collisional energy until no further multiplication is possible, and the channel saturates. Charge is replenished once the electron avalanche is clear of the channel.

3.2.3.2 Variation of PHD with incident angle

Operation in saturated mode requires the initiation of avalanches close to the channel entrance. However, the angle of incidence of an incoming beam alters the position of avalanche initiation, and hence the peak gain of an event. Figure 3.3 demonstrates the relationship between the grazing angle α of the beam, the polar angle ψ and the angle of incidence with respect to the channel axis, θ. The relation is simply

$$\sin\alpha = \cos\psi \sin\theta, \tag{3.1}$$

while the penetration depth D into a channel of radius r is given by

$$D = 2r\cos\psi\cot\theta. \tag{3.2}$$

Thus, for any particular value of ψ, penetration depth increases as incident angle θ decreases, and avalanches begin further down the channel, reducing the modal gain. Clearly, as α approaches 0°, photons can pass through the MCP unhindered. This problem is compounded by X-ray reflections down the channel should α fall below the critical angle θ_c. For any beam of finite width incident at $\theta \leq 2\theta_c$, $0 \leq \alpha \leq \theta_c$ for some photons in the beam, so that regardless of the angle of incidence, some fraction of X-rays will be reflected down the channel, producing events with sub-modal gain (Pearson, 1984). Figure 3.8 demonstrates the variation in PHD with incident angle.

3.2.4 Soft X-ray QE

The soft X-ray QE of MCPs is examined theoretically by Fraser (1982) and experimentally by Pearson (1984). At energies below ~ 8 keV, interactions between photons and the MCP glass are limited to a 100 Å thick semiconducting layer at the surface of the channel wall, enriched with K during the final stages of manufacture. The decrease in detection efficiency at shallower angles described in section 3.2.3.2, is partially countered by the absorption of X-rays closer to the surface of the channel. This increases the probability of the resulting photo- or Auger electron escaping into a channel to initiate an avalanche, and producing a detected event. These competing effects result in a QE curve with a local minimum when incident radiation is parallel with the channel axis and the beam passes down the channel, increasing to a maximum as the critical graze angle of reflection is approached. The response

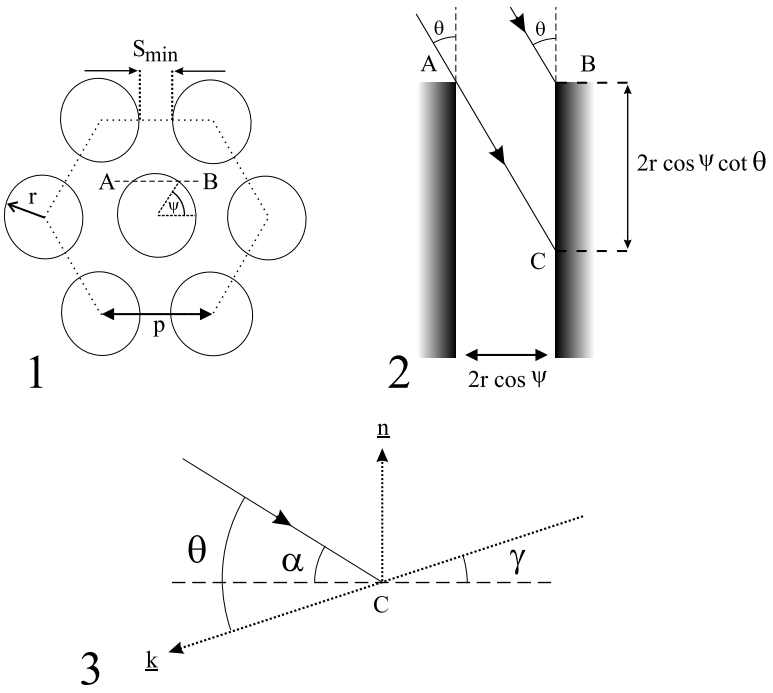

Figure 3.3: Angle of incidence of an X-ray beam. (1) Plan view of a channel and its nearest neighbours. Channel radius r, pitch p, and minimum septal thickness S_{min}. (2) Vertical section along the line AB, at polar angle ψ. X-rays incident at θ° to the plate normal illuminate the channel to a depth of $2r \cos\psi \cot\theta$. (In this case, the MCP has a 0° bias angle). (3) X-ray interaction with the channel wall. $\underline{\mathrm{n}}$ is the normal to the channel wall, and $\underline{\mathrm{k}}$ is a vector in the direction of the MCP surface normal. The point of incidence is C, and the grazing angle is α. γ is the channel bias angle. Reflected and refracted beams omitted for clarity (Fraser, 1982).

then decays as the graze angle increases and the X-ray absorption depth increases, reducing the probability of electrons escaping. This form is evident in all QE curves presented in this chapter.

The QE of bare glass MCPs is highly dependent on factors such as glass composition and plate geometry, but is generally low. Kowalski *et al.* (1986) determine a value of $\sim 8\%$ at 304 Å, while Hemphill *et al.* (1997) record QE values of $\sim 15\%$ at the same wavelength with different MCPs. Jelinsky *et al.* (1996) report higher peak bare glass QE (∼22% at 304 Å), and also demonstrate the large variation between MCPs from different suppliers and with various L:D values (recording up to a factor of 2 difference in QE near 800 Å). This relatively poor bare glass QE provides motivation for the work presented herein.

3.3 QE enhancement techniques

The treatments investigated in this study include application of reflection photocathodes, thermal annealing of a photocathode, and nitric acid etching of a bare MCP. These techniques are described below, while the precise "recipes" applied in the study are provided in section 3.5

3.3.1 Reflection photocathodes

The application of reflection photocathodes to MCP detectors is a well established technique, reviewed in several sources (Fraser *et al.*, 1982, Kowalski *et al.*, 1986, Jelinsky *et al.*, 1996) and modeled in detail by Fraser *et al.*

(1984). The principle behind this technology is illustrated in figure 3.4.

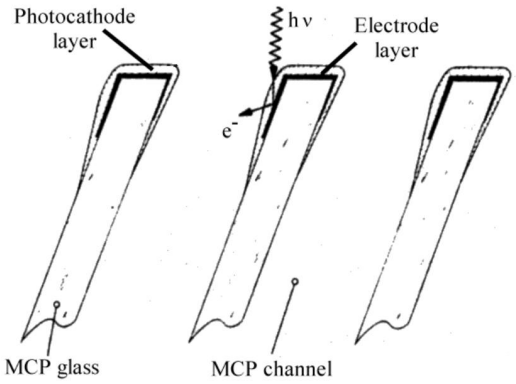

Figure 3.4: Operation of a reflection photocathode deposited onto an MCP with non-zero bias angle (note the decreasing thickness of photocathode with penetration depth, and preferential coating on one side of the channel). X-rays absorbed in the photocathode liberate electrons which are accelerated down the channel. After Siegmund *et al.* (1988).

Photocathodes are produced from material of high photoelectric yield, vacuum deposited onto the surface of the MCP such that the material penetrates into each channel for a distance equivalent to several channel diameters. Depending on the requirements of the optical system, the coating may be performed at normal incidence or at an angle to the MCP. Geometries incorporating non-zero coating or channel bias angles produce an asymmetric photocathode distribution (figure 3.4), which is betrayed by asymmetry in the resulting QE curves, as illustrated later in this chapter. To ensure that incident X-rays produce detectable events, the thickness of photocathode on the channel wall must be large compared to the secondary electron escape length of the material (approximately 215 Å in CsI), and comparable to the mean X-ray absorption depth for the required incident angles (Fraser *et al.*, 1984). Procedures adopted for the coating of MCPs at Leicester are given in appendix A.

Accurate modeling of photocathode operation (Fraser, 1983a,b, Fraser *et al.*, 1984) is a complex problem. However, the concept may be described simply. Consider figure 3.5. A parallel beam of monochromatic X-rays, of energy E, and intensity Γ_0 photons cm^{-2} sec^{-1}, is incident at an angle α to a photocathode of thickness T deposited on a substrate (the MCP glass). At the vacuum-photocathode interface, the beam is split into reflected and refracted (i.e. absorbed) components, with intensities $R(\alpha)\Gamma_0$ and $[1 - R(\alpha)]\Gamma_0$ respectively, where $R(\alpha)$ is the specular reflection coefficient for X-rays of energy E.

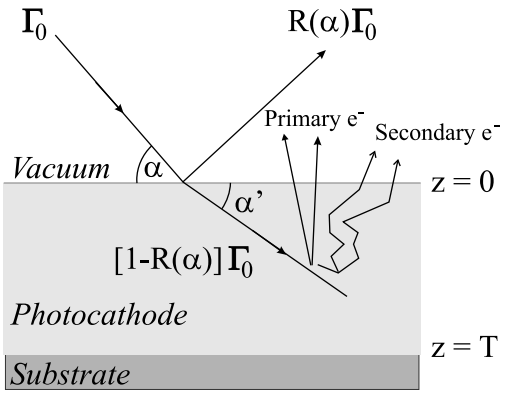

Figure 3.5: The absorption and reflection of X-rays in a photocathode, liberating primary and secondary electrons into the vacuum.

If the linear attenuation coefficient of the photocathode is μ, then the energy absorbed by the photocathode in a

layer between depths z and z+dz is given by the expression

$$dE(z) = \Gamma_0 E(1 - R(\alpha))\mu \csc \alpha' \cdot \exp(-\mu z \csc \alpha')dz \quad \text{keV cm}^{-2}\,\text{sec}^{-1}. \tag{3.3}$$

The absorbed energy excites primary and, more importantly, many secondary electrons in the material (by virtue of its high secondary electron yield). If L_s is the secondary electron escape length, then the probability of an electron escaping from a depth z into the vacuum and initiating an avalanche is simply

$$P_s(z) = P_s(0) \exp\left(-\frac{z}{L_s}\right), \tag{3.4}$$

where $P_s(0)$, the probability of escape at the surface, is a value close to unity. It is the high secondary electron yield, and escape path L_s of a photocathode material which makes the coating useful in enhancing detector QE.

MgF_2 was extensively used as a photocathode during the earlier years of detector development, primarily due to its stability in laboratory air rather than for its photoelectric yield (Fraser, 1983a). Today, CsI and KBr are in common use, due to their superior photoelectric properties (Kowalski *et al.*, 1986, Jelinsky *et al.*, 1996, Siegmund *et al.*, 1988). However, special handling precautions (such as storage and handling in dry nitrogen) are necessary to protect these hygroscopic materials from degradation in laboratory air (Lees *et al.*, 1993). CsI and KBr are examined in the following studies.

3.3.2 Thermal annealing of CsI photocathodes

The results of several investigations indicate that heating of photocathodes can increase photoyield and reduce susceptibility to degradation from water absorption. Evidence also suggests that this practice is effective in recovering hydrolysed photocathodes (Buzulutskov *et al.*, 1995). The mechanism which causes this increase in photoyield is the subject of considerable discussion; effects such as modification to the crystalline structure of the photocathode, elimination of residual water molecules from the material, and changes to the chemical composition of the surface layer, have been considered.

Of particular interest is the work of Lees *et al.* (1996), in which the effects of thermal annealing of CsI and KBr photocathodes on the X-ray QE of MCP detectors were examined. Lees *et al.* present SEM studies of pre- and post-annealed photocathodes, showing an increase in grain size in the annealed CsI coating, and no change in the morphology of KBr. A marked broadening of the high-gain tail in annealed CsI PHDs is observed, while only moderate differences are observed in the KBr distributions. The CsI observation is used to support the hypothesis that annealing increases the secondary electron escape length L_s, due to a reduction in defect scattering. Such modification to L_s would increase the probability of electron escape from a given depth (equation 3.4), and hence, increase QE. It is important to note, however, that the most significant effect of thermal annealing is to increase the photoyield of the material (up to factors of 5 over the non-annealed material). Lees *et al.* demonstrate QE increases which are relatively modest in comparison (the greatest ratio of annealed to non-annealed QE being approximately

1.1, occurring at large incident angles). These results were explained by models which revealed that annealing increases the proportion of high gain pulses, while the fraction of events which fail to excite any electrons remains unchanged.

The annealing procedure adopted in this study was similar to that described by Lees *et al.*, and is specified in section 3.5.3. Only CsI was considered for annealing in the present work, due to the relatively poor performance of annealed KBr photocathodes observed by Lees *et al.*.

3.3.3 Nitric acid etching

Hemphill *et al.* (1997) describe a chemical treatment which consists of soaking the MCP in a bath of 12 molar nitric acid at 80°C, followed by a vacuum bakeout. In the original study, this procedure resulted in almost doubling QE at 256 and 304 Å, with normal incidence values (for 13° bias MCPs) being 36% and 27% respectively. No change was reported in the form of the PHD, or in noise levels. Hemphill *et al.* also applied CsI and KBr to etched MCPs as part of their study, although data for this aspect of the investigation was only provided for incident radiation between 800 and 1400 Å. In this case, KBr coating of an etched MCP was found to increase QE by a factor of 3, and CsI by a factor of 2.4, with respect to the uncoated, acid etched values at 834 Å.

As in the case of thermal annealing, no definitive explanation exists for the effectiveness of acid etching in increasing the QE of MCPs. Hemphill *et al.* offer several possibilities. One suggestion is that etching roughens the MCP channels on small scales (large scale roughening would be expected to increase background noise due to field emission from surface features). This effect might be expected to alter the probability of a photon being absorbed or reflected from the channel wall, particularly at grazing incidences of illumination. Alternatively, changes in the chemistry of material near the surface might affect parameters such as the probability and threshold energy for photo- and secondary-electron emission. However, further investigations are required to resolve the issue. It is interesting to note that Martin (2000) examined untreated and acid-etched MCPs using scanning electron microscopy, reporting a *smoothing* of the etched plate on scales of $\sim$ 100 nm. Despite such uncertainties, the simplicity and effectiveness of this procedure as reported by Hemphill *et al.*, made it relevant for inclusion in this study.

3.4 Equipment and experimental procedure

3.4.1 Test facility

All data were obtained using the Detector Test Facility (DTF) in the Space Research Centre at Leicester University. The design of this facility is described in great detail by Milward (1986), but its principle components are outlined below. A schematic diagram of the DTF beam line is presented in figure 3.6.

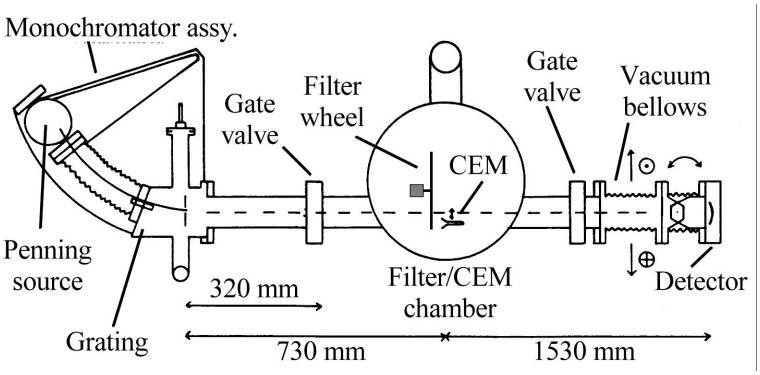

Figure 3.6: Schematic diagram of the Detector Test Facility beam line at Leicester University Space Research Centre (after Milward, 1986).

3.4.1.1 EUV source

The source of EUV radiation was a Penning glow discharge, consisting of two negatively biased cathodes, on either side of an annular anode which was held at ground potential. A discharge gas is flowed through the anode at low pressure (typically 10^{-4}mbar), while a potential of approximately 1.2 kV is established between cathodes and anode. A self-sustaining discharge is achieved when ions are accelerated towards the cathodes, producing photoelectrons which accelerate away from the cathodes, ionising more gas in the process. Photons arising from outer electron transitions in atoms of the discharge gas exit the source by means of a hole drilled in the anode ring. A magnetic field applied in the direction perpendicular to the surface of the cathodes enhances excitation by confining particle paths and increasing the number of collisions in the gas.

In the work which follows, He provides the 256, 304 and 584 Å emission lines, while the 161.7 Å line is an Al feature obtained by sputtering the cathodes using Ar gas.

3.4.1.2 Monochromator

Emission lines were isolated by means of a concave grating mounted in a Rowland circle arrangement, such that the grating and exit slit were held in a fixed position, while the source and entrance slit were moved around the perimeter of the circle. The desired line was obtained by moving the entrance slit and source to a position determined by the grating equation, and which was measured accurately by means of a micrometer and scale fitted to the turntable upon which the source was mounted.

3.4.1.3 Filter / CEM chamber

Monochromatic light from the source was passed into a chamber containing several components. Filters of various transmission values were mounted on a wheel, driven by a stepper-motor, such that the desired filter (or a completely open aperture) could be rotated into the beam. To avoid problems of excessive dead time, and to mitigate gain depression incurred by illuminating the same area at high count rates for long periods of time, filters of 1% and 5% transmission were used for the strong 304 and 584 Å He lines. The unfiltered position was selected for the

remaining lower intensity lines. Filtration was common to the CEM and MCP detector.

The CEM reference counter was mounted immediately behind this wheel, on an arm which allowed the device to be swung into the beam, and clear of the beam when the MCP detector was to be illuminated. The CEM was a Mullard type B419 BL, originally fitted to the facility during work on the *ROSAT WFC*. It was selected for its reasonable QE between 100 and 1000 Å, and because of its stability over timescales comparable to those of the project (Milward, 1986). The CEM output was fed into the same pulse-counting electronics and multichannel analyser used for the MCP detector signal.

3.4.1.4 Detector arm

The MCP detector was mounted on a platform at the end of a pair of flexible bellows, attached to the filter / CEM chamber. One set of bellows allowed horizontal and vertical movement of the detector, while the second allowed variation of the angle of incidence. Angle-resolved QE measurements could thus be made at any point on the active area of the MCP detector.

3.4.2 MCP detector

The detector was based on the design for the *ROSAT WFC* (Barstow & Sansom, 1990), apart from having flat MCPs and no repeller grid. Two MCPs were mounted in a chevron configuration, with the same bare glass plate used as the rear MCP in all measurements. Solid-edged MCPs were used throughout the work, and were produced by the Galileo Electro-Optics Corporation (now Burle Industries Inc.), USA; their specification is summarised in table 3.1. The front MCP was preceded by a nickel mesh, of transmission $\sim$90% at normal incidence. By holding this mesh at ground potential, charged particles were prevented from entering the active area and producing high noise rates.

Imaging was by means of a resistive anode readout , with four preamplifiers collecting charge from the anode and passing this signal to pulse counting electronics. A multichannel analyser was used for acquisition of PHDs, while a computer performed 2D imaging of the output (and also controlled stepper motors on the test facility). A switch box allowed signals from either the CEM or MCP detector to be passed to the counting electronics as required.

Pore size	12μm
MCP diameter	32.6mm
Active area	4.9 cm^2
L:D ratio	40:1
Open area fraction	62%
Resistance	$\simeq$ 230 MΩ @ 1000 V
Bias angle	10°

Table 3.1: Galileo MCP specifications (bare glass)

3.4.3 Procedure

QE was measured at 161.7, 256, 304, and 584 Å as a function of the incident angle of the beam with respect to the MCP surface. Emission lines were initially located by scanning the monochromator around the predicted position while recording the CEM count rate graphically on the MCA, and 'zeroing-in' on the required peak. Since QE determination required measurements on the emission peak and at a point on the low background continuum, a micrometer mounted on the Rowland circle allowed accurate determination of position, and repeatability of emission line and continuum positions. The procedure consisted of measuring emission line count rates for MCP and CEM, followed by MCP and CEM continuum rates, and finally a repeat set of emission rates, in quick succession. This practice averaged-out the effects of gradual variations in source intensity with time. Fluctuations on timescales comparable with a single MCP or CEM reading would not be averaged, leading to erroneous data values. Such fluctuations were rare, and usually symptomatic of poor gas flow or worn cathodes and anodes. In these cases, the problem was rectified and the reading repeated.

This sequence was repeated for each angular position (typically at 1° or 3° intervals). Count rates were determined from integrations of 10 seconds or more, depending on the intensity of the emission line. For a given angle, the averaged emission line count rate for the MCP detector, R_m, was determined by the expression

$$R_m = F\left\{\left(\frac{E_m + \acute{E_m}}{2}\right) - C_m\right\} \tag{3.5}$$

where F is the transmission of the filter (common to CEM and MCP measurements), C_m is the MCP continuum count rate, and E_m, $\acute{E_m}$ are the emission line count rates taken before and after continuum respectively. Using similarly defined quantities for the CEM gives

$$R_c = F\left\{\left(\frac{E_c + \acute{E_c}}{2}\right) - C_c\right\}. \tag{3.6}$$

The QE for that position is then simply

$$QE = \left(\frac{R_m}{R_c}\right) \times \left(\frac{Q_{CEM}}{T(\theta)}\right), \tag{3.7}$$

where Q_{CEM} is the CEM quantum efficiency. $T(\theta)$ is the transmission of the grounding mesh for an incident angle θ, and is given by

$$T(\theta) = \sqrt{T_0}\left\{1 + [\sqrt{T_0} - 1]\sec\theta\right\}, \tag{3.8}$$

where T_0 is the transmission of the mesh at normal incidence. CEM QE values were originally obtained in this facility by calibrating the device against an NBS (now NIST) transfer-standard photodiode. These figures are given

in table 3.2, and are compared to values determined in a study by Mack *et al.* (1976).

Wavelength (Å)	QE (%)	Mack *et al.*
161.7	6.4 ± 0.5	3.9 ± 1.0
256	6.7 ± 2.1	8.5 ± 0.9
304	9.7 ± 2.0	10.8 ± 1.0
584	15.2 ± 2.7	13.5 ± 2.0

Table 3.2: QE values for the CEM, as adopted in the current work, compared with those given in an independent study.

3.4.3.1 A note on error estimation

When interpreting data presented in the following sections, it is important to distinguish between several types of error which are implicit in the data. All QE plots include error bars calculated using Poissonian statistics, and standard formulæ for combining errors where appropriate. In most cases, these error bars are small due to the high signal to noise ratio of data which can be obtained from the test facility. However, these formal estimates do not take into account other sources of uncertainty, which may arise from, e.g., fluctuations in the output of the source. While gross source instabilities were detected and rectified during data acquisition, errors from small scale fluctuations will remain. The uncertainty in CEM QE values, listed in table 3.2, must also be considered. Although these errors effectively cancel when comparing data taken within this study, they become important when drawing comparisons with QE values quoted from other sources. Therefore, these values have been folded into the overall error estimates presented in tabulated data.

3.5 Quantum Efficiency enhancement processes

3.5.1 Preparatory measurements

MCP operating potentials were determined by illuminating the device with the 304 Å emission line, and adjusting voltages until the PHD was raised above the lower level discriminator of the counting electronics. Although considerably less rigorous than the formal optimisation technique adopted for the *J-PEX* detector (discussed in Chapter 4), this method was adequate for ensuring that counts were not lost through inadequate or excessive gain. The baseline detector settings are summarised in table 3.3.

Anode - rear MCP voltage	200 V
Rear MCP bias	1000 V
Interplate gap voltage	200 V
Front MCP bias	1000 V
Rear MCP resistance	224.72 MΩ @ 1000 V
Front MCP resistance	224.73 MΩ @ 1000 V

Table 3.3: MCP detector settings adopted for bare glass baseline measurements.

3.5.2 CsI photocathode

A Galileo MCP, the specifications of which have been given in table 3.1, was placed in a vacuum furnace, where it was baked at 270°C for approximately 48 hours to remove water molecules (which would compromise the photocathode). The input face of the MCP was coated with a 20mm diameter, 14,000 Å thick layer of CsI, leaving an annulus of bare glass around the plate edge. The MCP was then fitted in the detector. Post-bakeout MCP resistance was lower by approximately 42%, and the optimum front MCP voltage was determined to be 900 V. The resistance at this voltage was 145.16 MΩ.

J-PEX is a normal incidence spectrometer, and hence the enhancement technique to be applied to the detector must be selected on the basis of performance at 0° incidence. Normal incidence bare glass reference values were therefore obtained at all four wavelengths using the uncoated perimeter of the CsI-coated MCP. Angle resolved QE measurements for the CsI coated area were then taken, and the source spot was scanned across the diameter of the plate at normal incidence, to observe the step in efficiency between bare glass and CsI coated regions.

3.5.3 Thermal annealing of the CsI coated plate

After completion of plain CsI measurements, the front plate was removed from the detector, and subjected to a process of thermal annealing, repeating the procedure of Lees *et al.* (1996). The CsI-coated MCP was placed in a vacuum furnace, and the temperature increased over an 8 hour period to 250°C, at a pressure of 10^{-6} mbar. The plate was annealed at 250°C for 18 hours, and allowed to cool down gradually for a further 24 hours before being refitted in the detector.

After annealing, front MCP resistance was found to have increased by approximately 11% with respect to the pre-annealing value. Angle-resolved QE measurements were taken at all four wavelengths, and PHDs recorded for comparison with the pre-annealing data, using identical electronics settings.

3.5.4 Nitric acid etching of the front plate

A new bare glass front MCP was fitted in the detector to obtain reference measurements at 256 and 304 Å, and then subjected to the etching process described by Hemphill *et al.* (1997), *viz.*

1. MCP cleaned in isopropyl alcohol (IPA) for 30 minutes.
2. MCP placed in a bath of 12 molar nitric acid at room temperature.
3. Temperature of acid raised to 80°C over 45 minutes.
4. Temperature maintained at 80°C for 2.5 hours.
5. Acid & plate allowed to cool for 30 minutes.
6. MCP removed from acid and cleaned in IPA for 2 minutes.
7. MCP rinsed in distilled water and dried with N_2.
8. MCP baked in vacuum furnace for 2 hours at 120°C.

Operations 2-6 were carried out in the Department of Chemistry at the University of Leicester. The importance of step (3) cannot be over-stated; an earlier trial of acid etching in this study resulted in a shattered MCP, due to being taken from room temperature and immediately immersed in acid at 80°C.

MCP resistances were 102.99 MΩ (pre–etch), and 94.70 MΩ (post–etch). Angle-resolved QE measurements were taken, and PHDs acquired.

3.5.5 KBr photocathode

Following characterisation of the acid etched MCP, the plate was coated with a 14,000 Å thick layer of KBr. Since photocathode enhancement of QE relies upon processes occurring near the surface of the coating (section 3.3.1), use of an etched plate did not compromise the quality of KBr data.

To aid in evaluating the effects of photocathode application, a semicircular area of the MCP was masked off with Kapton heat-resistant tape, applied to the circular aperture placed over the MCP during the coating process. This resulted in an MCP with one half coated in KBr, and an etched but uncoated area with which to make comparison measurements. Cross scans through the glass and KBr region of the plate were taken at all four wavelengths to observe any efficiency step due to the presence of a photocathode, and to provide a secondary method of determining the change in QE resulting from photocathode application. Angle resolved QE measurements from the KBr coated region of the MCP were made, in addition to single QE measurements at normal incidence on the etched, but uncoated, region of the MCP, for comparison.

3.6 Results

3.6.1 Thermal annealing

Peak QE values for the thermally annealed CsI MCP are summarised in table 3.4. No significant increase in QE, with respect to plain CsI values, was detected. This apparent ineffectiveness of thermal annealing appears to be supported by the associated PHDs (figure 3.7), which reveal negligible change in shape between annealed and non-annealed data.

λ(Å)	Annealed CsI	Annealed/Plain CsI
161	32.1 (0.77)	1.04 (0.04)
256	20.5 (2.30)	0.70 (0.10)
304	22.5 (2.02)	0.72 (0.08)
584	45.1 (2.70)	1.63 (0.19)

Table 3.4: Measured QE values for bare glass and KBr zones of the KBr coated MCP. Figures in parentheses indicate the formal error estimate

However, a substantial increase in efficiency was obtained at 584 Å, as indicated in table 3.4. Given the absence of QE improvement at three other wavelengths, the 584 Å result must be considered as suspect until supporting investigations are conducted; at present, the possibility exists that this data set includes errors, perhaps as a result

of changes in CEM alignment, monochromator positioning, or electronics settings.

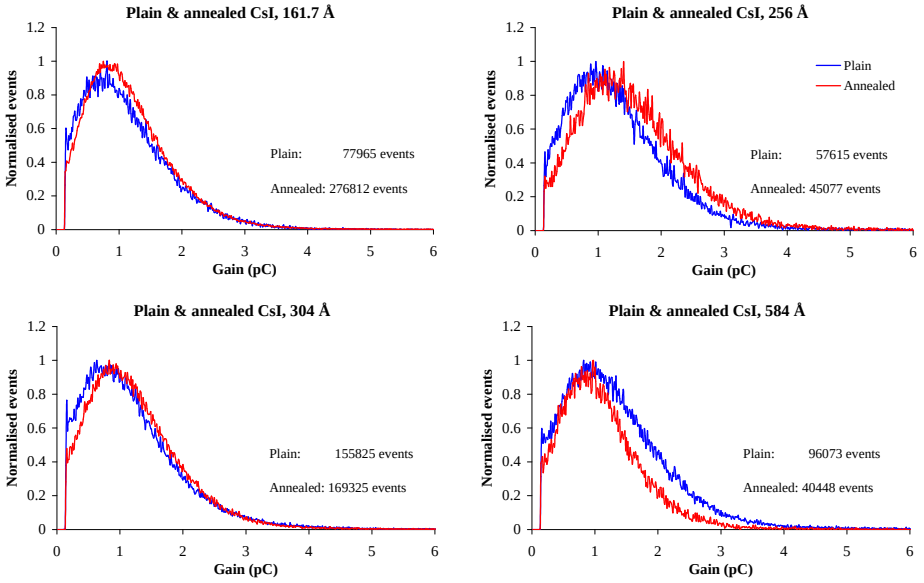

Figure 3.7: PHDs from front MCPs with plain and annealed CsI photocathodes. The number of events in each distribution is given. In each case, the rear plate was operated with 1000 V bias, the front at 900 V. The inter plate and rear plate – anode gaps were held at 200 V.

3.6.2 Nitric acid etching

No improvement in QE was detected as a result of the etching process conducted for this investigation. PHDs acquired before and after etching were compared, and found to exhibit negligible differences, as illustrated in figure 3.8.

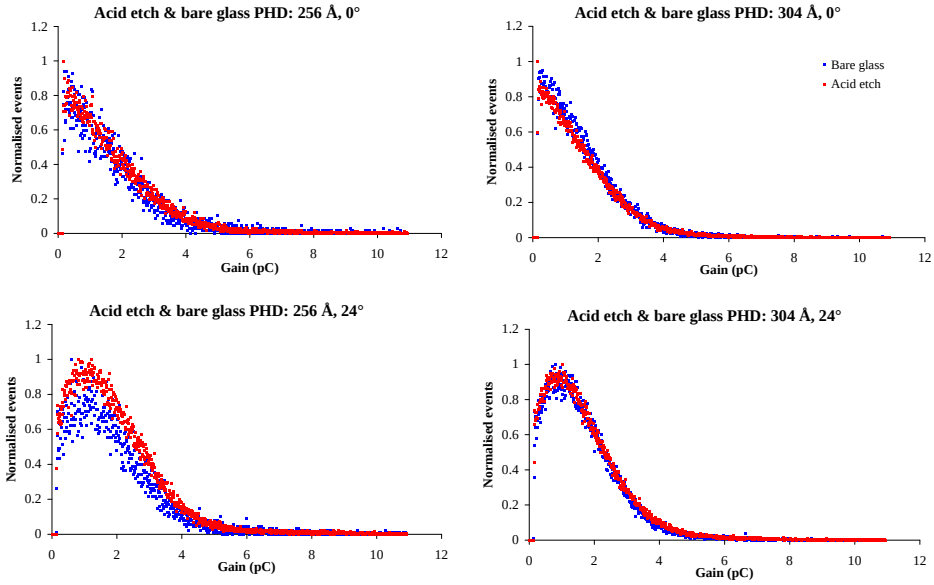

Figure 3.8: Bare glass and acid etch PHDs for 256 and 304 Å, at angles of incidence 0° (top panels) and 24° (bottom panels).

The peak etched-glass QE values, measured at all wavelengths considered in this work, are listed in table 3.5.

λ(Å)	Bare Glass QE	Acid-etched QE
161	13.1 (0.51)	16.1 (0.55)
256	18.4 (2.21)	17.2 (2.13)
304	26.6 (2.02)	19.6 (2.00)
584	18.2 (2.73)	16.0 (2.74)

Table 3.5: Bare glass & nitric acid–etch plate QE values for the current investigation. Errors in parentheses.

3.6.3 KBr photocathode

Application of the KBr photocathode was found to produce clear improvements in the QE of the detector (compared to bare glass) at all wavelengths with the exception of 256 Å, where negligible change was observed when formal errors are taken into account. However, the extent of improvement at the remaining three wavelengths was disappointing, and KBr appears to be inferior to CsI at these energies. Table 3.6 summarises the observed improvement over bare glass. These relatively minor increases in QE are reflected in the small steps exhibited in the cross scans, presented in figure 3.9.

λ(Å)	Etched glass QE	KBr/glass (Scan)	KBr/glass (QE)	KBr QE
161	17.8 (0.56)	1.17 (0.05)	1.12 (0.05)	19.9 (0.60)
256	21.0 (2.13)	0.89 (0.10)	0.97 (0.14)	20.3 (2.13)
304	24.3 (2.00)	1.07 (0.04)	1.28 (0.13)	31.1 (2.00)
584	19.2 (2.70)	1.41 (0.07)	1.55 (0.26)	29.7 (2.70)

Table 3.6: Measured QE values for adjacent etched glass and KBr zones of the KBr coated MCP. Errors in parentheses.

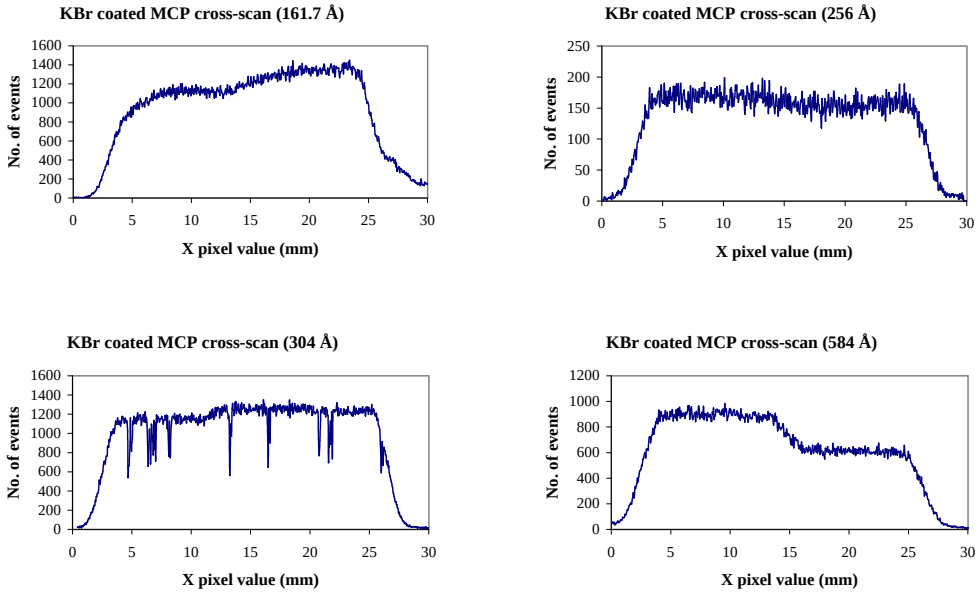

Figure 3.9: Horizontal scans through the acid-etched bare glass, and KBr zones, of the coated MCP. Spikes in the 304 Å data are believed to be caused by drop-outs during transfer of scan data from the multichannel analyser. X-positions approximate.

3.6.4 CsI photocathode

Scans across the bare glass perimeter and CsI area of the MCP (figure 3.10) demonstrate the effectiveness of this procedure, with the size of step on the photocathode/glass boundary being significantly greater than observed in the

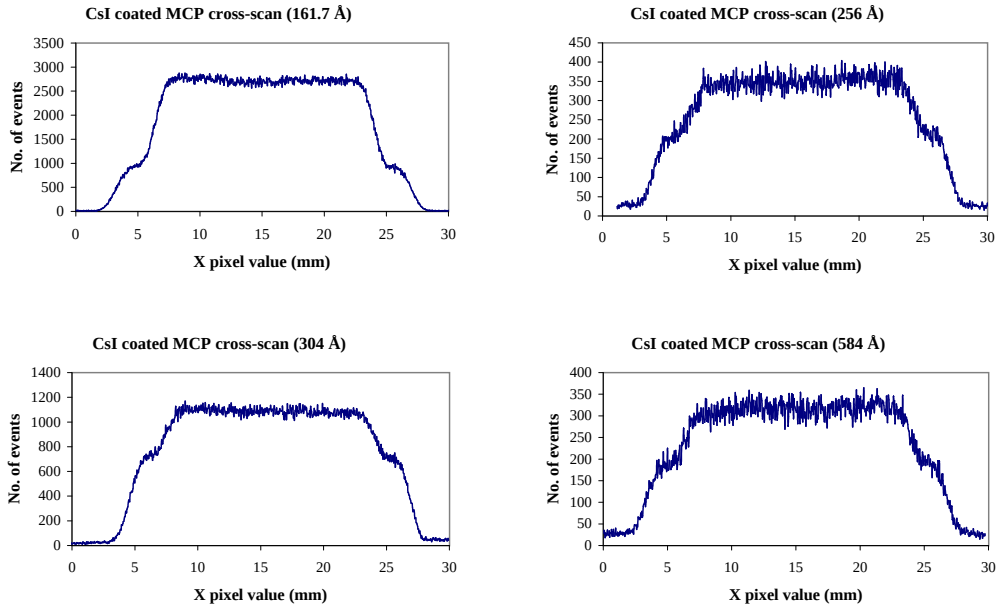

Figure 3.10: Horizontal scans through the bare glass and CsI zones of an MCP. X-positions approximate.

analogous KBr data (figure 3.9). Since the width of the bare glass region was greater than that of the source spot, the intermediate step in the data indicates the bare glass count rate. These data can be used to verify the CsI/glass QE ratios derived from individual efficiency curves; reasonable agreement is found between QE increases inferred from the scan profiles, and the angle-resolved QE data (presented in figure 3.11). Table 3.7 compares results from both types of data.

Comparison between PHDs from a bare glass MCP and the CsI coated plate reveals substantial modification of the distribution after coating, as shown for the two wavelengths closest to the *J-PEX* bandpass, in figure 3.12. The

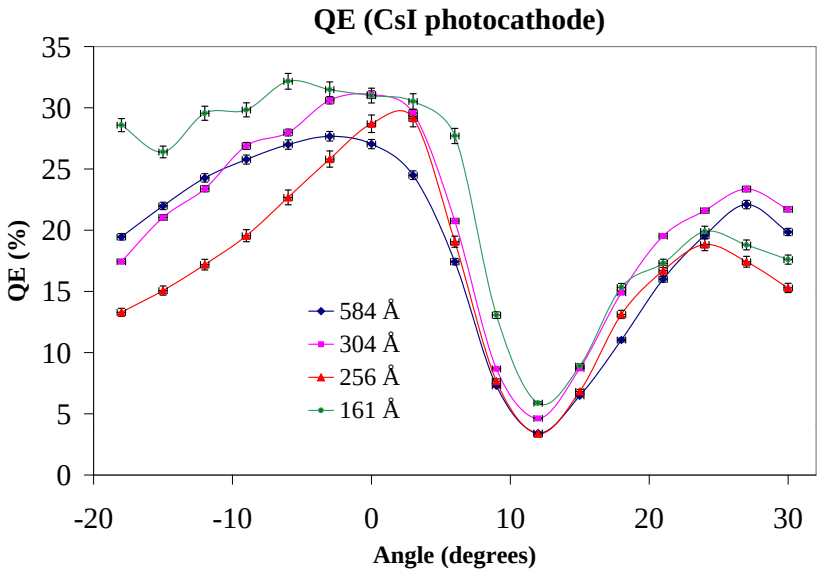

Figure 3.11: Angle-resolved QE measurements for a CsI coated MCP, at all four wavelengths investigated. The dips in the curves at a scale angle of $\sim 10°$ correspond to photon incidence along the channel axis. The asymmetry in the curves on either side of the dip is due to the preferential CsI deposition on one side of the channel. Error bars represent formal statistical errors, appropriate when comparing data taken within this study.

λ(Å)	CsI/bare(Scan)	CsI/bare(QE)	CsI QE
161	3.00 (0.11)	2.37	31.0 (0.78)
256	1.68 (0.15)	1.59	29.2 (2.21)
304	1.53 (0.07)	1.17	31.1 (2.02)
584	1.68 (0.15)	1.52	27.7 (2.73)

Table 3.7: Peak QE for a CsI coated MCP. The columns are, respectively, wavelength, ratio of CsI to bare glass count rate from normal-incidence cross-plate scans, ratio of peak QE values for CsI and bare glass from angle resolved data (at the angle corresponding to peak QE), and the peak QE for CsI obtained from angle-resolved data. Figures in parentheses indicate errors, including Poissonian statistical error and uncertainties in CEM efficiency.

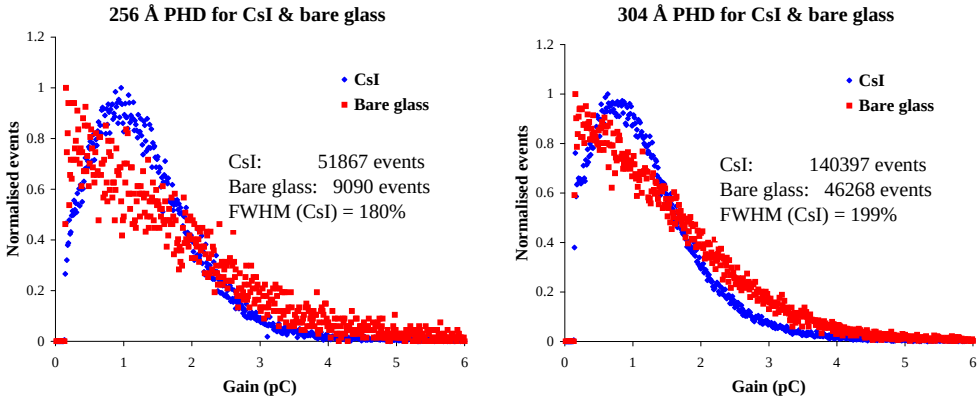

Figure 3.12: Comparison between PHDs from bare glass and CsI coated MCPs, operating at normal incidence and illuminated by 256 and 304 Å photons. The total number of events within each distribution is indicated in the plots, as is the FWHM of the CsI distributions.

CsI coated MCP exhibits a strongly peaked Gaussian distribution, in contrast to the pseudo-exponential form of the bare glass data for this angle.

3.7 Discussion

3.7.1 Thermal annealing

Contrary to results obtained in the soft X-ray band by Lees *et al.* (1996), annealing produced no QE improvement in the current work (the validity of 584 Å data being questionable). However, the thermal annealing study of Lees *et al.* was concerned with MCP detectors operating at wavelengths 4.84 Å $\leq \lambda \leq$ 44.3 Å, much shorter than those of the current investigation. Lees *et al.* observed a small increase in QE at large incident angles (annealed/unannealed $\sim$ 1.2 at 10° incidence to a 6° bias angle MCP), and broadening of the high-gain tail of the PHD. In the current study, no significant improvement in QE was measured for the three shorter wavelengths, and PHDs taken before and after annealing remained relatively unchanged. Evidence exists in the experimental work of Lees *et al.* to indicate that the effectiveness of thermal annealing is wavelength dependent (the ratio of annealed to non-annealed QE is consistently higher for Ru-L (2.56 keV) than for Si-K (1.74 keV) X-rays in that work). In the case of Si-K, thermal annealing was observed to *reduce* the QE of the MCP. In this respect, results from the present study appear consistent with those of Lees *et al.*, with reduced QE observed at 256 and 304 Å, and the higher energy 161.7 Å data showing negligible change. Unfortunately, the small number of wavelengths considered in this work do not permit a more positive statement to be made about any such dependence.

As indicated in section 3.3.2, the mechanisms responsible for the effectiveness, or otherwise, of thermal annealing are not well understood. Progress towards understanding the data presented here, and its relationship to the results of other studies, requires a better understanding of the process. This may be aided by extending the model produced by Lees *et al.* to a wider range of wavelengths, including those of the present study. However, as the aim of this investigation is the selection of a QE enhancement process appropriate to the *J-PEX* bandpass, any confirmation of improvement at longer wavelengths is, to a great extent, irrelevant. The apparent ineffectiveness of thermal annealing at EUV wavelengths, with supporting evidence from the similarity of pre- and post-annealing PHDs, excludes this technique from consideration in the *J-PEX* development program.

3.7.2 Nitric acid etching

Hemphill *et al.* (1997) describe a factor of 2 increase in QE at wavelengths around 256 Å following an acid etch process identical to that adopted in the current work. Table 3.8 compares peak QE values for nitric acid etched MCPs obtained during the current work, with those quoted by Hemphill *et al.*. Untreated, bare glass values are provided for comparison.

λ(Å)	Present work		Hemphill *et al.*	
	Bare	Acid	Bare	Acid
161	13.1 (0.51)	16.1 (0.55)	19.0	36.0
256	18.4 (2.21)	17.2 (2.13)	–	–
304	26.6 (2.02)	19.6 (2.00)	15.0	27.0
584	18.2 (2.73)	16.0 (2.74)	8.7	15.0

Table 3.8: Peak bare glass & nitric acid–etch plate QE values (%) for the current investigation, and as determined by Hemphill *et al.* (1997). Figures in parentheses indicate the error estimate, which has been calculated by adding Poissonian statistical errors, and uncertainties in CEM efficiency, (listed in table 3.2), in quadrature.

Although procedures for processing and testing of MCPs are the same in both studies, the glass composition of the MCPs is different (the Galileo plates of the current investigation are produced from Corning type 8161 glass compared to the Philips 297 composition of the plates used by Hemphill *et al.*). A more thorough investigation of the processes involved in the acid etch treatment is required before this discrepancy can be resolved, but such differences in plate composition may provide part of the solution. It is also relevant to note, again, the results of the SEM study of acid etched plates by Martin (2000), which suggest a smoothing of channel wall surfaces following the etching procedure. As previously stated (section 3.3.3), smoothening might be expected to lower QE due to the reduction in grazing angle of incident photons, which decreases the probability of photon absorption and subsequent photoelectron production.

3.7.3 KBr photocathode

As with the 584 Å annealed CsI data discussed in section 3.6.1, the poor performance of KBr at 256 Å may be a result of data errors. However, in a study of MCPs with KBr photocathodes, Siegmund *et al.* (1988) report a similar observation. Although their MCP detector was operated with a repeller grid fitted, the QE data are resolved into channel and web contributions. By considering only the channel component, it is possible to compare this

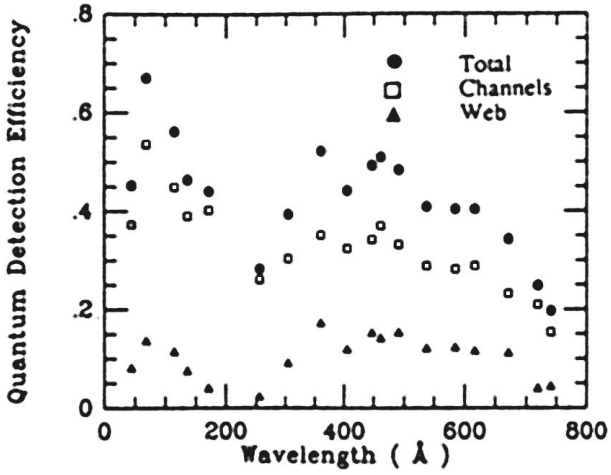

Figure 3.13: QE vs wavelength for a 15,000 Å thick KBr reflection photocathode for radiation at 10° graze angle to the channel axis, with a 120 V mm^{-1} repelling field. The local minimum at 230 Å is clearly defined, and the adjacent 256 Å data point is also noticeably weak (Siegmund *et al.*, 1988).

study with the current work. Figure 3.13 is taken directly from Siegmund *et al.* (1988), and shows a clear local minimum in QE close to 256 Å. Quoting directly from their paper:

> Below 256 Å we observe a [quantum detection efficiency] minimum at $\sim$ 230 Å, followed by a strong maximum centered at $\sim$ 70 Å. To first order this behaviour seems to follow the trend in the absorption coefficient for KBr.

Note that, although the minimum occurs at 230 Å, the adjacent 256 Å data point is also noticeably weak. It is therefore likely that the particularly low value of QE at 256 Å compared to other wavelengths obtained in the current work, is real.

A further interesting observation arising from the KBr measurements is that comparison between tables 3.8 and 3.6 reveals significantly different values for the two sets of acid etched glass data, with the values in table 3.6 systematically higher by a factor of $\sim$ 1.2. Several possible explanations exist for this apparent discrepancy. Since the detector was disassembled between acquisition of these data sets, it is possible that the detector was replaced on the test facility in a marginally different orientation, or that the front MCP was re-installed with a slightly different azimuthal angle. In either case, the grazing angle to the channel wall, at a given angle setting on the test facility, would be changed, with possible implications for the measured QE. More intriguing is the possibility that some aspect of the pre-coating procedure may have affected the masked region of the MCP. As outlined in appendix A, these procedures include heating the MCP to 100°C, and subjecting to a glow discharge clean. Yet even if real, comparison with data for the CsI photocathode demonstrates that the increase in acid-etched MCP QE is insufficient to make etching, or a combination of etching and KBr coating, of value to the *J-PEX* project. While the possibility exists that a genuine increase in QE has been achieved during coating preparations, further work is required before this observation can be confirmed and understood.

3.7.4 CsI photocathode

Siegmund *et al.* (1986b) have measured the QE of MCP detectors with a CsI photocathode of similar depth, on MCPs with an L:D ratio of 80:1, obtaining peak efficiencies of ∼34% for 584 Å and ∼29% for 304 Å, in reasonable agreement with the present values (when CEM QE uncertainties are considered). Kowalski *et al.* (1986) find efficiencies which are significantly lower at 256 Å and 304 Å, and higher for 161 Å. However, the plates used in the latter work are of different chemical composition, and are coated with a CsI layer only 5000 Å in depth. Good agreement is also found with data given by Barstow *et al.* (1986), who also used a 14,000 Å photocathode thickness. (In addition, Barstow *et al.* measure the contribution of the front surface to the overall efficiency to be around 6%). These comparisons are summarised in table 3.9.

λ(Å)	Kowalski		Barstow		Siegmund	
	Bare	CsI	Bare	CsI	Bare	CsI
161	12.0	42.0	–	–	–	–
256	8.0	22.0	–	31.0	24.0	34.0
304	8.0	21.0	–	–	21.0	33.0
584	–	–	–	–	16.0	39.0

Table 3.9: Peak QE values (%) for bare glass & CsI coated plates from previous investigations.

3.8 Conclusions

The processes discussed in this chapter have been the subject of investigation by other groups, and all have been reported to yield significant increases in QE. However, these previous trials were conducted under a wide variety of conditions, including different MCP compositions, bias angles, detector designs and wavelength coverage. The purpose of the present study was to evaluate all techniques using a standard set of conditions and methods, appropriate to the requirements of the *J-PEX* MCP detector. This work therefore provides an unambiguous set of data with which to select the optimum procedure. The peak QE values observed for each process considered in this study, and for bare glass plates, are shown in figure 3.14 and summarised in table 3.10.

λ(Å)	Bare glass	Acid etch	KBr	CsI	Annealed CsI
161	13.1 (0.51)	16.1 (0.55)	19.9 (0.60)	31.0 (0.78)	32.1 (0.77)
256	18.4 (2.21)	20.3 (2.13)	20.3 (2.13)	29.2 (2.21)	20.5 (2.30)
304	26.6 (2.02)	19.6 (2.00)	31.1 (2.00)	31.1 (2.02)	22.5 (2.02)
584	18.2 (2.73)	16.0 (2.74)	29.7 (2.70)	27.7 (2.73)	45.1 (2.70)

Table 3.10: Peak QE values (%) for bare glass and each of the four efficiency enhancement processes investigated in this study.

Two of the procedures (nitric acid etching and thermal annealing of a CsI photocathode) are found to produce minimal (and in some cases, detrimental) changes to QE. Significantly, the physical mechanisms responsible for the reported success of these two treatments in other investigations are poorly understood. In the case of acid etching, only data for the 161.7 Å emission line suggests a genuine, though small, improvement in QE. At the most significant wavelength (256 Å), negligible change in QE is observed when errors are taken into account. Thus, nitric acid etch may be ruled out as a chemical treatment process to be applied to the *J-PEX* detector.

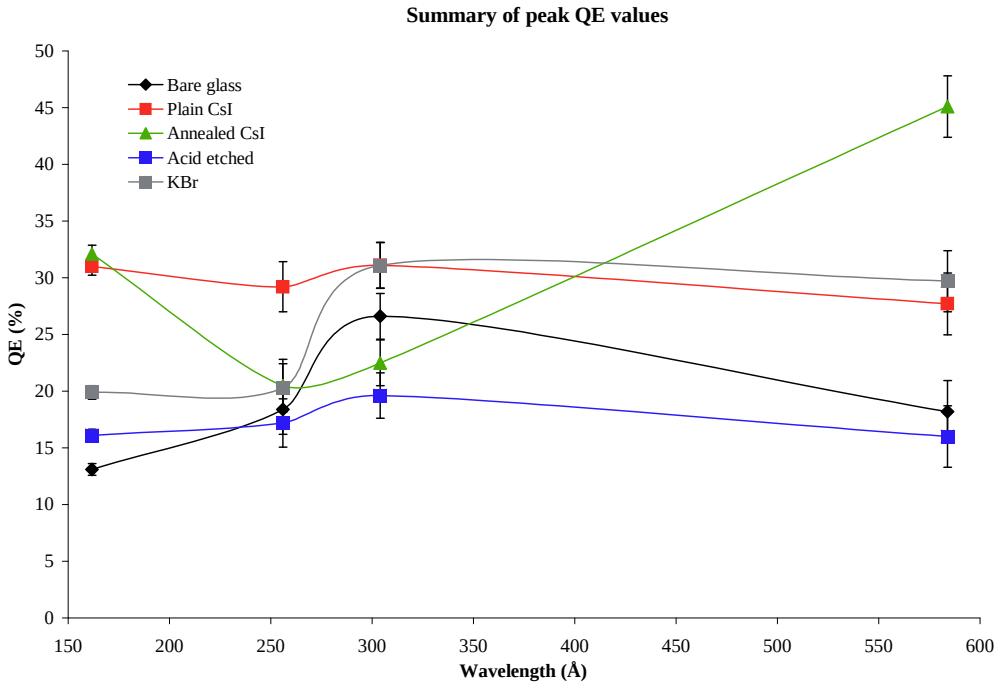

Figure 3.14: Peak quantum efficiency values (%) for each process and wavelength investigated. Note the dominance of plain (non-annealed) CsI at 256 Å, closest to the *J-PEX* waveband of the four wavelengths considered in this study. Curves are provided as an aid to clarity, and do not indicate any functional dependence of QE on wavelength.

Although a cursory glance at table 3.10 shows high QE values listed for the annealed CsI photocathode, it is clear that for all wavelengths except 584 Å, this treatment had no appreciable effect on improving the performance of the CsI photocathode. While the accuracy of high QE data at 584 Å has been questioned, the most significant observation is that thermal annealing appears to produce a serious *decrease* in QE at the important 256 Å wavelength. A wavelength dependence on the effectiveness of annealing has been suggested, but irrespective of the physical explanation for this observation, or the effectiveness of annealed photocathodes at other wavelengths, the poor performance of the annealed CsI at 256 Å is sufficient to reject this procedure.

Addition of a KBr photocathode has been shown to produce reasonable increases in QE at three wavelengths, with the results of direct, angle resolved efficiency measurements being supported by count-rate scans across the coated and uncoated regions of the MCP. However, the presence of a severe drop in the effectiveness of KBr at precisely those wavelengths covered by the *J-PEX* bandpass, as a result of the behaviour of the KBr absorption coefficient, makes this photocathode wholly unsuitable for application to the *J-PEX* detector.

Figure 3.14 shows that at 256 Å, the CsI photocathode appears to produce significantly higher QE than any of the other processes considered. This excellent performance justifies the apparent prevalence of CsI as the photocathode of choice in many of the programs described in the literature, and is corroborated by several independent studies into photocathode QE. Although the efficiency improvements offered by CsI may be matched, and in some cases exceeded, by other processes at longer and shorter wavelengths, its dominance at wavelengths relevant to the *J-PEX* program, evinced by data at 256 Å, is clear.

The work described in this chapter has highlighted the need for further investigations into the techniques of thermal

annealing and acid etching of MCPs. However, the primary aim of this study was selection of the optimum process with which to enhance the QE of the *J-PEX* detector. The data show that a plain CsI photocathode results in a QE value approximately 50% higher than any of the remaining procedures, and that therefore, an identical CsI photocathode should be applied to the front MCP of the *J-PEX* focal plane detector.

3.9 Summary

- The work described in this chapter is dedicated to identifying the most suitable process for maximising the QE of the *J-PEX* focal plane detector.
- Four processes have been considered: application of CsI and KBr photocathodes, nitric acid etching of an uncoated MCP, and thermal annealing of a CsI photocathode.
- Only the presence of a (non-annealed) CsI or KBr photocathode has been found to have a positive effect on detector QE.
- Thermal annealing produced no change in QE at 161.7 Å, and substantially reduced the effectiveness of a CsI photocathode at 256 and 304 Å. A substantial improvement in QE observed at 584 Å requires confirmation and further investigation.
- Acid etching of an MCP produced a small improvement at 161.7 Å, a reduction in QE at 304 Å, and no change at the remaining wavelengths.
- The apparent conflict between these results and those of earlier studies may be explained by the different MCP composition and wavelength of radiation used in this work.
- A KBr photocathode was found to produce reasonable improvement in QE at all wavelengths apart from that closest to the *J-PEX* bandpass (256 Å), due to a reduction in the KBr absorption coefficient around 230 Å. This feature makes KBr unsuitable for the *J-PEX* detector.
- A plain CsI photocathode is found to produce the most consistent improvement in QE across the wavelengths studied, and the best QE value at 256 Å. This performance is supported by similar results from other studies. CsI is therefore identified as the most appropriate method for increasing QE in the *J-PEX* detector.

CHAPTER 4

A HIGH RESOLUTION IMAGING MICROCHANNEL PLATE DETECTOR FOR EUV SPECTROMETRY

4.1 Introduction

THE LIMITED EXPOSURE TIME available on a sounding rocket flight, and the stringent performance requirements of the *J-PEX* mission, called for a detector which could deliver reasonable quantum efficiency with high spatial resolution, in a reliable, compact package. The basis of a suitable design already existed in the form of the Wide Field Camera (*WFC*) focal plane detector on board *ROSAT* (Barstow *et al.*, 1986). However, with more than a decade separating the two projects, advances in MCP and image readout technology have been incorporated into the new detector, updating the *WFC* concept and resulting in a design fit for use in a new generation of orbiting observatories.

This chapter is concerned with the development of the MCP detector built for *J-PEX* at the University of Leicester's Space Research Centre (SRC), incorporating a Vernier charge division readout anode and electronics developed at MSSL. Due to a variety of functional problems encountered during detector development, several modifications of the original design were necessary to produce a flight-worthy device. These problems and their solutions are described in subsequent sections. Section 4.2 provides a component-by-component description of the detector, followed in section 4.3 by a discussion of the MCPs in which the issue of low quantum efficiency in plates from certain manufacturing sources, is addressed. The operation of the Vernier anode, and a brief discussion of detector resolution, is presented in section 4.4.

4.2 Design of the J-PEX focal plane detector

4.2.1 Structure and assembly

Because of the limited space available inside the spectrometer, the detector needs to be compact in size. Strength is also important in order to survive the conditions encountered during launch and recovery (pre-launch vibration test specifications call for the assembly to withstand random vibration up to 12.7 g RMS). The detector must be sealed in its own vacuum enclosure until observations begin (to preserve the CsI photocathode which is hygroscopic, and to ensure that pressure is low enough to prevent electrical breakdown when power is applied), and re-sealed for re-entry. The active area of the detector accommodates *four* spectral tracks, one for each grating (the individual spectra to be co-added after flight) and an image of the target star from the EUV telescope, with adequate margin to allow for jitter in spacecraft attitude control. These requirements are met by the final design. The volume of the detector, excluding ion pump and electronics modules, is approximately 311 cm^3, with a circular footprint of diameter 12.5 cm. The active area is approximately 3.75 cm^2, and the layout of spectra and stellar image on this area is illustrated in figure 4.1. The overall design of the detector is shown in figure 4.2.

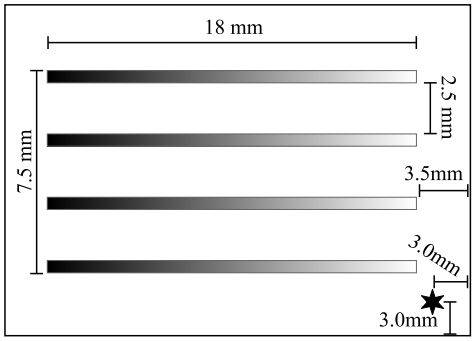

Figure 4.1: Layout of spectral tracks and stellar image within the imaging area (outer rectangle) of the detector.

The body is manufactured from stainless steel, in two sections. The MCP stack is accommodated on the base, which is fitted with ceramic high-voltage (HV) feedthroughs supplying the MCPs. Components in the stack slide over four electrically insulated locating studs and are held in place by a locking nut on the end of each stud. The readout anode is fitted from the rear of the base.

A thin Kapton annulus provides electrical insulation between the detector body, held at ground potential, and the remainder of the components which are negatively biased. A grid constructed from nickel mesh stretched over a copper ring is then placed on top of the Kapton and held at a low potential (-20 V). This defines the charge footprint and optimizes resolution and linearity. A more detailed discussion of the grid is provided in section 4.4.

Electrodes and spacers are manufactured from DiClad, a PTFE/woven fibreglass laminate produced by Arlon of Delaware, USA. Designed for use as a printed circuit board substrate in high frequency applications, the product has a low dielectric constant (ε_r) which is advantageous in reducing electrical stress due to field compression between insulators. NASA test data demonstrates its excellent low outgassing characteristics, justifying its selection as a core component in the detector. After machining, the front and rear surfaces of DiClad components are gold-coated to ensure good electrical contact.

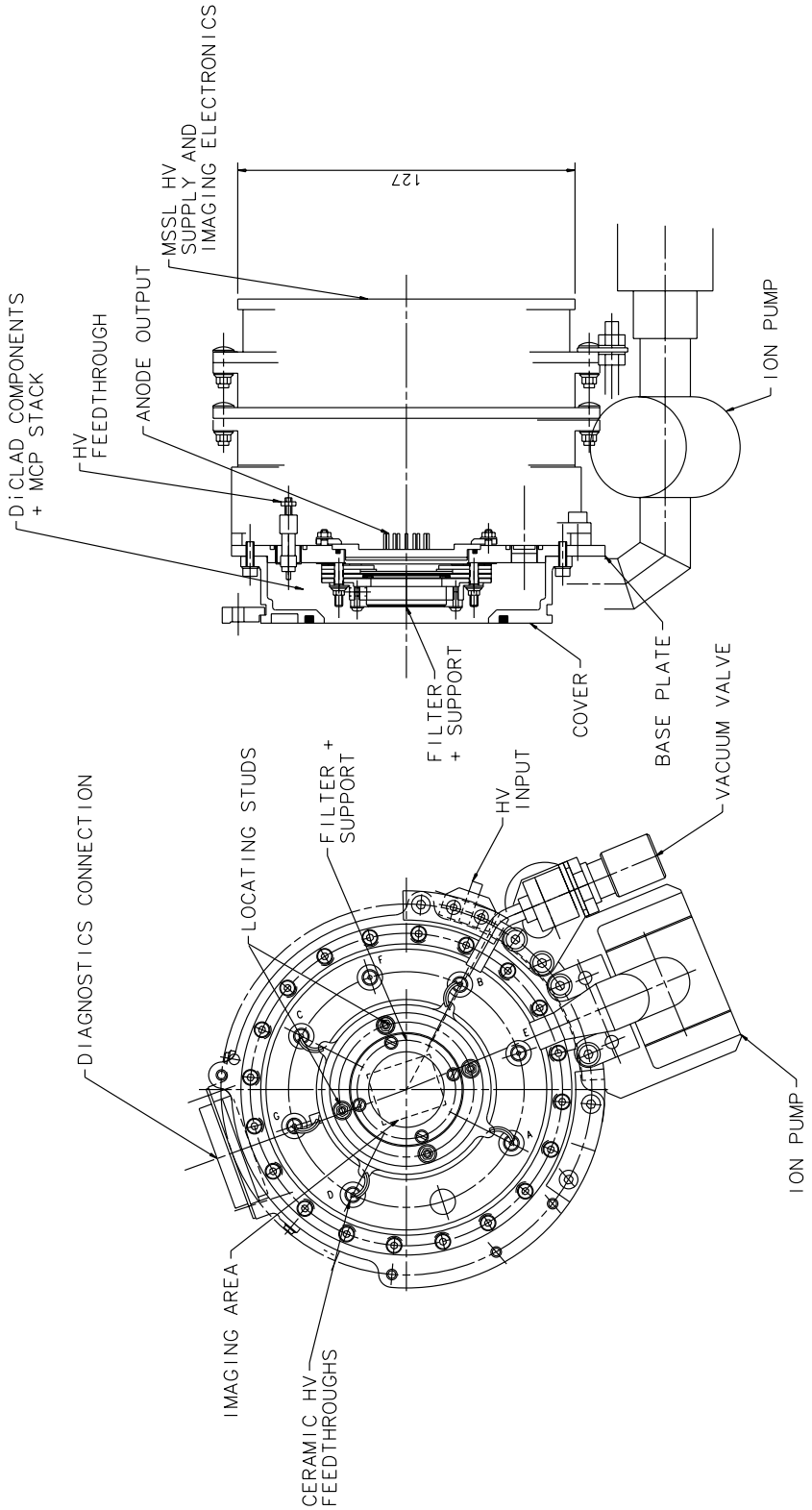

Figure 4.2: Overall design of the *J-PEX* focal plane detector, illustrating the primary components of the MCP stack and detector casing.

A layer of DiClad is placed over the top of the focusing grid, with an aperture slightly smaller than that of the rear MCP. A second layer sized to accommodate the plate is then added, forming a receptacle in which the MCP sits. A copper frame placed inside this "well" defines the active area of the detector, masking the anode from perimeter areas above. The rear MCP is then placed on top of the frame, with a $\sim$ 5mm MCP-to-anode gap. The second

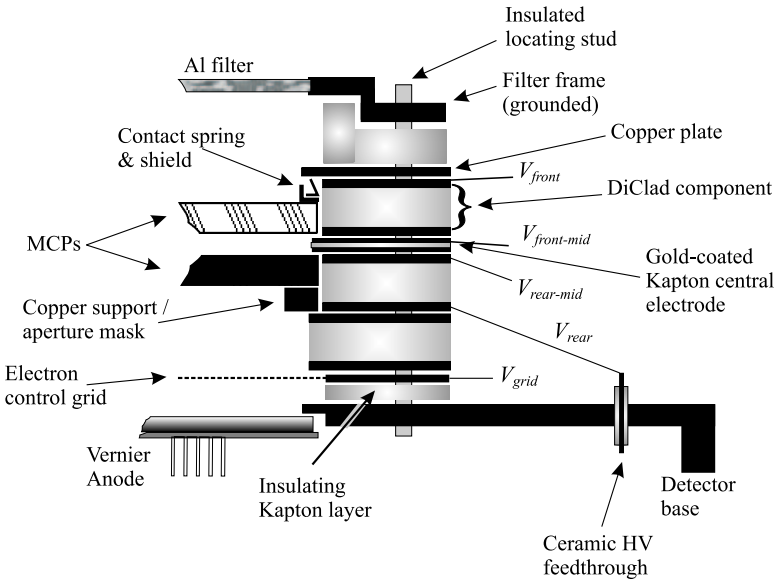

Figure 4.3: Cross-section through the MCP stack. Grey shaded areas represent insulators, black lines correspond to conductive surfaces. High voltage connections are shown in italics. (Some parts omitted for clarity.)

DiClad component is fitted with nickel wires connected to HV feedthroughs supplying the front and rear potentials for the bottom MCP. The rear face potential is thus applied to the MCP via the lower DiClad component and the copper frame, as illustrated in figure 4.3.

The thickness of the copper frame is such that the upper face of the rear MCP is flush with the top of its DiClad retaining ring. A thin ($\sim 180\mu$m) gold-coated Kapton sheet is then placed over the assembly. This provides an electrical contact for the two central MCP faces, while the Kapton substrate allows an inter-plate gap voltage to be established. A final DiClad component holds the front MCP, and is also connected to a pair of HV feedthroughs. The front MCP is fitted, and a spring added, providing an electrical contact and a regulated clamping pressure for the MCPs. A copper sheet is placed on top of the stack, compressing the spring and completing the connection to the HV supply.

The stack is completed by a thin ($\simeq 1100$ Å) Aluminium filter with a transmission of 56% at 256 Å, manufactured by Luxel Corporation, Washington, USA. This filter is mounted on a metal frame electrically insulated from the remainder of the MCP stack by a fibreglass spacer, and held at ground potential via the locating studs. The filter absorbs EUV background radiation scattered into the detector by the gratings and other structures in the spectrometer. This radiation is dominated by solar photons scattered by H and He atoms in the Earth's geocorona, producing lines at 1216 Å (Ly-α), 584 Å (He I) and 304 Å (He II) (collectively known as geocoronal emission lines). The intensity of the observed emission is a function of several variables, including viewing angle, magnetic environment, and the level of solar activity at a given time. However, on the night-side of the Earth, the flux from geocoronal emission lines falls by approximately two orders of magnitude with respect to levels on the daylit side, and is produced by resonant scattering of solar photons from atoms in the interplanetary medium (Adams & Frisch, 1977, Labov & Bowyer, 1991).

Since *J-PEX* is launched at night, it is the weaker night-time component which is of primary concern. Barstow (1983) presents a compilation of geocoronal fluxes from data presented by Weller & Meier (1974), Meier &

Weller (1974), and Weller (1981). From this work, values for the nighttime geocoronal background of $< 0.3 - 1$ Rayleigh[1] (He II 304 Å), $1 - 9$ Rayleigh (He I 584 Å) and $\sim 3 \times 10^3$ Rayleigh (H I 1216 Å, or Ly-α) are obtained (H I emission is altitude dependent, and so the latter figure corresponds to an altitude of 215 km, appropriate for the case of the *J-PEX* trajectory, which has a nominal apogee of 300 km). The focal plane detector has an imaging area of ~ 3.74 cm^2, and a field of view of diameter $\sim$ 15 arcmin corresponding to a solid angle $d\Omega = 1.5 \times 10^{-5}$ steradians. The resulting geocoronal fluxes are therefore 0.13 - 4.46 counts sec^{-1} (He II 304 Å), 4.46 - 40 counts sec^{-1} (He I 584 Å), and $\sim$ 13397 counts sec^{-1} (Ly-α). However, filter transmission and detector quantum efficiency must be included in the background flux calculation. Figure 4.4 shows the high transmission of a 1500 Å thick Al filter between $\sim 200 - 600$ Å, with an abrupt cutoff which blocks wavelengths longer than ~ 950 Å. This profile effectively prevents the high Ly-α flux from entering the instrument, and reduces the 304 and 584 Å lines by approximately 60%. Assuming a QE of $\sim$ 30% for the MCP detector (on the basis of the results presented in Chapter 3), the remaining He I and He II line fluxes are reduced to 18% of the values suggested above, i.e. 0.02 - 0.80 counts sec^{-1} (He II 304 Å), 0.80 - 7.2 counts sec^{-1} (He I 584 Å), compared to a predicted count rate of $\sim$ 30 counts sec^{-1} from G191-B2B, determined using results from *EUVE*.

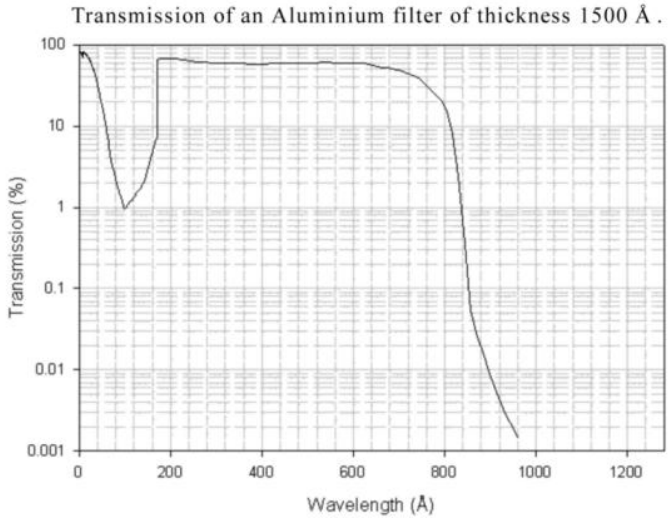

Figure 4.4: Transmission of a 1500 Å thick aluminium filter, demonstrating the long wavelength cutoff which reduces the flux from Ly-α geocoronal emission entering the spectrometer. Note that the filter fitted to *J-PEX* is of thickness $\sim$ 1100 Å. Figure courtesy of Luxel Corp.

A cover is placed over the base, followed by an electrically operated, hermetically sealed door. This design allows pump-down of the detector, independently of the rest of the instrument, *via* a valve fitting in the cover. External vacuum equipment is necessary to begin this operation, requiring the attachment of vacuum hoses, and is thus only possible when the detector is removed from the payload, or when the spectrometer door is open during ground tests. Once an acceptable vacuum is established ($\sim 10^{-5}$mbar or lower), the valve is closed and hoses removed. An integral ion pump then maintains the vacuum, attaining pressures in the low 10^{-6}mbar range (see figure 4.2). At approximately 70 minutes before launch, preparations are made for final arming of the rocket motors, after which access to the payload is no longer possible due to safety considerations. The external ion pump controller must therefore be removed at this time, and for the final 70 minutes before launch, the detector is not pumped. The door opens after launch once the pressure in the main spectrometer chamber is low enough to prevent coronal discharge, and is closed following observations, protecting the detector during re-entry. The door mechanism was

[1] 1 Rayleigh = 7.96×10^4 photons cm^{-2} sec^{-1} steradian^{-1}.

originally designed for SSULI (*Special Sensor Ultraviolet Limb Imager*), an optical remote sensing mission run by the U.S. Naval Research Laboratory (Thonnard *et al.*, 1994).

4.2.2 Repeller grid

Since the front MCP has an open area of approximately 63%, a significant proportion of photons incident onto the MCP fall onto the interchannel web, producing photo- and secondary electrons which are lost from the system. These electrons can be deflected back into the detector if an appropriate electric field is maintained above the front MCP, acting in the same direction as that established across the MCPs. Producing a force $\underline{F} = e\underline{E}$ (where *e* is the charge on the electron), this drives photoelectrons ejected from the interchannel web, back toward the MCP, where they may interact with adjacent channels (figure 4.5). Investigations into this technique demonstrate significant increases in QE for CsI coated MCPs, particularly at high angles of incidence and long wavelengths, as demonstrated by Fraser *et al.* (1984), who measure a front surface QE of up to 10% at 44.7 Å, with this value being a strong function of incident angle. Bare glass efficiency shows a more modest improvement, as shown in the study by Taylor *et al.* (1983).

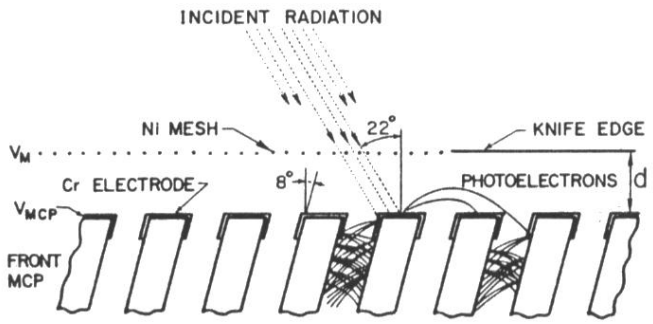

Figure 4.5: Action of a repeller grid, showing the spread of photoelectrons away from the source site. The electric field between mesh and channel plate is $E = (V_{MCP} - V_M)/d$. (After Taylor *et al.*, 1983.)

However, a typical photoelectron will be emitted with a component of velocity perpendicular to the field direction, returning to the surface of the plate some distance from the point of emission, and initiating an electron avalanche which effectively smears out the event. While increasing the $\underline{E}$ field limits the electron range, it also reduces the probability of the electron reaching neighboring channels, with any further increase in field strength producing a *decrease* in QE. Repeller grids, therefore, offer an increase in efficiency in exchange for degraded resolution, as illustrated in figure 4.6. For *J-PEX*, preservation of spatial resolution is the highest priority, and hence a repeller grid was not fitted.

4.2.3 Noise reduction

Early detector configurations suffered from an unacceptably high level of background noise ($\sim$ 17 counts s^{-1}), as illustrated in figure 4.7 (left). Noise PHDs were saturated, indicating an external source, but covering inspection apertures, and turning off potential sources of charged particles such as vacuum gauges, did not result in any noise reduction. Electrical effects related to the high voltages at the front of the detector were suspected, and attention

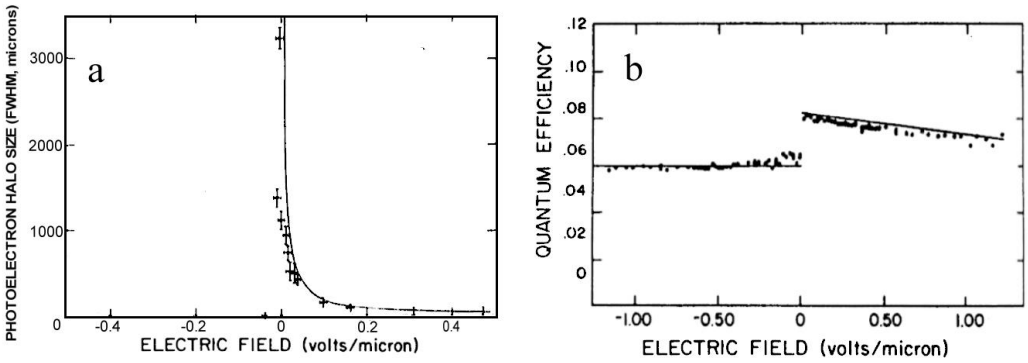

Figure 4.6: Performance of an MCP detector at 304 Å, as a function of the E field produced by a repeller grid above the front MCP. (a) QE; (b) FWHM of the electron halo produced by migration of surface-sourced events. Solid lines indicate theoretical predictions. (After Taylor *et al.*, 1983.)

turned to the possible existence of tracking paths and high field regions above the front MCP.

Several modifications to components such as the filter mounting ring and the front plate contact, were tested in an attempt to eliminate tracking events at the front of the detector. Although apparently producing slight reductions in noise, the minor changes in component position and clamping pressure inevitable during detector assembly could also lead to variations in the level and distribution of noise, even when no design changes were made. The marginal improvements returned by these early modifications led to their eventual abandonment, and hence they are not discussed further.

Enhanced perimeter noise in MCP detectors may be suppressed by designing a slight ($\sim$ 1mm) decrease in the aperture of successive component layers, such that the rear components have smaller apertures than those above, masking the readout anode from perimeter areas (Barstow, 1983). In line with this practice, the copper frame supporting the rear MCP was replaced with a version having a smaller aperture. The central electrodes were

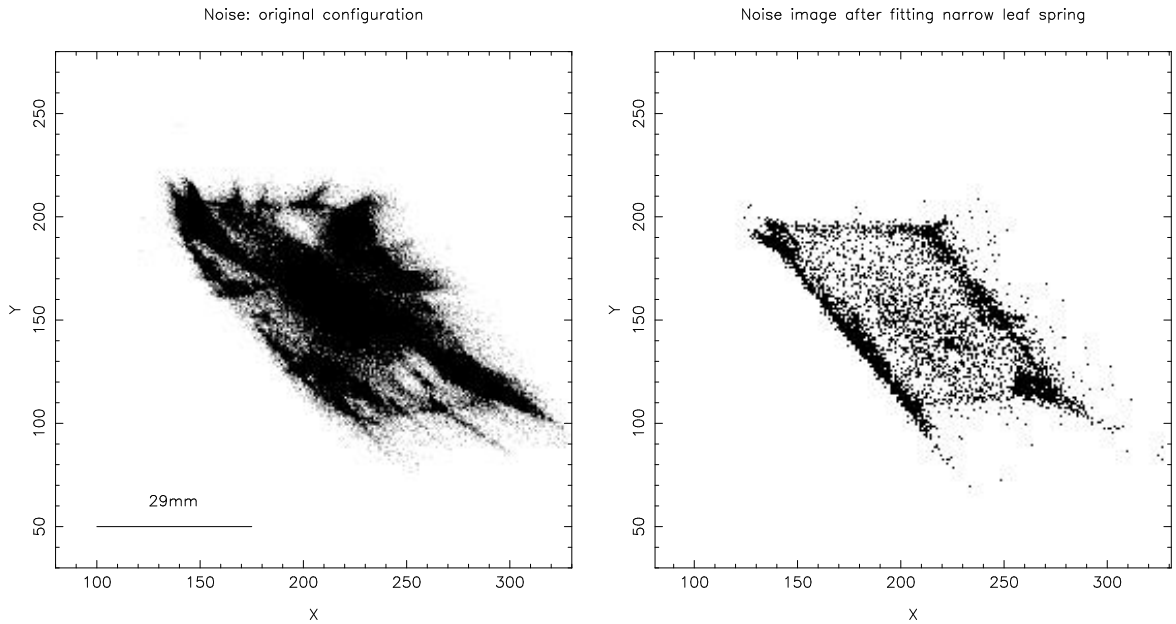

Figure 4.7: (Left) noise image from the first detector build (count rate $\simeq$ 17 counts/sec). (Right) noise after fitting a narrow leaf contact spring. Distortion in the images is due to crosstalk in the early test electronics, which employed a conventional wedge-and-strip anode. Axes units are in pixels.

similarly modified, and the front face contact (which compresses the spring) was redesigned to provide shielding from any charged particles entering through outgassing holes in the side of the filter mounting ring. The small resultant loss in imaging area was accompanied by a reduction in noise from 17 to 15 counts/sec.

More significant progress in noise reduction was made possible by the realization that the distribution of events appeared to be correlated with the geometry of the front spring. As shown in figure 4.7 (left), noise events were particularly dense around the corners of the imaging area, and these locations could be related to features of the contact spring, which was manufactured from a single sheet of metal, folded to produce the form shown in design (a) of figure 4.8. Although being easy to produce, this design was less than ideal due to the sharp edges and points which resulted, each a potential source of noise from field emission.

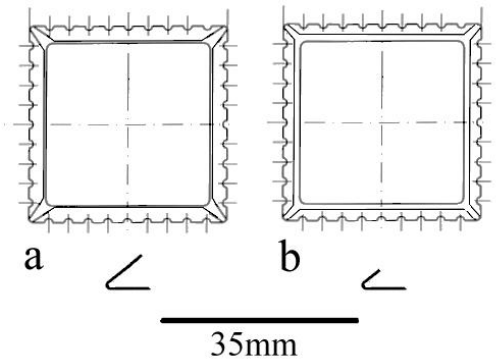

Figure 4.8: Detector contact spring. a: original design. b: modified with reduced top leaf. (Profiles shown under each spring).

While other designs of spring were available, the increased complexity of their manufacture would have been time consuming and expensive. Rather than eliminating high field areas entirely, an acceptable alternative was to increase their distance from the imaging area, and this was achieved by reducing the size of the top leaf of the spring, as shown in design (b) of figure 4.8. This modification was successful in reducing noise levels by $\simeq 60\%$, with particular improvement in the corners as illustrated in figure 4.7 (right).

As a further precaution, a shield was fitted underneath the spring to prevent electrons or ions produced by field emission from reaching the front MCP (figure 4.9, left). The shield was designed with all corners and edges radiused so that no further high field regions were added into the system. Introduction of the frame achieved a dramatic reduction in noise levels, with background rates of between 1.8 and 3.0 counts/sec being recorded (approximately 0.36 - 0.60 cts cm^{-2} s^{-1}). These levels were acceptable for the flight detector. Noise reduction steps are summarized in table 4.1.

Modification	*Noise rate*	*Comments*
Original configuration	17	See figure 4.7, left.
Reduced aperture components	15 Hz	Rate increasing with time.
Smaller top contact spring	10 Hz	Some perimeter noise (fig 4.7, right).
Spring cover fitted	1.8 - 3.0 Hz	Corners now quiet (fig 4.9, right).

Table 4.1: Major changes made to the detector design to reduce noise levels, as discussed in the text.

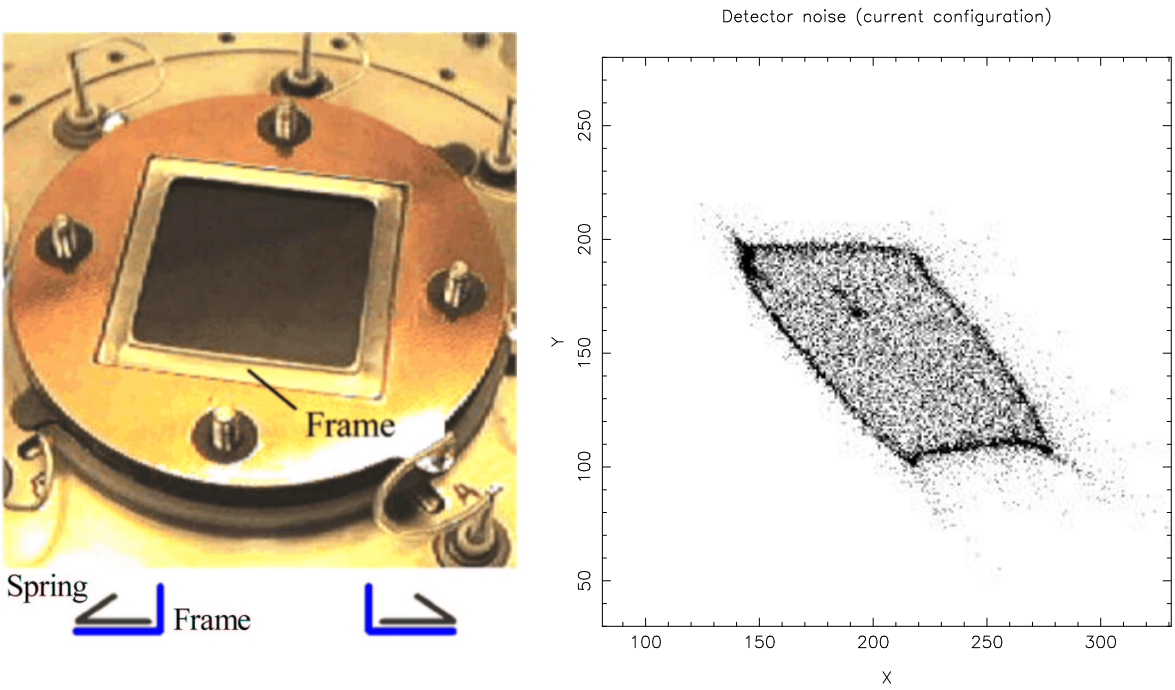

Figure 4.9: Left: Installation of the spring frame above the front MCP (before fitting of spring); the profile of the frame is also shown. Right: noise image after installation of a shield for the contact spring. Count rate $\simeq 3$ counts s^{-1}.

4.2.4 Electrical breakdown

During the course of detector trials, events were observed in which electronics (computers and multichannel analyser) "hung", resulting in loss of data. These incidents were accompanied by the power supply to the input face of the front MCP switching to an overload or current-limiting state, and the front plate ammeter showing a momentary overflow. MCPs were inspected following trip-outs, and in most cases no damage was detected, though small burn marks on the front input surface were found underneath the spring frame on several occasions. The timing of these events was variable; some were recorded within seconds of the detector reaching optimal voltage, although several days could elapse before a trip-out was observed.

The problem was confined to the front plate, affecting only the upper face PSU (the highest potential surface), and occurring when the front plate voltage was approaching its optimal value. To eliminate the PSU as a possible cause, a second unit (without overload protection) was used; the problem persisted, but the absence of overload protection resulted in damage to both front and rear plates. This damage consisted of a small area on the front plate in which channels appeared to have fused throughout their entire length, with a corresponding feature on the input surface of the rear plate. The location was coincident with the inside edge of the spring cover. The rear plate remained functional, and was eventually flown in the detector, while the front plate was replaced with a spare MCP of identical specification. Following this test, the original, protected PSU was reinstated.

Thermal overload in the plate was briefly investigated. Simple finite-element modeling based on the current drawn by the plates, and their area, suggested an unremarkable temperature of approximately 35°C. Attempts to provoke the problem by heating the detector while maintaining full power did not result in an increase of failures; nor could the problem be reproduced "on demand" when the potential was increased above its optimum value. Breakdowns

did not appear to be correlated with the fitting of any particular component, since returning the detector to its original configuration brought about no improvement in stability.

The major issues addressed in the ensuing investigation are outlined below.

4.2.4.1 Detector cleanliness

The frequency of trip-out events appeared to increase over periods of weeks as the number of detector build cycles accumulated, suggesting that the problem might be connected with component cleanliness or wear. In some cases, thorough cleaning of components using of degreasing agents, solvents, and vacuum bakeout procedures, appeared to extended the period between trip-outs. However, the improvement was not consistent, and it appears that the correlation was coincidental.

4.2.4.2 Choice of material

The suitability of the material used to manufacture electrodes was a subject of considerable discussion. The basic properties of DiClad were described in section 4.2.1. DiClad consists of a woven substrate made from PTFE-coated fibreglass, with copper cladding bonded to each side of the board. Concern centred on the nature of the substrate, which showed a tendency to take on a fibrous texture around machined edges, as illustrated in figure 4.10. It was proposed that in the high voltage environment of the detector, these fibres, when electrically charged, might produce E fields of sufficient strength to produce arcing or coronal breakdown in the presence of any residual atmosphere[2] within the detector cavity.

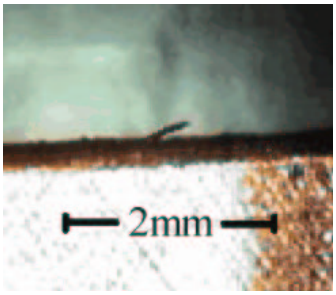

Figure 4.10: Optical microscope image showing the machined edge of a DiClad electrode, with an exposed fibre clearly visible. (Approximate scale only).

Attempts to remove fibres using abrasives resulted in further roughening of the DiClad edges. A more effective method was found to be gentle rubbing with a dry laboratory tissue, and with care it became possible to remove all of the major filamentary structure around the electrode edges.

A further area of concern was the porosity of the substrate. During the early phases of detector development, it was common practice to clean components with Isopropyl Alcohol (IPA) between builds, and to allow these components to dry in air prior to re-installation. This raised the possibility that small quantities of fluid might remain in the fibreboard, leading to considerable outgassing, and producing favourable conditions for coronal

[2]The provision of adequate outgassing paths is addressed later in this section.

discharge. Handling procedures were therefore modified, and all cleaning was followed by an 80°C bakeout for 1 hour at 1 atmosphere. Vacuum baking was performed on new components and before assembly of the flight build.

Removal of fibres and adequate drying of the DiClad did not appear to significantly reduce the frequency of trip-out events, but by removing potential failure-points, these practices were positive measures, and were retained for the remainder of the program.

4.2.4.3 Outgassing paths and electrical insulation

During a period of frequent trip-outs, the rear plate was powered down, and the front voltages reduced such that the potential across the plate remained unchanged, while the absolute potential of the stack was lower. The detector could be operated in this mode for an apparently unlimited period without the occurrence of trip-out events, suggesting that the problem was related to the E field above the front plate, rather than the bias across the MCP. The transient nature of these events, and their possible relationship to the E field around the front of the detector, suggested that outgassing was responsible. If insufficient time was allowed for evacuation of gas within the detector before applying power, any residual atmosphere in the region where the E-field is strongest, might provide a breakdown path, resulting in the observed behaviour. Attention turned to the provision of adequate outgassing paths and insulation inside the detector.

Components in the stack were tightly clamped to ensure good electrical contact and to prevent movement of the MCPs during flight. Consequently, little space was available between electrodes and insulators for gas within the assembly to escape. The initial detector design provided two principal outgassing paths: channels machined into the base plate linked the volumes inside and outside of the MCP stack (figure 4.11), while four holes drilled into the side of the filter holder allowed gas to escape through the top of the assembly.

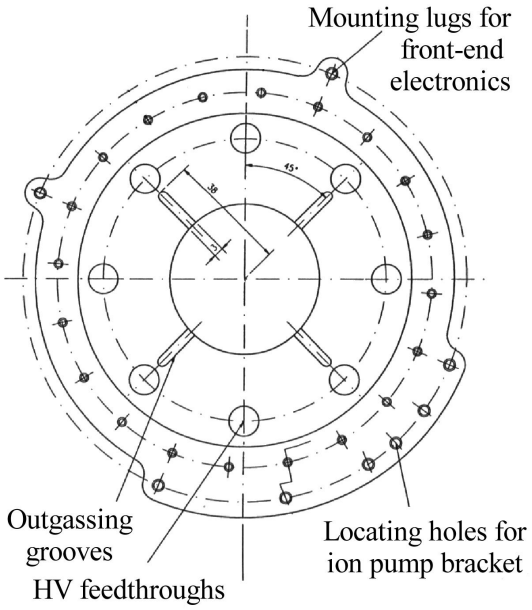

Figure 4.11: Detail of the detector base plate, illustrating the channels designed to provide an outgassing path between the interior and exterior of the MCP stack.

Inspection of the design revealed that a significant trapped volume existed in a column around each locating stud, enclosed by electrodes and insulators; the bottom of this column was sealed by the base plate, and the top by the filter adaptor and lock-nuts. Since the studs were not insulated, a circular area of conductor approximately 8mm in diameter around the locating hole of each component was etched away in the original design, to prevent shorting between studs and electrodes (these etched areas are visible in figure 4.9). However, any gas in this area increased the risk of breakdown. Three measures were implemented to reduce this risk:

- Locating studs were sleeved with vacuum shrink-wrap, from base to the level of the uppermost electrode, with the unsleeved thread providing a ground contact for the filter assembly.
- Electrodes and insulators were re-manufactured with a small outgassing scallop machined into each locating hole, permitting free movement of gas in the column (see figure 4.12).
- The insulator beneath the filter adapter was modified by the addition of channels crossing each locating hole, allowing the gas inside each column to dissipate from the MCP stack into the pumped volume (also illustrated in figure 4.12).

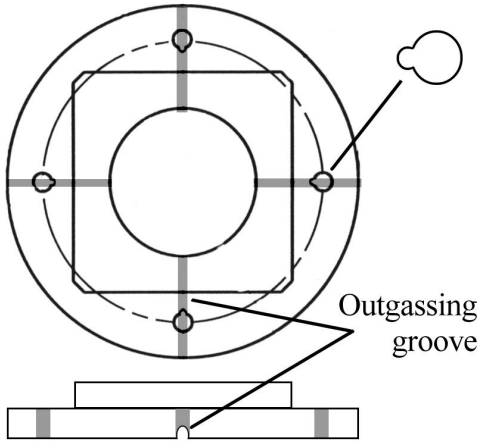

Figure 4.12: Top and side views of the fibre-board insulator, showing additional outgassing scallops machined into each electrode and insulator, and grooves ruled across locating holes in the fibre-board to allow the passage of gas into the outer volume.

Despite highlighting the relatively poor outgassing characteristics of the initial design, and provision of extra routes, these measures brought about no significant reduction in the frequency of breakdown events.

4.2.4.4 Power-up sequence

If significant outgassing in the high E field region at the front of the detector was occurring, a potential solution may have been a longer period of pump-down before applying power to the detector. However, Ohmic heating of the MCPs when power was finally applied would be expected to produce a large increase in the outgassing rate, as gas molecules adsorbed onto the channel walls were released[3]. Rather than extending the pump-down times, it was decided to exploit this heating effect to gently "self bake" the MCPs by gradual application of power.

[3] "Baking out", or the application of heat to components under vacuum, is a technique routinely used to achieve high levels of cleanliness in vacuum systems.

In the first trial, power was slowly applied over a period of 2 hours with constant UV illumination from a mercury vapor discharge lamp, after an initial period of 18 hours under vacuum. The illumination produced a count rate of approximately 200 counts/sec, and was intended to promote more rapid heating, and therefore outgassing, of the plates, while large E fields were avoided during this phase. This technique resulted in the frequency of failures being reduced, though not eliminated.

A second approach was to apply power gradually over a period of 5 days, the detector having been under vacuum for the previous 24 hours. This practice provided an extended time for outgassing, and resulted in notable successes. Uninterrupted operation was sustained for several days at full voltage before power was turned off (the detector remaining under vacuum). Following a 12 day gap, full power was re-applied instantly, and sustained for 14 days without incident.

Despite these achievements, subsequent detector builds did not respond to the practice with the same degree of stability. However, the partial success of these practices supported the hypothesis that outgassing was the source of breakdown events.

4.2.4.5 Solution of the breakdown problem, and the advantage of solid-edge MCPs

Trapped volumes still existed in the form of channels in the front MCP which were blocked by the spring frame on the input face, and the mid-electrode on the exit face. These channels posed the risk of outgassing in the strong E field region, and offered an explanation for the persistence of breakdown events. The hypothesis was supported by the appearance of spots underneath the spring shield following several incidents, while on one occasion, corresponding marks on both frame and mid electrode suggested breakdown *between* the MCP faces through the column of gas contained in these channels. Although an area of the rear plate was also enclosed by electrodes, the absence of anomalous readings from this MCP is most probably due to the inability of the weaker electric field to produce breakdown in gas released from these channels, and is consistent with this hypothesis.

In a study of identical MCPs carried out by Pearson *et al.* (2000), plates were successfully operated at potentials comparable to those employed in the *J-PEX* detector. Clearly there is no inherent instability with this type of MCP, but it is noted that significant differences exist between the construction of the laboratory detector used in the study by Pearson *et al.*, and the flight detector. Specifically, high clamping pressures were necessary in the latter device to prevent movement of the MCPs during launch. The laboratory detector design also avoided the solid "stack" of components, adopting a looser form, providing gas inside the volume with more freedom to pass into the pumping line.

The sealing of channels was unavoidable without substantial modification of the detector. However, an alternative solution was available in the form of "solid-edged" MCPs, in which the active area containing channels was surrounded by a solid glass perimeter, providing a firm contact area and removing the problem of trapped channels. The Galileo MCPs described in Chapter 3 were of this type, in contrast to the standard, soft-edge Photonis MCPs in which channels extended to the plate edges. As described in section 4.3, poor QE performance of the original plates incorporated in the detector made it necessary to select a different front MCP for the flight. The final choice

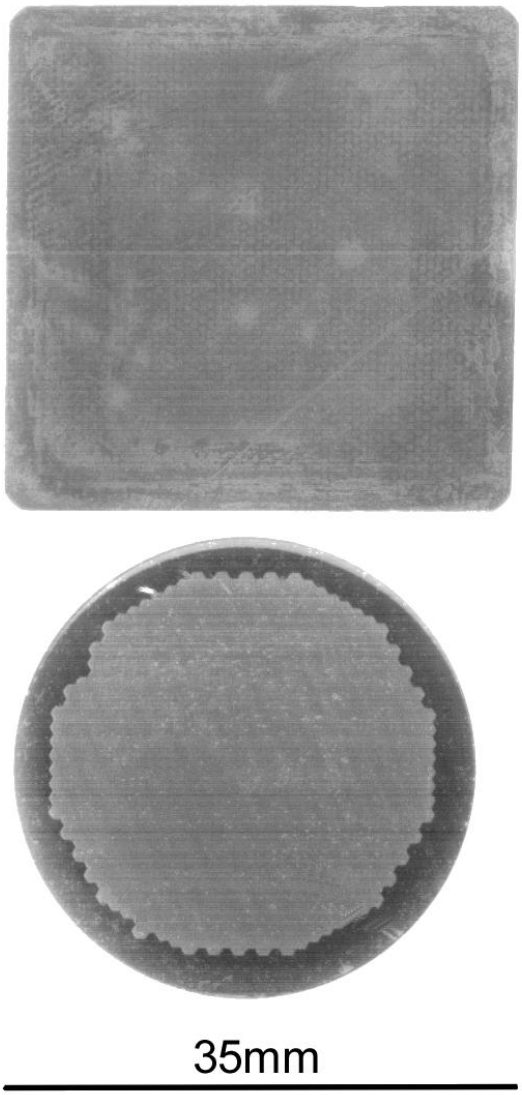

Figure 4.13: Microchannel plates used in the focal plane detector. Top: Photonis 6μm pore MCP, originally intended for both front and rear plates, but fitted in the rear only for flight (note the clear boule structure) . Bottom: Solid-edge Russian IKI plate, flown as the front MCP with a CsI photocathode. (Horizontal lines are an artifact of the imaging process.)

was a solid edged Russian plate, and its introduction brought about an end to the occurrence of breakdown events, despite the new MCP operating at similar bias levels, with equally strong E fields around the front of the detector. Details of all MCPs tested in the detector are provided in the next section, and in figure 4.13, the original Photonis plate design is shown along with a solid-edged Russian MCP.

4.3 Microchannel plates

The use of normal incidence optics produces a flat focal plane, in contrast to the curved focal surfaces of grazing incidence designs (Fraser, 1989), and so it was possible to use flat MCPs in this detector without compromising the off-axis imaging performance. To ensure optimum resolution from the system, MCPs with small pore size, manufactured by Photonis SAS (Brive, France) were initially selected. The specification of these plates is given in table 4.2.

Pore size	6μm
MCP size	35mm
Open area fraction	65%
L:D ratio	120:1
Resistance	$\simeq$ 90 MΩ @ 1650 V
Bias angle	13°

Table 4.2: Photonis MCP specifications

4.3.1 Determination of optimum bias voltages

Optimum bias voltages for front and rear plates were established by illuminating the detector with photons at 304 Å (since this emission line offered a much higher signal-to-noise ratio than 256 Å). The 2mm diameter circular source image was centred in the imaging area, and pulse height distributions were recorded for a series of voltages. The optimization procedure consisted of three stages. The voltages of the front MCP (V_f) and inter-plate gap (V_g) were fixed at sensible values (e.g. levels which produced acceptable, if not optimal, PHDs) while the rear MCP bias voltage V_r was varied, and its optimum setting determined. V_r was then fixed at this optimum level, V_g also remaining fixed, while V_f was adjusted. Having found the optimum bias voltages for the two MCPs, the gap voltage was then determined using the same procedure.

At each voltage setting, the modal gain and FWHM were recorded, and their values plotted against voltage to produce the curves illustrated in figure 4.14. Sharply defined distributions (e.g. those with a narrow FWHM) are preferential for imaging, since they reduce the dynamic range which must be processed by the charge sensitive pre-amplifiers that collect the signals from the imaging anode. Excessively high gain would compromise the detector's lifetime due to the increased charge abstracted per X-ray event (Whiteley *et al.*, 1984, Pearce *et al.*, 1995), while very low gain levels would result in poor imaging resolution (as explained later in section 4.4). Optimum bias levels were therefore a compromise between these considerations. Using this method, voltages of $V_r = V_f = 1650$ V, and $V_g = 200$ V were selected for the 6μm MCPs.

4.3.2 Low QE in small pore microchannel plates

An extensive investigation into the augmentation of MCP QE was described in Chapter 3. Two results from this study are of particular relevance to the work which follows:

- The peak QE of bare glass plates at 256 Å was determined to be approximately 18%.
- Application of a CsI photocathode of thickness $\sim$ 14,000 Å on the front MCP was the most effective method of improving QE, with peak values of 28% being measured at 256 Å.

As a consequence of this study, the front *J-PEX* MCP was coated with a 14,000 Å thick layer of CsI. However, QE measurements performed after coating revealed a detection efficiency dramatically lower than obtained in the earlier study, and considerably less than desirable for flight. The peak efficiency was slightly less than 8% at 256 Å, with low values also measured at 237 Å and 304 Å. Measurements made with an uncoated plate from the same

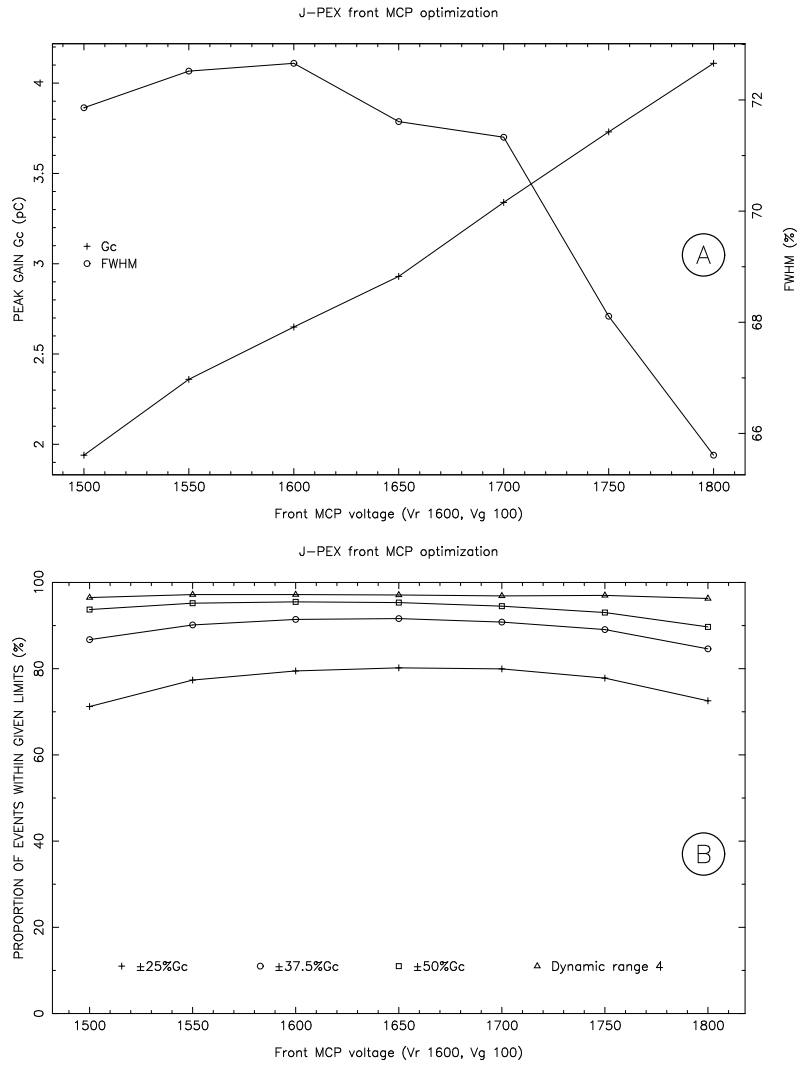

Figure 4.14: Plot used to determine the optimum bias settings for the detector (in this case, for a 6μm Photonis MCP as the front plate). Corresponding figures were generated for the rear MCP and gap voltage. Using these particular plots, the optimum MCP voltage was selected as 1650 V, constituting a compromise between narrow FWHM and low gain, while maximizing the fraction of total events held within the dynamic range (see text).

boule also revealed low bare-glass efficiency, compared with a Galileo MCP efficiency curve (figure 4.15). Pulse height distributions, although well formed ($\simeq$ 58% FWHM at 1650 V), exhibited relatively low gain (3.24 pC) as shown in figure 4.16.

4.3.2.1 SEM studies of 6μm MCPs

The disappointing performance of 6μm MCPs raised questions over the surface morphology of these plates. It was necessary to determine how far the nichrome electrode penetrated into the channels, and whether the CsI photocathode was implicated in the problem (e.g. due to blocking of channels, inadequate or excessive penetration depth, or uneven coverage). An analysis was performed with the Scanning Electron Microscope facility in the University of Leicester Clinical Sciences department, using an MCP from the same boule as that fitted in the detector, prepared and coated with CsI to the same specification using an identical process. Images showing the extent of the nichrome and CsI coatings are presented in figures 4.17 and 4.18 respectively.

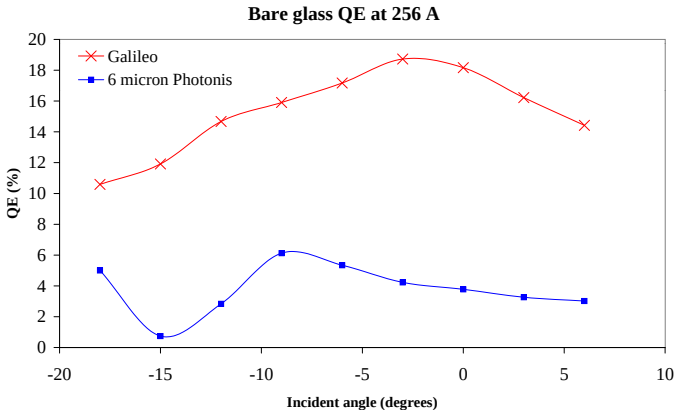

Figure 4.15: Angle-resolved QE measurements at 256 Å, for bare glass Galileo and Photonis MCPs.

Using the scale provided in the image, it is clear that the depth of nichrome penetration into each channel (end-spoiling) is one half of a channel diameter (3μm), as specified by Photonis. Images from the CsI analysis appear to show a significant buildup of photocathode on the plate surface (figure 4.18). However, this is an illusory effect of the non-conductive CsI accumulating charge in the SEM, and producing an exaggerated signal in the image. Optical microscopy of the same sample revealed that the channel pores were not clogged, although an acceptable depth of CsI had been deposited on the surface. The distribution of photocathode *within* the channels is also significant. For a plate with channel diameter D and bias angle β, the penetration depth P of any coating applied at normal incidence to the plate surface is simply

$$P = D \csc \beta. \tag{4.1}$$

For 6μm plates with a 13° bias angle, this depth is approximately 27μm. Figure 4.18 shows CsI up to 16μm inside the channels before the features become difficult to detect. This appears to be in general agreement with the geometric penetration depth estimate.

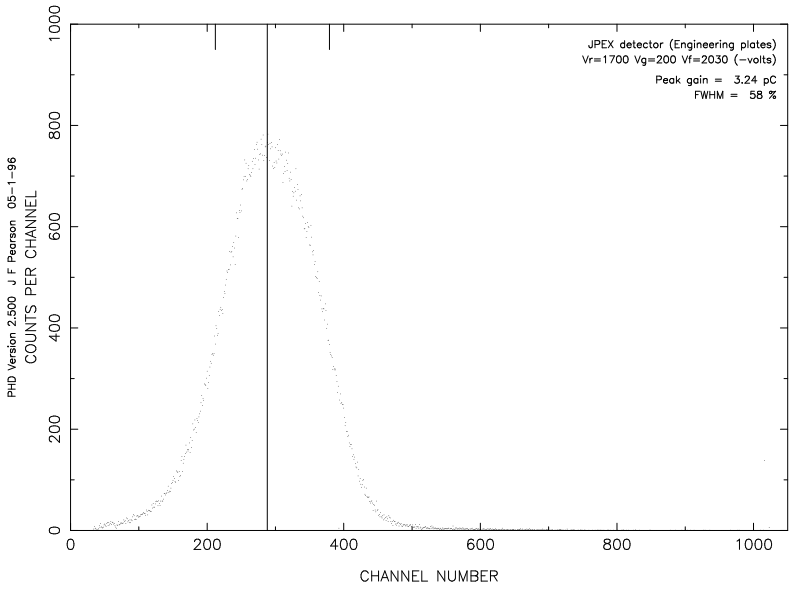

Figure 4.16: Pulse height distribution of a 304 Å source, exhibiting the low gain characteristic of the *J-PEX* MCPs.

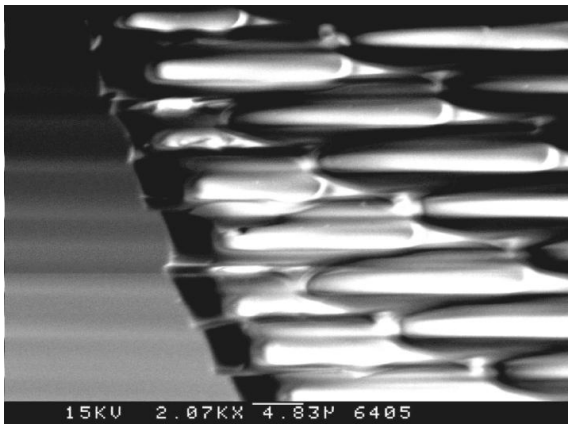

Figure 4.17: SEM image showing the penetration depth of the nichrome electrode (dark regions) into channels.

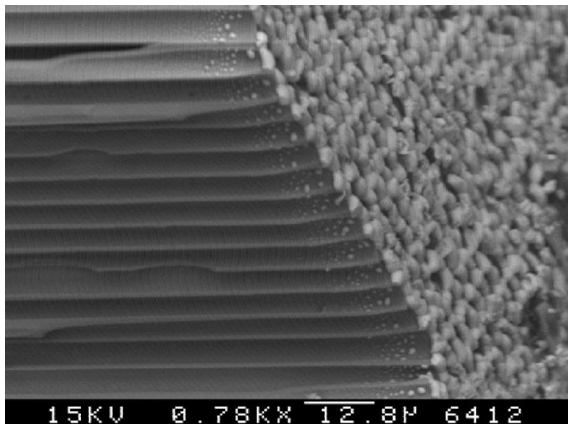

Figure 4.18: SEM image of channel entrances, illustrating the depth and distribution of the CsI photocathode.

4.3.2.2 Electronics cross-calibration

The high QE values described in the previous chapter were obtained using electronics originally designed for development work on the *ROSAT WFC*, and unsuitable for operation with the Vernier anode. All data from the *J-PEX* detector (once the Vernier anode was fitted) were obtained using the same purpose-built electronics that would later be employed during flight. It was therefore necessary to ensure that no significant disparity existed between the response of the two sets of electronics, and that events were not being lost by the *J-PEX* experimental ground support equipment (EGSE), resulting in an erroneously low QE. Discriminator settings were hard-wired into the EGSE, preventing adjustments from being made without considerable modification.

Cross-calibration of the electronics was achieved by using standard BNC T-pieces to tap each of the 9 preamp outputs to the EGSE. A pair of dual-sum-and-invert rack modules were used to combine the tapped signals, before being passed into a shaping amplifier and finally to an event counter. The arrangement allowed simultaneous rate measurements and PHDs to be made with both sets of electronics.

Readings were taken at 584 Å for a range of angles, with excellent agreement observed between results returned from the *ROSAT* electronics and the *J-PEX* EGSE. Figure 4.19 illustrates the comparison between PHDs taken at an incident angle of -3°. QE values obtained for this measurement were 4.8% (*ROSAT* electronics) and 4.7% (EGSE), indicating that the results obtained from the EGSE were consistent with those from the *ROSAT* electronics.

The quality of agreement deteriorated as the incident angle of radiation approached the bias angle of the front MCP. At such angles, photons could pass further into the channels before initiating an electron avalanche, and thus the low gain tail of the PHD was considerably enhanced. While the lower level discriminator (LLD) of the *ROSAT* electronics chain could be adjusted to include these events, the EGSE LLD could not, and hence low energy events were lost. However, this was not of immediate concern, since maximum QE (and cross-system agreement) occurred near normal incidence, as required by the spectrometer optical design.

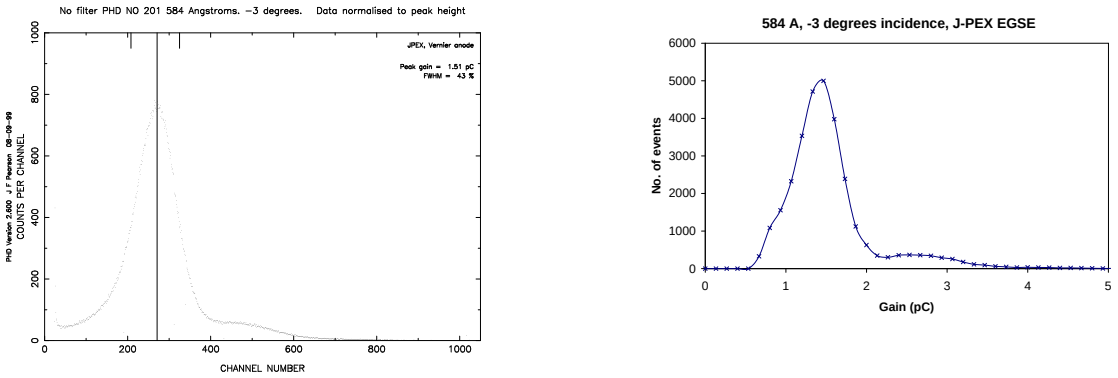

Figure 4.19: Pulse height distributions for the same 584 Å exposure, obtained from the *ROSAT* electronics chain (left) and the *J-PEX* EGSE (right), demonstrating the excellent agreement between the two systems.

4.3.2.3 QE of a reversed MCP

A suggestion was made that the low QE of 6μm MCPs might be related to the etching process which removes the soluble core glass to leave hollow channels, as described in Chapter 3. Specifically, it was proposed that the narrow pore diameter inhibited the capillary flow of acid, preventing complete etching of the channel. This problem would be expected to produce adequately etched glass close to the channel entrance facing into the stream of hydrochloric acid, but with etching deep within the channels becoming progressively less complete (although capillary action might be expected to remove core glass near the channel entrance on the reverse side of the plate).

In this scenario, a peaked PHD would be observed, since events initiated at the channel entrances would still produce a saturated output. However, photons admitted further into the channels by reflection would be unable to initiate an electron avalanche, since the channel walls at these locations would be shielded by a layer of core glass, and hence the secondary e^- yield would fall. The result would be a deficit of counts in the low energy tail of the PHD, and a corresponding fall in QE. To test the hypothesis, QE and PHD measurements were made with the front MCP reversed and rotated to preserve channel axis orientation. Any major differences in the composition of channel walls between front and rear surfaces would then be indicated by a variation between these measurements.

In figure 4.20, four PHDs are shown, at two angles, for normal and reversed front plate orientation. Low angles of incidence produce minor variations in the form of the PHD, while angles almost parallel with the channel axes show a more marked change in the low energy tail. However, little variation in the resultant QE was observed (complete QE data for this study is presented in table 4.3).

The results of this study are inconclusive. Since reversal of the MCP did not lead to an increase in QE, the experiment presented no solution for the *J-PEX* program. However, subtle changes in the form of the PHD suggest that some inhomogeneity in the channel wall composition *might* be present. Detailed SEM analysis of the channel walls will be required if this explanation for low QE in certain MCPs is to be explored further.

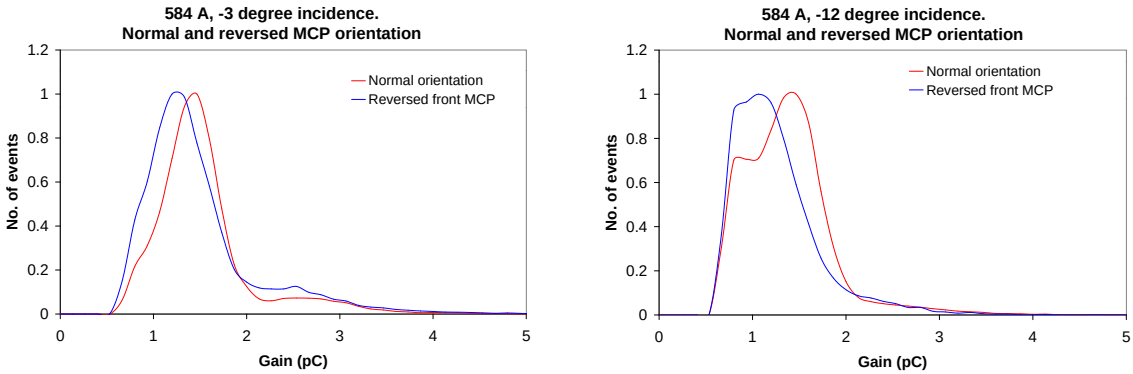

Figure 4.20: Pulse height distributions for "normal" and reversed front plate orientation at 584 Å. (Left) -3° incident angle, (right) -12° incident angle.

	ROSAT electronics		J-PEX EGSE	
Angle	**Normal**	**Reversed**	**Normal**	**Reversed**
-3°	4.8	6.0	4.7	4.8
-12°	3.6	5.2	2.4	3.0
-14°	1.7	2.3	1.2	1.2
-18°	4.7	6.4	3.4	3.8
-24°	4.9	6.8	4.5	5.4

Table 4.3: QE measurements at 584 Å for normal and reversed 6μm front MCPs, measured using *ROSAT* and *J-PEX* EGSE electronics.

4.3.2.4 Comparative studies of 6μm MCPs

An independent study of 6μm Photonis MCPs at Leicester offered the possibility to cross-check results with those from the *J-PEX* program. These MCPs were supplied in 50mm x 50mm format, from standard and radio-isotope free low noise glass, by Photonis SAS for a European Space Agency Technology Research Programme (TRP). The results of the TRP study are presented by Pearson *et al.* (2000).

Although the TRP plates were identical in specification to those used in *J-PEX*, they were produced from a more recent boule. Efficiency measurements for the standard glass MCPs, using Carbon-K photons (277eV), indicated a bare glass QE of approximately 35%. While this energy is higher than the *J-PEX* bandpass, the measurements raised hopes for higher QE across the EUV/SXR band. Gains for these plates appeared to be three times higher than in the *J-PEX* plates operating at similar potentials. Furthermore, optical microscopy indicated that the quality of TRP MCPs was higher, with fewer broken channels ("Rosettes"), and the absence of obvious boundaries between fibre draws, in contrast to the *J-PEX* plates, which are illustrated in figure 4.21. Studies were conducted with the intention of adopting two TRP MCPs as flight plates. Two sets of data were taken:

- C-K measurement with the original TRP plates fitted in the *J-PEX* detector.
- 304 Å QE with TRP plates in the *J-PEX* detector, before and after coating with CsI.

All data were obtained using the standard *J-PEX* detector-electronics combination; C-K measurements were obtained on the Vacuum Test Facility (VTF) employed for the TRP study, using the same X-ray source and propor-

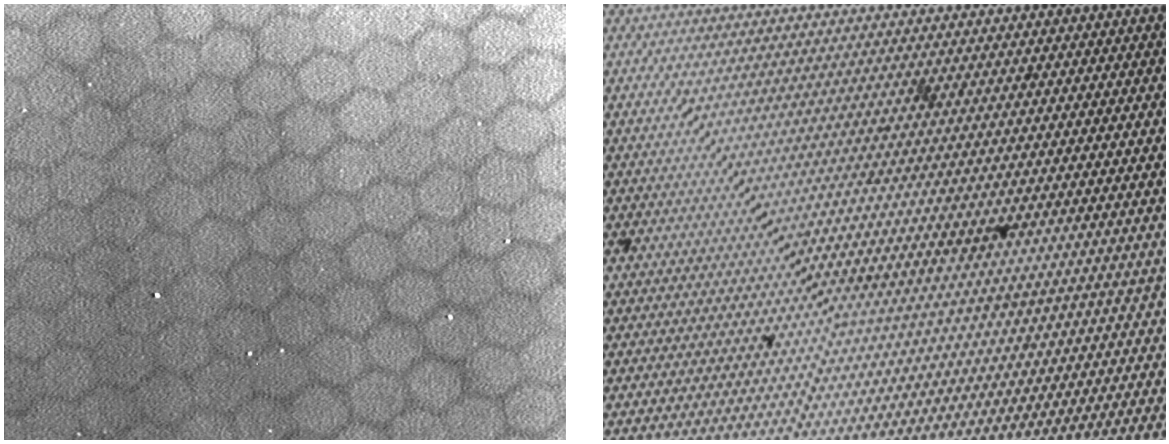

Figure 4.21: Optical microscope images of a *J-PEX* 6μm MCP, showing the clearly defined "chickenwire" boundaries between individual fibre draws (left), and an example of merged and broken channels ("Rosettes", right).

tional counter system. The results of the C-K QE measurements are shown in figure 4.22, compared to data from the original TRP program. The excellent agreement between these two data sets provided evidence that the *J-PEX* EGSE was not a contributory factor in the problem of low QE.

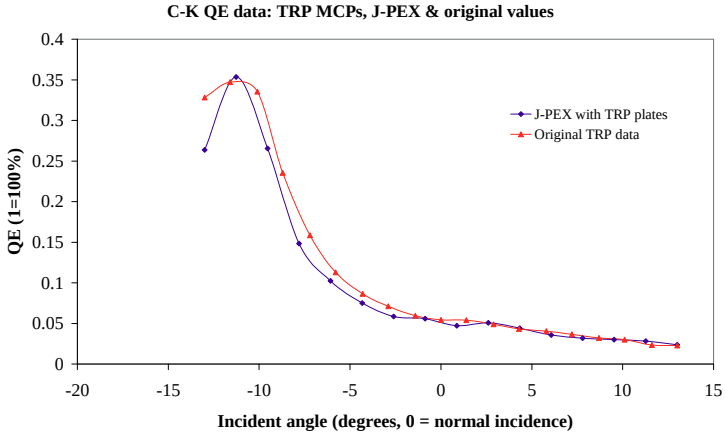

Figure 4.22: QE measurements at Carbon-K (277eV) as a function of incident angle. The peak value of 35% is in excellent agreement with the results of the TRP program (also shown), which were obtained using a different detector + electronics combination.

Pre-coating reference measurements at 304 Å were taken at 3 angles near the response peak, after which the front MCP was coated with 13,700 Å of CsI, and angle-resolved QE measurements taken (figure 4.23). The effect of the photocathode is observed in the asymmetry of the efficiency curve, such that the peak response is lower on one side of the minima than the other (a consequence of coating one side of each channel preferentially, due to the non-zero bias angle of the MCP). The enhancement of efficiency with respect to the uncoated MCP at positive angles demonstrates that the photocathode is producing an increase in QE. However, it is evident that the peak efficiency of these plates remained unchanged. Note that the error bars in figure 4.23 reflect formal counting statistics, and that fluctuations in the Penning source output over short timescales are not accounted for.

Results from the *J-PEX*/TRP study indicated that unusually low QE values were not attributable to the electronics, and that although C-K measurements from the *J-PEX* build were in excellent agreement with previously obtained data, the EUV response of TRP MCPs was no higher than that of the original *J-PEX* 6μm plates. This observation

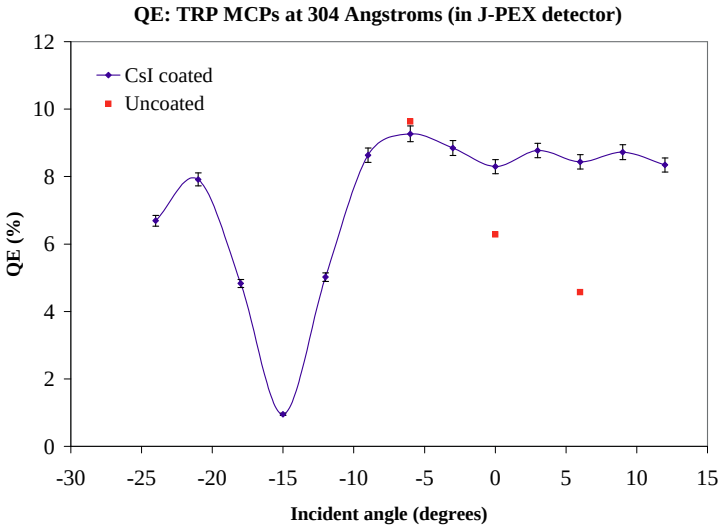

Figure 4.23: QE measurements at 304 Å as a function of incident angle, before and after the front MCP was coated with CsI. Error bars are based on formal counting statistics only, and do not account for short-term source fluctuations.

suggests that low QE might be a characteristic of the MCPs themselves, and indeed, low QE measurements have been reported by others (e.g. Siegmund *et al.*, 1996, Jelinsky *et al.*, 1996).

4.3.2.5 AXAF and high reduction temperature MCPs

Lees & Pearson (1997) have described an imaging detector incorporating a pair of Photonis 100mm x 100mm MCPs. Among other applications, this large area device formed the basis of the focal plane detector in the High Resolution Camera (HRC) on-board *AXAF* (subsequently renamed *Chandra*). The authors kindly made available a large area MCP from the research project, which was scribed and cracked to fit the 35mm^2 format used in *J-PEX*. This presented an opportunity to evaluate MCPs of similar composition to the 6μm plates in terms of glass type and manufacturing process, but with the more common 12.5μm pore size. The specifications of this MCP are presented in table 4.4.

Pore size	12.5μm
Pitch	15.0μm
MCP size	35mm (scribed from 100mm)
Open area fraction	65%
L:D ratio	120:1
Resistance	$\simeq$ 230 MΩ @ 1650 V
Bias angle	6°

Table 4.4: Specifications of the Photonis 12.5μm pore *AXAF*-type plate

An extra DiClad spacer was added to the top of the MCP stack to accommodate the thicker plate (1.5mm, compared to the standard 0.72mm *J-PEX* units). Angle-resolved QE measurements were then taken at 256 Å and 304 Å. Since Lees & Pearson (1997) considered only C-K (0.28 keV) and Si-K (1.74 keV) energies in their study (obtaining peak efficiencies of 35% and 44% respectively), a comparison of the type carried out with TRP MCPs was not possible. The results of the EUV study at 256 Å are presented in figure 4.24, along with data from a 6μm pore Photonis MCP which had been processed with a high temperature (420°C) final bakeout by the manufacturer before delivery, in an attempt to restore QE. This MCP was fitted in the detector and evaluated upon completion of

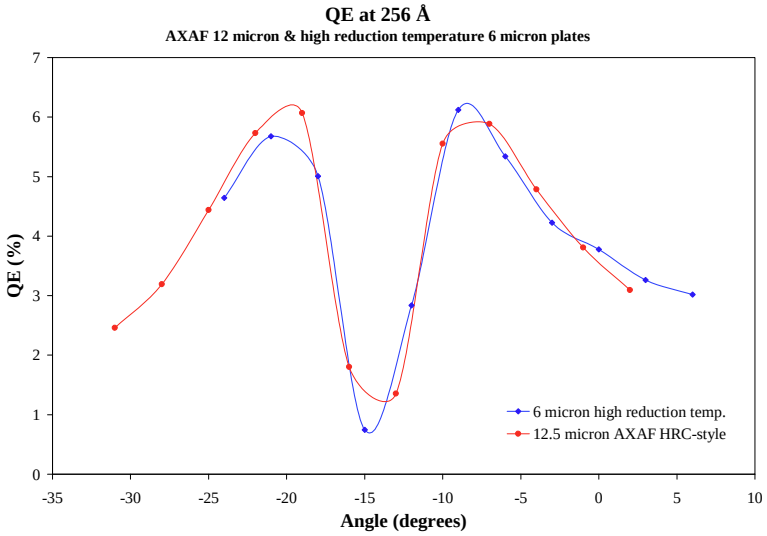

Figure 4.24: QE measurements at 256 Å as a function of incident angle. Two curves are shown, corresponding to the response of the 12.5μmpore *AXAF* HRC-style MCP, and the 6μm high reduction temperature MCP supplied by Photonis for evaluation. Both plates were uncoated.

work with the *AXAF*-type plate.

Results from these tests revealed peak QE values of around 6% at 256 Å, similar to those obtained from the original *J-PEX* MCPs, and those used in the TRP study. While the failure to increase QE by subjecting MCPs to a higher reduction temperature is disappointing, the *AXAF* MCP result is particularly significant, indicating that the precise mechanism for QE suppression is apparently unrelated to pore size.

4.3.2.6 Introduction of a repeller grid

The rationale for omission of a repeller grid in the detector design was explained in section 4.2.2, but in view of the QE problem, it was important to determine whether the introduction of a grid would improve performance. A grid made from 92% transmission nickel mesh supported by a copper annulus, was fitted underneath the filter mounting, approximately 2.3mm above the front MCP. In a test similar to that of Taylor *et al.* (1983), the grid was used to establish $\underline{\mathrm{E}}$ fields spanning the range ± 0.4 V $\mu\mathrm{m}^{-1}$. QE measurements were made as a function of field strength, and a continuous record of count rate was kept using a multichannel analyser.

Negligible variation in count rate was observed until a field of approximately 0.013 V $\mu\mathrm{m}^{-1}$ was established above the front MCP, whereupon rates approximately 10% higher than the base level were recorded (figure 4.25). Raising the field to 0.02 V $\mu\mathrm{m}^{-1}$ was accompanied by a further increase in count rate, beyond which no further improvement was observed. However, QE values did not change significantly; measurements showed that these extra events were due to noise, producing similar increases in count rate on and off the 584 Å emission line. These results suggested that the QE deficit could not be attributed to a loss of events falling on the interchannel web. Therefore the repeller grid was removed.

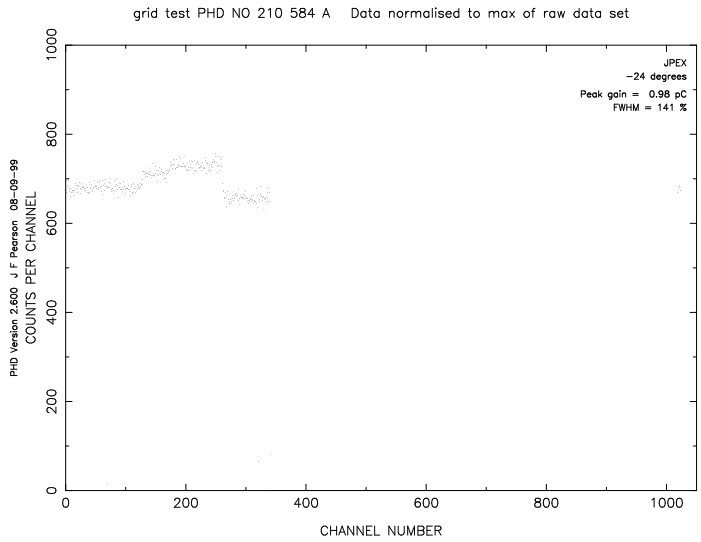

Figure 4.25: Section of a count rate trace recorded during repeller grid tests.

4.3.3 Russian microchannel plates

Although high efficiencies had been obtained from Galileo MCPs, their use in the *J-PEX* flight detector was precluded by "bowing" of the MCP surface. This distortion was believed to be caused by the differential cooling of glass in the active area and the solid edge, leading to extreme fragility of the glass when clamped inside the detector.

Pore size	12μm
MCP diameter	32mm
Active area	4.8 cm^2
L:D ratio	50:1
Open area fraction	62%
Resistance	$\simeq$ 320 MΩ @ 1000 V
Bias angle	8°

Table 4.5: Russian solid-edge MCP specifications

An alternative source of plates was available in the form of the Russian MCPs described in detail by Pearson *et al.* (1993). The specification of these plates is given in table 4.5. Measurements made with a Russian plate as the front MCP in the *J-PEX* detector produced QE values close to 11% for bare glass, although the resulting pulse height distribution was broad. However, with a 14,000 Å thick layer of CsI applied, the performance of these plates was considerably improved. QE values of $\simeq$ 15% were achieved (figure 4.26), and the pulse height distribution was clearly defined (figure 4.27).

A decision was taken to retain the 6μm pore rear plate, but to fly the detector with a CsI coated Russian MCP fitted as the front element. This compromise was driven by several factors, including project time constraints and the need to preserve detector resolution. Comparison between figures 4.27 and 4.16 shows that the modal gain of the system with a Russian front MCP was slightly lower than that of the original build. However, recovery of QE was, at this stage, an overriding priority, and the Russian MCP was selected as a flight component. Insufficient time was available for an investigation into the issue of gain, and while it may be tempting to blame the problem on

retention of a 6μm pore rear MCP of questionable performance, this suggestion is entirely speculative at present.

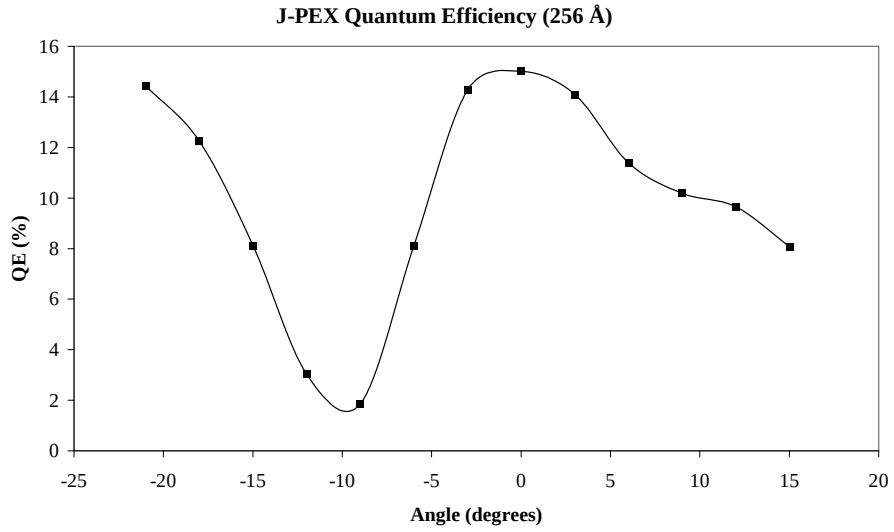

Figure 4.26: Quantum efficiency of the *J-PEX* focal plane detector at 256 Å, when fitted with a Russian front MCP.

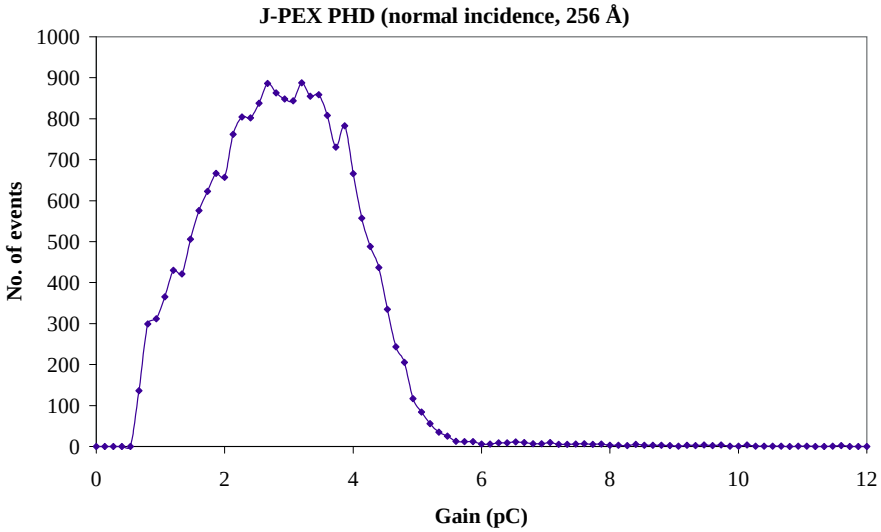

Figure 4.27: Normal incidence pulse height distribution of an IKI MCP at 256 Å.

4.3.4 The aging of Aluminium filters

The effects of oxidation on the transmission of aluminium filters produced for EUV and soft X-ray applications have been discussed elsewhere (Powell, 1989, Barbera *et al.*, 1997). Of particular importance to the current work is data provided by Powell (1989), demonstrating the difference in transmission between new and “aged” filters at three wavelengths (256, 304 and 584 Å).

Colleagues at NRL measured the transmission of a recently produced filter at the Brookhaven National Synchrotron Radiation Source in January 1998. Its transmission was found to be 50% at 256 Å (Kowalski & Cruddace, Private communication), and as this met flight specifications, the filter was fitted to the detector during part of the QE evaluation. No special precautions were taken for storing the filter when not in use, other than being kept in a

protective metal container.

As part of the investigation to determine the cause of the low detector QE, the transmission of this filter was re-measured in the same EUV test facility used for detector development work at Leicester. The measurement, made approximately 10 months after the Brookhaven data, revealed a significant deterioration in transmission. Transmission values similar to those quoted by Powell (1989) were obtained at 3 wavelengths as summarised in table 4.6.

λ (Å)	T_{new}(J-PEX)	T_{new}Powell (1989)	T_{aged}Powell (1989)	T_{aged}(J-PEX)
256	0.5	0.49	0.32	0.38 ± 0.01
304	–	0.43	0.26	0.33 ± 0.01
584	–	0.16	0.05	0.10 ± 0.01

Table 4.6: Aluminium filter transmissions for new and aged units. Measurements of the original *J-PEX* filter are compared with values given by Powell (1989).

These results suggest that the process of oxidation is not complete immediately after production of the filter, and that a significant degradation in transmission has occurred at some point during the period between the two measurements, possibly due to poor storage conditions. As a result of these findings, a replacement filter was procured. A transmission of $56 \pm 1\%$ was measured at 256 Å, and the filter was stored in vacuum or a low-humidity atmosphere when not in use.

4.4 The Vernier charge division readout anode

The initial detector design incorporated two 6μm pore MCPs, to achieve a spatial resolution of 10μm FWHM[4]. However, the resolution reached by the MCPs must be matched by that of the imaging anode. For the *J-PEX* detector with an active area of approximately 20 x 30mm, 10μm positional sensitivity requires the use of 2000 x 3000 pixels, beyond the capability of traditional readout technologies such as the Wedge-and-Strip anode (WSA). The design and operation of the WSA has been described by Siegmund *et al.* (1986a), who quote a limiting resolution of 80μm for the system used in their study. This is a consequence of the readout pattern varying linearly in two orthogonal directions. Since such anodes rely on charge division for positional sensing, the positional resolution of a WSA is proportional to the charge resolution of the electronics, and this quantity is limited by electronic noise, primarily from the preamplifiers (Lapington, 1995).

The Vernier anode overcomes this limitation by adopting a cyclic pattern variation as opposed to the linear geometry of the WSA. Using this design, the effect of uncertainty in charge measurement upon resolution is significantly reduced, (although low gain levels introduce errors due to the difficulty in measuring very small charge quantities), and performance beyond that required by the *J-PEX* design and mission objective becomes a possibility. The Vernier anode has been developed at MSSL, and is described in detail elsewhere (Lapington *et al.*, 1991, Lapington, 1995, Lapington *et al.*, 1998, Lapington *et al.*, 1999). However, the anode's ability to deliver adequate resolution is critical to the overall performance of the detector, and hence a short discussion of its operation is

[4] Although the charge cloud spread in a chevron MCP configuration is greater than 1 channel, centroiding the point spread function of each event enables positional information to be recovered from this "blurring".

appropriate.

The anode consists of nine electrically isolated electrodes, which are etched by laser onto an insulating quartz substrate, sputter-coated with a gold conductive surface layer; the width of each electrode varies sinusoidally. Like the WSA, for a given event, the charge collected by each electrode is proportional to the ratio of electrode widths at that position.

The electrodes are arranged into triplets, each consisting of three electrodes with slightly different wavelengths (providing the "Vernier" effect). Triplets are interleaved, such that the first electrode from triplet A is adjacent to the first from triplet B, which is adjacent to the first from triplet C, etc, with one pitch of the pattern containing all nine electrodes. The phase of each triplet is linearly offset from pitch to pitch, producing the arrangement shown in figure 4.28. When an event is incident on the anode, the charge distribution between the electrodes of each triplet defines 3 phases A, B and C, (one per triplet) which are combined to produce the final resultant phases, X, Y and Z defined by

$$\begin{aligned} X &= A + B \\ Y &= B + C \\ Z &= A + C - \frac{X}{n^2} - \frac{Y}{n} \end{aligned} \tag{4.2}$$

where n is an integer, the significance of which is illustrated in figure 4.28: triplet offsets are calculated such that the resultants X and Y (representing the "fine position") are orthogonal, with equal wavelengths, while values of Z are discrete in phase-space. Each of these values defines a *coarse position* (there are 4 x 4 = 16 coarse positions in the system of figure 4.28, hence $n = 4$ in this case), so that the entire imaging area may be divided into zones, each assigned a unique value of Z. The resultant fine and coarse position co-ordinates are combined to generate a unique 2-D co-ordinate for any position on the pattern.

This arrangement overcomes the positional ambiguity which might otherwise arise due to the repetition of electrode periods within each pitch (Lapington, 1995). The combination of cyclic electrode design and carefully engineered phase-offsets allow the Vernier anode to attain resolutions exceeding those of more conventional designs. Figure 4.29 shows an image taken with the Vernier anode and flight electronics, using a Photonis 12.5μm pore MCP stack. The individual pores, missing pores and boule boundaries in a 1mm diameter illuminated area are clearly visible. The resolution in this image is 10μm FWHM.

4.4.0.1 Electron control grid

As described briefly in section 4.2, a grid is placed between the MCP stack and the anode, and held at a low potential (-20V). The grid spreads the electron charge cloud exiting the MCP over a diameter sufficient to span several pitches of the anode pattern ($\approx 636\mu$m), thus avoiding digitization effects (Sanderson & Lapington, 1999, Lapington *et al.*, 1998). A further function of the grid is to control the trajectories of secondary electrons emitted from the anode, which can lead to significant image nonlinearities (Lapington, 1997). Primary electrons from the

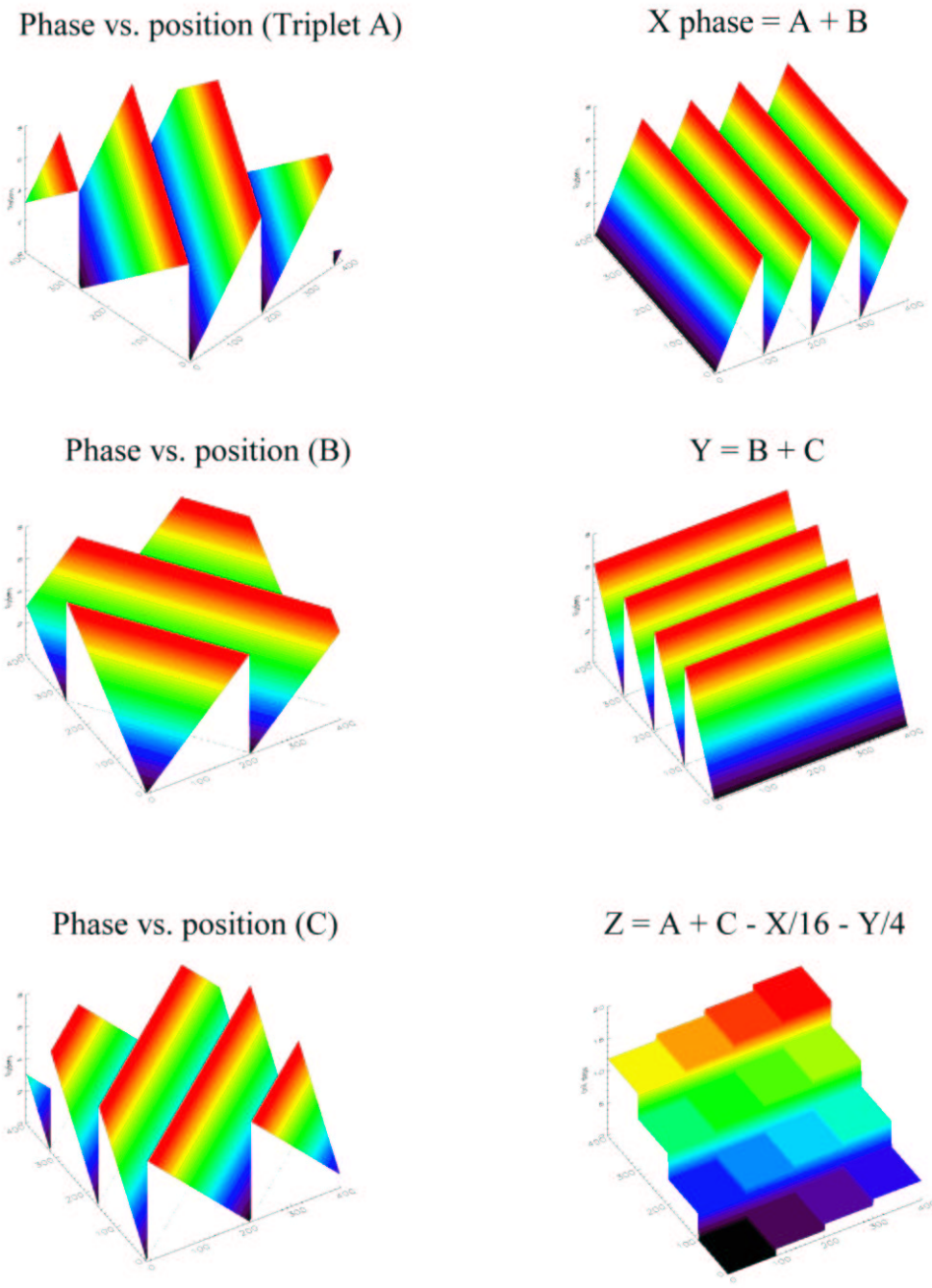

Figure 4.28: The left column of plots show variation of phase of each triplet with respect to pattern X and Y coordinates. Plots in the right column show variation of the resultant phases, with Z containing discrete values by means of subtraction of fractional X and Y components. *Courtesy of J.S.Lapington, MSSL / University of Boston.*

MCP initiate the release of secondaries from the anode surface, which effectively extend the size of the electron charge footprint and, unless the distribution can be kept uniform, degrade centroiding accuracy. The grid provides a means of restricting the range of these secondaries. Finally, a fraction of primary electrons from the MCP collide with the grid and produce secondary electrons which are attracted towards the anode. At low grid potentials, these electrons have insufficient energy to induce further emission from the quartz. Instead, they remove the positive charge left on the anode insulator when secondary electrons are released from the anode by the incident charge packets from the MCP. If left unregulated, this charging would lead to imaging distortions (Lapington *et al.*, 1998).

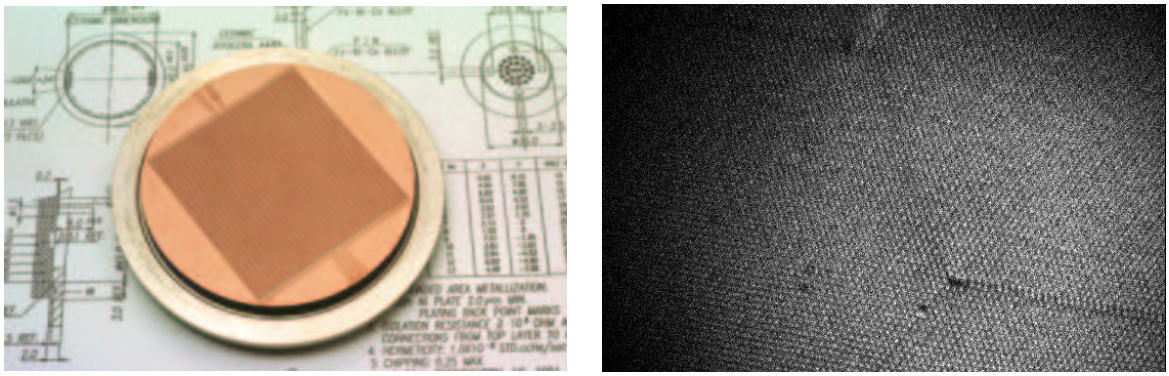

Figure 4.29: Left: the Vernier anode. Right: image taken with the anode and flight electronics, of a 1mm diameter illuminated area on a detector with 12.5μm pore MCPs; pores and boule boundaries of the top MCP are clearly imaged, representing a readout resolution of 10μm FWHM. The electronic noise limited resolution of 4μm FWHM is degraded by centroid errors in the MCP charge cloud. *Images courtesy of J.S.Lapington.*

4.4.0.2 Electronics

Charge sensitive preamplifiers and the detector HV PSU are mounted on the rear of the detector immediately behind the anode. Preamplifiers are internally wired to the anode *via* ten connections to the pins on the rear of the substrate. The PSU provides a single high voltage line, which is input to a resistor-divider chain mounted around the anode on the outside of the detector casing. This design prevents anomalous voltage distribution between detector components during power switching which would otherwise be present with multiple PSU solutions, and simplifies the overall design of the power supply. These components are collectively referred to as the *Front End Electronics*

Preamplifier signals are routed to a series of shaping amplifiers and processors in a *plate electronics* module mounted inside the payload skin adjacent to the detector. Two modules house most of the spectrometer electronics, controlling operations such as detector power switching, door operations, and providing the telemetry system. Timers installed in the launch vehicle control sequencing of events during flight *via* the plate electronics, although an uplink is provided to override detector switching should this be necessary.

4.4.0.3 Difficulties in resolution optimization

The task of determining optimal mechanical and high voltage settings to maximize resolution was limited by the *J-PEX* project timescale, and complicated by the practical difficulties of mounting a resolution mask in contact with the surface of the front MCP. In the case of 6μm plates, pinhole masks caused rapid thermal runaway (and subsequent destruction) of the front MCP on one occasion[5], and a large increase in the frequency of high voltage breakdown events, presumably due to the large numbers of blocked channels. The degree of beam divergence in the test facility ruled out the possibility of mounting the resolution mask above the surface of the front plate, and hence no formal resolution measurement was made with 6μm MCPs.

[5]This trial was conducted using a laboratory detector at MSSL, demonstrating that the highly sensitive nature of these MCPs was not peculiar to the *J-PEX* detector configuration.

A resolution mask made from aluminium foil was successfully included in the detector when fitted with an uncoated 12μm pore Russian MCP. However, this measurement was hampered by large numbers of low gain events, believed to be produced in field emission from a contaminant of unknown composition, visible as a smoky deposit on the exit surface of the front MCP. With an amplitude below 80mV, these events fell below the LLD of the imaging electronics, and were equivalent to severe electronic noise which artificially limited resolution. The "real" nature of these events was confirmed by switching off emission sources and reversing the bias on the grid to +9V, so that secondary electrons from the anode were captured. In this configuration, only pulses of *positive* polarity were observed in the output, demonstrating that the low level signals were produced by primary electrons incident on the anode, and not simply electronic noise. Furthermore, a slight ($\sim$ 10V) retarding potential in the inter-plate gap was found to eliminate the events completely, indicating that they were produced by low energy electrons formed in (or close to) the inter-plate gap. No similar events were observed in the flight MCP, but since this plate was coated with a photocathode, contact with a mask was not possible, ruling out a resolution measurement in this configuration.

As a consequence of these problems, measurements made with the pinhole mask (figure 4.30) could only constrain the resolution, setting an upper limit of 20μm FWHM. However, electronic noise measurements and direct imaging of detector features (e.g. "hot spots" in previous representative builds) suggest a value closer to 15μm FWHM.

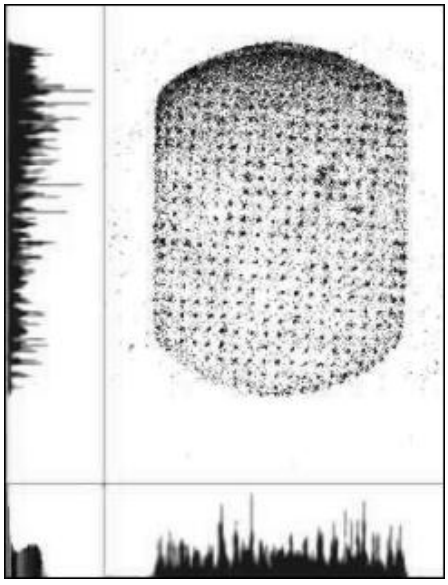

Figure 4.30: Image from the flight detector fitted with a resolution/linearity pinhole mask in contact with the (uncoated) front MCP at 304 Å.

4.5 Summary

- This chapter has outlined the development of a compact MCP-based detector for use in normal-incidence EUV spectrometry, with a quantum efficiency of approximately 16% at 256 Å and a resolution better than 20μm FWHM.
- The detector is designed to achieve maximum spatial resolution by employing small pore (6μm) MCPs and the latest development in charge division readout anodes, while noise levels in the detector are kept to a minimum through the use of a dedicated shielding structure.

- Low values of QE have been measured in many MCPs during this work. Electronics cross-calibration has verified that this deficit is real, though a series of studies provided no obvious explanation for the problem. Trials with 6 and 12μm pore Photonis MCPs have demonstrated that the effect is independent of pore size, and the results of a plate reversal study suggest some inhomogeneity in channel wall composition may be present, affecting secondary electron yields deep inside the pores.

- A clear explanation for the poor QE of MCPs tested in this work has yet to be found, but it is noted that Siegmund *et al.* (1996) and Jelinsky *et al.* (1996) also highlight the problem.

- The detector has been fitted with a Russian 12μm pore Russian front MCP coated with 14,000 Å of CsI, which delivers acceptable QE and gain, while a 6μm Photonis MCP has been retained in the rear of the detector.

- Data obtained during this work suggests that thin film Aluminium filters are subject to a deterioration in transmission over timescales of months or years, possibly as a result of oxidation, and that special precautions may be necessary in the storage and handling of these filters to ensure that they remain in optimum condition.

The assembled detector is illustrated in figure 4.31.

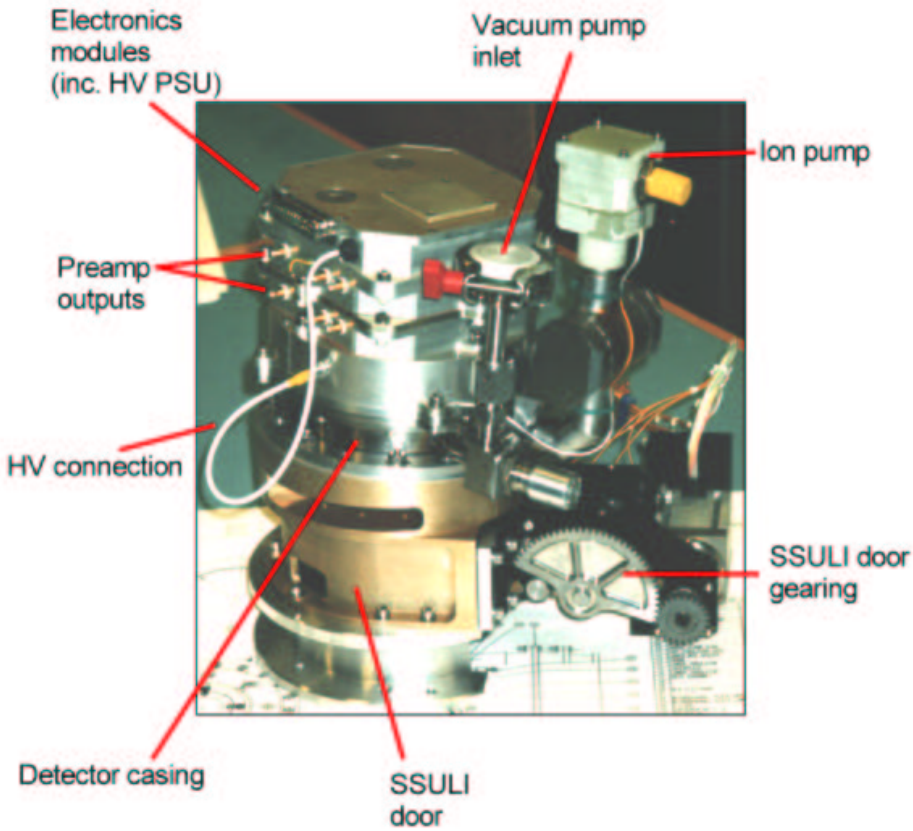

Figure 4.31: The assembled flight detector, prior to integration in the *J-PEX* spectrometer. Principal components are labeled.

CHAPTER 5

A SURVEY OF CIRCUMSTELLAR FEATURES IN HOT DA WHITE DWARFS

5.1 Introduction

DESPITE THE INCREASING SUCCESS of stratified models in quantitatively predicting atmospheric composition (as discussed in Chapter 1), certain observations are nevertheless suggestive of processes which may modify equilibrium abundances. As highlighted by Holberg *et al.* (1997c), two of the most intensively studied white dwarfs exhibit features which may be indicative of accretion. Feige 24, a DA white dwarf + dM 1.5 system, is one of the most interesting of these objects. Vennes & Thorstensen (1994) showed that the white dwarf exhibits a He II 1640 Å absorption line, the equivalent width of which is modulated in phase with the orbital motion of the system. It was proposed that this spectral line might be caused by absorption due to material located at the L1 Lagrangian point, or alternatively, in an accretion spot on the white dwarf surface (implying that the white dwarf rotation period was tidally locked to the orbital period). Additionally, Dupree & Raymond (1982) reported multiple components in the C IV 1550 Å doublet, associated with the white dwarf and a circumstellar cloud, while Vennes & Thorstensen suggested the existence of a third component, possibly due to mass loss from the MS companion. A considerable body of literature also exists for the eclipsing binary system V471 Tauri, which consists of a DA white dwarf + detached K2V companion. In this case, variations observed in X-ray and optical wavelengths, indicative of the accretion of material on to the white dwarf (Barstow *et al.*, 1992, Clemens *et al.*, 1992), have been confirmed by Sion *et al.* (1998).

5.1.1 Circumstellar features in the DO white dwarfs

Circumstellar features appear to be relatively common in the He-rich DO white dwarfs. As discussed by Holberg *et al.* (1999b), of the 11 DO stars included in the survey presented by Holberg *et al.* (1998), 6 show circumstellar features, all blueshifted with respect to the photospheric velocity. Further, of the 7 stars with $T_{\rm eff}$ in excess of 70,000K, all but one show these features. In contrast, only 5 of the 44 DA's show circumstellar features, with no clear dependence on temperature. Holberg *et al.* (1999b) argue that these cannot be of an interstellar origin, since the observed lines (C IV, Si IV and N V) are highly ionised and uncharacteristic of the ISM. If this material *was* of an interstellar nature, then high column densities of ionised gas would be required, and should be observed along adjacent lines of sight to stars at greater distances. In reality, no such correlation is observed. A further argument against an interstellar origin for these features is that, in the stars considered by Holberg *et al.* (1998), all appear to be blueshifted with respect to the photospheric velocity. Genuinely interstellar lines should bear no particular relation to the photospheric velocity. Such features may be indicative of mass loss.

Several studies of circumstellar components in DO white dwarfs exist in the literature. For example, Sion *et al.* (1997) observed C IV, Si IV and N V features, at a mean velocity blueshifted by ~ 39.75 km s^{-1} with respect to the photospheric velocity of the hot DO star KPD 0005+5106. These were accompanied by emission features, possibly due to heating of the corona through mass loss (it is interesting to note that, within stated uncertainties, the velocity of non-photospheric features match that of one of the two ISM velocity components identified along the line of sight to this object). *IUE* spectra of the DO star PG 1034+001 also revealed the same ions blueshifted with respect to the photospheric velocity (Sion *et al.*, 1985, Fritz *et al.*, 1990). Werner *et al.* (1996) confirm the existence of possible mass loss related features in KPD 0005+5106, and also discuss the PG 1159-type star RXJ 2117+3412. In this case, the observed profiles of certain highly ionised features (e.g. C IV and O VI) are found to be much broader than those predicted by models, suggesting that this may be consistent with mass loss. With the detection of O VIII emission common to both stars, possibly as the result of shock-heating in the wind, these objects provide strong evidence for the existence of ongoing mass loss in hot white dwarfs.

5.1.2 Circumstellar features in the DA white dwarfs

The apparently common circumstellar features in DO white dwarfs might lead one to expect similar phenomena to be prevalent in the DA group, which includes approximately 80% of the known white dwarfs (Sion *et al.*, 1997). Yet, as noted by Holberg *et al.* (1999b), only a small number of these objects have revealed highly ionised species at non-photospheric velocities, and as the examples of Feige 24 and V471 Tauri show, some of these observations can be explained in terms of the interaction between binary components. An excellent example of non-photospheric features in an *isolated* white dwarf is CD-38°10980 ($T_{\rm eff} \sim 24,800$ K, $\log g \sim 8.09$). Using co-added *IUE* echelle spectra, Holberg *et al.* (1995b) discovered Si and C absorption features in this star at velocities displaced by -12 km s^{-1} with respect to the photosphere. The presence of transitions from excited or quasi-metastable levels was cited as evidence that these features did not arise from the ISM along the line of sight, and instead the observations were explained in terms of a dense gaseous halo in close proximity to the star, perhaps an extension to the atmosphere, for which similar temperature and electron densities were derived. Holberg *et al.* also showed

that the stellar photosphere was effectively devoid of both Si and C.

A study of the DA star REJ 1614-085 ($T_{\rm eff} \sim 38,500$ K, $\log g \sim 7.85$) was presented by Holberg *et al.* (1997b), who found evidence for weakly blueshifted components in the C IV and Si IV lines, at $\approx 30\%$ of the strength of the photospheric lines, and shifted by -25 and -40 km s^{-1} respectively. P-Cygni profiles were not observed in these features. Similar features were also discovered in the hot ($T_{\rm eff} \sim 57,000$ K) DA, REJ 0457-289 (Holberg *et al.*, 1997c).

Circumstellar components have occasionally been reported, and subsequently ruled out, in certain stars. GD 659 was believed to possess circumstellar features (e.g. Holberg *et al.*, 1995a) until the photospheric velocity measurement was revised, and was found to match these features. Similarly, circumstellar features were reported in Wolf 1346 by Vennes *et al.* (1991), also on the basis of apparently sound evidence, but the velocities and strengths of these lines were later shown by Holberg *et al.* (1996) to be entirely consistent with photospheric material.

5.1.3 A note on P-Cygni profiles

It is important to appreciate the difference between the circumstellar features observed in DO and DA white dwarfs, which form the subject of this chapter, and the classical "P-Cygni" profiles which are observed in objects supporting strong mass loss or energetic winds. A typical P-Cygni line profile is shown in figure 5.1, taken from the study by Kingsburgh *et al.* (1995), while figure 5.2 is a schematic which illustrates the origin of these features.

The blueshifted absorption feature in the P-Cygni profile is produced by material ejected in the stellar wind, in the direction toward the observer (i.e. material in front of the star). By definition, this material must differ from the photospheric velocity by an amount in excess of the stellar escape velocity, and so the absorption feature is blueshifted by several thousand km s^{-1} with respect to the photospheric value. The feature is very broad, since the line of sight to the star passes through a cloud of radially-emitted material, so that the value of blueshift varies across the face of the star as seen by the observer. In addition to the blueshifted absorption feature, an emission feature can be observed redward of the photospheric line. This emission is produced by radiative de-excitation in the ionised stellar wind. The observer is prevented from seeing the maximum redshift, since material in this zone is occulted by the stellar disc. The redshifted component is also broad, due to the range of radial velocity components in the emitting medium.

In contrast to the P-Cygni profile, the highly ionised, non-photospheric components observed in the white dwarfs considered in this chapter differ from the photospheric velocity by a few tens of km s^{-1}. These components are relatively narrow, also spanning a range of only a few tens of km s^{-1}(and in some cases much less), and emission redward of the photospheric component is not observed. Further, this work has revealed both blueshifted and *redshifted* components in these stars. It is therefore evident that the non-photospheric absorption features discussed in the remainder of this chapter are quite distinct from the standard P-Cygni profile.

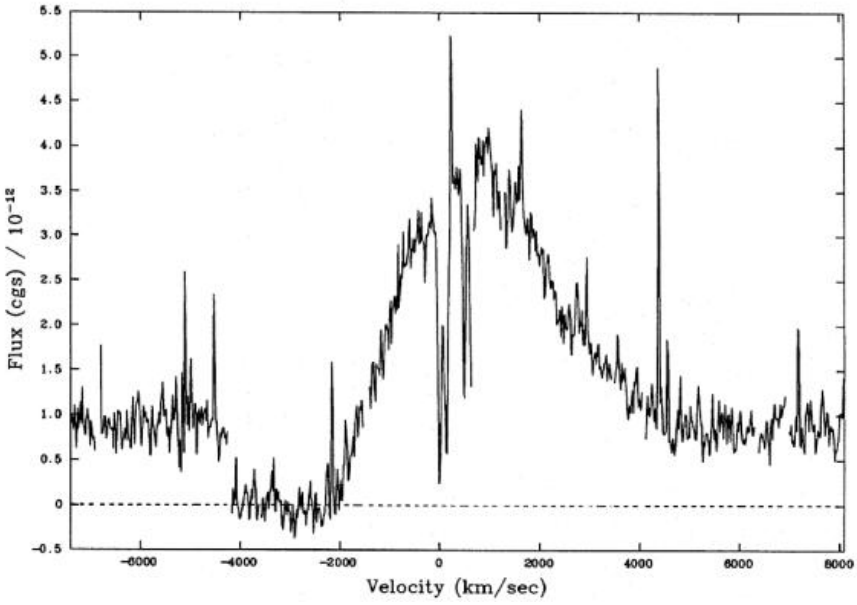

Figure 5.1: The C IV 1548, 1550 Å resonance doublet of the WO Wolf-Rayet star Sand-1, showing a distinctive P-Cygni profile. The blue edge of the highly broadened, saturated absorption component yields a terminal (wind) velocity of 4200 $\mathrm{km\,s^{-1}}$. This non-photospheric feature is considerably broader, and the measured velocity is two orders of magnitude greater, than observed in the circumstellar features considered in the current work. (Diagram from Kingsburgh *et al.* 1995).

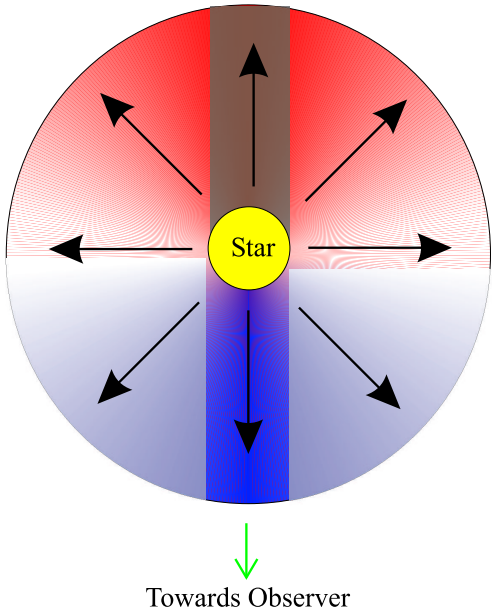

Figure 5.2: Schematic showing the origin of the P-Cygni profile. Black arrows indicate the velocity of material lost in the stellar wind. Matter with the maximum redshift is hidden from the observer by the star, while absorbing gas in front of the star is observed over a range of blueshifts, giving rise to the broadened absorption feature blueward of the photospheric velocity. The broad redshifted portion of the P-Cygni profile is produced by material to the side of the star.

5.1.4 A search for non-equilibrium processes in DA white dwarfs

Data from the *STIS* instrument on board HST have allowed the study of white dwarf spectra to be carried out with an accuracy impossible to achieve with earlier instruments, and at a resolution which permits more precise examination of intrinsic line profiles. A more sensitive search can now be made for signs of mass loss and accretion, which may still be important in determining precise elemental abundances, despite the improved results brought about by the introduction of stratified models.

Section 5.2 of this chapter consists of a phenomenological study of a sample of hot DA white dwarf stars for which either *GHRS*, *STIS* or high resolution *IUE* echelle spectra were available. In each star, the resonance doublets of C IV, N V and Si IV are examined for signs of multiplicity (whether in the form of asymmetry or distinct components). Statistical tests are applied to determine the significance of proposed secondary features, and in some cases, elemental abundances are considered as additional evidence for the presence of non-equilibrium processes. In section 5.3, the results of this study are discussed, and a variety of explanations for the presence of highly ionised non-photospheric features in certain white dwarfs, are considered.

5.2 Observations and data analysis

5.2.1 Overview

In the following section, spectra from each of the sample stars are studied for evidence of highly ionised, non-photospheric features; objects with previously recognised features of this nature, are noted as such in the text. As well as parameters such as line velocity and equivalent width, which are measured directly from the spectra, several other quantities are calculated for a selection of stars, to support the discussion presented in section 5.3. These quantities are introduced below, and are followed by brief analyses of each stellar spectrum. Stars are considered in temperature order (highest to lowest).

5.2.1.1 Calculation of gravitational redshift

Any measurement of apparent photospheric velocity using absorption lines in the white dwarf spectrum will be comprised of two parts (assuming that heliocentric corrections to the data have already been applied). The first component is the true photospheric, or radial, velocity of the star, while the second arises from gravitational redshifting of photons which lose energy in escaping the strong gravitational potential of a white dwarf. Absorption features formed in the white dwarf atmosphere will contain both of these components. However, the gravitational redshift component will be weaker in features which are formed by absorption in material further from the stellar surface (e.g. a circumstellar cloud), and will be effectively zero for a cloud with a sufficiently large inner radius. The gravitational redshift at the stellar surface therefore defines a range of velocities, with respect to the apparent photospheric value, at which shifted features *may* be attributed to material residing within the gravitational well of the star.

Gravitational redshifts can be measured directly in binary systems such as Feige 24 (Dupree & Raymond, 1982, Vennes & Thorstensen, 1994), but for isolated systems, the velocity component due to gravitation redshift, $v_{\rm grav}$, can be estimated using the standard formula,

$$\frac{\lambda_{obs} - \lambda_{rest}}{\lambda_{rest}} = \frac{v_{\rm grav}}{c} = \frac{GM}{c^2 R}, \tag{5.1}$$

where G is the universal constant of gravitation, M is the stellar mass, R is the radius (of the star, or of the

circumstellar cloud), c is the speed of light, and $\lambda_{obs,rest}$ are the observed and rest wavelengths of the absorption line, respectively. Substituting values for the physical constants, the expression for $v_{\rm grav}$ becomes simply

$$v_{\rm grav} \approx 6.36 \times 10^2 \frac{M_*}{R_*} \ {\rm m\,s^{-1}}, \tag{5.2}$$

where solar units are to be used for the white dwarf mass and radius. In the work which follows, estimates using this expression are used to identify features which could be explained by material residing within the gravitational potential of an object.

5.2.1.2 Estimation of the velocity of the local interstellar cloud

Although interstellar lines in the spectra of white dwarfs may be used to determine line of sight ISM velocities for each star, it is instructive to consider the possibility of velocity components from the *local interstellar cloud* (LIC). The LIC is a diffuse cloud of material, approximately 20 – 30 light years across; the Sun is situated inside, but near the edge of, this cloud. From this position, the majority of material lies in the direction of the Galactic Centre, with H I column densities of up to $\sim 10^{19}$ cm^{-2} being measured over a few tens of pc (Gry, 1996). The LIC is itself embedded in a region of much lower density (< 0.02 atoms cm^{-3}) - the *local bubble*, extending to distances of between 50 pc and at least 250 pc from the Sun, depending on direction. This bubble is believed to have been formed by the blast wave from a nearby supernova detonation occurring several million years ago - an idea supported by the relatively high ionisation fractions of H and He in the LISM (27% and 35% respectively; Barstow *et al.*, 1997a). Lallement *et al.* (1995) present a study of the structure of the LIC, confirming that it can be described with reasonable accuracy by a cloud moving at 26 ± 1 km s^{-1} (heliocentric velocity) towards $l_{\rm II}$ = $(186 \pm 3)^\circ$, $b_{\rm II}$ = $(-16 \pm 3)^\circ$, or α = 74.5°, δ = +15°. Contributions to the LIC velocity field from minor additional cloud components are discussed by Lallement *et al.*, though their velocity vectors differ by a sufficiently small amount that the main vector, $v_{\rm LIC}$, quoted above, may be exclusively used in the current work.

The velocity of absorption lines from the LIC in a particular star, $v_{\rm LIC^*}$, may be estimated from the projection of $v_{\rm LIC}$ onto the target direction. This is an exercise in simple spherical trigonometry, and results in the formula

$$v_{\rm LIC^*} = 26\{\cos(90 - b_*)\cos(106) + \sin(90 - b_*)\sin(106)\cos(186 - l_*)\}, \tag{5.3}$$

where l_* and b_* are, respectively, the galactic longitude and latitude of the star.

5.2.1.3 Curve-of-growth analysis

The curve of growth is a diagnostic tool for determining quantities such as temperature and column density in a gas from measurements of the equivalent width of spectral features. Spectral lines can be broadened by a number of effects including collisional broadening, modification of the energy levels of an atom due to nearby charges (the

Stark effect), line splitting due to the presence of magnetic fields (the Zeeman effect), and large-scale phenomena such as atmospheric turbulence, stellar rotation and even expansion of the atmosphere itself. Spectral lines therefore contain much information about conditions within the emitting or absorbing medium.

Two sources of broadening are of particular importance: *natural broadening* and *Doppler broadening*. The absorption or emission feature produced by any given atomic transition is not infinitely narrow, because of the effects of the uncertainty principle, which dictates that the product of the spread in energy ΔE, and the duration of the event Δt, must satisfy $\Delta E \Delta t \sim \hbar$, where $\hbar$ is the Planck constant divided by 2π. Hence, any spectral feature has a finite or *natural* width . The resulting line profile is known as a Lorentz, or natural, profile (Rybicki & Lightman, 1979, chap.10). Doppler broadening refers to the effects of thermal motion in a gas, with the motion of each atom producing a Doppler shift in the emission or absorption wavelength. The thermal motions of a population of atoms are random, so that the resulting absorption or emission feature is spread out.

The combined effects of natural and Doppler broadening lead to a line profile which can be described as an average of the Lorentz profile over the various velocity states of the atom. This function is referred to as a *Voigt profile*. By modeling the Voigt profile of any single spectral line, it should therefore be possible to determine the number density of absorbing atoms and degree of Doppler broadening in the population. However, the spectral resolution of existing instrumentation is considerably poorer than would be required to perform this analysis. Therefore, an alternative technique is used to determine these parameters from observations of several transitions of the same ion: the *curve of growth*.

A large number of atoms are required to produce a spectral line. Ignoring for now the shift in measured wavelength due to major effects such as radial velocity, the majority of atoms will absorb radiation very close to the resonance wavelength of that particular transition. The "wings" of an absorption profile are produced by atoms which are subject to one or more of the perturbing mechanisms which modify energy levels or absorbing wavelength. While these atoms represent a small fraction of the total population and account for a negligible amount of the total line absorption[1], an increasingly large population of absorbing atoms results in more flux being removed in the line wings; hence, as number density increases, so does the extent of the wings. Sufficiently high densities result in line saturation, where the removal of flux is complete in a region about the central wavelength, and the zone of saturation grows with further increases in density.

The curves of growth used in this work (for example, figure 5.9) consist of plots of log W/λ (the ratio of equivalent width to wavelength), against log $(Nf\lambda)$ where N is the number density of those atoms available for the particular transition, and f is the oscillator strength. These curves have three branches. For small values of Nf, the line core is not saturated and intensity is $\propto Nf$, while at intermediate values of Nf, the line centre is saturated, but absorption in the wings is still relatively weak, and intensity increases slowly with Nf. Finally, for large enough Nf, the wings become important, and intensity becomes $\propto \sqrt{Nf}$. Note also that because Doppler broadening is determined by the random thermally induced motions in a heated gas, and is therefore an indicator of temperature, whereas the rate of collisions in a gas is influenced by pressure and density, the manner in which a line "grows" is dependent on the temperature and density of a star, producing multiple curves on the plot corresponding to the

[1]The absorptivity of an atom falls to about 2% of its maximum value at a distance of only 0.003 Å from the line centre (Aller, 1971).

value of the Doppler parameter b (km s^{-1}). This parameter is based on the assumption of a Maxwellian velocity distribution among atoms, and is thus given by:

$$b = \sqrt{\frac{2k_BT}{m} + \xi^2}\ , \tag{5.4}$$

where k_B is Boltzmann's constant, T is the temperature of the gas, and m is the mass of the species under consideration. The term in ξ^2 is an additional parameter which accounts for the small-scale turbulent motion of the gas. The technique is explained in detail by Aller (1971), Mihalas (1978) and Emerson (1996).

The codes used to generate curves of growth were donated by J.B.Holberg, and are identical to those used in a study of the interstellar line of sight to REJ 1032+532 (Holberg *et al.*, 1999c). These codes generate theoretical curves for a range of Doppler parameters, for each ion of interest (velocities are marked on each curve in units of km s^{-1}). In the present work, the theoretical curves have been used to determine N and b for selected stars by fitting (by eye) measurements of the equivalent width of circumstellar features. Because of the subjective fitting method, the small number of data points, and the difficulty in measuring the equivalent widths of features which are close to, or superposed on, primary photospheric lines, these results are offered only as suggestions of the conditions which may prevail inside the circumstellar material.

5.2.2 The survey stars

The sample of stars used in this work was chosen to match that of Barstow *et al.* (2001b), with the addition of the super-hot DA PG 0948+534, since *GHRS*, *STIS* or high resolution *IUE* echelle spectra were readily available for these objects. Table 5.1 summarises the survey stars and their basic physical parameters. Values for temperature and gravity were taken from Barstow *et al.* (2001b). The adopted visual magnitudes were those of Marsh *et al.* (1997b), except where otherwise stated. The mass, radius and distance to each star was estimated using the evolutionary models developed by Wood (1995), taking the stated values of $T_{\rm eff}$, $\log g$ and m_v as input parameters.

The results of the survey are summarised in table 5.2, which includes the measured velocities of interstellar, photospheric, and any non-photospheric highly ionised lines, for all stars in the sample. This table also includes calculated values for gravitational redshift, escape velocity, and the velocity of the local interstellar cloud in that direction. The relevance of these calculated parameters, and their derivation, are discussed in section 5.3.

5.2.3 Comments on individual objects

5.2.3.1 PG 0948+534

PG 0948+534 is the hottest star in this sample. Strong ISM lines are observed, many of which are saturated, and at least two velocity components are present. However, the N I and Si II features are most accurately described by three components, with self consistent velocities: the primary component lies at -0.26 $\pm$ 1.26 km s^{-1}, with

Star	T_{eff} (K)	log g	M ($M_\odot$)	R ($R_\odot$)	m_v	D (pc)	Source
PG 0948+534	90,000	7.27	0.478	0.027	13.71[e]	193.8	*STIS*
REJ 1738+665	71,300	7.53	0.540	0.024	14.61	243	*STIS*
REJ 0558-373	63,000	7.66	0.580	0.019	14.37	295	*STIS*
REJ 2214-492	62,100	7.23	0.464	0.027	11.71	69	*IUE*
REJ 0623-371	59,700	7.00	0.399	0.033	12.09	97	*IUE*
WD 2218+706	56,900	7.00	0.396	0.033	15.40[c]	436	*STIS*
Feige 24	56,400	7.36	0.546	0.021	12.56	78	*STIS*
REJ 2334-471	54,600	7.58	0.536	0.020	13.44	104	*IUE*
G191-B2B	54,000	7.39	0.510	0.021	11.73	50	*STIS*
GD 246	53,700	7.74	0.646	0.016	13.09	72	*STIS*/*IUE*
REJ 0457-281	53,600	7.80	0.612	0.016	13.95	108	*IUE*
PG 1123+189	52,700	7.52	0.511	0.021	14.13	147	*STIS*
HZ 43	49,000	7.90	0.561	0.018	12.99	71	*IUE*
REJ 1032+532	46,300	7.78	0.585	0.016	14.46	127	*STIS*
REJ 2156-546	45,900	7.74	0.568	0.017	14.44	129	*STIS*
PG 1057+719	39,555	7.66	0.519	0.018	14.68[b]	411	*GHRS*
REJ 1614-085	38,500	7.85	0.596	0.015	14.01	86	*GHRS*
GD 394	38,400	7.84	0.592	0.015	13.08	57	*IUE*/*GHRS*
GD 153	37,900	7.70	0.520	0.017	13.35[a]	73	*IUE*
GD 659	35,300	8.00	0.662	0.013	13.37	53	*STIS*/*IUE*
EG 102	20,200	7.90	0.573	0.014	12.76[d]	25	*IUE*
Wolf 1346	20,000	7.90	0.572	0.014	11.52[f]	14	*IUE*

[a] Bohlin *et al.* (1995) [b] Holberg *et al.* (1997b) [c] Napiwotzki & Schönberner (1995)
[d] Greenstein (1984) [e] Holberg *et al.* (1995b) [f] Dahn *et al.* (1988)

Table 5.1: Stars included in the survey of circumstellar features, in descending temperature order. Mass, radius and distance calculated from the evolutionary models of Wood (1995). Visual magnitudes taken from Marsh *et al.* (1997b) unless otherwise stated.

Star	v_{esc}	v_{grav}	v_{LIC}	v_{ISM}	v_{phot}	v_{shift}
PG 0948+534	2645	11.3	10.003	-0.255 ±1.262	-14.245 ± 0.222	
REJ 1738+665	3365	14.2	-3.463	-18.555 ±0.089	30.188 ±0.274	-17.802 ±0.328
REJ 0558-373	3477	19.6	25.190	11.614 ±1.399	22.742 ±2.812	7.147 ± 0.768
REJ 2214-492	2526	10.9	-8.543	-1.719 ±0.514	33.486 ±0.452	
REJ 0623-371	2143	7.7	14.460	16.404 ±0.696	41.151 ±0.555	
WD 2218+706	2143	7.6	4.927	-10.110 ±0.185	-38.693 ±0.230	-16.337 ±0.668
Feige 24	2588	17.0	20.518	8.217 ±0.097	80.333 ±0.500	ΔV=25.0 ±3.5
REJ 2334-471	3253	17.0	-2.618	15.145 ± 1.520	40.565 ± 2.072	
G191-B2B*	2679	15.4	20.583	8.6	25.204 ±0.255	7.558 ±0.187
GD 246	3498	25.7	2.395	-5.783 ±0.118	-13.285 ±0.252	
REJ 0457-281	3749	24.3	18.915	14.479 ±2.151	76.913 ±0.830	21.760 ±1.269
PG 1123+189	3111	15.5	-0.357	-0.666 ±0.058	12.549 ±0.526	
HZ 43	4461	19.8	-8.825	-16.857 ±2.074	—-	
REJ 1032+532	3663	23.3	7.405	0.835 ±0.205	38.160 ±0.404	
REJ 2156-546	3606	21.2	-9.649	-8.393 ±0.176	-19.944 ±0.683	-1.645 ±0.764 ?
PG 1057+719	3384	18.3	6.508	-2.894 ±0.685	75.352 ±2.588	
REJ 1614-085	3845	25.3	-25.293	-29.556 ±0.334	-37.313 ±0.401	-71.418 ±6.633
GD 394	3801	25.1	-2.160	-7.282 ±1.422	28.747 ±0.910	
GD 153	3444	19.4	-8.645	-8.424 ±2.683	12.447 ±2.067 ?	
GD 659	4254	32.4	6.121	9.766 ±0.223	34.277 ±0.172	-2.970 ±2.996 ?
EG 102	3934	26.0	1.053	-1.371 ±3.847	-0.685 ±1.435	
Wolf 1346	3934	26.0	-10.759	-15.379 ±0.948	24.319 ±1.406	

*ISM velocity from Sahu *et al.* (1999); no error quoted. Value for ISM velocity determined from current work (using lower resolution data) is $v_{ISM} = 16 \pm 1$ kms^{-1}.

Table 5.2: Measured velocities for interstellar, photospheric and non-photospheric lines for surveyed stars. Tentative identifications are marked "?". All velocities in km s^{-1}.

the secondary and tertiary components at -22.8 ± 1.17 and 22.1 ± 2.37 km s^{-1} (figure 5.3). The photospheric lines (including the resonance doublets of C IV and Si IV) exhibit narrow, symmetrical profiles and are apparently devoid of any shifted components, defining $v_{\rm phot}$ = -14.25 ± 0.22 km s^{-1}. A remarkably strong, multi-component C II 1335.7076 Å line is observed, also shown in figure 5.3. The velocity components match those of other ISM lines, although the -23 km s^{-1} feature is very weak, manifesting itself as a broadening on the blue side of the line. Excited Si II transitions such as 1265, 1309 and 1533 Å are not observed (Holberg *et al.* (1995b) used the presence of these lines in the white dwarf CD -38° 10980 to infer the existence of a circumstellar cloud around the star). Therefore, although multiple clouds of interstellar material are detected along the line of sight to this star, no evidence of highly ionised non-photospheric material is found.

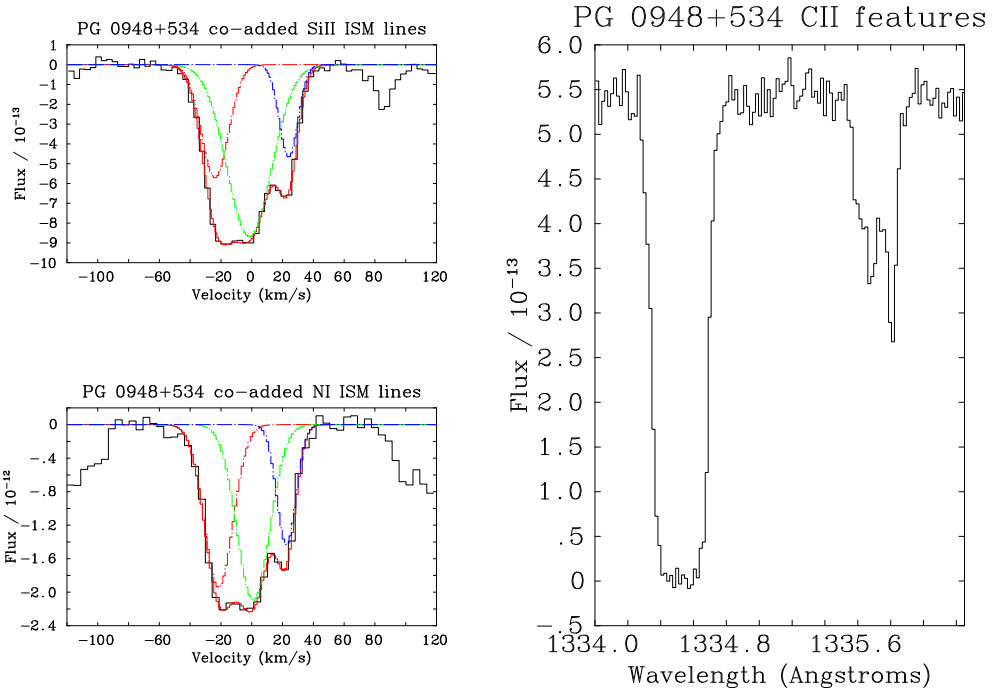

Figure 5.3: Upper left: co-added interstellar Si II lines in REJ 0948+534, with three-component Gaussian fit. Lower left: analogous plot for N I. Right: interstellar C II lines at 1334 & 1335 Å.

5.2.3.2 REJ 1738+665

REJ 1738+665 is the hottest DA white dwarf to be detected by *ROSAT* (Barstow *et al.*, 1994b). A photospheric velocity of $v_{\rm phot} \approx 30 \pm 1$ km s^{-1} is determined, based on absorption features arising from Fe, Ni and O which show no multiple components; interstellar lines indicate a line of sight ISM velocity of $v_{\rm ISM} \approx -18 \pm 1$ km s^{-1}. The line of sight velocity of the LIC is estimated to be $v_{\rm LIC*} \approx -3.4$ km s^{-1}.

Clear evidence is found for the presence of circumstellar material in this star. Figure 5.4 shows the C IV resonance doublet in REJ 1738+665, with shifted components at -18.5 ± 0.5 km s^{-1} dominating the 30 km s^{-1} photospheric contribution. Shifted features with similar velocities are determined for several other species, although in each case the photospheric component is dominant. The Si IV doublet shows clear evidence of multiplicity, with non-photospheric velocity components observed at -17.7 ± 0.7 km s^{-1}. Viewed individually, the lines of the N V

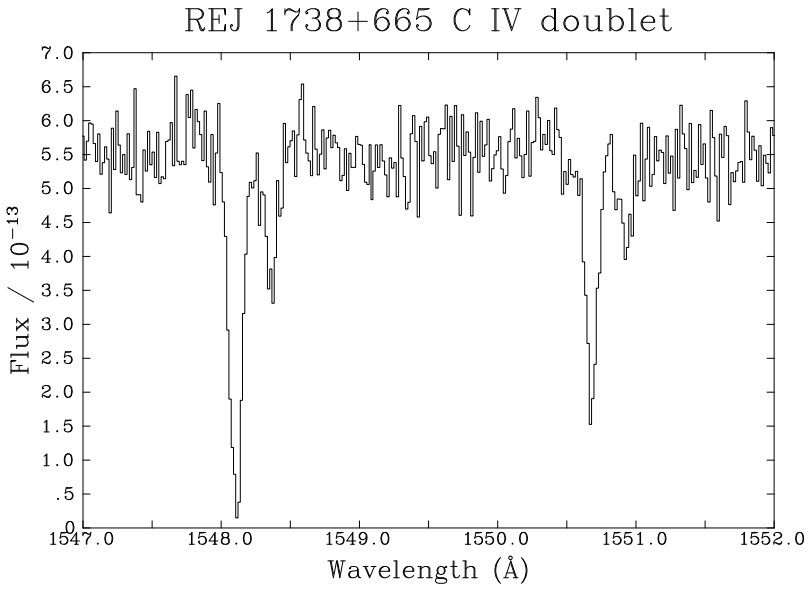

Figure 5.4: Clear multiplicity in the C IV doublet of RE 1738+665, with the photospheric components dominated by the blueshifted lines.

doublet (1238.821 and 1242.804 Å) show no evidence of companions, but co-addition of these features suggests an extra, weak component at -15.2 ± 2 km s^{-1}. The O IV doublet (1338.612 and 1343.512 Å) shows no additional features, but the O V line at 1371.292 Å is accompanied by a weak shifted component at -18.7 ± 0.5 km s^{-1}. Curves of growth for the C IV and Si IV features are shown in figure 5.5. Values of log N (C IV) = 13.25 and log N (Si IV) = 13.27 are obtained, with $b = 4$ km s^{-1}. Note that an improved fit to the Si IV data can be obtained using the $b = 6$ km s^{-1} curve, corresponding to log N (Si IV) = 13.08, although this requires that two separate Doppler parameters be ascribed to the circumstellar material.

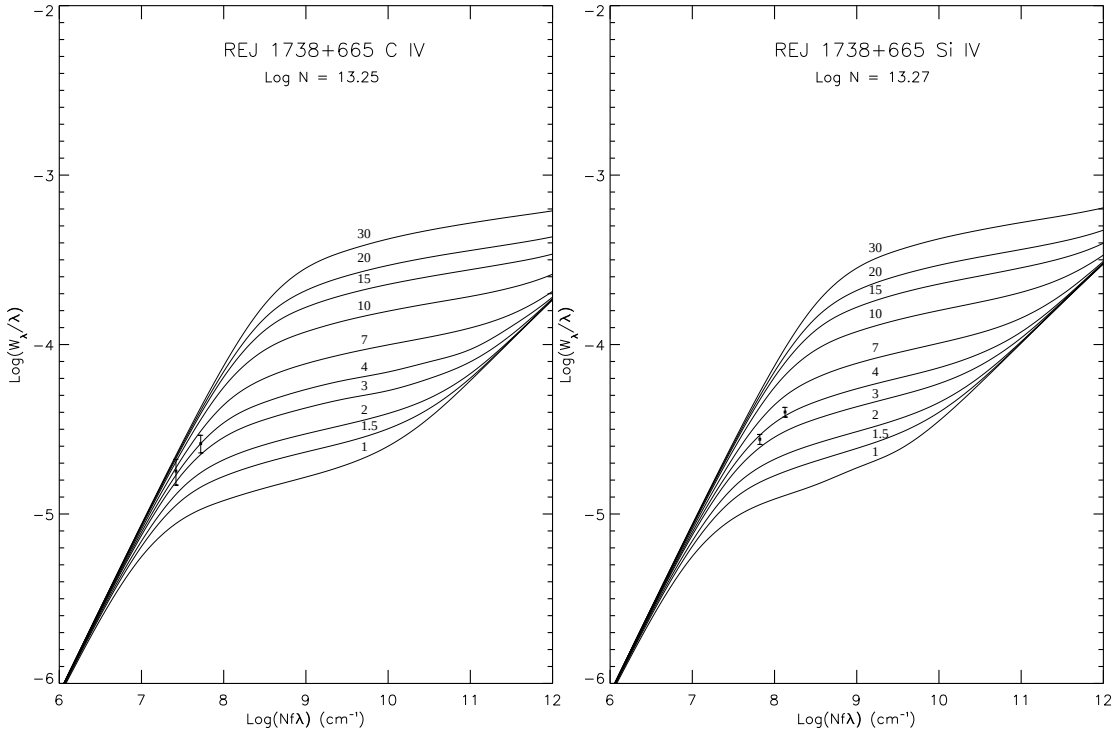

Figure 5.5: Curves of growth for REJ 1738+665. Separate curves in each plot correspond to different values of the Doppler parameter, b (indicated in km s^{-1}).

This is a particularly significant object, since the velocities measured for these shifted features differ from $v_{\rm ISM}$ by less than 0.75 km s^{-1}. This raises the possibility that they may be produced by photoionisation of the ISM within the Strömgren sphere around the star. However, Tweedy & Kwitter (1994) present evidence for the possible existence of a planetary nebula around the star, based on the observation of N II features at optical wavelengths. The non-photospheric features of REJ 1738+665 may therefore be produced by ionisation of the ancient planetary nebula remnant surrounding this star. The relationship between planetary nebulæ and highly ionised non-photospheric lines is explored in section 5.3.

5.2.3.3 REJ 0558-373

The C IV 1548 and 1550 Å lines in this star are moderately asymmetrical. Following the method outlined by Holberg *et al.* (1997b), the lines were fitted first by a single Gaussian, and then a double Gaussian distribution, and a standard *F*-test comparison used to determine whether a significantly better fit to observation was obtained with the latter. When applied to the C IV resonance lines of REJ 0558+164, this test suggests that a dual Gaussian fit is preferred over a single line, above the 98% confidence interval, for each feature. No corresponding asymmetries are observed elsewhere in REJ 0558-373.

For the 1548 Å line, the individual components are found at 7.0 ± 1.0 and 26.8 ± 1.2 km s^{-1} (with equivalent widths of 79 and 68 mÅ respectively). Corresponding values for the 1550 Å line are 7.9 ± 1.2 and 21.8 ± 1.0 km s^{-1} (13 mÅ and 150 mÅ). Fits to each line are illustrated in figure 5.6. For comparison, $v_{\rm phot}$ = 22.7 ± 2.8 km s^{-1}, and $v_{\rm ISM}$ = 11.6 ± 1.4 km s^{-1}, and hence the longer wavelength component of each C IV line is in reasonable agreement with the photospheric value.

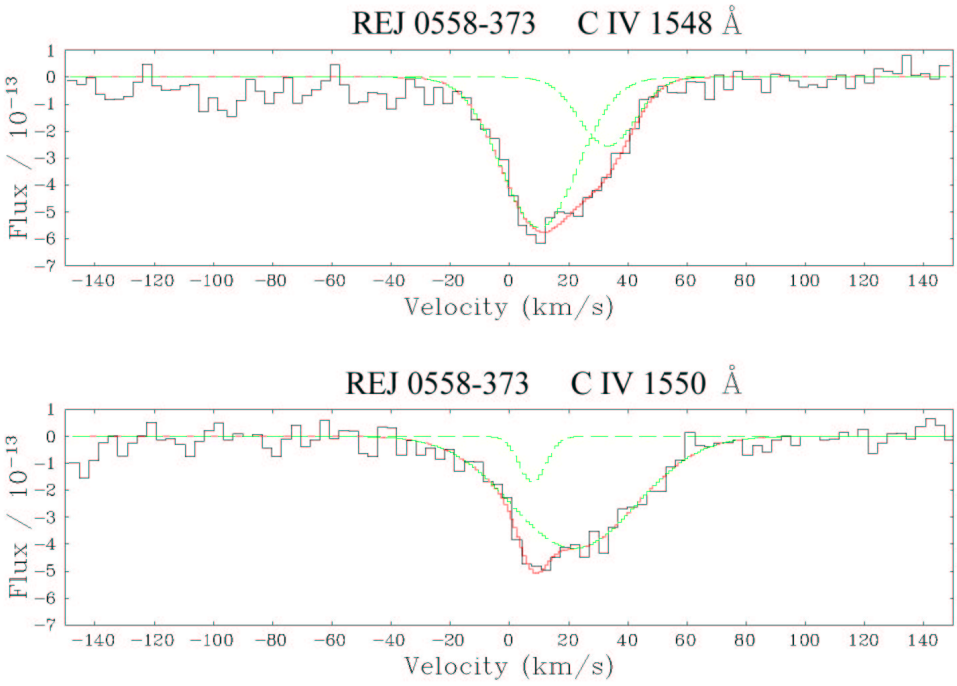

Figure 5.6: Lines of the C IV doublet of REJ 0558-373, in velocity space, with compound Gaussian fits overlaid. Black histogram: *STIS* data. Red curve: compound fit. Green curves: component Gaussians.

v_{grav} is estimated as $\approx$ 20 km s^{-1} for this star, which is greater than the $\sim$ 10 km s^{-1} difference between the photospheric and shifted C IV components. It is therefore possible that the blueshifted, non-photospheric C IV features could be formed by material *within* the potential well, rather than the weakly shifted outer regions. However, the non-photospheric components lie close to the velocity of the ISM, raising instead the possibility that the star is ionising material in its local interstellar environment. In either case, the absence of corresponding features in other strong lines is puzzling.

5.2.3.4 REJ 2214-492

Weighted averages of line velocity measurements indicate v_{ISM} = -1.719 ($\pm$0.514) km s^{-1}, and v_{phot} = 33.486 ($\pm$0.452) km s^{-1}. These values compare well with those of Holberg *et al.* (1998), who find v_{ISM} = -0.71 (0.88) and v_{phot} = 33.91 (0.47) km s^{-1} respectively. However, a significant difference exists between the velocity of each line in the C IV doublet, with 1548 Å at 30.5 $\pm$ 2.1 km s^{-1}, and 1550 Å at 40.4 $\pm$ 2.7 km s^{-1}, if each of the two lines is assumed to be made up of only one absorption feature.

Visual inspection of the C IV doublet revealed slight asymmetries, particularly in the 1548 Å line. The results of an *F*-test showed that for the 1548 Å line, the dual fit was found to be superior to the single Gaussian at the 99.9% confidence level, with velocity components at 5.37 and 38.36 km s^{-1}, and equivalent widths of 31.1 and 99.3 mÅ respectively. A dual Gaussian fit to the 1550 Å line produced a less obvious improvement (at the 90% confidence level) with components at 36.2 and 80.6 km s^{-1}, and equivalent widths of 137.6 and 14.8 mÅ respectively. The primary Gaussian components of the doublet are thus found to lie at velocities more consistent with each other and the overall photospheric value. The status of putative non-photospheric contributions in the C IV doublet is less certain; although the 5 km s^{-1} feature in 1548 Å appears to provide a good match to observation, the lack of

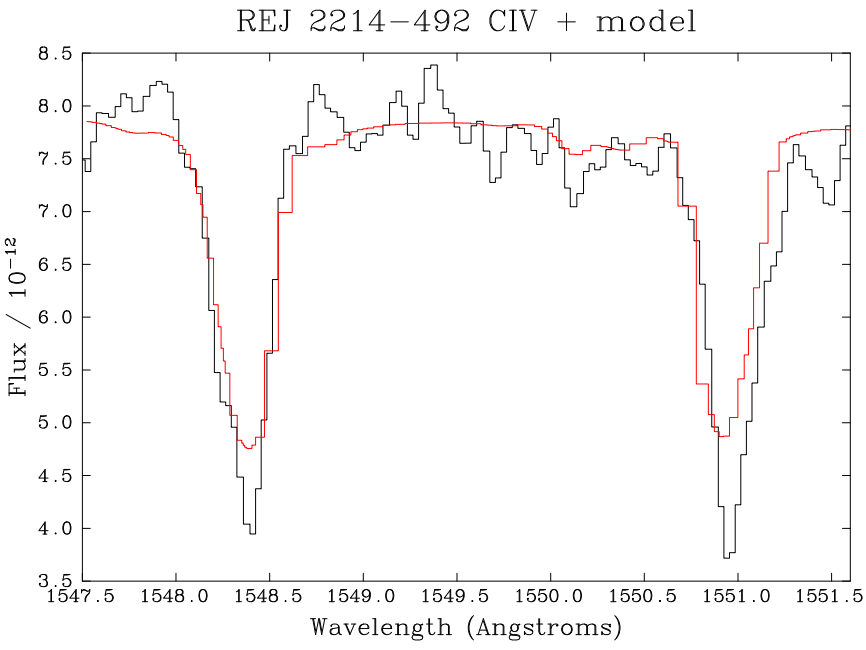

Figure 5.7: Observed C IV doublet in REJ 2214-492 (black) compared to a synthetic spectrum with log N(C)/N(H) = -6, smoothed to the resolution of *IUE*.

a corresponding feature at 1550 Å prevents confirmation of its reality. No evidence was found for multiplicity in other photospheric lines.

Line profiles were compared with those from a model spectrum, produced using the TLUSTY and SYNSPEC codes, and adopting the heavy element abundances determined by Barstow *et al.* (2001b) (with N(C)/N(H) = 1.0×10^{-6}). After smoothing the model to the resolution of *IUE*, no significant differences were apparent in the shapes of model and observed C IV lines (figure 5.7), casting further doubt on the presence of shifted features in this star.

5.2.3.5 REJ 0623-371

The photospheric velocity determined in this work ($v_{\rm phot}$ = 41.15 ±0.56) agrees with that of Holberg *et al.* (1998). The current value for $v_{\rm ISM}$ is somewhat lower than that of Holberg *et al.*, (16.404 ±0.696 km s^{-1} c.f. 19.48 ±0.85 km s^{-1} respectively), and the principal source of this difference lies in a more precise determination of the C II line velocity. Holberg *et al.* estimate the velocity of this line to be 14.07 ±3.24 km s^{-1}, compared to the new value of 13.33 ±1.138 km s^{-1}. When incorporated into the weighted average, this low error estimate leads to the C II line having a significant effect on the final value. This point may be illustrated by adopting the C II error estimate of Holberg *et al.* while retaining the new C II velocity, which brings the new average ISM velocity into agreement with the earlier value.

No compelling evidence exists for the presence of shifted components in the spectrum of REJ 0623-371, but as in the case of REJ 2214-492, a significant difference is observed in the velocity of the lines in the C IV doublet (1548 Å = 38.6 ±2.3 km s^{-1}, 1550 Å = 47.6 ±2.2 km s^{-1}). In contrast, the lines of the N V and Si IV resonance

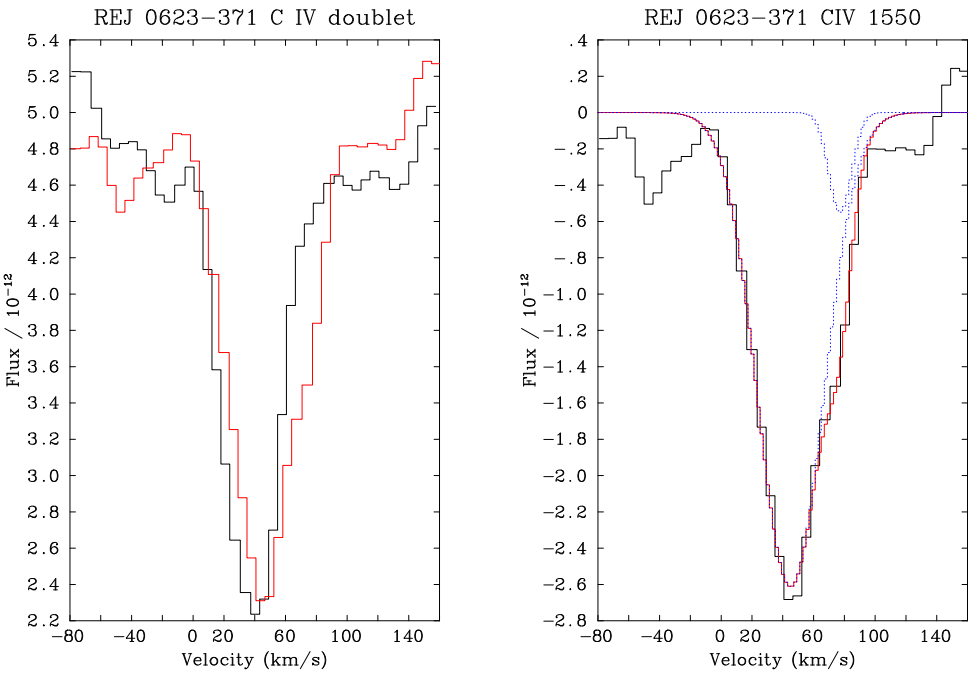

Figure 5.8: Left: lines of the C IV doublet in REJ 0623-371, in velocity space, demonstrating the difference in velocity of the two lines. Right: dual Gaussian fit to the 1550 Å C IV line.

doublets, which are of comparable equivalent width, agree within the estimated error. Determining the reality of any features in the doublet is complicated by considerable structure in the continuum level around each line, though by restricting Gaussian fits to the region below this structure, useful comparisons between the level of agreement found with single and double Gaussian profiles, may be obtained. Using this method, a dual Gaussian fit is preferred to a single feature only at the 88.8% level for the 1548 Å line. However, results for the 1550 Å line are less ambiguous, suggesting a dual fit at 98.9%. The resulting Gaussians have velocities of 45.1 and 77.3 $\mathrm{km\,s^{-1}}$, and equivalent widths of 128.5 and 10.8 mÅ respectively (see figure 5.8). Therefore, while the quality of the available data is insufficient to prove the existence of non-photospheric, high ionisation features in the star, the results of this analysis provide some justification for proposing repeat observations at a higher signal-to-noise ratio (S/N).

5.2.3.6 WD 2218+706

This object is unusual and important in several respects. Lines of the C IV and Si IV doublets are clearly multiple, dominated by a photospheric contribution, but with accompanying components of comparable equivalent width at a velocity of -16.3 $\pm$ 0.7 $\mathrm{km\,s^{-1}}$. These features are therefore *redshifted* with respect to the photospheric velocity (v_{phot} = -38.7 $\pm$ 0.2 $\mathrm{km\,s^{-1}}$), possibly representing the infall of material onto the white dwarf. Gravitational redshift therefore provides no viable explanation for these lines.

WD 2218+706 is surrounded by an old planetary nebula, with the designation DeHt5, and is discussed by Napiwotzki & Schönberner (1995). In a study of planetary nebula dynamics, Dgani & Soker (1998) show that in regions where the ISM is reasonably dense (such as the galactic plane), Rayleigh-Taylor instabilities can develop in the outer regions of planetary nebulæ, leading to fragmentation of the halo, and allowing the surrounding ISM to pass into the inner regions of the nebula where photoionisation can occur. Although WD 2218+706 is out of the galactic plane ($b_{\mathrm{II}} = 11.6°$), and therefore lies in a region where the mean ISM density may be expected to be relatively low, Kun (1998) describes the morphology of a nearby giant molecular cloud complex consisting of a large number of distinct regions previously identified in independent surveys; several are found close to WD 2218+706, and two are of particular interest (Lynds 1217 and Lynds 1219). The central portions of these clouds have galactic coordinates within less than 0.5° of this star, and their distance limits (from 380 to 450 pc) encompass the distance to WD 2218+706 (440 pc, from Napiwotzki & Schönberner). This raises the possibility that the star may lie in an area where the ISM is particularly dense, allowing instability and inflow to take place (a curve of growth analysis for the non-photospheric features in WD 2218+706 suggests column densities of N (C IV) = 4.17×10^{13} $\mathrm{cm^{-2}}$ and N (Si IV) = 4.07×10^{13} $\mathrm{cm^{-2}}$, each with a Doppler parameter of 6 $\mathrm{km\,s^{-1}}$). However, in the absence of less equivocal evidence, this explanation must be regarded as conjecture. Alternative explanations, such as the presence of a hidden companion, are also deserving of investigation, and this work is currently in progress.

During the course of the WD 2218+706 study, evidence was found for the existence of trace amounts of He in the *STIS* spectrum. This work is described in more detail by Barstow *et al.* (2001), but is worth summarizing here. No evidence exists for the He II 4686 Å absorption line, characteristic of the DAO class of white dwarf

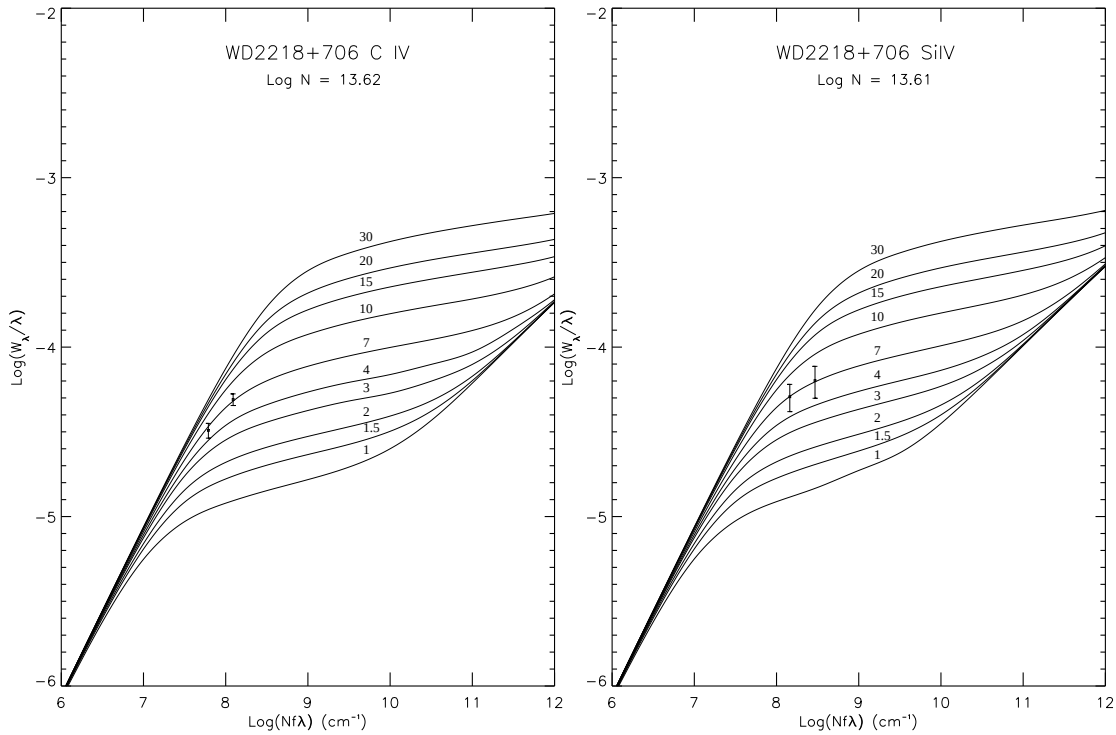

Figure 5.9: Curves of growth for the redshifted C IV and Si IV features in WD 2218+706. Separate curves in each plot correspond to different values of the Doppler parameter, b (indicated in km s^{-1})

star, in the spectrum of WD 2218+706. However, the He II 1640 Å line is apparent in the *STIS* spectrum, and is shown in figure 5.10. With a measured radial velocity of -35.4 ± 2.5 km s^{-1}, this line lies very close to the estimated photospheric value, and is substantially different to the observed interstellar velocity. Further, as stated by Barstow *et al.*, the 1640 Å line has an n=2 lower level, which should not be populated in collisionless interstellar material, while any helium in the surrounding planetary nebula would be expected to be found in emission. Hence a photospheric origin appears to be the most satisfactory of these three possible sources.

As discussed in Chapter 1, the detection of helium in an isolated DA white dwarf is of great importance for this field of study. Yet despite the apparently unambiguous detection in WD 2218+706, other data suggest that in common with previous DA objects exhibiting He features, this star has an unusual origin. The surface gravity of WD 2218+706 ($\log g \approx 7.00$) is suspiciously low for an isolated white dwarf. This may be explained by appealing to the existence of an (unseen) companion. White dwarf stars with masses below ~ 0.5 M$_\odot$ cannot be produced by single-star evolution, since their progenitors would have such low mass that they do not complete their main sequence evolution within the Hubble time. The existence of low mass objects such as WD 2218+706 may be explained in terms of close-binary evolution, in which the progenitor star fills its Roche lobe and loses mass to the companion. This loss of material prevents helium ignition from taking place. Instead, the star, consisting of a He core surrounded by a H-rich envelope (which still supports nuclear reactions at the base), contracts slowly towards the low-mass, He-core white dwarf configuration (Driebe *et al.*, 1998, Napiwotzki, 1999). Nevertheless, there is no direct evidence for the existence of a binary companion. Further, the range of possible masses for this star (given uncertainties) does not preclude AGB evolution, leaving open the possibility that WD 2218+706 *is* the product of single-star evolution, and does indeed represent the first detection of He in an isolated DA white dwarf.

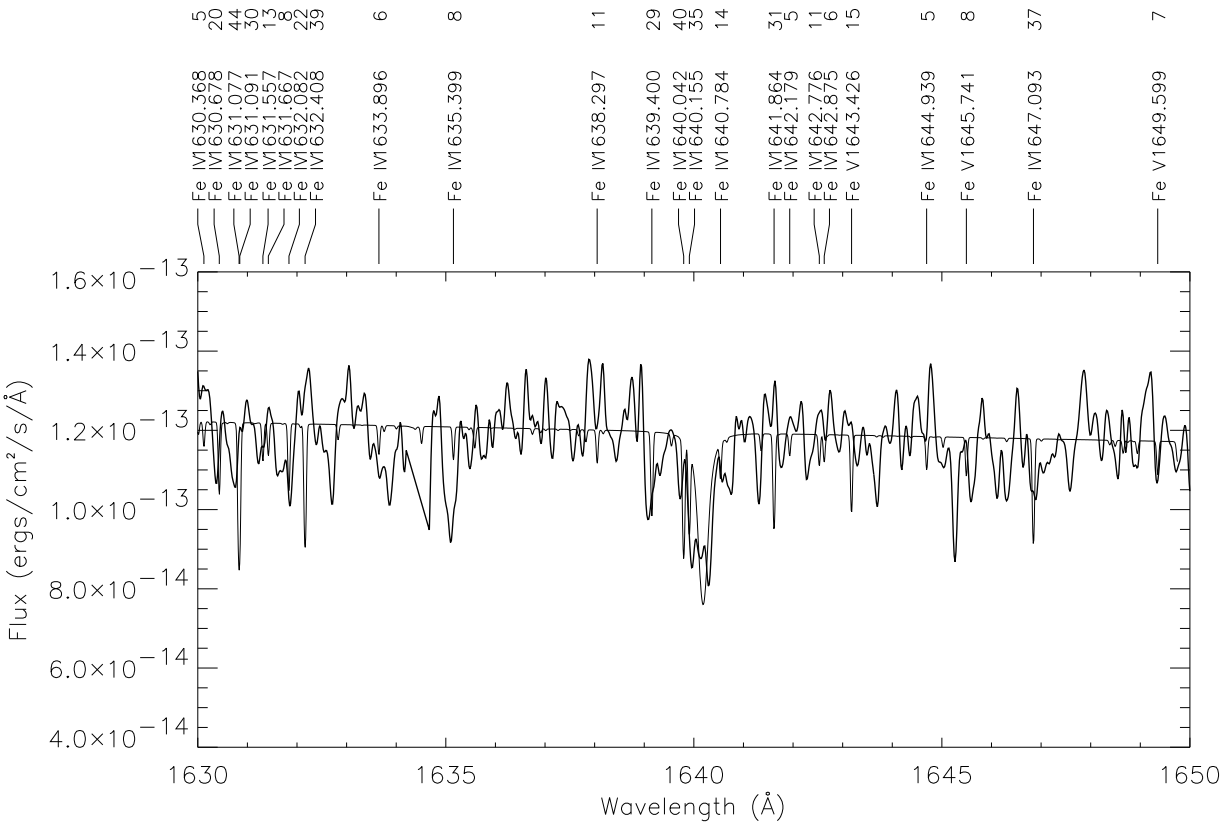

Figure 5.10: STIS spectrum of WD 2218+706, showing the detected He II 1640 Å line. The raw observed spectrum is noisy in this region and has been smoothed by a 0.04 Å (rms) Gaussian function. The smooth curve is a synthetic spectrum calculated for an abundance (He/H) of 3×10^{-5}. The strongest lines other than He are identified with their rest wavelength and predicted equivalent width (mÅ). Figure from Barstow *et al.* (2001).

5.2.3.7 Feige 24

Feige 24 is a white dwarf+red dwarf binary system, and is the subject of several detailed studies (e.g. Dupree & Raymond, 1982, Vennes & Thorstensen, 1994). Two *STIS* datasets were available for this star, acquired on November 29$^{\rm th}$ 1997 (binary phase 0.73–0.75) and January 4$^{\rm th}$ 1998 (binary phase 0.23–0.25), these phases essentially representing the orbital quadrature points. Vennes & Thorstensen estimate a systemic velocity of 62.0 $\pm$ 1.4 km s^{-1}. For the current study, the systemic velocity has been estimated by taking the median of the photospheric values obtained from each data set (31.6 and 129.1 km s^{-1}), resulting in an estimated systemic velocity of 80.3 $\pm$ 0.5 km s^{-1}. $v_{\rm ISM}$ is estimated at 8.2 $\pm$0.1 km s^{-1}.

Feige 24 is already known to exhibit multiple components, in the lines of the C IV doublet only. In this work, the dominant components match the photospheric velocity of each dataset, and secondary features are observed to remain at 7.8 $\pm$ 0.2 km s^{-1}, irrespective of the orbital phase. This stationary component has been discussed by Dupree & Raymond, who suggest that the most likely source is a Strömgren sphere excited by the white dwarf, and measure column densities of log N(C IV) = 13.55 $\pm$ 0.18 cm^{-2} using curves-of-growth. Vennes & Thorstensen investigated the possibility that the material responsible resides in the photosphere, in a circumstellar shell, or in a wind from the red dwarf companion.

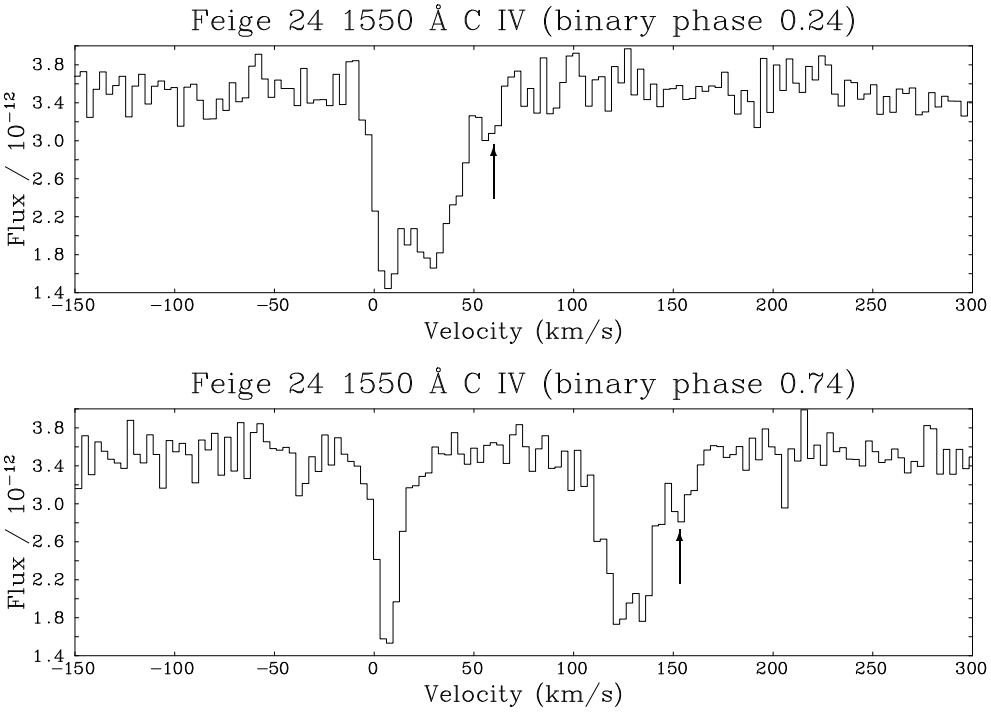

Figure 5.11: The C IV 1550 Å feature of Feige 24 as observed at the two quadrature points. The stationary circumstellar component is clearly visible, as is the photospheric component. Arrows indicate the position of the suggested third component, which appears to move with the photospheric feature.

The current study shows no shifted components in any of the other resonance lines (e.g. Si IV or N V). However, there is some evidence for a *third*, very weak component on the red side of each photospheric line in the C IV doublet, most obviously at 1550 Å. If each dataset were to be viewed in isolation, this structure would most probably be attributed to noise, as reflected in the results of an *F*-test, showing that a dual fit is not preferred over a single Gaussian. Nevertheless, the presence of similar features in *both* spectra makes simple statistical noise a less satisfactory explanation. The velocity of this third component, measured with respect to the photospheric component, is remarkably consistent. For the 1550 Å line, ΔV = +28.49 and +28.52 km s^{-1} for the two datasets[2]. For 1548 Å, in which the feature is less well defined, ΔV = +22.53 and +22.20 km s^{-1}. It should be noted that this feature does *not* resemble the third component reported by Vennes & Thorstensen (1994). The authors of this earlier study show a component in both 1548 and 1550 Å lines which is blueshifted by $\sim$ 200 km s^{-1} with respect to the photospheric component. This feature was observed in only one of the four phase-resolved spectra considered by Vennes & Thorstensen, and is not detected in the current work.

The gravitational redshift estimate made during this study, $v_{\rm grav} \approx 17$ km s^{-1}, is somewhat higher than that derived by Vennes & Thorstensen ($v_{\rm grav} \approx 9 \pm 2$ km s^{-1}), but is still too low to explain the secondary C IV components. However, their velocities agree, within error, with that of the ISM, and hence a link between the star and its immediate surroundings (beyond any circumstellar shell) cannot be discounted. Alternatively, Vennes & Thorstensen estimate that a C IV column density from 8×10^{11} to 8×10^{13} cm^{-2}, (corresponding to equivalent widths of between 4–400 mÅ for the non-photospheric component of the 1550 Å line), would be consistent with mass loss from the red dwarf companion. Although insufficient data are available to derive an unambiguous C IV column

[2]To obtain an accurate photospheric velocity for the first spectrum, in which photospheric and stationary features are blended, the second spectrum was subtracted, effectively canceling out the stationary component.

density in this study, the estimated value of $\sim 1.5 \times 10^{13}$ cm^{-2}, is within the range of possible values obtained by Vennes & Thorstensen, and the equivalent width of the 1550 Å line (24 mÅ) is also consistent with the large range allowed by earlier estimates.

5.2.3.8 REJ 2334-471

Values measured for $v_{\rm ISM}$ and $v_{\rm phot}$ are in good agreement with those obtained by Holberg *et al.* (1998). The relatively poor quality of the spectrum precludes unambiguous identification of any non-photospheric features, particularly in the case of the C IV lines. Although the definition of the N V doublet is improved, it is still insufficient to yield good quality results; certainly, there is no evidence of multiplicity in the 1242 Å line, although a dual Gaussian with components at 19.7 and 43.51 km s^{-1} produces a fit which is preferred over a single feature at the 93% confidence level.

It is therefore interesting that each line in the Si IV doublet (1393 & 1402 Å) is fitted reasonably well (above the 95% confidence interval when compared to a single feature) by double Gaussian profiles similar in velocity and equivalent width. Each line can be described by a double Gaussian with V_1 = 34.00 $\pm$0.82 km s^{-1}, EW_1 = 48.85 $\pm$0.95 mÅ, and V_2 = 54.64 $\pm$1.58 km s^{-1}, EW_2 = 22.74 $\pm$3.25 mÅ). This result is problematic since neither of the Gaussian velocities are in agreement with the average photospheric value, although a considerable spread in individual photospheric velocity measurements is observed, so that the discrepancy cannot be used to infer the absence of such features. Until spectra with improved S/N are available, the presence of non-photospheric components in this star must therefore be regarded as speculative.

5.2.3.9 G191-B2B

G191-B2B is clearly of great significance throughout this thesis, and the latest observational results obtained using the *J-PEX* spectrometer are discussed in Chapter 6. Good *STIS* data are currently available for this highly studied white dwarf star, confirming the results of Bruhweiler *et al.* (1999) which showed that both lines in the C IV doublet include a shifted component. The wavelength and equivalent width of these features have been estimated by fitting multiple Gaussians to the data, as shown in figure 5.12; these results were first presented at the 12th International Workshop on White Dwarf Stars, held in 2000 at the University of Delaware (Bannister *et al.*, 2001). The component at photospheric velocity is of greater equivalent width, and the shifted elements are observed at velocities of 7.6 $\pm$0.2 km s^{-1}. However, there is no evidence for corresponding features in any of the other lines examined. The calculated figure of $v_{\rm grav} \approx 15.4$ km s^{-1} is comparable with the velocity difference between photospheric and shifted high ionisation features, suggesting that the non-photospheric material probably resides outside the limit of the potential well.

The velocity of the highly ionised non-photospheric features is substantially different to the value of the interstellar features ($v_{\rm ISM} = 16 \pm 1$ km s^{-1} as determined in this work), and at first sight, photoionisation of the cloud responsible for the primary ISM features does not appear to provide a viable explanation. However, the value quoted for $v_{\rm ISM}$ is based on analysis of an E140M (medium resolution) *STIS* dataset, with a resolution $\frac{\lambda}{2\Delta\lambda} = 45800$.

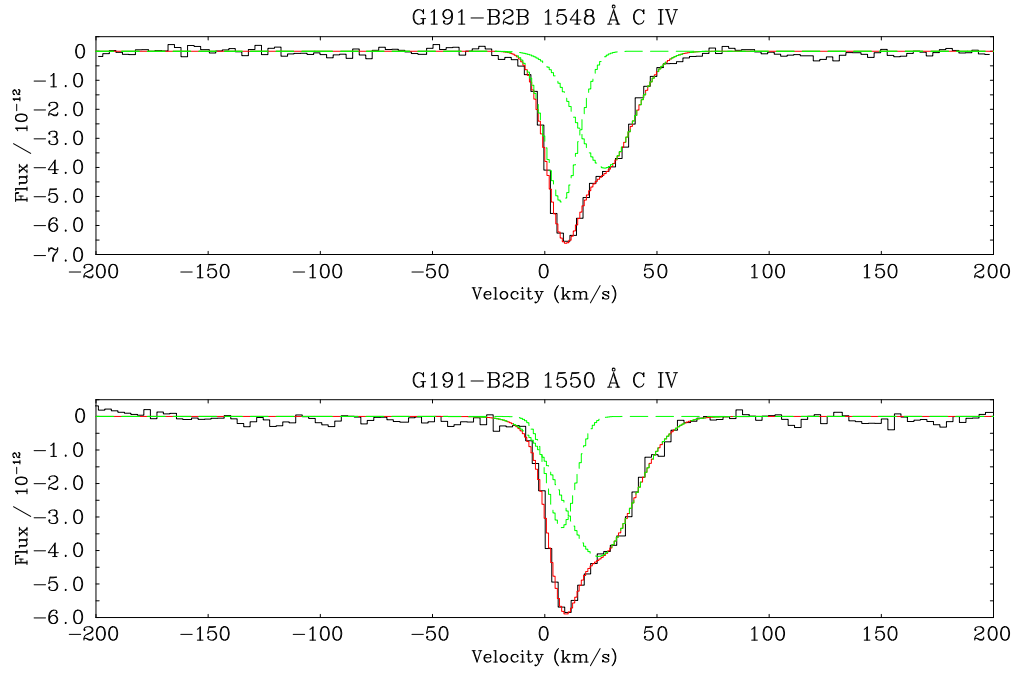

Figure 5.12: The C IV doublet of G191-B2B, in velocity space, with compound Gaussian fits (red), and the individual Gaussian components (green).

Sahu *et al.* (1999) describe observations made with the E140H grating ($\frac{\lambda}{2\Delta\lambda} = 114000$), and clearly show *two* distinct interstellar components, with velocities of $\sim 8.6\,\mathrm{km\,s^{-1}}$ and $\sim 19.3\,\mathrm{km\,s^{-1}}$, the latter component having a velocity close to the predicted value of v_{LIC} (estimated at $20.583\,\mathrm{km\,s^{-1}}$ in this study). Clearly, the highly ionised non-photospheric components have a velocity which is very close to the $8.6\,\mathrm{km\,s^{-1}}$ interstellar cloud.

A curve-of-growth analysis was performed for the C IV features in G191-B2B. As in the case of Feige 24, the availability of only two datum points prevents any rigorous constraints from being placed on the implied C IV column density, though the value of log N (C IV) = 13.38 is not dissimilar from the results of Vennes & Lanz (2001), who use synthetic modeling techniques to estimate a value of log N (C IV) = 13.80. The Doppler parameter suggested by the current analysis, $b = 10\,\mathrm{km\,s^{-1}}$, is significantly higher than the value of $b = 5.2\,\mathrm{km\,s^{-1}}$ presented by Vennes & Lanz; this discrepancy may also be explained by the lack of available data in the current work.

5.2.3.10 GD 246

IUE and *STIS* data were available for this star, permitting a selection of useful cross-checks to be made. Photospheric and ISM line velocities measured from the *IUE* data are in good agreement with those of Holberg *et al.* (1998). The photospheric velocity estimated from *STIS* data differs from the *IUE* value by 1 $\mathrm{km\,s^{-1}}$, although this is within the *IUE* error bounds. The *STIS* ISM velocity (-5.78 $\pm$0.12 $\mathrm{km\,s^{-1}}$) is marginally outside the *IUE* estimate (-7.87 $\pm$1.00 $\mathrm{km\,s^{-1}}$).

IUE and *STIS* data clearly show the C IV doublet lines as singular, and at the photospheric velocity. The N V lines at 1238 and 1242 Å, not observed in the *IUE* data, *are* visible in the *STIS* spectrum but are very weak (with

equivalent widths of 4.5±1.5 and 3.1±2.1 mÅ respectively). More interesting are the lines of the Si IV doublet, which show signs of slight asymmetric broadening with *IUE*. A standard *F*-test shows the double Gaussian form preferred over a single component at only the 63% level for 1393 Å, and 79% for 1402 Å, with similar values being obtained from *STIS* data. *STIS* shows the 1393 Å line as being devoid of any secondary components, while a sharp feature (only one bin, or 0.02 Å in width) is observed on the redward edge of the 1402 Å line. Although *IUE* data also hint at a broadening on this side of the line, the unconvincing dual Gaussian fits as revealed by *F*-tests, and the extreme narrowness of the extra feature in *STIS* data, suggest that this is due to noise and coincidence. The results of these comparisons appear support the validity of the *F*-test in determining the authenticity of putative shifted features

5.2.3.11 REJ 0457-281

The exceptionally low H I column density to this star (1.3×10^{17} atom cm^{-2}), was revealed in the discovery paper by Barstow *et al.* (1994c). Along with G191-B2B, this white dwarf was the first to have phosphorous and sulphur identified in its spectrum (Vennes *et al.*, 1996). Later, Holberg *et al.* (1998) showed that the photospheric Si IV and C IV resonance lines of REJ 0457-281 are accompanied by blue-shifted features (shown in figure 5.13).

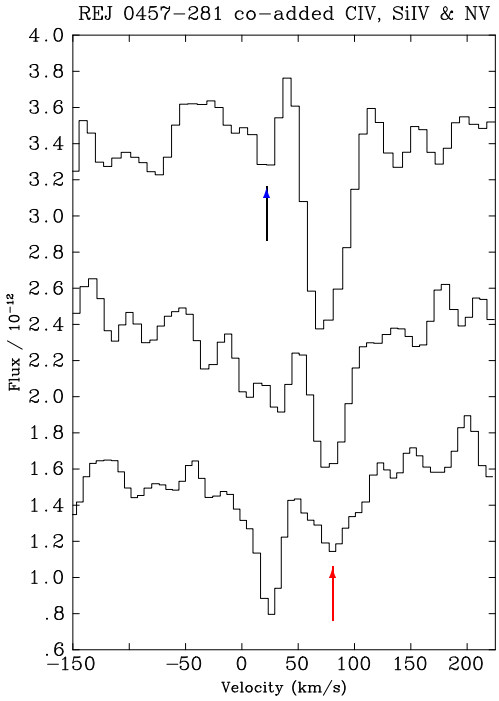

Figure 5.13: From top to bottom, the co-added lines of the N V, Si IV and C IV doublets in REJ 0457-281. Red arrow indicates the approximate photospheric velocity, blue shows the position of the shifted components, present in each species.

Few interstellar and photospheric lines are clearly identifiable in this star, making precise velocity measurements difficult. The ISM velocity estimate of Holberg *et al.* is confirmed, but somewhat higher photospheric velocities are derived. Co-addition of the C IV doublet lines clearly reveals two velocity components: one at 22.5 ±1.39 km s^{-1}, and the photospheric component at 81.26 ± 2.65 km s^{-1}. A curve of growth analysis for the

non-photospheric components suggests log N (C IV) $\approx$ 14.26 with a Doppler parameter $b \approx 4$ km s^{-1}. For the co-added Si IV doublet, corresponding velocities are 19.08 $\pm$ 4.31 km s^{-1} and 80.65 $\pm$ 1.38 km s^{-1}. Although multiple velocity components are not clear in the N V doublet, there is, nevertheless, evidence to suggest that they are present (figure 5.13). The 1238 Å N V line is a narrow, well defined feature at 76.33 $\pm$ 4.78 km s^{-1}, accompanied by a weaker blueshifted feature at 16.55 $\pm$ 4.61 km s^{-1}. The main 1242 Å line has a similar velocity (76.91 $\pm$ 4.38 km s^{-1}), but shows only tentative evidence for a blueshifted component.

From these data, a weighted average is computed for the photospheric and blueshifted velocity components, suggesting $v_{\rm phot}$ = 76.91 $\pm$ 0.83, (c.f. 69.60 $\pm$ 1.97 from Holberg *et al.*), and $v_{\rm shift}$ = 21.76 $\pm$ 1.27. Thus, the estimated velocity shift of the blueshifted features relative to the photospheric components agrees, within the stated error, with the 53 km s^{-1} value of Holberg *et al.*.

5.2.3.12 PG 1123+189

In the photometric study of white dwarfs by Green *et al.* (2000), this object is one of those listed as having a significant IR excess, suggesting the possibility of a (hitherto unobserved) low mass companion to the star.

The *STIS* spectrum for this object is limited in coverage (1163 – 1361 Å), and has relatively low S/N. However, many interstellar lines are visible in the spectrum, and a value of $v_{\rm ISM}$ = -0.67 $\pm$ 0.06 km s^{-1} is obtained. Although photospheric features are difficult to distinguish in the data, by co-adding the N V lines at 1238 and 1242 Å with those of Ni V between 1250 and 1336 Å in velocity space, a single absorption feature is clearly visible, suggesting a value of $v_{\rm phot}$ = 12.55 $\pm$ 0.53 km s^{-1}. The quality of these data is insufficient to confirm or rule out the presence of non-photospheric features with any degree of confidence.

5.2.3.13 HZ 43

A well studied object, HZ 43 is a member of the group of white dwarfs which can be adequately modeled with an atmosphere devoid of any heavy elements. Several ISM lines are observed, leading to an estimate of $v_{\rm ISM}$ which agrees with that of Holberg *et al.*. Co-addition of the spectrum at the wavelengths of the major N, C, Ni and Si lines fails to reveal any photospheric features. Similarly, co-addition, in velocity space, at the wavelengths of the excited Si transitions (1264, 1265, 1309 and 1533 Å) also shows no new features.

5.2.3.14 REJ 1032+532

This object is the subject of a comprehensive study by Holberg *et al.* (1999a,c). In the current work, the measured value of the primary ISM features, $v_{\rm ISM}$ = 0.835 $\pm$0.205 km s^{-1}, agrees, within error, with that of Holberg *et al.* (1999c). A previously noted secondary component to the Si II 1193, 1260 and 1526 Å lines is found to have a velocity of -30.43 $\pm$1.39 km s^{-1}, also in agreement with the value quoted by Holberg *et al.*. A value of $v_{\rm phot}$ = 38.16 $\pm$0.40 km s^{-1} is determined for the photospheric velocity. In none of the photospheric lines is any compelling evidence found for the existence of secondary components. The excited Si II lines found around some

stars possessing circumstellar clouds (Holberg *et al.*, 1995b) are absent, and a search for the ultra-high ionisation species C V, observed in other cases of mass loss, was unsuccessful.

5.2.3.15 REJ 2156-546

This object is considered by Barstow *et al.* (1997a) and Marsh *et al.* (1997a). Barstow *et al.* determined limits to the heavy element abundance in REJ 2156-546, and described this object as being similar to HZ 43 in having a reasonably pure H atmosphere. The *STIS* spectrum of REJ 2156-546 shows clear interstellar lines, indicating $v_{\rm ISM}$ = -8.39 ±0.176 km s^{-1}. These new, high resolution data also appear to show features due to photospheric material. The lines are weak, and unambiguous identifications are limited to the strong resonance doublets of Si IV and C IV, although there may be features from N V and Ni V at the detection limit. To obtain a reliable value for $v_{\rm phot}$, the Si IV lines (1393 & 1402 Å) were co-added in velocity space, producing a clear feature at -17.79 ±1.33 km s^{-1}, with an equivalent width of 11 mÅ. Co-addition of the C IV doublet, however, appears to reveal *two* features (figure 5.14). The first, at -20.71 ±0.80 km s^{-1}, is weak (4.7 mÅ), and very close to the supposed value of $v_{\rm phot}$. The dominant second component lies at -1.65 ±0.764 km s^{-1}, and has an equivalent width of 20 mÅ. The weighted average of putative photospheric features produces a value of $v_{\rm phot}$ = -19.94 ±0.68 km s^{-1}.

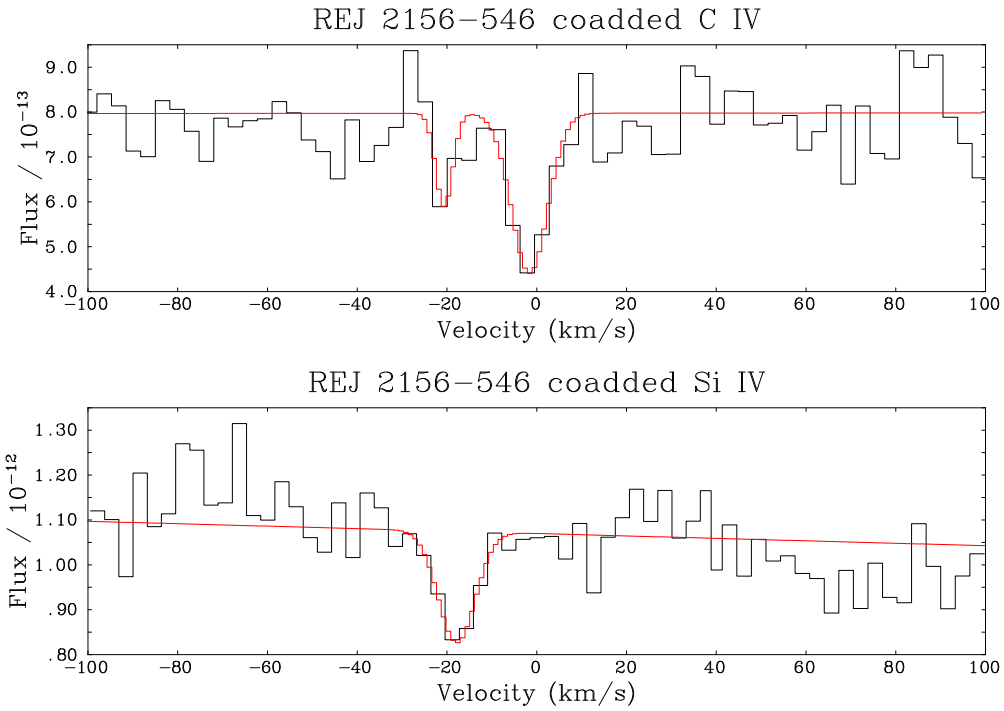

Figure 5.14: Co-added Si IV and C IV features in REJ 2156-546, with Gaussian fits overlaid.

It is tempting to cite REJ 2156-546 as another example of a white dwarf exhibiting highly ionised features that are redshifted with respect to the photosphere. That features from Si IV and C IV are present in the co-added spectrum would not appear to be contentious. However, the proposed C IV feature lying at a similar velocity to the single Si IV line is admittedly weak, and spectra of improved S/N will be required before these results can be regarded as incontrovertible. Nevertheless, if it is assumed that the object is devoid of any non-photospheric features, whether blue- or redshifted, then the relatively large difference in velocity between the Si IV line and the dominant C IV

feature (approximately 16 km s^{-1}) is somewhat difficult to explain. Clearly, this is an object deserving of further attention.

5.2.3.16 PG 1057+719

This object (alternative ID REJ 1100+713) is also included in the photometric study of white dwarfs by Green *et al.* (2000), although unlike PG1123+189, no significant IR excess was detected. It is a reasonably well studied object, and belongs to the low opacity, metal poor class which includes the majority of DA white dwarfs. Holberg *et al.* (1997b) presented a study of this star and REJ 1614-085 (see below). Their results revealed no signs of circumstellar features.

The current survey confirms the results of Holberg *et al.*, revealing no shifted features in the *GHRS* data. Co-addition of the ISM lines results in $v_{\rm ISM}$ = -2.89 $\pm$0.69 km s^{-1}. As expected for a low EUV opacity object, no significant photospheric lines are observed. To detect any signs of photospheric features, a series of 10 Å - wide sections were extracted from the data, each centred on the rest wavelength of one of the lines of the N V, C IV and Si IV resonance doublets. The sections were then transformed into velocity space, and co-added. The presence of barely-detectable quantities of N, C and Si might then be expected to produce a noticeable reduction in continuum level around the photospheric velocity. The co-added data does indeed reveal a feature, with a velocity of 75.35 $\pm$ 2.59 km s^{-1}, consistent with the value of $v_{\rm phot}$ = 76.1 $\pm$3 km s^{-1} determined from Balmer line fitting. However, as indicated by Holberg *et al.*, weak individual features found near the expected positions of these lines show a considerable spread in velocity, casting some doubt on their authenticity, and hence the significance of this co-added feature must not be over-stated.

5.2.3.17 REJ 1614-085

Holberg *et al.* (1997b) found the amount of Si in the spectrum of REJ 1614-085 to be an order of magnitude under-abundant compared to the predictions of radiative levitation calculations, while N appears to be three orders of magnitude over-abundant. Two velocity components were observed in the line of sight ISM, but most significant for the current work is the result that the lines of the C IV and Si IV doublets exhibit weak blueshifted features, as illustrated in figure 5.15.

Results from this study suggest that the primary ISM component lies at a velocity of -29.56 $\pm$ 0.33 km s^{-1}, and the secondary component at +48.64 $\pm$ 1.15 km s^{-1}. These values compare reasonably well with those of Holberg *et al.*, who find velocities of -27.05 $\pm$ 1.5, and +47.40 $\pm$1.50 km s^{-1} respectively. Similar agreement with the earlier study is also found when considering the photospheric and blueshifted features. The photospheric velocity is found to be $v_{\rm phot}$ = -37.313 $\pm$0.401 km s^{-1}, in excellent agreement with Holberg *et al.*. As recorded previously, no clear evidence exists for a secondary component to the photospheric N V lines, although it should be noted that the centroid positions of Gaussian fits to these lines are found to differ by approximately 5 km s^{-1}. In the case of the Si IV doublet, the secondary components are shifted by -40 km s^{-1} relative to the primary features, as determined by Holberg *et al.* (1997b); for the C IV doublet, this figure is -29 km s^{-1}, compared to the figure of -25 km s^{-1}

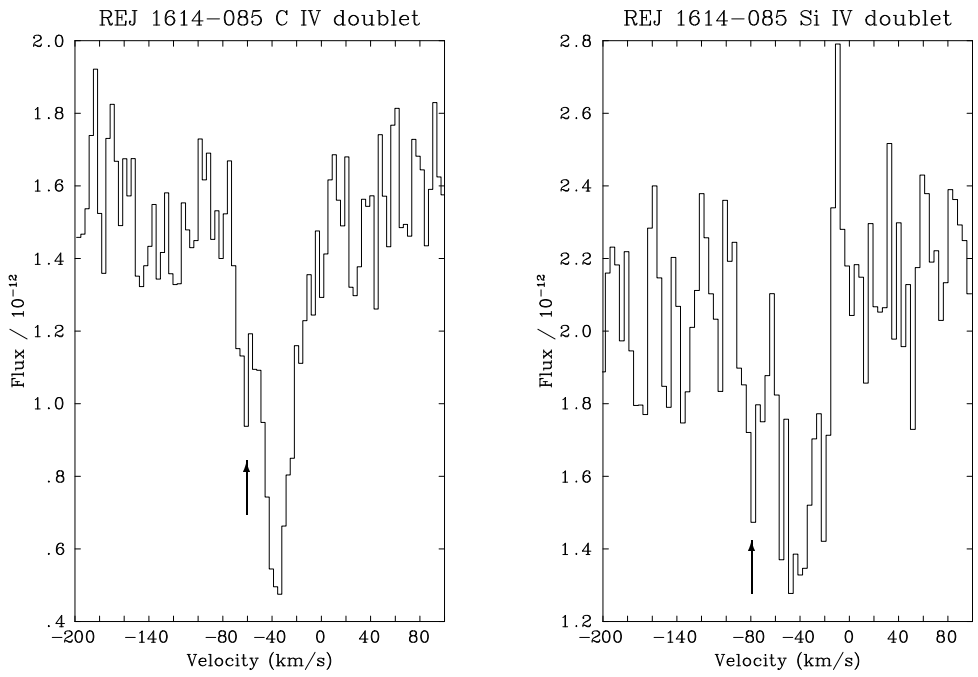

Figure 5.15: Co-added lines of the C IV (left) and Si IV (right) doublets in REJ 1614-085, in velocity space. The blueshifted components previously noted by Holberg *et al.* (1997b) are indicated by arrows.

quoted by Holberg *et al.* (1997b). This apparent discrepancy is most likely to be a result of the different positions chosen for line demarcation in the two studies. A curve of growth analysis performed on the shifted C IV features suggests log N (C IV) $\approx$ 13.5, and the Doppler parameter $b \approx 2$ km s^{-1}, though with only two data points, these values are particularly poorly constrained, and must not be over interpreted.

The data set used in the current work is identical to that analysed by Holberg *et al.*, and no new features have been revealed in this revisit.

5.2.3.18 GD 394

GD 394 is a particularly unusual star. It is one of the few white dwarfs found to be photometrically variable in the EUV, though no signs of spectroscopic variation have been detected. Also included in the study by Holberg *et al.* (1997b), and in contrast to REJ 1614-085, GD 394 has an extreme overabundance of Si compared with model predictions. As Dupuis *et al.* (2000) state, this extreme Si abundance, and the observed variability, give a unique status to GD 394. Dupuis *et al.* present spectroscopic and timing analyses of GD 394, which suggest the presence of a large EUV-dark spot on the surface of the star, sharing the stellar rotation period of 1.150 days. Episodic accretion is proposed as the source of this spot, with a (hypothetical) magnetic field concentrating accreted material onto the magnetic poles. No evidence exists for the presence of a magnetic field in GD 394, though only upper limits can currently be placed on the strength of any such field. A further difficulty in explaining these observations arises from the fact that GD 394 appears to be an isolated star, and hence no obvious candidate exists for the source of accreted material, other than the immediate stellar neighbourhood.

The star has received much attention in multi-waveband studies. Early results suggested that the velocity of Si III and Si IV lines in the spectrum differed considerably from the established radial velocity, and that these lines were therefore of a circumstellar origin. It was also suggested that the absence of any observable Si II features in *IUE* data, which models predicted would be present, represented further evidence for the non-photospheric nature of the heavy elements. However, Barstow *et al.* (1996) demonstrated that the previous radial velocity measurement, obtained from the Balmer lines, was in error, and a revised value was obtained, more consistent with the velocities found for the Si features. Furthermore, by using the latest NLTE models available at the time, Barstow *et al.* (1996) showed that the predicted abundance of photospheric Si would yield Si II line strengths within the noise of the *IUE* spectrum, and hence the absence of Si II features did not require a non-photospheric solution. Interestingly, Dupuis *et al.* (2000) report no convincing time dependence of the Si abundance; three optical spectra from ground based instruments show a factor of 10 enhancement in the Si abundance, though these observations represent only a small fraction of the total number of spectra included in their study. Chayer *et al.* (2000) report the first firm detection of heavy elements other than Si in the spectrum of GD 394, with spectra from the Far Ultraviolet Spectroscopic Explorer (*FUSE*) showing lines of Fe III and P V in the photosphere, as well as a large number of Si III and Si IV lines.

Values of $v_{\rm ISM}$ = -7.28 ± 1.42 and $v_{\rm phot}$ = 28.75 ± 0.91 are obtained in this work for the velocity of ISM and photospheric features respectively. As reported by Holberg *et al.* (1997b), the inventory of photospheric lines is dominated by Si III, with additional contributions from the Si IV doublet. Holberg *et al.* also observe photospheric Al III lines at 1854.7159 and 1862.7900 Å. However, C IV and N V are conspicuous only by their absence; co-addition of the data for these wavelengths reveals no trace of features.

No record exists, in recent literature, of circumstellar features in the spectrum. The *IUE* data reveal no sign of C IV or N V, and *GHRS* data are available only for the ranges 1290 – 1325 Å and 1383 – 1419 Å, which do not include these ions. However, many Si lines are visible in the higher resolution *GHRS* data, and neither individual features or the co-added profiles of all visible Si lines show any form of asymmetry or other qualities which may indicate the presence of circumstellar features. GD 394 is therefore one of the few stars in this survey for which it can be stated that no shifted features exist, at the resolution of currently available data.

5.2.3.19 GD 153

Another example of a star which may be modeled with a pure-H atmosphere, GD 153 is a frequently observed standard star. It is unsurprising that no obvious photospheric features are observed in the *IUE* spectrum of this star, although several ISM lines are recorded, indicating a value of $v_{\rm ISM}$ = -8.424 ± 2.683 km s^{-1}. This velocity agrees with that obtained by Holberg *et al.* (1998).

While individual photospheric lines are not observed, co-addition of spectral regions corresponding to the wavelengths of the principal resonance doublets (C IV, Si IV and N V) in velocity space reveals an interesting, though weak, feature around 12.5 km s^{-1}. This feature, shown in figure 5.16, may be worthy of further investigation, but additional data with higher S/N will be required before a more positive identification can be made.

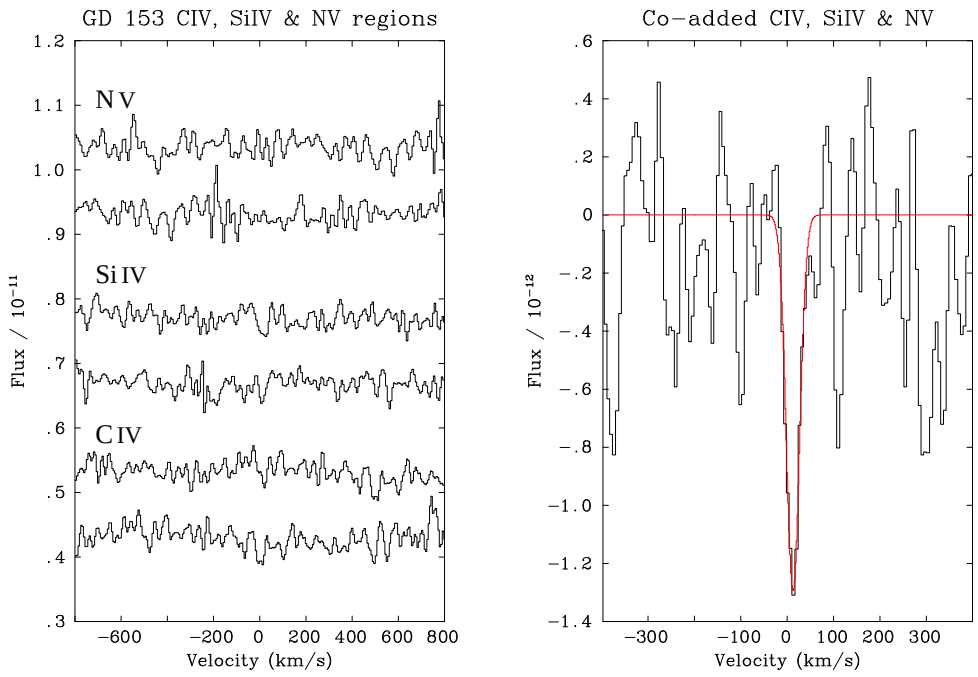

Figure 5.16: Left panel: regions of the GD 153 spectrum corresponding to the resonance doublets of C IV, Si IV and N V. Right panel: co-addition of these regions (in velocity space) revealing a possible, weak absorption feature at 12.45 $\pm$ 2.08 km s^{-1}. A single Gaussian profile is shown fitted to this feature for clarity.

5.2.3.20 GD 659

Both *IUE* and *STIS* data are available for this star, although the *STIS* spectrum is of limited coverage (1160 – 1357 Å). The ISM velocity determined from the *IUE* data ($v_{\rm ISM}$ = 12.33 $\pm$ 1.52 km s^{-1}) agrees with that of Holberg *et al.* (1998), while the *IUE*-based photospheric velocity appears to be somewhat lower than previously quoted ($v_{\rm phot}$ = 33.51 $\pm$ 1.03 km s^{-1}, c.f. 40.31 $\pm$ 1.83 km s^{-1} from Holberg *et al.*). Note that, as described in section 5.1.2, these features were, until recently, attributed to circumstellar material, and are listed accordingly by Holberg *et al.*.

Since these measurements were made with identical data sets, this discrepancy must be ascribed to differences in choices of continuum levels and line boundaries used during the measurement process. However, the available *STIS* data also point to a lower photospheric velocity, with $v_{\rm phot}$ = 34.28 $\pm$0.17 km s^{-1}, in agreement with the *IUE* estimate made in this study. Furthermore, the *STIS* ISM velocity is also lower than the *IUE* value, at $v_{\rm ISM}$ = 9.77 $\pm$ 0.22 km s^{-1}. These *STIS* velocities, based on higher resolution data with better S/N, are adopted for GD 659 in table 5.2. Although the resonance doublets of N V, Si IV and C IV are clearly visible in the *IUE* data, the resolution is insufficient to observe well defined Gaussian profiles, and thus the sensitivity to any non-photospheric components is low. However, the profiles appear to be narrow, ruling out any obvious multiplicity in these lines. More significantly, the *STIS* data show the lines of the N V doublet as narrow and symmetrical, effectively ruling out the existence of non-photospheric N V components.

One interesting feature, clearly visible in the C IV 1548 Å line, though present also in the 1550 Å line, is a weak feature near 0 km s^{-1} (figure 5.17). Fitting a double Gaussian to the co-added C IV lines, velocities of 36.74 $\pm$ 2.56 km s^{-1} (primary), and -2.97 $\pm$ 3.00 km s^{-1} (secondary) are obtained. The secondary component is

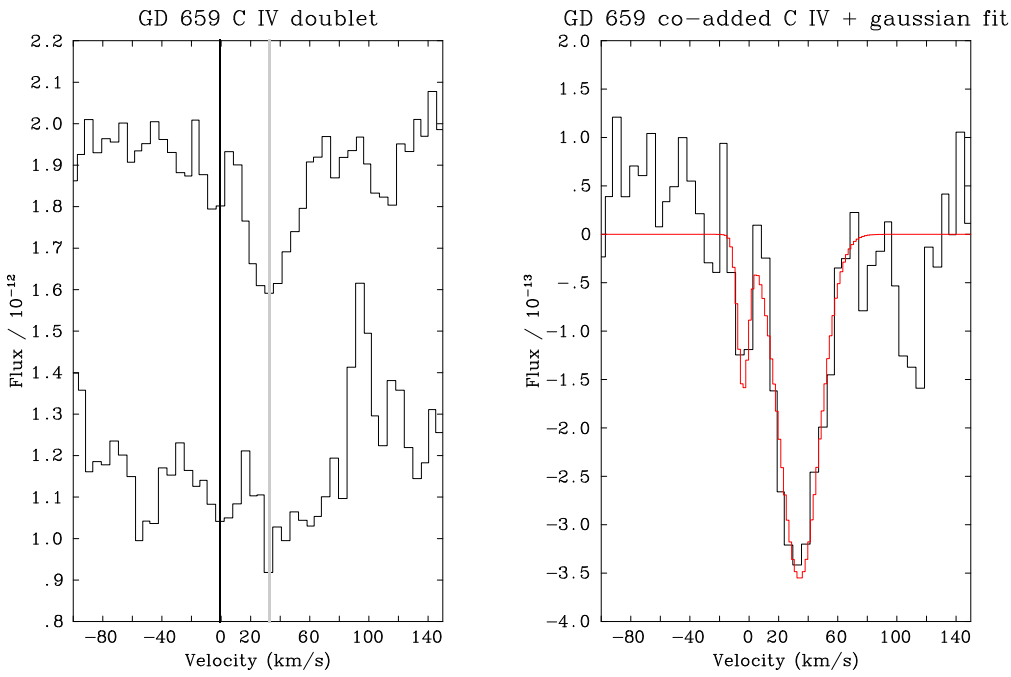

Figure 5.17: Left: the 1548 Å (top) and 1550 Å (bottom) C IV features in GD 659. Gray lines indicate the position of a possible secondary component near 0 km s^{-1}, and the primary photospheric line. Flux levels have been adjusted by a constant to allow plotting of features in the same panel. Right: co-addition of the C IV features, with a best-fit double Gaussian profile overlaid.

weak (with an equivalent width of 6 mÅ compared to 36 mÅ for the photospheric component), and is of comparable strength to scatter in the adjacent continuum regions. Although an *F*-test indicates that a dual Gaussian fit is preferred over a single component at the 94% confidence interval, the similarity between this feature and the natural scatter in the data suggests that this is simply noise. However, high resolution *STIS* data for this region will be required in order to rule out the existence of shifted components in GD 659 with confidence.

5.2.3.21 EG 102

Holberg *et al.* (1997a) showed that Mg II (4481 Å) and excited Si II was present in the optical spectrum of this cool (T_{eff} = 20,000) star. Since radiative levitation calculations predict that much higher temperatures are required before Mg can be suspended in the atmosphere, observable quantities of this species in EG 102 were interpreted as indicative of ongoing accretion, either from a low mass companion (for which no evidence was found) or from a diffuse interstellar cloud. Later, Holberg *et al.* (1998) analysed the *IUE* NEWSIPS spectrum of EG 102 and noted the presence of Al II and Al III lines at the photospheric velocity. This observation was also interpreted as being a product of ongoing accretion. Photospheric and ISM velocities determined for EG 102 in this work are in good agreement with those measured by Holberg *et al.* (1998).

Data provided by Chayer *et al.* (1995b) indicate an abundance of log(N(Al)/N(H)) = -9 for a star with log *g* and T_{eff} similar to those of EG 102. The Al abundance in EG 102 has been estimated by fitting data with a pure H model spectrum into which Al has been added, using the code SYNSPEC. After smoothing the output spectrum to the resolution of *IUE*, abundances of order log N(Al)/N(H) $= 1 - 5 \times 10^{-8}$ are obtained. These figures are

significantly higher than those suggested by Chayer *et al.*, but as discussed in section 5.1, the results of Chayer *et al.* do not account for stratification of abundances, and the failure of this theory to accurately predict the Al abundance in EG 102 cannot be used to infer the presence of accretion processes in the star.

5.2.3.22 Wolf 1346

The presence of Si, apparently in the photosphere of Wolf 1346, was revealed by Bruhweiler & Kondo (1982) but later questioned by Vennes *et al.* (1991), who noted that discrepancies existed between the velocity of Si II lines and that of the photosphere, and found that abundances determined from the Si II lines were inconsistent with the non-detection of Si III in the *IUE* spectra of this star – observations more suggestive of a circumstellar origin. The problem was resolved by Holberg *et al.* (1996), who revised the photospheric velocity value and used the advanced non-LTE code TLUSTY to derive a Si abundance 0.5 dex lower than that of Vennes *et al.*, confirming the photospheric nature of the Si lines.

The measured velocities of features normally associated with the ISM appear to fall into two groups, at -16.19 $\pm$ 0.10 km s^{-1} and -7.67 $\pm$ 3.07 km s^{-1}. Interestingly, when considering the velocities of *isolated* features, these groups appear to contain separate species (O I, C II and S II at -16 km s^{-1}, and Si II at -7 km s^{-1}). However, this segregation breaks down when those interstellar Si II features which are blended with photospheric features, are included. For example, the ISM component of the 1260 Å Si II line, lies at -16.73 km s^{-1}.

The photospheric lines (which are limited to Si II and Si III) show a considerable spread in measured velocities (from 19 to 33 km s^{-1}), with the weighted mean value being $v_{\rm phot}$ = 24.32 $\pm$ 1.41 km s^{-1}. Considering this spread in velocities, the reality of the two ISM groupings is questionable. Data from Holberg *et al.* (1998) also show this grouping, though only four ISM lines are recorded (compared to ten in the current study). Holberg *et al.* treat these velocities as belonging to the same group, and give a weighted mean ISM velocity of -14.85 $\pm$ 1.50 km s^{-1}. For the current work, the analogous value is $v_{\rm ISM}$ = -15.38 $\pm$ 0.95 km s^{-1}. Thus, both $v_{\rm ISM}$ and $v_{\rm phot}$ are found to agree with the values presented by Holberg *et al.*.

In addition to the Si features noted by Holberg *et al.*, lines of Al III are clearly visible at the photospheric velocity. These features do not appear to be noted in previous studies of Wolf 1346 (Holberg *et al.*, 1996, 1998). To estimate the Al abundance in Wolf 1346, the 1854 and 1862 Å lines were reproduced adding quantities of Al to a spectrum generated from a pure H+He non-LTE model (N(He) = 10^{-8} N(H)), and the output smoothed to the resolution of *IUE* (~ 0.2 Å FWHM). An abundance of N(Al) = 2.2×10^{-9} N(H) was found to match the observed 1862 Å line well, and is close to the value of $\sim 1 \times 10^{-9}$ N(H) implied by the graphical results of Chayer *et al.*. A greater abundance (N(Al) = 6.0×10^{-9} N(H)) was required to match the 1854 Å feature; however, the region around this line exhibits unusual structure, possibly due to instrumental effects (although the data are not flagged as being suspect). Note that the models used to determine these abundances are *not* stratified, and hence these values are likely to be revised considerably when suitable stratified models become available. The aluminium lines and synthetic spectrum are illustrated in figure 5.18.

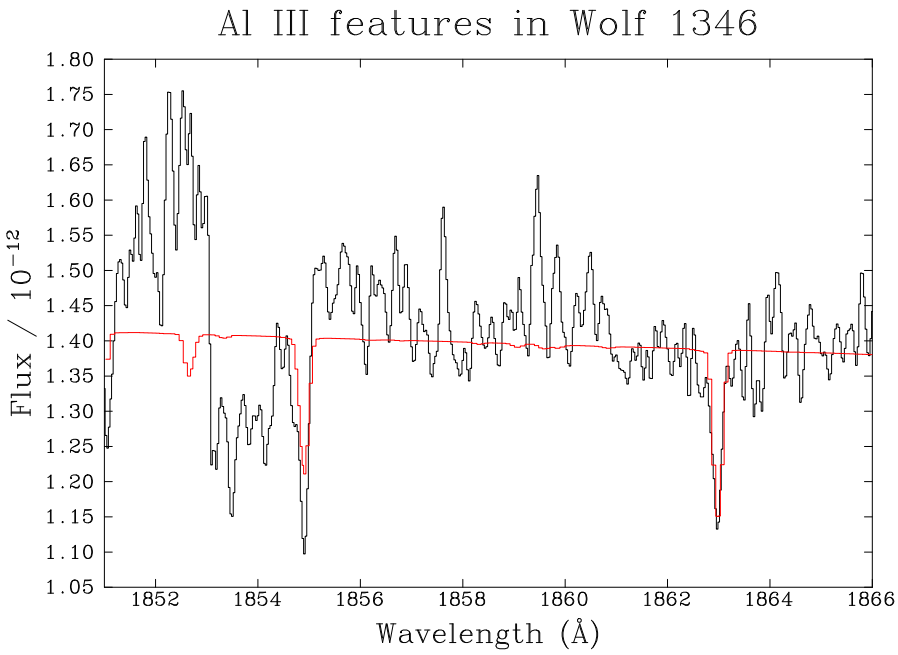

Figure 5.18: 1854 & 1862 Å Al III lines in Wolf 1346, with model spectrum superimposed. The Al abundance inferred from the 1862 Å line is approximately 2.2 $\times 10^{-9}$ N(H). Structure in the continuum level around the 1854 Å line complicated abundance measurements using this feature.

5.3 Discussion

The velocities of interstellar, photospheric and non-photospheric features (if detected) have already been presented in table 5.2. Of the twenty two stars in the current sample, four were previously known to possess features from highly ionised species at non-photospheric velocities (this description is more acceptable than "circumstellar", since the nature of such features is still a subject for discussion). These stars are Feige 24 (a known binary system), REJ 0457-281, G191-B2B and REJ 1614-085. In addition, the relatively cool star EG 102 is believed to be accreting material from its surroundings, as indicated by the presence of Mg II and the over-abundance of Al III in the spectrum.

As a result of this survey, three new DA white dwarfs may be added to the list of those exhibiting unambiguous, highly ionised components at non-photospheric velocities: REJ 1738+665, REJ 0558-373, and WD 2218+706. A fourth object, REJ 2156-546, shows features which may also be interpreted as non-photospheric, although data of improved S/N will be required before this observation can be confirmed. Further, the data suggest that Feige 24 may possess a hitherto unrecognised tertiary velocity component, visible in the C IV doublet and redshifted with respect to the photospheric velocity. A weak blueshifted component in GD 659 is also suggested, though this is exceedingly faint, comparable with the structure of adjacent noise, and hence regarded as a tenuous identification until further data become available. Table 5.3 lists, for each of the stars exhibiting circumstellar features, which ions these features are found in. It is apparent that observations of circumstellar features are restricted to resonance transitions, and are most common in the C IV 1548, 1550 Å doublet (the resonance lines are most strongly coupled to the stellar radiation field, and hence are more susceptible to radiative levitation).

Star	Species
REJ 1738+665	**C IV, Si IV,** N V, O V.
REJ 0558-373	**C IV.**
WD 2218+706	**C IV, Si IV.**
Feige 24	**C IV.**
G191-B2B	**C IV.**
REJ 0457-281	**C IV, Si IV,** N V.
REJ 2156-546	C IV.
REJ 1614-085	**C IV, Si IV.**
GD 659	C IV.

Table 5.3: Ionic species contributing to observed or suspected circumstellar features. Ions responsible for principal features (i.e. those which are clearly identifiable without the need for co-addition) are indicated in bold; other species should be regarded as tentative identifications.

5.3.1 The importance of high resolution, high S:N data

Comparison between tables 5.1 and 5.2 reveals an interesting observation: of the eleven *IUE* spectra considered in this study, only one (REJ 0457-281) shows signs of highly ionised, non-photospheric components. In contrast, five out of the eleven available *STIS* spectra reveal such features (with a further detection in one of the three available *GHRS* spectra). The low number of detections in *IUE* data is not surprising, given the generally low signal-to-noise ratio of the instrument, and the fact that its resolution (0.08 Å at 1400 Å) is equivalent to a velocity of 17 $\mathrm{km\,s^{-1}}$ (compared to $\sim$ 3.2 $\mathrm{km\,s^{-1}}$ with the *STIS* E140M grating, and $\sim$ 1.28 $\mathrm{km\,s^{-1}}$ in the E140H configuration). The non-detection of circumstellar components in *IUE* data should therefore be regarded as placing an upper limit on the velocity of any shifted features, rather than being evidence of absence. *STIS* data may yet reveal non-photospheric features in these objects.

The need for consistently high resolution data with adequate S/N, covering *all* stars in follow-up studies is clear. Consider the case of G191-B2B discussed earlier, in which only the highest resolution *STIS* data were able to show secondary features in the ISM lines (and hence reveal a possible connection between the circumstellar components and the local ISM). These features were not observed in the *STIS* E140M data. However, all of the *STIS* spectra included in this survey were acquired in the E140M configuration. This raises the possibility that more stars in the current sample possess highly ionised non-photospheric features, albeit at smaller velocity differentials to the photospheric components, and that even the resolution of available *STIS* data is simply insufficient to reveal them. Alternatively, is conceivable that other stars possess circumstellar features, but that these components are extremely weak, and are hidden within the noise of existing data. In this case, the availability of instrumentation with higher throughput, producing data of superior S/N, will be vital in detecting these features. Restricting this discussion to currently available facilities, it is clear that only when *STIS* data (ideally from the E140H configuration) are available for all stars in this sample, will a more comprehensive study of the distribution of circumstellar features in white dwarfs become possible.

5.3.2 Influence of position and intervening ISM column

5.3.2.1 Spatial distribution

The distribution of stars included in this survey is depicted in figure 5.19; no correlation is apparent between the presence of circumstellar features, and the position of objects on the sky. Since the sample stars encompass a relatively wide range of distances (between approximately 14 and 436 pc), the absence of such a positional dependence is not surprising.

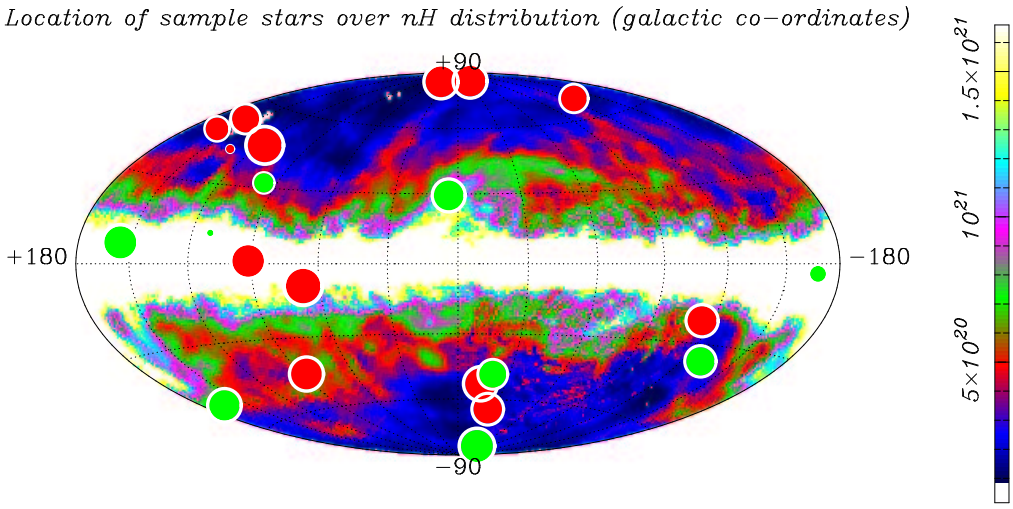

Figure 5.19: The distribution of stars included in the sample, plotted in galactic coordinates. Green symbols indicate stars in which circumstellar features are observed, with all other objects plotted in red. Symbol size indicates distance (larger = closer). Objects are plotted over the galactic H I map of Dickey & Lockman (1990) (units are cm^{-2}).

5.3.2.2 ISM column density

Determination of ISM column densities to objects may be achieved by fitting models to the observed ISM Ly-α profile (after removing the stellar contribution to line+continuum using a stellar model), as demonstrated by Barstow *et al.* (1994c) and Holberg *et al.* (1999c). Alternatively, absorption by an intervening column may be included as free parameter in spectral models, which are fitted to observations using χ^2 reduction techniques (e.g. Barstow *et al.*, 1999b). These methods provide the *average* column density (i.e. they are insensitive to "clumping" along the line of sight, which would only be resolved by analysis of multiple velocity components in each ISM feature).

As an extension to this simplification, it may be assumed that, *ceteris paribus*, a more distant star will be observed through an intervening column, N(H I), of greater density. For the purposes of this study, the figure of interest is therefore the volume density n(H I) along the ISM column, where, in the general case,

$$N\left(\mathrm{H\,I}\right) = \int_0^s n\left(\mathrm{H\,I}\right) ds \ , \tag{5.5}$$

and where s is the distance to the star. For a homogeneous column, $n(\mathrm{H\,I}) \approx N(\mathrm{H\,I})/s$.

A correlation may be sought between the volume density of the intervening ISM column to a star, and the existence or absence of circumstellar features around that object. Previously determined column densities are available for many of the sample stars, while approximations may be made for others using the synthesis maps of Frisch & York (1983), and the contour maps of Paresce (1984). These columns are listed in table 5.4, showing that a relationship between circumstellar features, and the average density of interstellar material along the line of sight, is not observed. For example, both REJ 1738+665 and REJ 0457-281 possess clear circumstellar features, yet their line of sight ISM volume densities are significantly lower than objects without similar features.

Star	N(H I) (cm^{-2})	n(H I) (cm^{-3})	Reference
REJ 1738+665[a,*]	$< 5.0 \times 10^{18}$	$< 6.7 \times 10^{-3}$	Barstow *et al.* (1994b)
REJ 0558-373*	$1 \rightarrow 5 \times 10^{20}$	$1.1 \rightarrow 5.5 \times 10^{-1}$	Frisch & York (1983)
REJ 2214-492	5.8×10^{18}	2.73×10^{-2}	Wolff *et al.* (1998)
REJ 0623-371	5.0×10^{18}	1.67×10^{-2}	Wolff *et al.* (1998)
WD 2218+706*	$> 10^{21}$	$> 7.4 \times 10^{-1}$	Frisch & York (1983)
Feige 24*	3.25×10^{18}	1.35×10^{-2}	Wolff *et al.* (1998)
REJ 2334-471	8.5×10^{18}	2.65×10^{-2}	Wolff *et al.* (1998)
G191-B2B*	$2.1 \pm 0.1 \times 10^{18}$	1.4×10^{-2}	Barstow *et al.* (1999b)
GD 246	$> 1.51 \times 10^{18}$	$> 6.8 \times 10^{-3}$	Fruscione *et al.* (1994)
REJ 0457-281*	$(1.3 \pm 0.7) \times 10^{17}$	3.9×10^{-4}	Barstow *et al.* (1994c)
PG 1123+189	1.10×10^{19}	2.4×10^{-2}	Holberg *et al.* (1999d)
HZ 43	$9.3 \pm 0.1 \times 10^{17}$	4.2×10^{-3}	Barstow *et al.* (1995)
REJ 1032+532	4.2×10^{18}	1.1×10^{-2}	Holberg *et al.* (1999d)
REJ 2156-546*	4.1×10^{18}	1.0×10^{-2}	Holberg *et al.* (1999d)
PG 1057+719	2.75×10^{19}	2.17×10^{-2}	Wolff *et al.* (1998)
REJ 1614-085[a,*]	$\approx 5 \times 10^{20}$	≈ 1.89	Paresce (1984)
GD 394	4.4×10^{18}	2.5×10^{-2}	Barstow *et al.* (1996)
GD 153	6.03×10^{17}	2.68×10^{-3}	Fruscione *et al.* (1994)
GD 659*	3.2×10^{18}	2.0×10^{-2}	Holberg *et al.* (1999d)
Wolf 1346	1.10×10^{18}	2.55×10^{-2}	Fruscione *et al.* (1994)

*Circumstellar features observed or suggested.

[a] Total column (N_H) quoted

Table 5.4: H I column densities for the survey stars, obtained from a variety of previous studies. Data from Frisch & York (1983) and Paresce (1984) should be interpreted as broad estimations only. No data available for REJ 0948+534 or EG 102.

This result should not be surprising. Dupree & Raymond (1983) consider a DA white dwarf with T_{eff} = 60,000K and log g = 8.0, and find that the Strömgren radius ranges from 0.07 pc (for n(H)=10^2 cm^{-3}) to 30.8 pc (n(H)=0.01 cm^{-3}). The work of Dupree & Raymond is, admittedly, rather dated (for example, the heavy element features in white dwarf spectra are attributed to the ionisation of circumstellar material). However, these figures still provide a useful order of magnitude estimate for the sphere of influence of the white dwarf. It could also be argued that the quoted Strömgren radii represent upper limits, since the extra opacity from photospheric heavy elements would be expected to reduce the intensity of the radiation field at specific wavelengths. In either case, the Strömgren radius is typically a small fraction of the distance to the star, and since the distribution of material along the line of sight is unlikely to be homogeneous, the observed average value of n(H I) may not accurately reflect conditions within the Strömgren sphere.

5.3.2.3 The velocity of circumstellar features and the ISM

While the results of Dupree & Raymond (1983) may require revision in the light of more recent research, the possibility of a white dwarf ionising nearby interstellar material must nevertheless be considered. In such a case, highly ionised non-photospheric components may be observed at velocities similar to those of the intervening ISM (although as discussed in the preceding section, the measured interstellar velocity may not reflect that of the cloud component near the star). Depending on the relative velocities of star and ISM, this mechanism can produce both red- and blue-shifted features.

The majority of stars with circumstellar components show little agreement between $v_{\rm shift}$ and $v_{\rm ISM}$, but it is useful to consider the residual value of $|v_{\rm ISM} - v_{\rm shift}|$, as presented in figure 5.20. These data show that in the majority of objects possessing circumstellar features, the difference in velocity between these and the primary interstellar cloud is typically 10 km s^{-1} or less (exceptions being REJ 1614-085 and GD 659). The most interesting cases are found in REJ 1738+665 and G191-B2B, where excellent agreement is found between $v_{\rm ISM}$ and $v_{\rm shift}$, suggesting that the shifted features arise in a Strömgren sphere of material belonging to the primary identified ISM component.

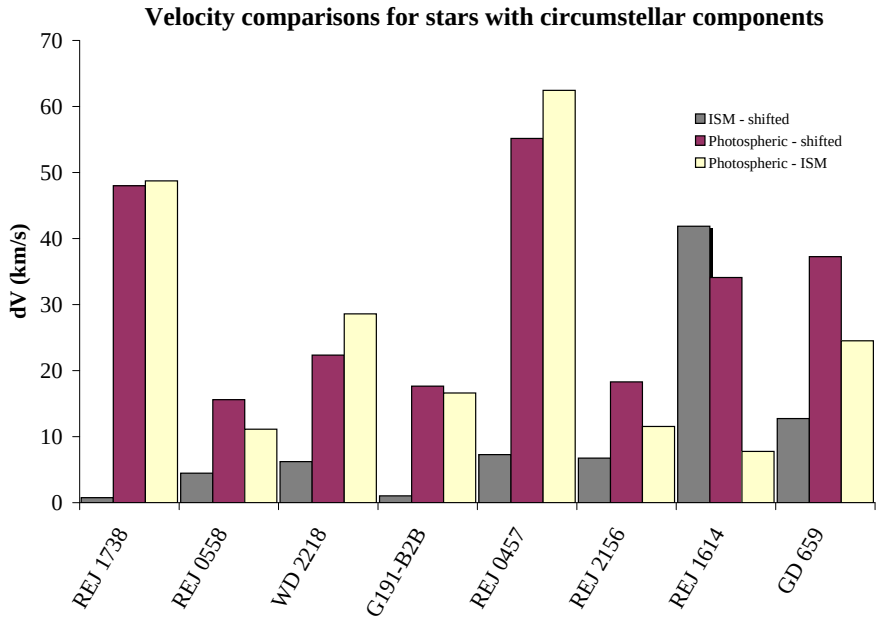

Figure 5.20: Comparison between photospheric, ISM and circumstellar velocities in stars showing highly ionised non-photospheric features (Feige 24 omitted since $v_{\rm shift}$ and $v_{\rm phot}$ vary with orbital position, while $v_{\rm ISM}$ is stationary). This plot also demonstrates small residuals between $v_{\rm shift}$ and $v_{\rm ISM}$ in most other stars, when compared to residuals for $v_{\rm phot}$-$v_{\rm shift}$ and $v_{\rm ISM}$-$v_{\rm phot}$.

More detailed investigations are required before this hypothesis can be confirmed. In particular, a detailed analysis of the ion populations and spectral characteristics of such a system is essential. The code CLOUDSPEC is ideally suited to this task, and has already been applied to a similar problem on a larger scale - that of interstellar absorption of the flux from a starburst galaxy (Hubeny *et al.*, 2000). The case of G191-B2B also acts as a caution against over-interpretation of these results; no correlation between $v_{\rm ISM}$ and $v_{\rm shift}$ would have been recognised if not for the higher resolution data discussed by Sahu *et al.* (1999). Such detailed spectra were unavailable for the present sample, and it is certainly possible that similar correlations with hitherto undetected ISM components will be found in future studies based on E140H grating spectra. Despite the relatively narrow wavelength coverage available with this instrument, the current results justify a comprehensive program of E140H white dwarf observations, possibly

tuned to a bandpass covering the C IV resonance doublet, which is most frequently accompanied by shifted features.

5.3.3 Metallicity and mass loss

MacDonald (1992) presents a detailed theoretical consideration of the interaction between the flow of ISM material around a white dwarf star, and the weak stellar wind. In this work, the rate of mass loss, $\dot{M}$, from the white dwarf is estimated using theory developed by Abbott (1982), *viz.*

$$\dot{M} \approx 2 \times 10^{-15} \left(\frac{L}{L_{\odot}} \right)^{2} \frac{Z}{0.02} M_{\odot} \ \mathrm{yr}^{-1}, \tag{5.6}$$

where Z is the metallicity, relative to solar abundances, of a star with luminosity L and mass M.

At first sight, equation 5.6 provides an apparently invaluable means for estimating the rate of mass loss for stars in the current sample, and hence predicting the likelihood of observing circumstellar features. However, caution must be exercised, since the work of Abbott is concerned with the envelopes of O- to G-type stars, and results are found to be most successful for OB stars. Conversely, the theory does not explain mass loss rates in Wolf-Rayet stars, which are somewhat different in structure.

In addition to questioning the suitability of this theory for objects other than those on the main sequence, serious difficulty is encountered when attempting to quantify metallicity in a consistent and meaningful way. White dwarf metallicities have previously been expressed in terms of a reference star of similar type - for example, Wolff *et al.* (1998) express the metallicity of a sample of 20 white dwarfs relative to the abundances in G191-B2B. Expressing metallicity in terms of a star with similar structure may be useful for comparative purposes. However, the theory of Abbott is formulated in terms of solar abundances (since it deals mainly with main sequence objects). In this case, the internal structure and physics are significantly different to those of a degenerate object, and the task of defining a "meaningful" metallicity for white dwarfs in terms of solar units, is fraught with difficulty.

The accuracy of numerical results in this section must be viewed with these important considerations in mind. Nevertheless, it is interesting to compare the *relative* mass loss rates of sample objects calculated using equation 5.6, while regarding absolute values with suitable scepticism. Individual abundances have been calculated by Barstow *et al.* (2001b). These values were determined by matching observational data to a synthetic spectrum calculated using SYNSPEC, based on a model of appropriate T_{eff} and log *g* generated by the non-LTE code TLUSTY. This information is available for all objects in the sample except PG 0948+534, and is reproduced in table 5.5. The metallicity parameter, Z, is expressed in terms of solar units, estimated using the solar abundances published by Grevesse & Sauval (1998). For each star, this value is calculated using the general expression

$$Z = \left(\sum_{z>2} A_{*}(z) \right) \left(\sum_{z>2} A_{\odot}(z) \right)^{-1}, \tag{5.7}$$

where $A_{*,\odot}$ is the abundance of the element of atomic number z relative to hydrogen in the star and in the Sun[3] respectively. Only "metals" (elements heavier than He) are included. Note that although equation 5.7 should be evaluated for all elements above He in the periodic table, only clearly identifiable species, as presented in table 5.5, have been considered in this work.

Star	C/H	N/H	O/H	Si/H	P/H	S/H	Fe/H	Ni/H	Z	L	$\dot{M}$
REJ 1738+665*	2.0E-8	3.0E-7	3.0E-7	1.0E-6			4.0E-6	5.0E-7	5.18E-3	12.59	8.21E-16
REJ 0558-373*	8.0E-7	3.0E-7	3.0E-6	2.0E-6	2.0E-8	2.5E-7	1.0E-5	1.5E-6	1.51E-2	4.61	3.22E-16
REJ 2214-492	1.0E-6	7.5E-8	9.6E-7	7.5E-7			1.0E-5	1.0E-6	1.17E-2	9.38	1.03E-15
REJ 0623-371	1.0E-6	1.6E-7	9.6E-7	3.0E-7			1.0E-5	1.0E-6	1.14E-2	11.69	1.55E-15
WD 2218+706*	4.0E-7	1.0E-6	1.0E-5	6.5E-7			2.0E-5	5.0E-7	2.76E-2	9.64	2.56E-15
Feige 24*	1.0E-7	3.0E-7	5.0E-7	3.0E-7			1.0E-5	2.0E-6	1.12E-2	5.86	3.84E-16
REJ 2334-471	2.0E-8	5.0E-7		3.0E-7			1.0E-5	5.0E-7	9.59E-3	2.88	7.97E-17
G191-B2B*	4.0E-7	1.6E-7	9.6E-7	3.0E-7	2.5E-8	3.2E-7	1.0E-5	5.0E-7	1.07E-2	3.16	1.07E-16
GD 246				1.0E-7					8.47E-5	2.23	4.21E-19
REJ 0457-281*	4.0E-7	1.6E-7	9.6E-7	1.0E-7	2.5E-8		1.0E-5	5.0E-7	1.03E-2	1.85	3.53E-17
PG 1123+189									—-	2.75	—-
HZ 43									—-	1.49	—-
REJ 1032+532	4.6E-7	5.0E-5		5.6E-8					4.28E-2	1.03	4.52E-17
REJ 2156-546*									—-	1.06	—-
PG 1057+719									—-	0.64	—-
REJ 1614-085*	4.8E-7	2.5E-4		1.0E-8					2.12E-1	0.43	3.90E-17
GD 394				8.0E-6					6.77E-3	0.45	1.39E-18
GD 153									—-	0.56	—-
GD 659*	2.0E-7	6.3E-4		1.6E-8					5.34E-1	0.24	3.01E-17
EG 102				1.0E-7					8.47E-5	0.03	6.54E-23
Wolf 1346				3.2E-8					2.71E-5	0.03	1.91E-23

*Circumstellar features observed

Table 5.5: Photospheric heavy element abundances of the surveyed stars, determined from far-UV spectroscopy (no data available for PG 0948+534). Note that gaps in the table for those stars up to (and including) REJ 0457-281 are mostly due to the absence of data for a particular spectral range rather than a true absence of the element itself. For the remaining, cooler stars, gaps in the table reflect genuine absence of these species at abundances detectable by *IUE* or *STIS*. From Barstow *et al.* (2001b).

Stellar luminosities quoted in table 5.5 have been calculated from the familiar expression

$$M_\odot - M_* = 2.5 \log \left(\frac{L_\odot}{L_*} \right) \ ,$$

from which

$$L_* = 10^{0.4\{M_\odot - M_*\}} L_\odot \ , \tag{5.8}$$

where $\mathrm{M}_\odot$ represents the absolute bolometric magnitude of the Sun (+4.7), or the star (calculated using the stellar models of Wood, 1995).

No clear correlation is found between $\dot{M}$ and the presence of circumstellar features, although loss rates extend to lower values for objects without these features (figure 5.21). The lowest values are found in the coolest stars, as expected given the dependence of equation 5.6 on luminosity and metallicity. However, it is noted that GD 246 ($\mathrm{T_{eff}}$ = 53,700K) is significantly hotter than REJ 1614-085 ($\mathrm{T_{eff}}$ = 38,500K) despite having an appreciably lower calculated loss rate. While the subset of stars which exhibit non-photospheric components lacks any object with $\dot{M} < 3 \times 10^{-17} M_\odot$ yr^{-1}, (compared to a minimum value of $1.9 \times 10^{-23} M_\odot$ yr^{-1} for those with no circumstellar components), the number of objects in this survey is insufficient to determine the authenticity of a lower limit to the mass loss rates in stars showing highly ionised, non-photospheric components.

[3]Using data provided by Grevesse & Sauval (1998), $\sum_z A(z)_\odot \approx$ 1.18E-3, where z=6, 7, 8, 14, 15, 16, 26 and 28, reflecting the elements considered in table 5.5.

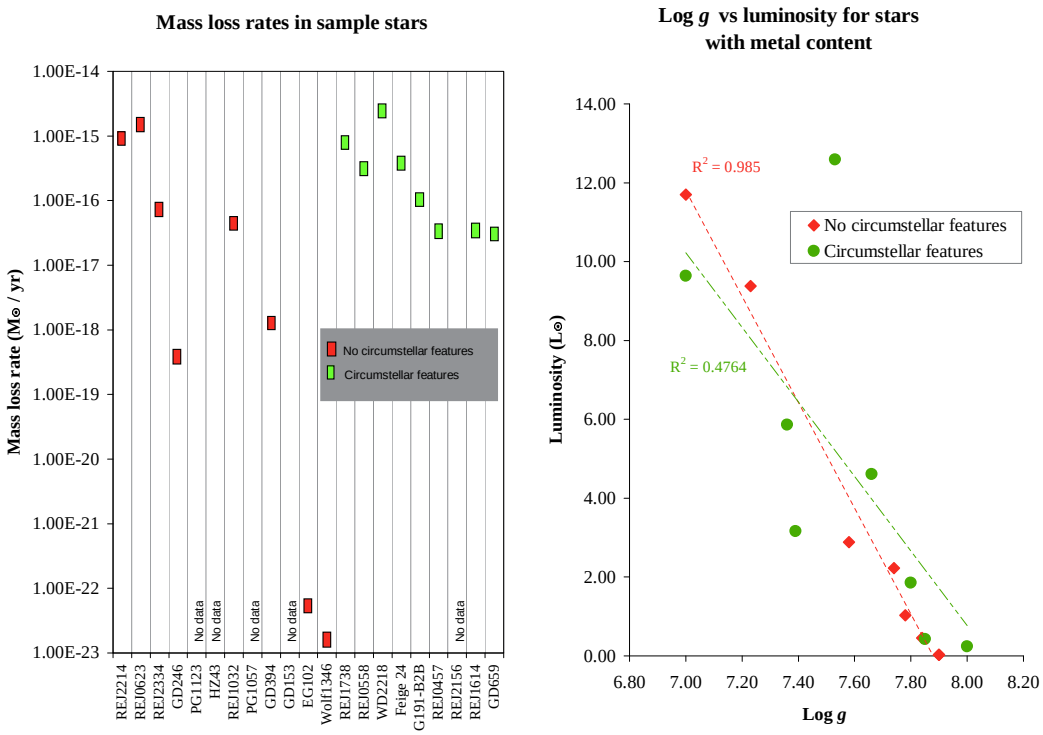

Figure 5.21: Left: calculated mass loss rates for those sample stars containing metals, as defined in table 5.5. Stars for which no metals are present or for which data are unavailable are listed as such. Right: log g plotted against luminosity for stars with known metal content.

5.3.4 Gravitational Redshift

Values for v_{grav}, calculated using equation 5.2, are included in table 5.2. The presence of material in the gravitational potential well of a star provides no explanation for objects in which material appears to be infalling, as in the case of WD 2218+706, Feige 24, REJ 2156-546, and REJ 1614-085. The mechanism may also be ruled out for two further stars, REJ 1738+665 and REJ 0457-281, in which the calculated gravitational redshift is substantially lower than required to explain the velocity of non-photospheric components.

For the three remaining stars, the gravitational redshift is comparable to the velocity difference between photospheric and circumstellar components. However, if the calculated values of v_{grav} are assumed to be reasonable, only circumstellar features in REJ 0558-373 may be explained by the presence of matter inside the gravitational well (at approximately 5 stellar radii from the surface). In the cases of G191-B2B and GD 659, the non-photospheric components differ from v_{phot} by an amount equal to, or slightly greater than, the value of v_{grav}. This suggests that the material lies at a radius greater than that at which gravitational redshifting produces observable changes in line velocity. It is therefore apparent that, with the possible exception of REJ 0558-373, blueshifted features in the spectra of objects in this study cannot be explained by the presence of material within the gravitational potential well of the star.

5.3.5 Non-photospheric material and its relation to planetary nebulæ

The existence, or possible presence, of a planetary nebula (PN) around two of the survey stars has already been addressed (in the cases of REJ 1738+665 and WD 2218+706), though little attention has been paid to the possibility of nebular material around the remaining objects. However, mass loss and the production of a PN as a white dwarf progenitor leaves the AGB, are relatively well accepted processes (though the precise details are certainly not (Langill *et al.*, 1994)). It is therefore pertinent to ask whether the presence of non-photospheric, highly ionised features examined in this work, is consistent with material from a (now ancient) PN around the star[4].

Expansion velocities for PNe are widely available in the literature (e.g. Weinberger, 1989). The study by Napiwotzki & Schönberner (1995) is particularly relevant, since it deals specifically with old planetaries: as such, the central stars are in the advanced stages of transition into the white dwarf area of the H-R diagram. Since most stars in the current study are more highly evolved than those covered by Napiwotzki & Schönberner, average temperatures are cooler, and any nebular material presumably of lower density and more widely dispersed. Direct detection of nebular emission around these stars is therefore difficult, excepting the two cases previously highlighted. Nevertheless, absorption features produced by such material should be observed at velocities consistent with typical PN expansion values. The possibility that circumstellar features discussed in this chapter are of this origin may thus be assessed by comparison with the expansion velocities noted by Napiwotzki & Schönberner.

Figure 5.22 shows the distribution of expansion velocity (in this case plotted against nebula radius) for the objects investigated by Napiwotzki & Schönberner. No data are available for the radius of any PNe which may surround stars in the current survey; however, an analogous velocity can still be derived in the form of the difference between the velocity of circumstellar and photospheric features, as listed in table 5.2. Note that WD 2218+706 (DeHt5) is common to both studies, and in this case the true value of v_{exp}, as determined by Napiwotzki & Schönberner, is considerably different to the *infalling* velocity found in the current work. It is therefore clear that the non-photospheric features of WD 2218+706 discussed in the current study are not produced by the observed planetary nebula (though it must be noted that this result does not rule out the nebula as a *source* of this material).

The observation of features which are redshifted with respect to the photosphere is not incompatible with the nebula hypothesis in general. For example, Tweedy & Napiwotzki (1994) discuss the planetary nebula Sh 2-174 and the white dwarf GD 561 observed on one edge of this nebula. The objects are found at similar distances, and [O III] emission in the nebula is located immediately adjacent to the white dwarf. These observations, the statistical improbability of GD 561 being an isolated white dwarf which happens to be wandering through the nebula, and the difficulty in explaining the existence of a small nebula other than being of PN origin, confirm that GD 561 is indeed the source of the planetary nebula. The distinctly non-spherical morphology of Sh 2-174 is far from unique in studies of old PNe (Tweedy & Napiwotzki and references therein). Severe asymmetries are attributed to interaction between the nebular material and the surrounding ISM through which it moves. Given the location of GD 561 relative to the central region of Sh 2-174, it is clear that the PN material may produce spectral features which are either blue- or red-shifted with respect to the photosphere, depending on the angle from which

[4]The author is indebted to R. Napiwotzki for useful discussions relating to material in this section.

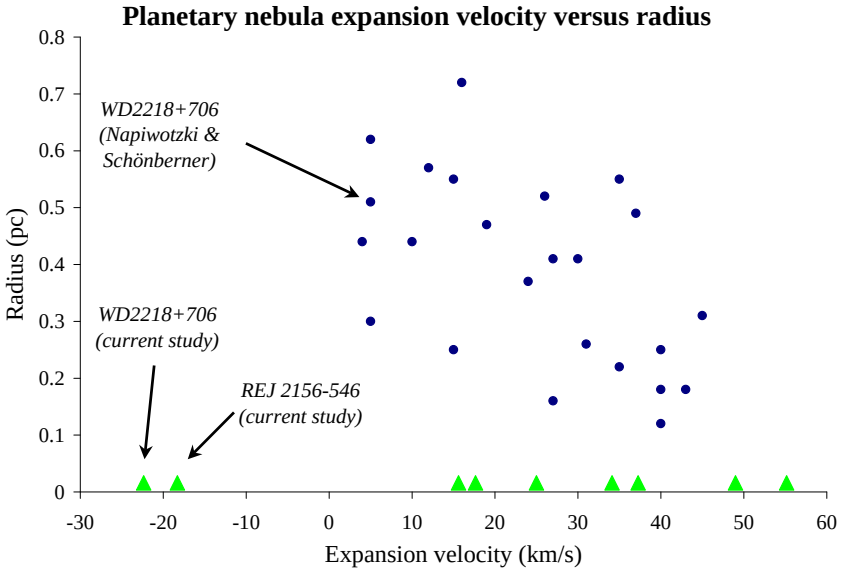

Figure 5.22: Blue points: Nebula expansion velocity v_{exp} plotted against nebula radius, for stars studied by Napiwotzki & Schönberner (1995). Green triangles: $v_{\rm phot}$- $v_{\rm shift}$ for stars in the current work (no values for radius are available). See text for discussion.

the system is viewed. Thus, redshifted features in the spectrum of REJ2156-546 may still be explicable in terms of an undetected, asymmetrical PN.

The similarity between typical PN expansion velocities and the velocity difference between photospheric and shifted components in the current study is shown in figure 5.22. For all but two of the stars in this work, $v_{\rm phot}$- $v_{\rm shift}$ is of a similar order of magnitude as the expansion velocity typical of old PNe. Two stars (WD 2218+706 and REJ 2156-546) are shown with the negative values of $v_{\rm shift}$ discussed above - but the absolute values, $|v_{\rm phot}$- $v_{\rm shift}|$, are consistent with the remainder of the sample. In contrast, radiatively driven winds from the surface of a white dwarf should be of a similar order to the stellar escape velocity, i.e. $\sim$ 1000 km s^{-1} or more (MacDonald, 1992). These results may therefore suggest some form of link between the origin of the non-photospheric absorbing matter, and the old, dispersed PN material surrounding these stars.

The encouraging results of this comparison suggest that further work on the link between highly ionised non-photospheric features, and planetary nebulæ is justified. Although the planetary nebula hypothesis appears to contradict the earlier suggestion that shifted features were related to interstellar material within the Strömgren sphere of a white dwarf, it seems entirely possible that *both* of these mechanisms operate in different objects. Correlating typical PNe densities with the column densities derived from curve of growth analysis might provide further evidence of any relationship between these two apparently separate entities. Unfortunately, this comparison is complicated by the considerable difficulty in estimating the masses of PNe, which arises from uncertainties in the distances to nebulæ, and from the ongoing debate as to whether these objects are (typically) ionisation or mass bounded. In addition, detailed modeling of the interaction between the white dwarf and surrounding material should determine whether stellar radiation alone is sufficient to produce the observed ionisation, or whether additional excitation (perhaps in the form of shock-heating) is required (Napiwotzki, private communication). These investigations lie outside the scope of this thesis, but are nevertheless essential and promise continuation of the work discussed in the preceding pages.

5.4 Summary

- The work described in this chapter is concerned with the detection and interpretation of highly ionised absorption features at non-photospheric velocities, in high resolution UV spectra of hot DA white dwarfs. These features may be indicative of accretion or mass loss in white dwarfs – processes which may explain the non-equilibrium abundances (compared with the predictions of radiative levitation theory) observed in many objects.

- Four of the stars in the sample were previously known to show non-photospheric features: Feige 24, REJ 0457-281, G191-B2B and REJ 1614-085. This work has revealed at least three new objects with multiple components in one or more of the principal resonance lines: REJ 1738+665, REJ 0558-373 and WD 2218+706. A fourth object, REJ 2156-546 also shows some evidence of multiple components, though further observations will be required for their reality to be confirmed.

- The presence of material within the gravitational potential well of a white dwarf is found to be an unsatisfactory explanation for the production of these features.

- Predicted mass loss rates based on the luminosity and metallicity of stars show no correlation with the presence of shifted features. However, these mass loss rates are calculated using theories developed for main sequence stars, and may be inappropriate for application to highly evolved objects. Further, the quantification of metallicity is a highly subjective measurement, and is likely to be a major source of uncertainty in these calculations.

- A possible correlation is observed between the velocity of shifted features and that of the ISM. This is particularly obvious in REJ 1738+665 and G191-B2B, which show very close matches between $v_{\rm ISM}$ and $v_{\rm shift}$. For most of the remaining stars, the difference between these velocities is less than 10 km s^{-1}. Higher resolution observations are required to detect the presence of multiple ISM velocity components, which may reveal further correlations – as demonstrated by the case of G191-B2B.

- An alternative (or additional) source of shifted features may be found in planetary nebulæ. Velocities of shifted features with respect to the photosphere in this study are found to be entirely consistent with the expansion velocities typical of old PNe. By appealing to the irregular morphology of highly evolved nebulæ, both blueshifted and redshifted features may be explained.

- The non-detection of highly ionised non-photospheric features in many of the stars investigated may indicate their absence, but equally, may reflect the limited resolution and signal-to-noise ratio of available data. This is particularly important when considering non-detections in *IUE* data, where velocity differentials of less than 17 km s^{-1} between photospheric and shifted components are below the resolution limit of the instrument, and where the S/N ratio is inferior to that of more modern instruments such as *STIS*. This highlights the importance of acquiring consistently high resolution data for all stars in this and future samples. Three (and possibly four) new identifications of circumstellar features have been made using medium resolution (E140M) *STIS* spectra; these successes demonstrate the value in high resolution studies of this type, and justify an extension of the program to include higher resolution data of improved S/N for an expanded sample of objects.

CHAPTER 6

J-PEX FLIGHT & DATA ANALYSIS

6.1 Introduction

J-PEX WAS SUCCESSFULLY LAUNCHED from the LC-36 Athena rail at White Sands Missile Range, New Mexico, USA, on Wednesday 21st February 2001, at 22:00 hours local time (figure 6.1). In the fifteen minutes which followed, telemetry from the instrument recorded an almost perfect flight, with the accumulation of clear spectral data from G191-B2B being observed in real-time. The Aerojet MK VI-D attitude control system (ACS) maintained spectrometer pointing, achieving drift rates of < 1 arcsec sec^{-1}, and 303 seconds of useful spectroscopic data were acquired (total on-target time was 313 seconds, but 10 seconds were lost due to an erroneous slewing command being issued, and subsequently corrected, from the ground station).

Figure 6.1: Launch of J-PEX 36.195 from White Sands Missile Range. February 21st 2001, 22:00 hrs local time.

Raw output from the *J-PEX* spectrometer consisted of an MCP detector image of the wavelength-dispersed light from G191-B2B, reflected by the four multilayer gratings. Transformation of these data into useful "data products" involves a series of tasks including extraction of numerical data from the image, wavelength calibration, cross-correlation to align the individual tracks, and final co-addition of the tracks. The stages involved in producing a *J-PEX* spectrum of G191-B2B are discussed in section 6.2 of this chapter.

Production of a spectrum is followed by data analysis, in which the scientific goals of *J-PEX* (detection of the presence of helium in the spectrum of G191-B2B and determination of its location) are addressed. This task is accomplished with the aid of stellar models, and is described in section 6.3.

6.2 Data extraction

6.2.1 Raw data

The left panel of figure 6.2 shows raw data acquired during the *J-PEX* flight. The EUV telescope image (labeled) is superimposed on a spectral track (note also the fainter EUV image above the main feature, acquired after the erroneous slew command). Also visible in the image are features due to hot spots, the four principal spectral tracks, and several fainter tracks produced during the slewing operation which was carried out early in the flight. The right panel of figure 6.2 shows the same data, but corrected for instrument pointing using the EUV telescope image. Note the labeling convention adopted for each of the four grating spectra, as indicated in figure 6.2 (the four flight gratings were selected from a larger batch of optics, hence the non-consecutive grating designations).

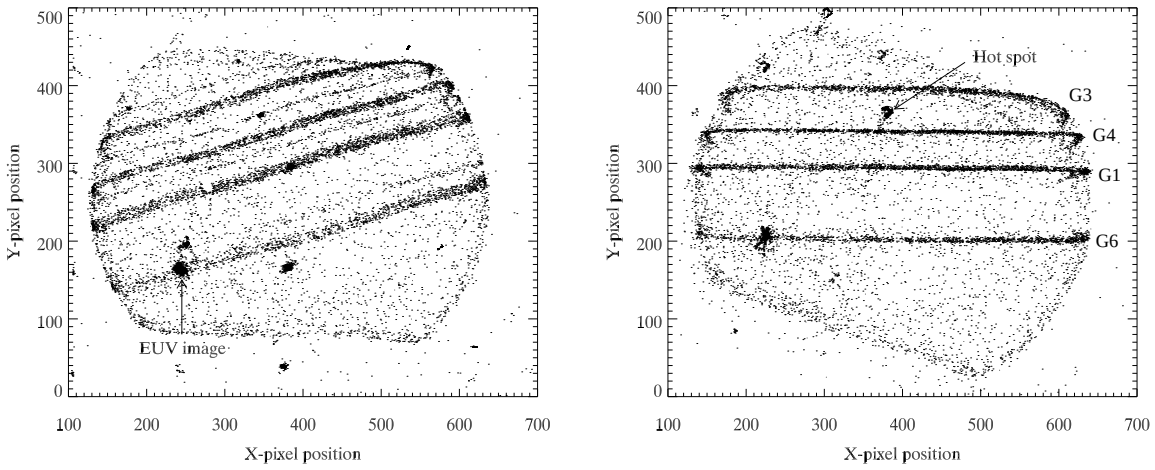

Figure 6.2: Left: raw image, returned from the instrument during flight. Right: identical data after correction for instrument drift, and rotated such that the dispersion axis is horizontal to simplify extraction. Curves near the ends of each spectral track are thought to be due to the influence of E fields around the Vernier anode. In the label convention adopted for the project, the grating/spectral track designations are indicated.

"Aspect reconstruction" was achieved by determining the centroid position of the EUV mirror image as a function of time, using the time tag attached to each MCP event. The resulting displacement-versus-time plot (see figure 6.3) was then used to deconvolve the motion of the instrument from the entire MCP dataset[1]. Note that detector artifacts

[1]This operation was carried out by J.S.Lapington of MSSL, and is not discussed further.

such as labeled, which are fixed in the detector coordinate frame, are trailed following this operation, betraying the deconvolution path. The entire image has been rotated by 17° to align the spectral dispersion axis with the horizontal axis, thus simplifying the extraction task. (The spectral axes are tilted with respect to the major axis of the imaging area due to the rotational orientation of the detector inside the instrument).

6.2.2 Image nonlinearities

Distortion at the ends of each spectral track is evident in figure 6.2. These nonlinearities are believed to be due to the influence of electric fields around the Vernier anode in the MCP detector. The spatial linearity of the detector was evaluated in the laboratory using a pinhole mask (see figure 4.30). This image was then used to construct a linearity matrix which was applied to all subsequent images, with the aim of removing large scale nonlinearities in the data. No evidence of the distortions shown in figure 6.2 was found at this time; however, the spacing (pitch) of the linearity mask was relatively coarse and may have been inadequate to reveal these particular effects. Further, the immediate electromagnetic environment of the detector in the laboratory configuration is different to that encountered inside the spectrometer, where high voltage power supplies and other components are found in close proximity to the sensitive imaging electronics. Hence, the possibility remains that these nonlinearities are of an electromagnetic nature, and were introduced after the linearity mask was imaged, when the detector was installed in the payload.

The dispersion linearity of the gratings is less questionable. All gratings were tested at the Brookhaven National Synchrotron Light Source, USA, prior to the February 2000 flight (Kowalski & Cruddace, Private Communication); no evidence of non-linearities was detected as a result of these tests. During the optical alignment phase of integration work at NRL, excellent registration was observed between Penning source emission features from each grating. This suggests that unless each grating incorporates identical nonlinearities, then the effects observed in figure 6.3 do not originate in the spectrometer optics. A final observation which tends to exonerate the gratings is that the distortions are visible only at the boundaries of the imaging area, while the wavelength range contained within each band is different. For the nonlinearities evident in figure 6.3 to reside in the gratings, the eight highly localised regions of distortion must all coincide with the boundaries of the imaging area. This explanation is considerably less plausible than the effects of strong $\underline{\mathrm{E}}$ fields in regions of high potential difference around the imaging anode and electronics, during times when the detector is installed in the spectrometer.

6.2.3 Histogram extraction

With the dispersion axis of each spectral track being parallel to the horizontal coordinate axis (after rotation), the x location of each event is related to wavelength. Histograms were produced, using bespoke codes written in *IDL*, by taking a spectral track, defined by a selection rectangle tightly constrained around the feature, and dividing the x-axis into bins of length δx.

The size of each bin had to be chosen to preserve the theoretical resolution of the *J-PEX* instrument ($\lambda/\Delta\lambda \approx 5000$). Because of the analogue nature of the Vernier anode readout, image data are not in the form of events at

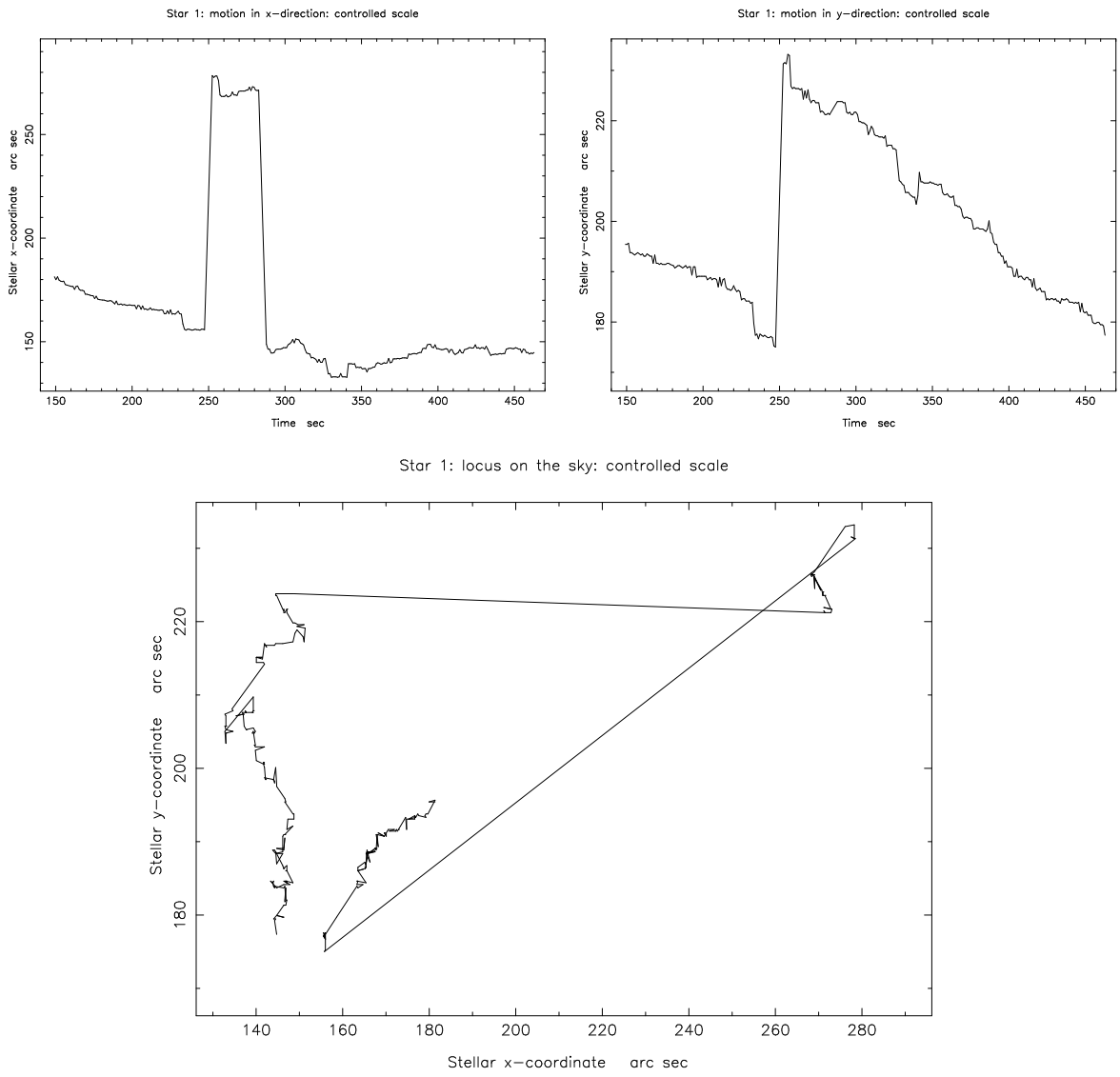

Figure 6.3: Movement of the CCD image of G191-B2B during flight. Top left: x-displacement versus time. Top right: y-displacement versus time. Bottom: x(y). Note the slewing operation at approximately T +250 s, and the corrective slew (in x only) at T +280 s. These figures are presented to demonstrate the form of the deconvolution path determined during aspect-reconstruction of the MCP image.

integer pixel locations, but are given as a pair of floating point x and y values for an event of gain g pC (with $0 \leq x \leq 768$ and $0 \leq y \leq 512$). However, when displaying the data as an image , these positions are rounded to the nearest integer. Therefore, images such as those in figure 6.2 have already been subject to binning by the display software, though the raw data remain unaffected. In this context, a pixel may be considered as one display element, though event positions are specified to fractions of a pixel.

Using laboratory calibration images of a Penning discharge source (considered in more detail in the next section), an approximate scale of 0.05 Å per display pixel was established (or $\lambda/\Delta\lambda \approx 4700$ at the central wavelength of 235 Å, close to the theoretical instrument resolution). To avoid loss of information, a 0.2 pixel bin size ($\approx$ 0.01 Å) was selected, over-sampling the data by a factor of approximately 5. The number of events in each bin, for all y-positions within the selection zone, were then counted - the resultant curve (number of counts versus x-position) constituting an uncalibrated “raw” spectrum. This process resulted in four spectra with common bin

sizes, but with slight offsets in the central wavelengths of each bin (due to the differing start and end points of each extraction window). Since the spectral analysis codes used later in this work operate most reliably with spectra on common wavelength grids, the spectra were then rebinned to a common 0.02 Å grid (still over-sampling the data by a factor of 2.5, if the theoretical resolution is assumed).

Pre-flight dark exposures revealed a detector noise count rate of less than 5 events $\sec^{-1}$ over the entire imaging area. Further, as shown in figure 6.4, the total number of background events (noise, sky background + scattered starlight) was negligible compared to the intensity of the spectral tracks. Therefore, no background correction was performed in this analysis.

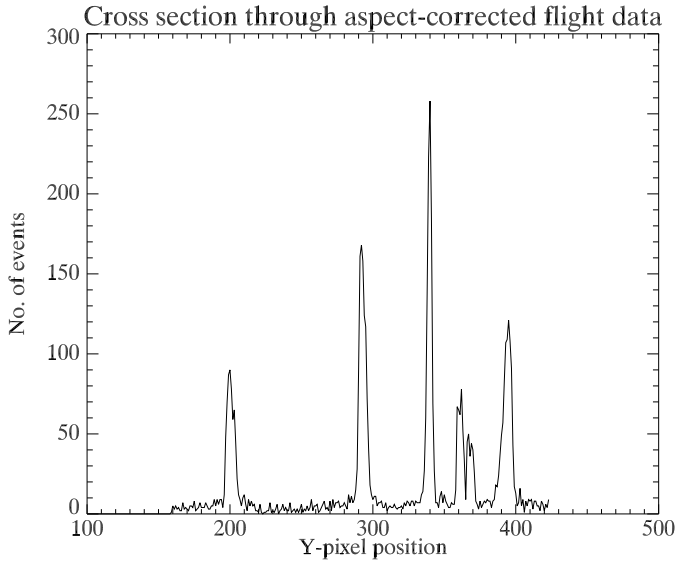

Figure 6.4: A cross section of the aspect-corrected flight image in the y direction, summing over approximately 250 x display pixels centred around x=320. The double-peaked feature centred around y-pixel 365 is a hot spot, which does not impinge on the spectra. Diffuse background levels between spectral tracks are low, and are not subtracted in the following analysis.

A final step in the preparation of histograms was the manual removal of two significant artifacts: the EUV mirror image crossing the G6 spectrum, and a count enhancement in G4 due to a nearby hot spot. Both of these operations were performed manually; EUV image removal was achieved by setting the count level in the affected G6 bins to zero, while correction for the G4 labeled took the form of a 5 count subtraction from all bins in this region (5 counts being the visual estimate of event enhancement in this region).

6.2.4 First order wavelength calibration

The end result of the histogram extraction was a file, for each track, listing the number of counts in each bin. The next stage of processing converted x-pixel position (or, equivalently, bin number) into a wavelength, λ. This was achieved using a calibration image taken in the laboratory at NRL, in which the spectrometer was illuminated using a Penning discharge source to produce a helium line series from each grating. The image is shown in figure 6.5.

Using the same software employed to extract the stellar spectra, histograms of the Penning source emission lines were plotted as a function of x coordinate. Since the absolute wavelength of each feature was known, it was possible to plot $\lambda(x)$ for the strongest helium lines in the spectrum, and perform a linear fit to the data, to produce

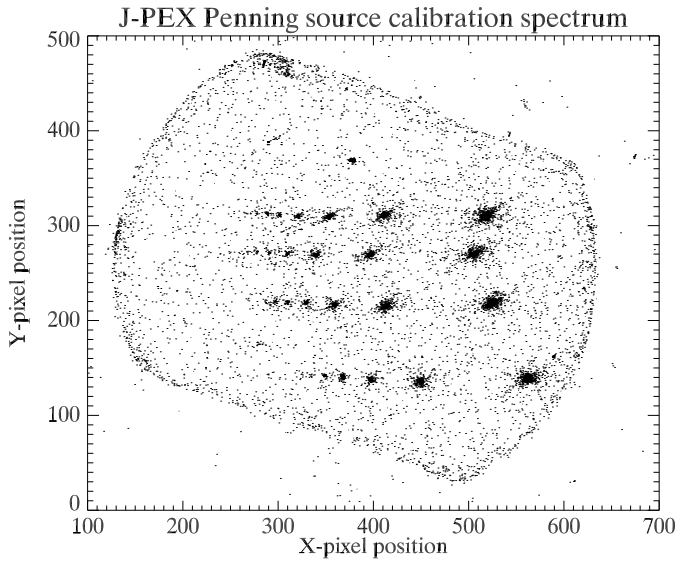

Figure 6.5: Penning source calibration image from the *J-PEX* spectrometer, with helium spectra clearly visible from each grating. The most intense (rightmost) spot in each track is 243.0 Å, followed by 237.3, 234.3, 232.6, 231.5, 230.7 and 230.1 Å.

a final wavelength calibration. However, analysis of these data showed that the dispersion relation in each spectral track was not linear, possibly due to the presence of E fields in the rear of the detector above the Vernier anode (this non-linearity is obvious in the topmost spectral track of figure 6.2).

A complete understanding of this distortion would require a significant investment of time and resources, introducing unacceptable delays in the analysis of the *J-PEX* flight data. Instead, a compromise was devised in which the data from each grating were fitted by a 3rd order polynomial, which was in turn applied to the flight spectra. The coefficients of the four polynomials are given in table 6.1. Note that the use of polynomials should not be taken as an implication that the distortions are of this form. These expressions merely provided a convenient and simple means of introducing a non-linear correction to the data, and are not offered as a formal description of the problem.

Grating	a	b	c	d
G6	-1.03×10^{-5}	2.02×10^{-3}	0.160	213.952
G1	8.66×10^{-6}	-2.80×10^{-3}	0.548	206.268
G4	3.24×10^{-5}	-7.98×10^{-3}	0.911	199.229
G3	1.55×10^{-6}	-3.73×10^{-4}	0.295	214.924

Table 6.1: Wavelength calibration coefficients for polynomials of the form $\lambda = ax^3 + bx^2 + cx + d$, where x is the pixel coordinate of the event.

Figure 6.6 illustrates the effectiveness of the polynomials in calibrating the Penning source spectra. The left panel shows histograms from each of the four gratings; the spectra are clearly subject to linear shifts relative to each other, but (as the coefficients in table 6.1 indicate), they do not share the same dispersion relation. After application of the polynomial calibration, registration between identical wavelengths from each grating is much improved, and the absolute wavelength calibration appears to provide sensible results.

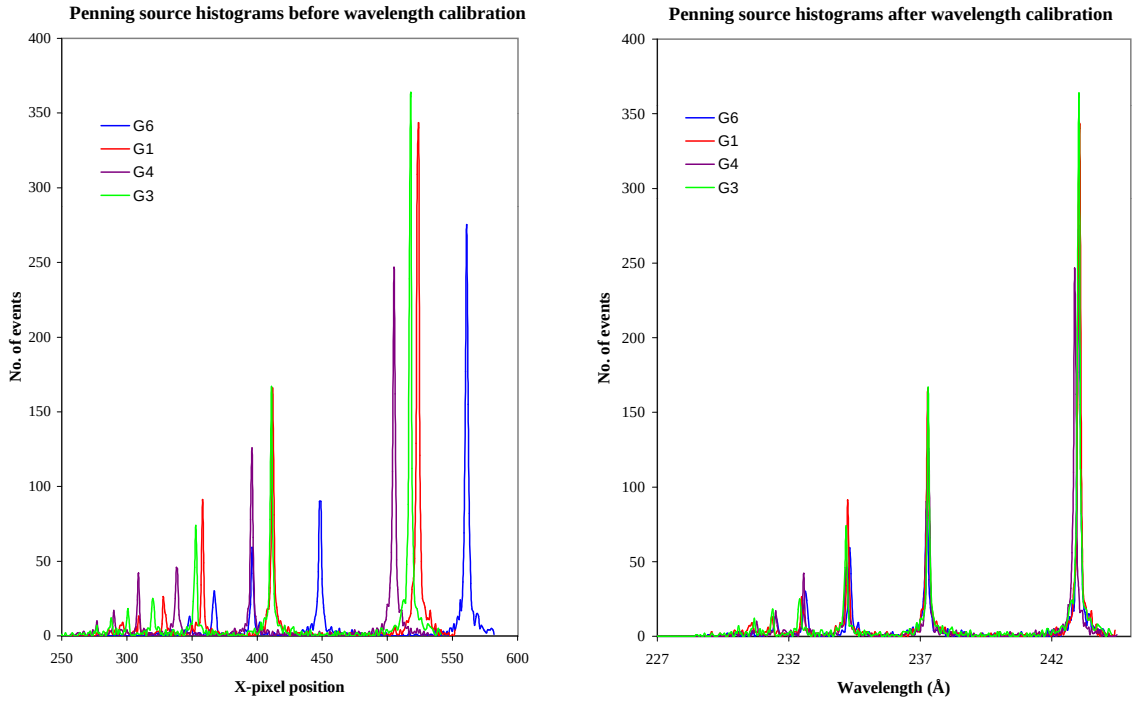

Figure 6.6: Left: counts per x-pixel coordinate for the Penning spectra of figure 6.5; the strong 243 Å line is visible on the right, although the location of the peak varies considerably between gratings. Right: spectra after application of polynomial pixel-wavelength functions, showing improved registration and wavelength calibration. The emission line wavelengths are at 243.0, 237.3, 234.3, 232.6, 231.5, 230.7 and 230.1 Å.

6.2.5 The position dependence of non-linearities

During the process of pre-flight grating alignment, a number of Penning source calibration images were acquired for alternative grating positions. By extracting the spectral histogram from several such images, and determining the polynomial wavelength approximation as outlined in the previous section, the position dependence of each grating dispersion relation could be observed. The main calibration image (NRL-133) is shown with two further images overlaid (NRL-110 and NRL-145) in figure 6.7. Of the two comparison images, NRL-110 shows the greatest shift in emission line position with respect to the adopted calibration image. Polynomial approximations to the dispersion relation were determined for each grating, and the resulting functions are shown in figure 6.8. When applied to the four extracted histograms from each image, these polynomial functions produced good registration and wavelength calibration of all emission features visible in the data.

Figure 6.8 shows that the closest agreement between polynomial functions is found for gratings G3 and G4. A slight variation between the solutions for G1 is observed at low pixel values (particularly obvious in the NRL-110 data), but grating G6 in NRL-110 shows the most significant deviation from the expected function, while solutions for the same grating in images NRL-133 and NRL-145 are in excellent accord. Inspection of figure 6.7 shows that the largest shift in grating position is found in G6, followed by G1. Image NRL-110 shows these spectra displaced a considerable distance from their locations in NRL-133, while the NRL-145 spectra show only slight displacements relative to those in NRL-133. These observations are reflected in the similarities and differences between the polynomial functions of figure 6.8.

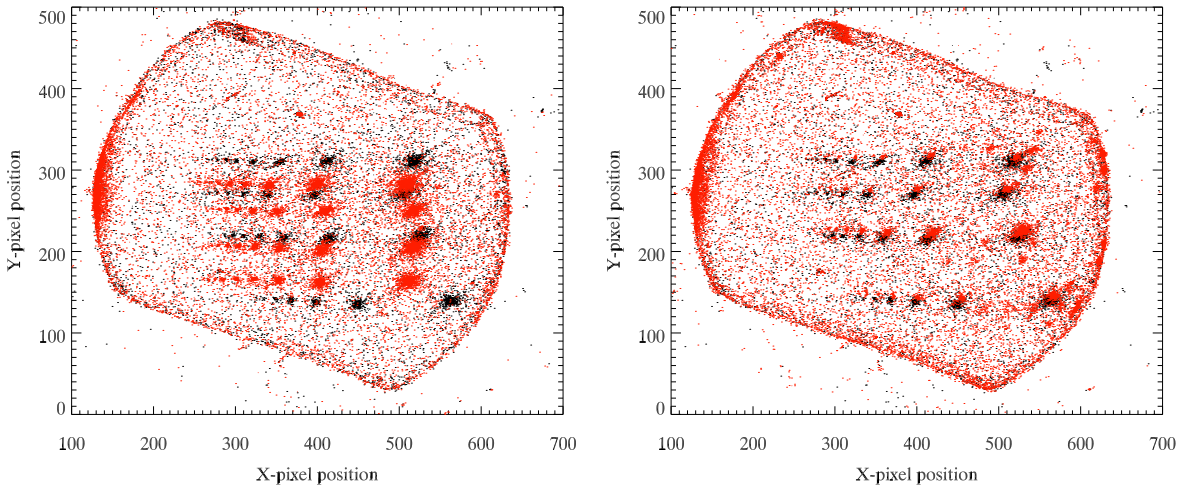

Figure 6.7: Penning source images acquired during the grating alignment phase of instrument integration at NRL. The image used to determine the dispersion relations adopted for the remainder of this analysis (NRL-133), is shown in black (this image was acquired once the gratings were locked down into their final flight positions). The images overlaid in red were taken with gratings in slightly different positions. These images are (left) NRL-110 and (right) NRL-145.

The shifts observed in the NRL-110 positions are such that the spectrum from grating G3 is almost coincident with that of G4 in NRL-133. This alignment may be used to test the hypothesis that the non-linearities observed in each dispersion relation are a function of position within the active area of the detector. In this case, much greater agreement should be observed between the polynomial for G3 in NRL-110, and that of G4 in NRL-133,

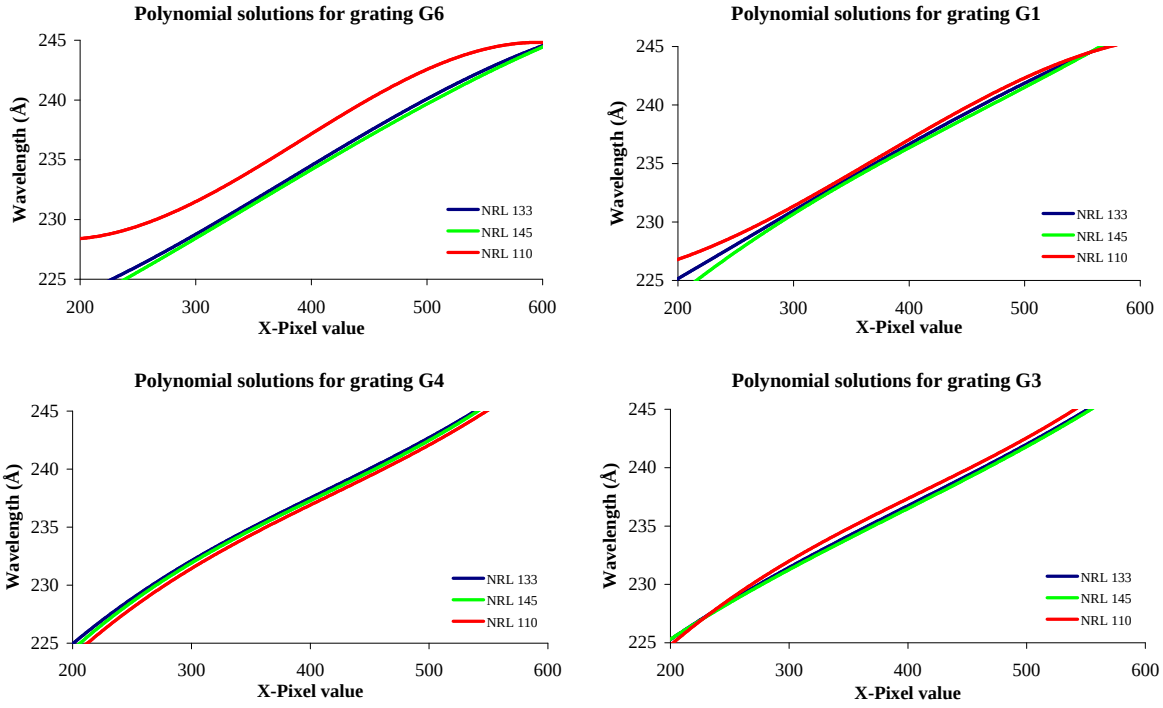

Figure 6.8: Polynomial wavelength solutions for three Penning source images, including image NRL-133 which was used to determine the final wavelength solution. The most significant displacement in spectrum position from the adopted location (determined by image NRL-133) is for grating G6 in image NRL-110. Despite the large difference in the form of this dispersion relation, application of this polynomial resulted in good registration of the G6 spectrum with those in the remaining images.

since these spectra occupy similar positions in the imaging area. Figure 6.9 shows this comparison. Almost perfect registration is observed in the solutions for G3 in NRL-110 and G4 in NRL-133, as expected for a position-dependent distortion. Included in this figure is the solution for G3 in NRL-133, showing a subtle but significant difference in form, compared to the first two functions. This figure, showing as it does the correlation between spectra in *similar locations*, rather than from *identical gratings*, appears to support the suggestion that the non-linearities observed in the wavelength dispersion relations for the *J-PEX* spectrometer are position-dependent.

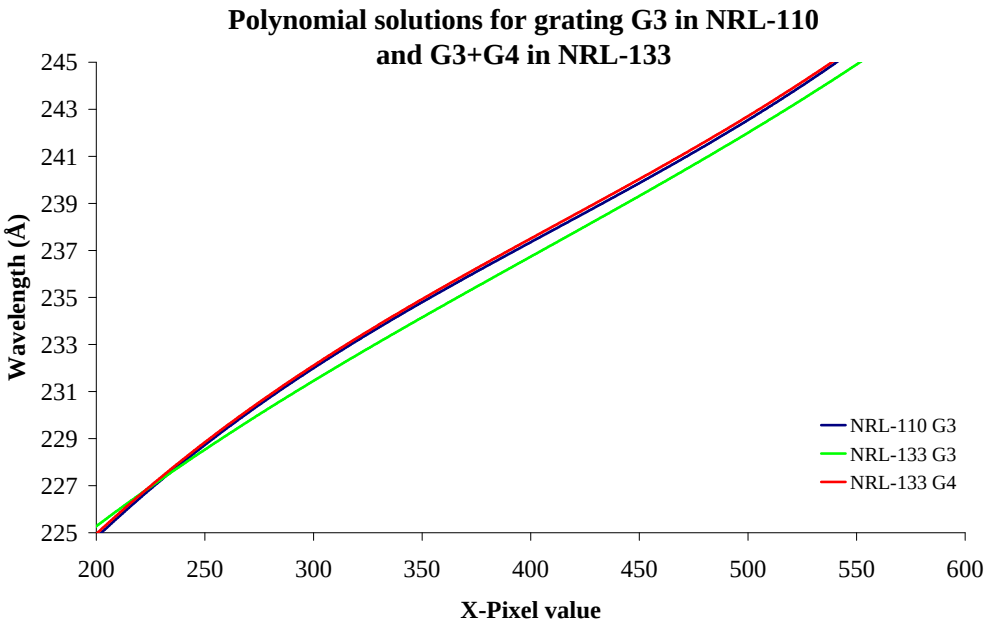

Figure 6.9: The polynomial wavelength solution for grating G3 in calibration image NRL-110, compared with those of gratings G3 and G4 in NRL-133. The agreement between the solution for G3 in NRL-110 and G4 in NRL-133 is so great that the curves are almost perfectly coincident in this plot, while the form of the solution for G3 in NRL-133 is clearly different.

Although these observations are informative, few images are available for alternative spectral positions (and none exist with spectra in the locations observed during the flight). This prevents the construction of a comprehensive position-dependency map, which might otherwise have provided an accurate solution to the wavelength calibration problem.

6.2.6 Co-addition

6.2.6.1 Image shifts & wavelength uncertainty

Ideally, wavelength calibration could be followed by co-addition of individual tracks into a single stellar spectrum. However, attention has been drawn to distortions evident in the flight image. If the stellar tracks and Penning features were found in identical regions of the image, use of polynomial functions alone might provide adequate calibration of the data. Unfortunately, two observations show that this is not the case. First, the post-calibration Penning source histograms (figure 6.6) show that registration of emission features is clearly imperfect. Ignoring this deficiency during co-addition of the spectra would lead to smearing out of the fine detail upon which the success of the project depends. Second, and more serious, is the fact that the flight spectra and Penning features

do *not* occupy similar locations, as comparison of figures 6.2 and 6.5 reveals.

The shift in absolute position of spectral tracks is also accompanied by a change in their relative spacing. The most likely explanation for this difference in geometry appears to be a change in stress on the payload, from the horizontal 1-g environment of the optical alignment bench used while calibrating the instrument, to the 0-g conditions experienced during flight. Differences in the four polynomial solutions of the calibration image show that the form of the distortion varies across the image area, but as indicated earlier, the paucity of data for other regions prevents derivation of a general, position-dependent dispersion function. Further, unless a set of unambiguously identifiable features are found in each stellar spectrum, no information is available on shifts which may have occurred parallel to the dispersion axis. Such identification is heavily reliant on an *a priori* wavelength calibration, and thus it becomes clear that accurate co-addition of the flight spectrum is a non-trivial task.

6.2.6.2 Cross-correlation analysis of spectra

One solution to the problems described above is the use of cross-correlation techniques to search for similarities between spectra. The output from such analyses can therefore provide information on image shifts along the dispersion axis, considerably simplifying the task of co-addition. The cross-correlation value, P of any two data sets is given by the expression

$$P_{xy}(L) = \frac{\sum_{k=0}^{N-L-1} (x_{k+L} - \bar{x})(y_k - \bar{y})}{\sqrt{\left[\sum_{k=0}^{N-1} (x_k - \bar{x})^2\right]\left[\sum_{k=0}^{N-1} (y_k - \bar{y})^2\right]}}, \tag{6.1}$$

where $\bar{x}$ and $\bar{y}$ are the means of the sample populations x = (x_0, x_1,..., x_{N-1}) and y = (y_0, y_1,... , y_{N-1}), respectively (in this case, the number of events per bin in the spectra, using identically sized bins in each data set). L is the lag of the distribution (the wavelength by which one spectrum is offset with respect to the other). The resulting cross-correlation value, P, is a number between +1 and -1, corresponding to perfect correlation and anti-correlation respectively. This technique is described in more detail by Walpole & Myers (1989).

Equation 6.1 is useful for correlating spectra with matching dispersion relations, which are offset from each other by some unknown wavelength. It is less applicable in cases where knowledge of the dispersion relation is poor, or where this relation differs between data sets. Both of these caveats apply to the *J-PEX* spectra, and thus a modification was made to the algorithm, such that in addition to a range of offsets, a sequence of moderate ($\pm$ 10%) linear scaling factors was applied to the comparison spectrum. This algorithm was then used to search a two-dimensional region of lag/stretch parameter space for values yielding the best match between spectra.

Using this technique, offsets and scaling factors were identified and applied to the G3, G4 and G6 spectra in order to provide the best match to G1 (which was judged to be of highest quality). These parameters are summarized in table 6.2, and the correlation parameter space for the G1/G3 analysis is shown in figure 6.10.

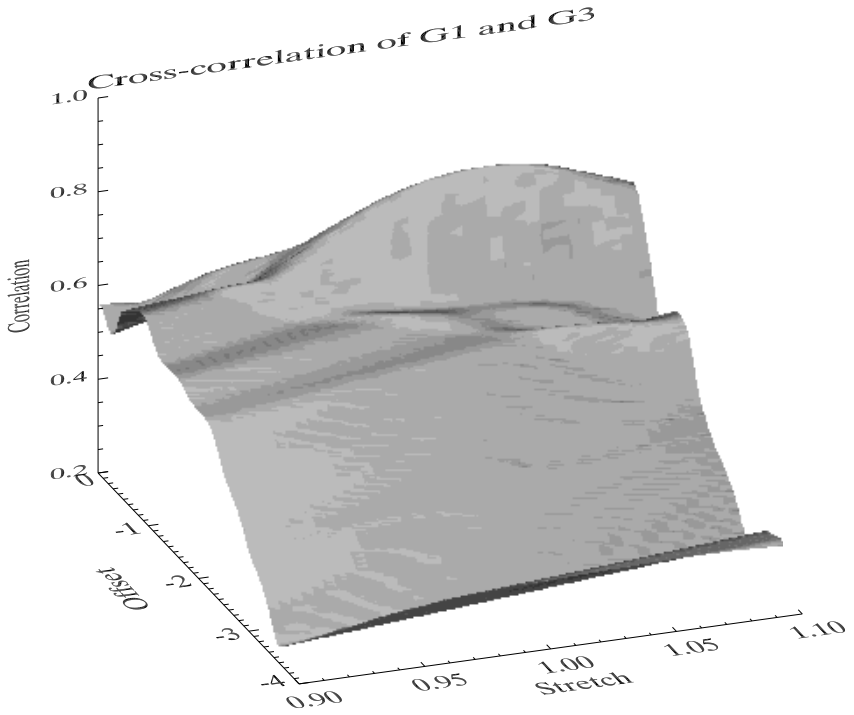

Figure 6.10: Results of a cross-correlation analysis of spectra from gratings G1 and G3. The closest alignment was found at an offset of -0.594 Å and a stretch factor of 1.040, for G3.

This process of cross-correlation resulted in successful co-addition of the four grating spectra. However, since all offsets and stretches were performed to fit the G1 track, the co-added data inherited the wavelength scale of this track. To ensure that the flight spectrum had as accurate a wavelength scale as possible (given the uncertainties already described), an additional cross-correlation was performed, matching the co-added data to an *EUVE* medium wavelength spectrum of G191-B2B. This operation resulted in a shift of the entire co-added *J-PEX* spectrum, of 2.878 Å towards shorter wavelengths, and a 1% stretch of the data, centred on 232.529 Å. The results of this adjustment are shown in figure 6.11.

Figure 6.12 shows the individual spectral histograms following extraction, wavelength calibration and cross correlation, together with a first attempt at co-addition.

Grating	Offset (Å)	Stretch factor	Central λ	P
G6	-0.790	1.035	234.926	0.658
G4	-0.072	1.005	234.893	0.763
G3	-0.594	1.040	234.368	0.835

Table 6.2: Wavelength offsets and stretch factors corresponding to the optimum correlation with spectrum G1. A negative offset indicates a shift of the spectrum toward shorter wavelengths, while linear stretches of the spectra were performed about the quoted central wavelength. The quantity P is the cross-correlation value defined by equation 6.1.

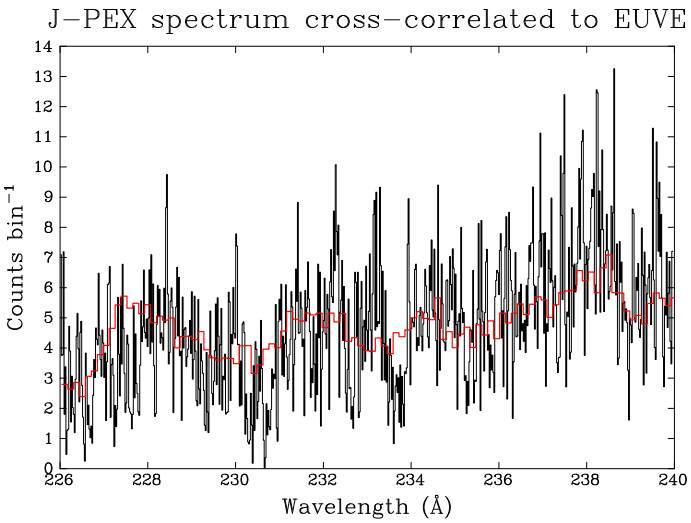

Figure 6.11: The *J-PEX* co-added flight spectrum (black), cross-correlated with a medium waveband *EUVE* spectrum of G191-B2B (red). No binning has been performed on the *EUVE* data, and the increased resolution of *J-PEX* is readily apparent from this plot. (Note that the *EUVE* data have been re-scaled to approximate flux levels in the *J-PEX* spectrum.)

6.2.6.3 Flux calibration & statistical errors

Conversion from the count spectrum discussed up to this point, into a true photon spectrum, was achieved using knowledge of the quantum efficiency of each grating, and the efficiencies of other components in the instrument.

Grating quantum efficiencies were measured at the Brookhaven National Synchrotron Light Source, USA (Kowalski & Cruddace, Private Communication), prior to the first *J-PEX* flight (36.162). Following this unsuccessful flight, the peak efficiencies were re-evaluated, and the QE curves scaled accordingly. Figure 6.13 shows the average grating efficiency profiles as a function of wavelength (the geometrical area of each grating was measured at 114.0 cm^2) . These data, and efficiency values for the collimator, UV filter, and detector, allowed an effective area curve for the complete instrument to be constructed. Collimator throughput was measured at NRL to be 90%, while measurements at Leicester showed that the UV filter chosen for flight had a transmission of 49.5%. As

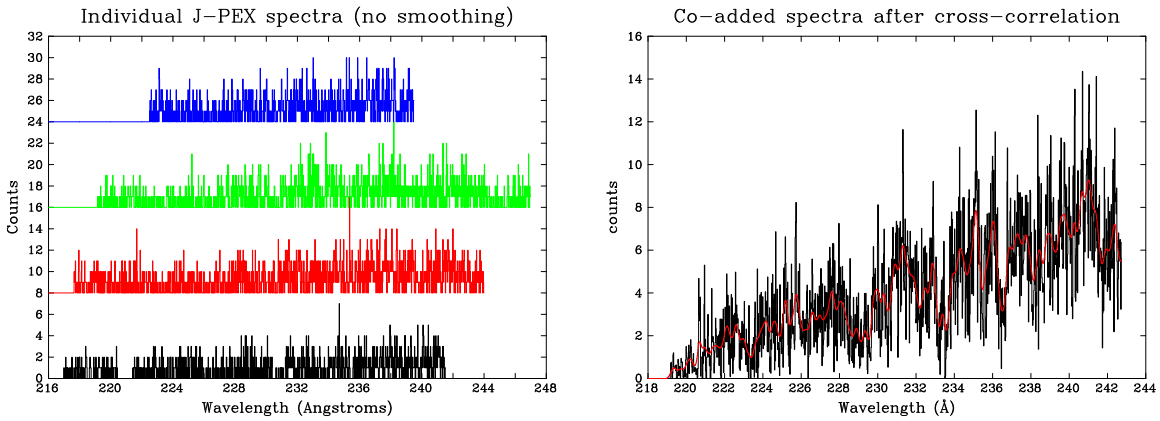

Figure 6.12: Left: raw spectral histograms extracted from the flight image (figure 6.2). An 8 count offset has been added between spectra to separate data for clarity. Note the region of zero counts in the G6 (black) spectra, following removal of the EUV telescope image. Right: co-addition of the four tracks using cross-correlation parameters quoted in table 6.2. The black curve is un-smoothed data, while the red curve shows the same spectrum after smoothing with a Gaussian having a FWHM of 0.2354 Å.

discussed in Chapter 3, the MCP detector quantum efficiency was found to be 14.6% at 256 Å, and this value was adopted for the entire *J-PEX* bandpass (225 - 245 Å).

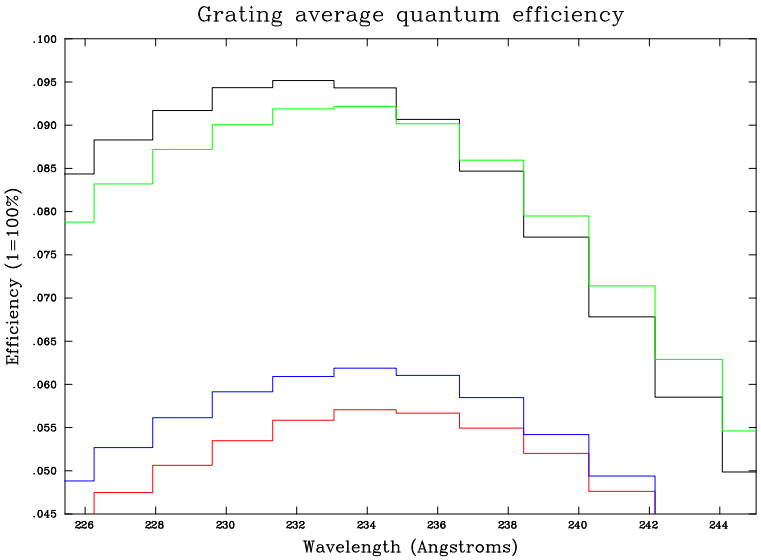

Figure 6.13: QE of the *J-PEX* gratings, scaled to the peak values measured following flight 36.162. (Black = G1, green = G4, blue = G6, red = G3.)

By multiplying the curves in figure 6.13 by these constants and dividing by the exposure time (303 seconds), instrument sensitivity profiles were obtained. Dividing the co-added count spectra by these curves results in a photon flux spectrum.

The statistical uncertainty for each datum point was calculated on the basis of fractional errors. This is simply an application of standard Poissonian statistics to the count spectrum, so that the error associated with a bin containing N events is given by $\sqrt{N}$, and hence the fractional error is just $\frac{\sqrt{N}}{N} = \frac{1}{\sqrt{N}}$.

Figure 6.14 illustrates the end product of this first phase of data processing and extraction. The data are binned to 0.02 Å, and are shown with error bars calculated using the method outlined above. The data presented in this figure do not represent a completely reduced spectrum of G191-B2B, but were regarded as suitable input for the analysis phase of this study.

6.3 Analysis of the J-PEX spectrum of G191-B2B

6.3.1 Overview

A precise determination of the abundance and location of helium in the spectrum of G191-B2B requires the application of sophisticated computational techniques, to produce model spectra for a range of abundances which may then be compared (using a χ^2 test) with the observational data. To illustrate this principal, figure 6.15 shows two simulations of *J-PEX* spectra. The data have been generated using non-LTE models of G191-B2B produced using the stellar atmosphere code TLUSTY, generating the synthetic spectra with SYNSPEC. Also shown in this figure

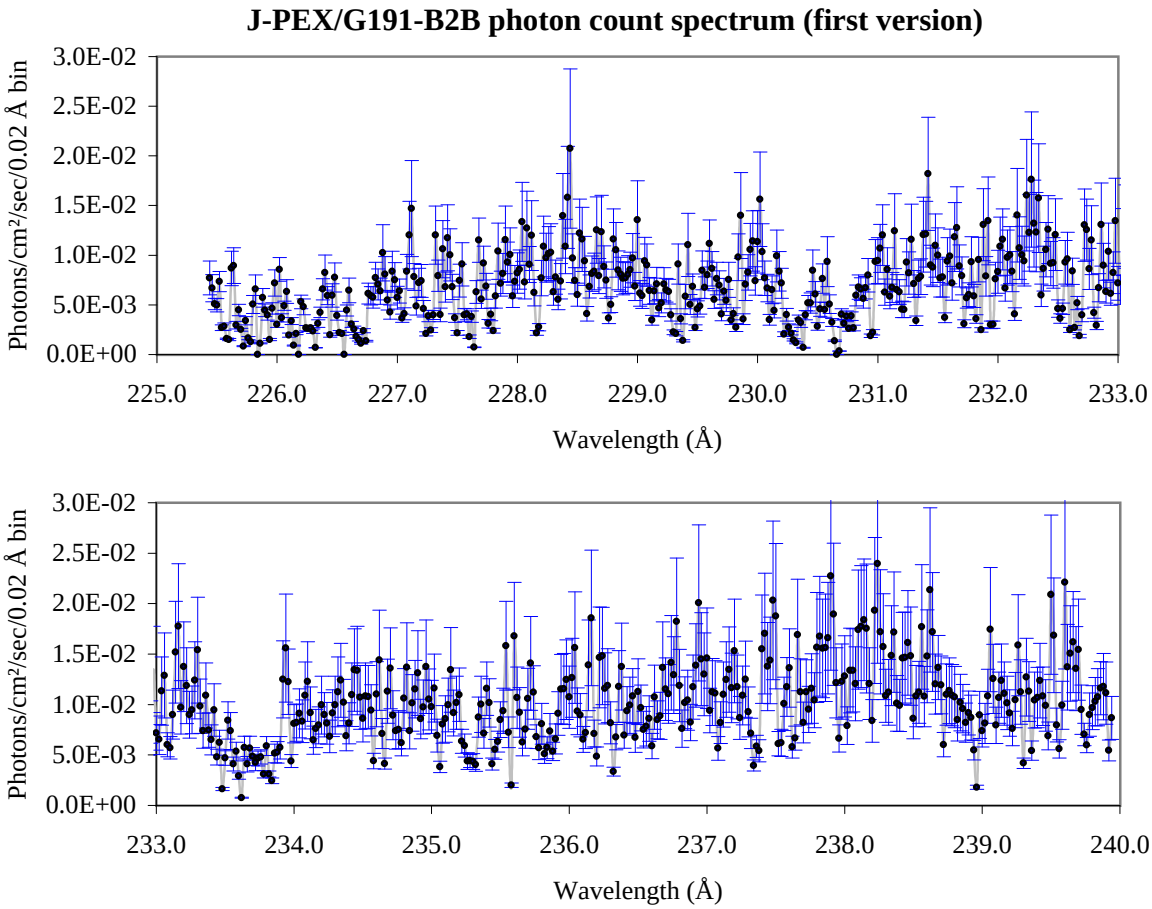

Figure 6.14: The spectrum of G191-B2B obtained by J-PEX, after wavelength calibration, cross-correlation, co-addition and flux correction. Data are shown in 0.02 Å bins, and the error histogram is shown in blue.

is the *J-PEX* flight spectrum, re-binned to match the 0.05 Å resolution of the models.

The lower panel in figure 6.15 clearly demonstrates the diagnostic value of such models. The most significant difference in the spectra is observed below the 228 Å He II Lyman limit, where the presence of interstellar or circumstellar helium is responsible for a considerable level of flux suppression. This sensitivity to the location of He arises from the very different conditions under which it exists in the ISM or in the photosphere. In addition to differences in the population of energy levels in the He atom, photospheric material is subject to pressure broadening, and the convergence of *broadened* lines towards the 228 Å limit produces an effective edge at $\approx$ 235 Å, in comparison to the sharper 228 Å feature produced by interstellar material (Barstow *et al.*, 1997a). The clear differences between the simulations in figure 6.15 reflect substantially different conditions along the line of sight to the star, but by using grids of models in which interstellar and photospheric He abundances are allowed to vary in small increments, χ^2 fit tests can identify the closest match to observational data, and thus the location and abundance of material can be established.

6.3.2 Long wavelength corrections to the spectrum

The nominal bandwidth of the *J-PEX* instrument is 225–245 Å. However, figure 6.12 shows that this coverage has not been achieved in three of the four spectra, which contain extended short wavelength data at the expense

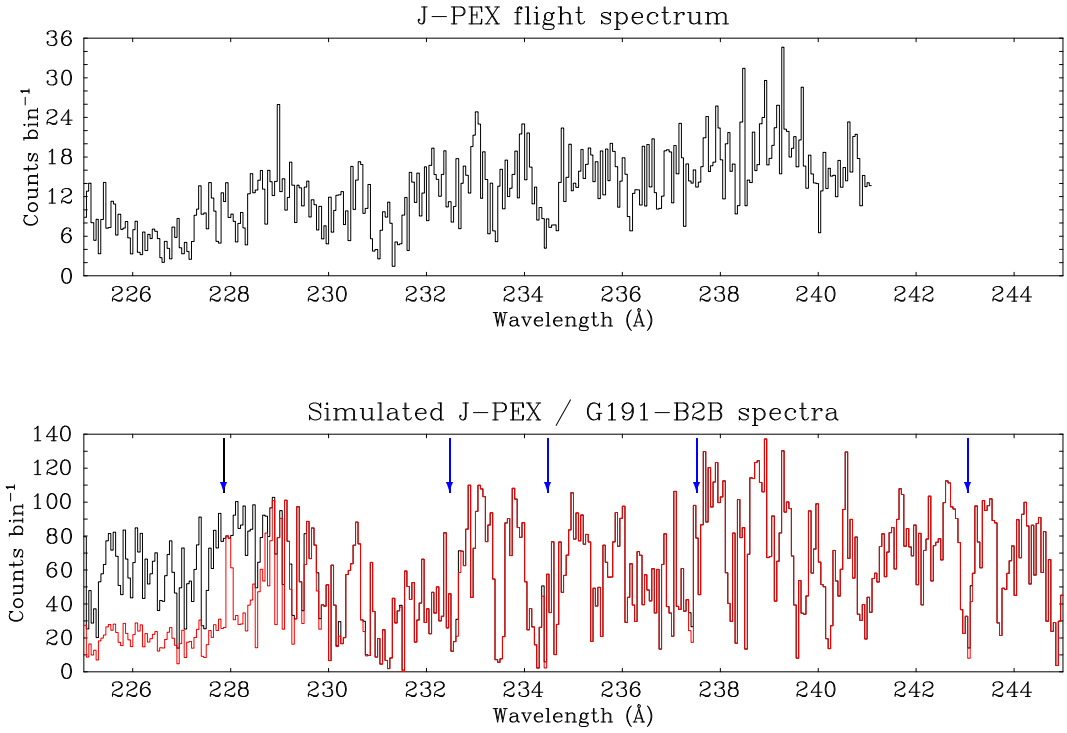

Figure 6.15: Top: *J-PEX* spectrum rebinned to 0.05 Å to match the simulated spectrum bin size. Bottom: simulated *J-PEX* spectra of G191-B2B, including Poisson noise at the level expected in a 400s observation. Black: photospheric He abundance $= 5 \times 10^{-5}$, with no interstellar / circumstellar He II. Red: photospheric He abundance $= 10^{-5}$ and interstellar/circumstellar He II column density of 8×10^{17} cm^{-2}. Note the substantial difference in flux level shortward of the 228 Å He edge. Blue arrows indicate (from left to right): the He II Lyman limit, and He II lines at 232.7, 234.5, 237.5 and 243.3 Å.

of the longer wavelengths. This shift in bandpass is most probably due to changes in grating alignment along the dispersion direction, moving long wavelength photons out of the imaging area (note also that substantial areas of the G3 data have been rejected in the extraction process, due to gross distortions in the spectral track). The loss of longer wavelength information is unfortunate, since it contains the strong He II 243.3 Å feature – a valuable diagnostic for determining the location and abundance of helium, which is visible in the simulations of figure 6.15.

This important spectral region is not entirely lost, however; gratings G4 and G1 both include 243.3 Å data, though only G4 covers the entire nominal bandwidth. Data extraction has therefore been extended to these regions, accepting that, with only half of the total effective area available, the quality of these data is considerably lower than elsewhere.

Following extraction of the two long wavelength sections, the offset and stretch parameters suggested by the original cross-correlation analysis (summarized in table 6.2) were applied. However, after these transformations, visual inspection of the spectra suggested that the best alignment was produced by a further 0.19 Å shift (towards longer wavelengths) in G1. Confirmation of this shift was obtained by performing a second cross-correlation on the sections, restricting the analysis to the 240 – 245 Å region. The results identified an optimum correlation using a 0.206 Å shift and a 10% stretch of G1 with respect to G4 – consistent with the visual inspection. This additional transform has been applied to the long wavelength segment of flight data, which is visible in the "final" spectrum presented in figure 6.16 as the lower resolution data longward of 240 Å (these data have been scaled by a constant

to preserve continuity in flux levels).

The need for additional processing of these data is not unexpected. The approximate nature of the polynomials as a solution to wavelength calibration has already been noted, and as the functions in figure 6.8 demonstrate, a significant change in the coefficients is observed for relatively small displacements in spectral position. The result of each cross-correlation analysis is an average, identifying a single offset and stretch for application to the entire spectral track. The second transformation required for the long wavelength segments simply highlights the deficiencies in this procedure. By restricting correlation to a small portion of the spectrum, the resulting transformations are more closely tailored to that particular region. These observations therefore suggest that instead of fitting a single function to each spectral track, a sequence of polynomials should be applied across the wavelength range to achieve the most accurate co-addition of spectra. This is precisely the form of the *cubic spline*, and future modifications to the data extraction procedure should incorporate this fitting method for maximum accuracy in spectral co-addition. However, in view of time constraints in the current phase of work, and the general effectiveness of the polynomial functions applied thus far, this remains a recommendation, and is not implemented in the remainder of the study.

6.3.3 Preliminary results from the J-PEX data

Although analysis and interpretation of data from the *J-PEX* flight is an ongoing process of refinement and remodeling, the first phase of analysis, in which the photon positions are corrected for pointing drift and jitter, and the spectra from the four gratings are co-added, is complete. The data reveal some exciting results, but as discussed in the preceding sections, further improvements in the processing of the spectra are likely, and hence the results presented here are a preliminary interpretation. The *J-PEX* flight spectrum is shown compared to a best–fit model, in figure 6.16.

The observed spectrum (error bars in figure 6.16) has been compared with predictions based on a stellar atmosphere of homogeneous composition, and including interstellar H I, He I and He II absorption. However, as shown by Barstow *et al.* (1999b), the atmosphere of G191-B2B is apparently best described by a model in which Fe abundances are stratified. The homogeneous atmosphere adopted in this work is the most current of the available codes, and incorporates the most recent atomic data, including highly ionised species such as O VI reported by Barstow *et al.* (2001a); for the purposes of determining the abundance and location of helium in a 20 Å wide spectrum, the choice of a homogeneous model is acceptable, although stratification must be included in future analysis, when updated models become available.

To model the *J-PEX* flight spectrum, the H I and He I column densities were fixed at values obtained from analysis of the broader band, lower resolution *EUVE* spectrum (Barstow *et al.* 1999b[2]; H I = $2.15\ (\pm 0.14) \times 10^{18}$ cm^{-2}, He I = $2.18\ (\pm 0.29) \times 10^{17}$ cm^{-2}), and the values for temperature and gravity (T_{eff} = 54,000K, log g = 7.5) were taken from the latest optical analysis presented by Barstow *et al.* (1998, 1999b). The interstellar He II column density and photospheric He abundance were allowed to vary freely and the best match to the model obtained

[2]Errors in these values were estimated by taking the standard deviation of the range of H I and He I columns suggested by the models of Barstow *et al.* (1999b). Note, however, that models fe7 and fe8 in that work were not included when determining the standard deviation; the Fe abundance profiles in these models were determined from the balance of radiative levitation and gravitational settling, and neither produced results in good agreement with observations.

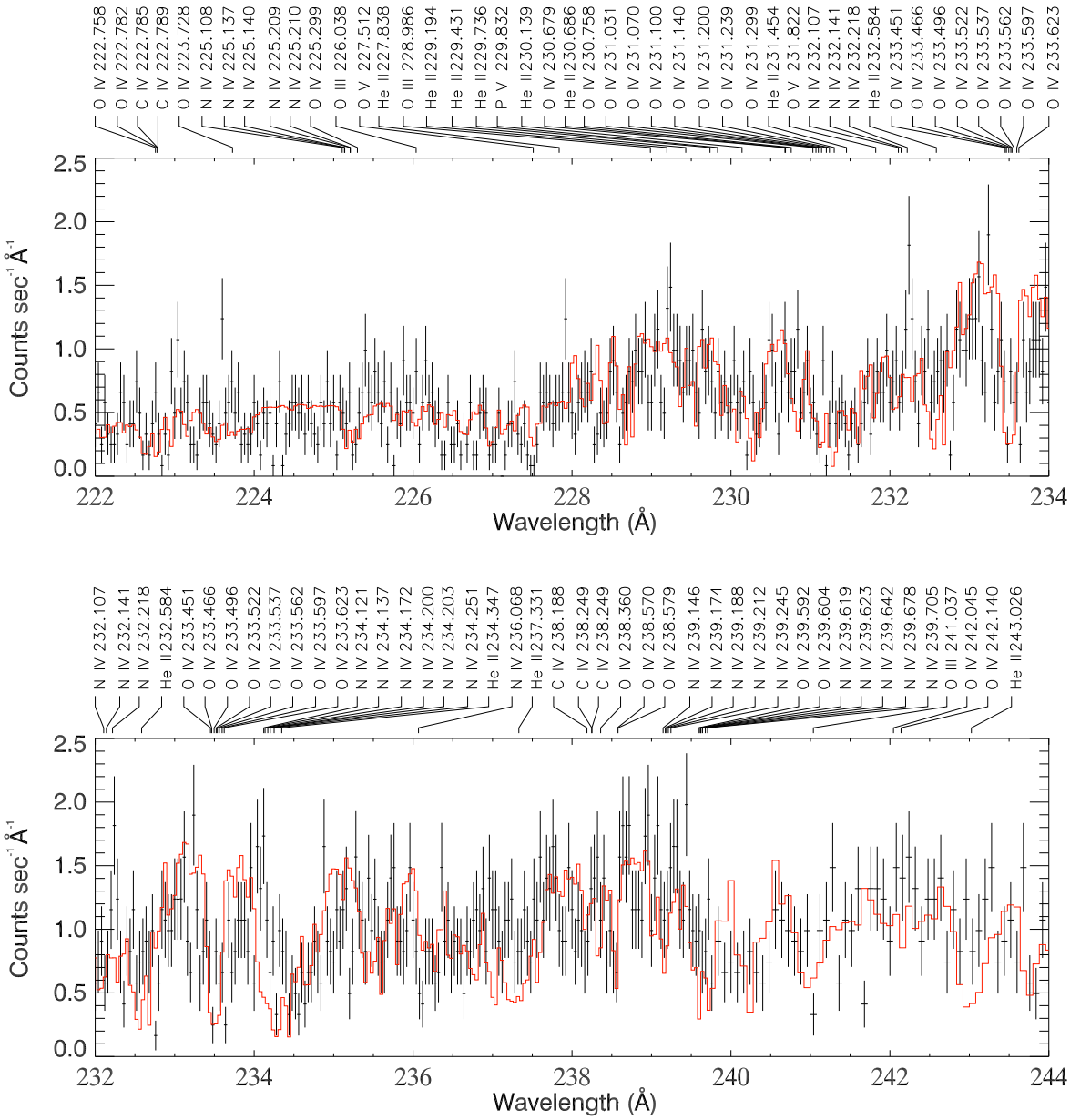

Figure 6.16: The spectrum of G191-B2B, obtained with the *J-PEX* spectrometer (black error bars). The best-fit theoretical model of the star and ISM, as described in the text, is shown as the red histogram. The strongest predicted lines of He, C, N, O, and P are hot spots with their ionisation state and wavelength. Lines of Fe and Ni are too numerous to include here and account for the unlabeled individual features and broader absorption structures.

using the χ^2 minimisation technique described earlier in this chapter. The best-fit model folded through the *J-PEX* instrument response, assuming a nominal 0.05 Å resolution (FWHM), is shown in figure 6.16 (red-line histogram). The good agreement between model and data is striking, with the most prominent resolved feature being a blend of O IV lines around 233.5 Å. Many other features are present, most of which are blends of large numbers of Fe V and Ni V lines.

The results of this analysis provide compelling evidence for the presence of interstellar or circumstellar He II along the line of sight. The existence of this material is betrayed by the suppression of flux in the 220 – 227 Å band, compared to the levels observed longward of the 228 Å edge. This is a characteristic of interstellar material, and

cannot be explained by photospheric helium which, as indicated earlier, produces an edge-like feature near 235 Å due to the effects of pressure broadening of the lines which converge to the series limit.

The best-fit model includes an interstellar He II column density of $\sim$ 6 ($\pm$0.1) $\times$ 10^{17} cm^{-2}. Assuming the amount of He III is negligible, the ionisation fraction of He ($f_{\rm He}$) can be calculated from the simple formula given by Barstow *et al.* (1997a), i.e.

$$f_{\rm He} = \frac{N_{\rm He\ II}}{(N_{\rm He\ I} + N_{\rm He\ II})}, \tag{6.2}$$

where $N_{\rm He\ I,II}$ are the column densities of He I and He II respectively. Adopting a He I column of 2.0×10^{17} cm^{-2} (from model fe6 in the *EUVE* analysis of Barstow *et al.*, 1999b) produces an ionisation fraction of 0.75 ± 0.03, where the uncertainty has been estimated using the standard error combination formulæ[3]. This is significantly higher than the "typical" ionisation fractions of 0.2 – 0.5 measured by Barstow *et al.* (1997a). However, as discussed in Chapter 5 a circumstellar C IV component in the far-UV spectrum of G191-B2B has been identified. It is therefore possible that part of the ionized He II revealed in the *J-PEX* data may also be in the form of circumstellar material. The best-fit model spectrum implies that photospheric helium is also present, though the strongest predicted photospheric line at 243.3 Å is only marginally detected at the S/N of these data – an unfortunate consequence of the loss of long wavelength data in two of the spectral tracks, described earlier. Additional evidence for the presence of photospheric He II is found in the broad "bump" between $\sim$ 227 – 232 Å, also characteristic of the overlapping series of interstellar He II absorption lines superposed on a continuum. The precise shape of this feature is most faithfully reproduced using a combination of warm interstellar He II and dense photospheric material. The inferred photospheric He abundance (relative to H) is $8.23 \pm 1.41 \times 10^{-5}$, about four times the limit imposed by the absence of detectable He II at 1640 Å in the *STIS* spectrum. To explain this apparent discrepancy, the photospheric He must be in a stratified configuration as suggested by Barstow & Hubeny (1998). Further refinement of the analysis is needed before the presence of photospheric He in G191-B2B can be quantified unambiguously; indeed, the S/N of these data may ultimately be inadequate for this purpose. This issue is addressed in Chapter 7.

While good overall agreement is found between model and observed spectra, some important features of the flight data are not well reproduced. For example, the observational data appear to show absorption lines at 230.6 and 235.2 Å which are not found in the model. The observational data also exhibit a flux level in the 234.0 – 234.5 Å region which is significantly higher than produced by the model. The reason for this lower than predicted absorption is as yet unclear. It should, however, be noted that much of the atomic data used to calculate this and other stellar models, is *calculated* rather than *measured*. Consequently these unpredicted features may be indicative of deficiencies in the atomic theory, rather than spurious "artifacts" in the observed spectrum. These points illustrate the importance of undertaking high resolution spectroscopy of astronomical targets, not only for advancing our understanding of astrophysical phenomena, but for the testing and refinement of theories which underpin much of modern physics. The extreme conditions found in white dwarf stars provide some of the most rigorous tests for these theories.

[3] If $Z = f(A, B)$ where the independent variables A and B have associated errors ΔA and ΔB, then the final error ΔZ is as follows: for $Z = A \pm B$, then $\Delta Z = \sqrt{(\Delta A)^2 + (\Delta B)^2}$. For $Z = A \times / \div B$, then $\Delta Z = Z\sqrt{\left(\frac{\Delta A}{A}\right)^2 + \left(\frac{\Delta B}{B}\right)^2}$

6.4 Summary

- This chapter has covered the extraction, reduction and analysis of the EUV spectrum of the white dwarf G191-B2B, returned from the first successful flight of *J-PEX*.

- Significant problems have been encountered in wavelength calibration. These problems are attributed to non-linearities in the dispersion relation for each of the four spectra. It has been shown that these non-linearities appear to be position dependent. The source of this problem is possibly (though not certainly) related to the existence of E-fields above the readout anode.

- Complications have been introduced into the wavelength calibration as a result of gross shifts in the position of the spectra from their laboratory-determined locations. These shifts probably result from significant changes in stress on the optical assembly in the transition from the 1-g loading of the laboratory, to the microgravity environment of flight. The unknown change in position along the dispersion axis prevents identification of any clear wavelength reference prior to co-addition. A further consequence is the loss of important long wavelength data in two of the four spectra.

- These problems have, to some extent, been overcome by the application of a $3^{\rm rd}$ order polynomial approximation to the dispersion relation for each spectrum. The coefficients were determined from Penning source emission spectra acquired during the alignment and focus phases of work at NRL. The wavelength offsets required for co-addition of spectra have been determined by cross-correlation analysis, which also applies appropriate linear stretches in the wavelength scale as a second order correction to the dispersion function. Extraction of long wavelength data has emphasized the approximate nature of the wavelength calibration, requiring further cross-correlation for accurate co-addition. A cubic-spline approximation to each dispersion relation is suggested for future re-analysis of the data.

- Despite these challenges, the resulting spectrum represents the highest resolution EUV data currently available for an astronomical object, and is of sufficient quality to achieve some, though not all, of the mission objectives.

- Results of the analysis demonstrate the presence of interstellar helium in the spectrum of G191-B2B, with a He II column density of $\sim 6\ (\pm 0.1) \times 10^{17}$ cm^{-2}, and an implied He ionization fraction of ~ 0.75. This is higher than typical LISM values, and is consistent with the presence of some of the helium in a circumstellar cloud, the existence of which was suggested in Chapter 5.

- The best fit model spectrum implies that photospheric He II is also present in this star, with an abundance relative to H of $8.23\ (\pm 1.41) \times 10^{-5}$. However, the most significant photospheric line is only marginally detected at the S/N of these data. While the existence of a photospheric He component is supported by other features in the data, further analysis of the spectrum (and possibly the acquisition of higher S/N data on a future flight) will be required before more definite conclusions can be drawn.

- If the inferred photospheric He abundance is confirmed, the absence of detectable He II in the *STIS* spectrum supports the stratified He configuration proposed by Barstow & Hubeny (1998).

CHAPTER 7

CONCLUSIONS

7.1 Introduction

THE PRECEDING CHAPTERS have addressed the task of performing high resolution spectroscopic investigations of hot white dwarfs, beginning with a brief summary of the history of this field (Chapter 1). A large fraction of the work described in this thesis concerns the development and flight of a normal incidence EUV spectrometer, the design of which may form the basis for a new generation of high resolution EUV instrumentation; an introduction to this project, named *J-PEX*, has been presented in Chapter 2. Development of the MCP focal plane detector for *J-PEX* was the author's primary task in the hardware phase of this project, with a large fraction of this effort devoted to enhancing the quantum efficiency of the detector. The results of a laboratory study into the efficacy of several processes, culminating with the selection of a suitable treatment for the *J-PEX* focal plane detector, have been presented in Chapter 3. The instrumentation phase of the project is completed in Chapter 4 with a discussion of the development of the detector itself. This chapter covers the basic design of the device, modifications introduced to overcome certain functional issues, the low efficiency measured for the MCPs originally chosen for flight, and the process of preflight calibration and testing. The theme of the project changes to astronomical spectroscopy in Chapter 5, in which a survey of highly ionised absorption features at non-photospheric velocities is presented for a sample of hot white dwarf stars. In addition to adding three objects to the list of stars known to possess such features, this work demonstrates the importance of improving the spectral resolving power and throughput of astronomical instrumentation – goals to which the *J-PEX* project is devoted. The study of circumstellar features is also relevant to the work in Chapter 6, which covers the reduction and analysis of data from the first successful flight of *J-PEX*.

The main results of the project are summarised in this final chapter, together with suggestions for future work.

7.2 Summary of current results

7.2.1 The development of instrumentation for EUV spectroscopy

The instrumentation development work described in this thesis is concerned with the *J-PEX* high resolution EUV spectrometer design described in Chapter 2, with much of the work of the author being devoted to the focal plane detector fitted to this instrument. *J-PEX* represents one of the first in a new generation of instruments employing optics operating at near-normal incidence. The conventional grazing-incidence mirrors found in earlier instruments, with their limited collecting area, are replaced by $Mo_5C/Si/MoSi_2$ multilayer coated gratings which act as both dispersion and light collection elements. Manufactured by Carl Zeiss, using multilayer coatings developed at NRL and LLNL, these gratings have a total geometric area of 512 cm^2 and have a spherical figure with a 2m focal length. This arrangement enables *J-PEX* to achieve an effective area in excess of 5 cm^2 and a resolving power of 4700 at 235 Å. Diffracted radiation is focused onto the MCP detector, the development of which was discussed at length in Chapter 4, mounted along the grating optical axis to minimize optical aberrations. The sounding rocket attitude control system (ACS) permits highly precise pointing and target tracking. However, since residual drifts in pointing, if unchecked, would smear the spectrum and reduce resolution, *J-PEX* is equipped with an optical telescope and CCD detector, in addition to a multilayer coated mirror which focuses an image of the target onto the MCP detector. By imaging the target throughout the entire period of the observation, a post-flight aspect solution can be constructed, thus recovering resolution.

As with all astronomical instruments, sensitivity is of great importance to the success of *J-PEX* and in Chapter 3, CsI was identified as the most appropriate photocathode for application to the *J-PEX* focal plane detector, to enhance the quantum efficiency of the system. Chemical methods of efficiency enhancement (specifically, nitric acid etching of the front MCP), reported elsewhere as being effective, were found to have little effect on detector efficiency, and were detrimental to the structure of the MCP. Thermal annealing of CsI yielded no further increase in QE, and the absorption coefficient of KBr (which was observed to produce an overall increase in QE) produces a local minimum in the efficiency curve of an MCP at 230 Å, which is not only in the *J-PEX* wavelength band, but close to the important 228 Å He II edge. The poor results obtained from procedures which have been reported positively elsewhere, have been attributed to different MCP glass compositions used in this and other studies. Furthermore, the precise mechanisms by which procedures such as nitric acid etching and thermal annealing can bring about QE increases, are not yet understood.

A further efficiency issue was raised in Chapter 4, with the discovery of low QE in the 6μm pore MCPs originally intended for flight. Investigations with 12μm pore plates revealed that this problem was not restricted to MCPs with small channels, and a search of the literature showed that the phenomenon had been noted elsewhere (Siegmund *et al.*, 1996, Jelinsky *et al.*, 1996). Scanning Electron Microscopy of coated and uncoated MCPs revealed no anomalous features in the structure of the MCPs or coatings. To date, this problem has not been solved, and remains under investigation. A degree of recovery from the problem of low efficiency was achieved in the *J-PEX* detector, by adopting MCPs from a store of old Russian (IKI) units held at Leicester for evaluation (Pearson *et al.*, 1993). When coated with a CsI photocathode, these plates delivered QE values of $\sim$ 15%, compared with $\sim$ 9%

for the 6μm MCPs and more recent plates tested at Leicester. In summary, work on microchannel plate efficiency conducted during this project resulted in the selection of a 12μm pore solid-edge Russian plate coated with a 14,000 Å thick layer of CsI for use in the first flight of *J-PEX*.

Chapter 4 was concerned with the design, development and testing of the *J-PEX* focal plane detector. The detector design owes much to the devices fitted in the *ROSAT* Wide Field Camera, but incorporates advances in MCP and readout technology made since the 1990 launch of *ROSAT*. Although, as stated above, MCPs with 6μm pores were originally intended for use in the detector, their poor QE and a succession of high voltage breakdown events experienced with these plates ruled them out for flight. Following lengthy investigations, the cause of the breakdowns is now believed to be coronal discharge in the residual atmosphere contained within pores covered by the high voltage contacts, which run around the perimeter of both upper and lower surfaces of each plate. This problem was solved by adopting solid edged MCPs, allowing electrical contacts to be made without enclosing channels. No solid edged 6μm MCPs were available, and so 12μm pore units were fitted, chosen for electrical and mechanical stability, and on the basis of their superior sensitivity. During this time, judicious changes were made to the detector design to aid the escape of residual gas from the interior volume, reducing the risk of breakdowns elsewhere in the detector.

Early trials of the detector revealed problems with high background noise levels ($\sim$ 17 counts sec^{-1}); pulse height distributions showed that these events were subject to the full gain of the system, and hence were from a source external to the MCPs. This noise was attributed to field emission from high voltage detector components above the front MCP, and successfully suppressed by implementing a series of design changes. These included re-designing the high voltage contact spring, and introducing a spring shield, to prevent ions or electrons produced by field emission from reaching the MCP stack. These measures were successful in reducing background noise rates to less than 3 counts sec^{-1}, over the entire imaging area. Optimum MCP bias levels were determined, and "tuned" to the high resolution Vernier anode readout developed and provided by MSSL.

Development work carried out in this project resulted in delivery of a detector with a quantum efficiency of $\sim$ 16%, and a spatial resolution of between 15 and 20μm . Excellent electrical stability was achieved, with steady behaviour recorded during the entirety of pre-flight testing and integration work in the months leading up to both sub-orbital flights, and flawless performance during missions 36.162 and 36.195. These missions were intended as a "proof of concept", and were targeted at the brightest DA white dwarf, G191-B2B, to achieve maximum S/N in the short time available. The primary goal of the observations was the detection of helium in the spectrum of the star. In the first flight (NASA 36.162) from White Sands Missile Range (WSMR) on 25$^{\text{th}}$ February 2000, incomplete monitoring of high-altitude winds caused mission termination 43 seconds in to the flight (3 seconds before sustainer burnout). Telemetry indicated that the instrument functioned nominally, and starlight was briefly observed in CCD images as spectrometer tumbled, before power was turned off. The payload obtained no scientific data but was recovered without damage. A proposal to refurbish and refly the instrument was granted, and the second mission (36.195) took place on 21$^{\text{st}}$ February 2001. The highly successful outcome of this flight is described in Chapter 6.

7.2.2 High resolution spectroscopy of hot DA white dwarfs

Two chapters devoted to high resolution studies of white dwarf stars have been presented in this thesis: a survey of circumstellar features observed in a sample of hot DA white dwarfs, and analysis of the spectrum of G191-B2B returned from the first successful flight of *J-PEX*.

In Chapter 5, high resolution data from the E140M grating on the *STIS* instrument onboard the Hubble Space Telescope have been used to search for highly ionised absorption features at non-photospheric velocities, which may be indicative of accretion or recent mass loss in these stars. Such features are already known to exist in four hot DA white dwarfs, which have been included in the sample (Feige 24, REJ 0457-281, G191-B2B and REJ 1614-085). The survey, which also includes data from the earlier *GHRS* instrument on HST, and spectra acquired by *IUE*, has revealed a further three objects in which these features are observed (REJ 1738+665, REJ 0558-373 and WD 2218+706), with similar features also suspected in REJ 2156-546.

A series of studies have been performed in an effort to identify the mechanisms responsible for producing these features. It has been determined that gravitational redshifting of material in the potential well of the white dwarf cannot, in most cases, account for the observed features. Nor is any correlation observed between the presence of circumstellar features and stellar metallicity or predicted mass loss rates. However, the theories used to estimate mass loss rates may be unsuitable for application to white dwarf stars, and considerable difficulty surrounds the consistent and meaningful quantification of their "metallicity", so that these results are of questionable reliability.

Two stars (REJ 1738+665 and G191-B2B) show a correlation between the velocity of circumstellar features and the line of sight ISM; for the remaining stars showing such features, the difference between these velocities is typically less than 10 $\mathrm{km\,s^{-1}}$. The possibility of ionisation of the ISM within a Strömgren sphere around particular stars has therefore been raised. Further interesting similarities are observed between the expansion velocities of highly evolved planetary nebulæ, and the velocity of circumstellar features with respect to the photospheric value. Previous morphological studies show that the presence of planetary nebula remnants around white dwarf stars may explain features which are blueshifted or redshifted with respect to the photosphere, depending on line of sight geometry.

Although work on data returned from *J-PEX* flight 36.195 is ongoing, Chapter 6 contains an account of the reduction of these data and current status of the analysis; these results are already encouraging. A significant obstacle to the accurate extraction of spectral histograms from the flight data has been the lack of reference points for wavelength calibration. This is due to limited pre-flight calibration data, shifts in the spectra from their laboratory-determined positions during flight, and image distortions, possibly due to the presence of E fields above the readout anode. The problems have been overcome by applying a series of cross-correlation analyses to identify appropriate shifts and scalings to align the four spectra, thereby providing reference points for co-addition. Absolute wavelength calibration has been achieved using a combination of reference images (in the form of Penning discharge spectra taken during instrument focus tests) and cross correlation with an existing *EUVE* spectrum of G191-B2B.

While more work remains to be done in reducing the data, the current spectrum is already providing new informa-

tion about this star. The results of an analysis using a homogeneous atmospheric model demonstrate the presence of interstellar helium in the spectrum, with a He II column density of $\sim 6\ (\pm 0.1) \times 10^{17}$ cm^{-2}, and an implied He ionisation fraction of ~ 0.75. This is higher than typical LISM values, and is consistent with the presence of some of the helium in a circumstellar cloud, the existence of which was suggested in Chapter 5. The best fit model spectrum implies that photospheric He II is also present in this star, with an abundance relative to H of $8.23\ (\pm 1.41) \times 10^{-5}$. Other gross features in the data also suggest the presence of some photospheric helium, but no direct detection has been possible: the most significant photospheric line is only marginally detected at the S/N of this data. If the presence of this photospheric helium is confirmed, then the absence of He II features in the *STIS* spectrum of G191-B2B supports the stratified He configuration proposed by Barstow & Hubeny (1998), and provides further justification for the use of the stratified abundance calculations, described in some detail in Chapter 5, which are enjoying considerably greater success than previous theories in determining quantitatively the abundances observed in metal-rich DA white dwarfs.

7.3 Completing the picture: the role of J-PEX in white dwarf research

The observations of which *J-PEX* is capable, are of great importance to studies of white dwarf composition and evolution. This point may be demonstrated by considering the apparently unrelated results described in chapters 5 and 6.

J-PEX data for G191-B2B contain information relating to line of sight column density, and atmospheric composition, and are discussed in Chapter 6. One particularly interesting result is the high He ionisation fraction (0.75) suggested by these data, significantly higher than the "typical" ionisation fractions of 0.2 – 0.5 measured by Barstow *et al.* (1997a). However, as the results of Chapter 5 reveal, this material cannot simply be assumed as entirely interstellar in origin. The existence of highly ionised, non-photospheric features in the spectrum of G191-B2B has been presented as evidence for the possible presence of a circumstellar cloud of material around the star. In view of these observations, it is at least conceivable that some of the He II may reside in this cloud. If a more typical ionisation fraction for interstellar He is assumed (for example, $f_{\rm He} = 0.2 - 0.5$) then the implied column density for interstellar He II is reduced to $0.5 - 2.0 \times 10^{17}$ cm^{-2}; the possibility then exists that the remaining material is located in the same cloud which is responsible for the non-photospheric C IV features. This is of considerable significance: high resolution data has led to the identification of a possible circumstellar cloud around G191-B2B, and provides an alternative explanation for the high interstellar He ionisation fraction obtained from *J-PEX* data. Without evidence for the presence of circumstellar material, the results of the *J-PEX* analysis, taken at face value, would lead to erroneously high estimates for the density of the interstellar column.

Spectroscopic observations provide a wealth of information about the nature (composition, physical conditions and evolutionary history) of white dwarf stars, and can reveal much about the composition of the intervening ISM. Yet without adequate resolution and S/N in the data, these results can be misleading, as the case of G191-B2B demonstrates. While the location of certain observed species may be relatively unambiguous, the nature of many features may only be revealed by high resolution studies of the type presented in Chapter 5, in which

small differences in the velocity of spectral features can be used to detect discrete distributions of material, whether interstellar, circumstellar or photospheric. The availability of such high resolution data permits the composition of white dwarfs to be determined with minimal risk from unrelated "contamination" of abundances, arising from unresolved material in the line of sight. The importance of obtaining adequate S/N in data was demonstrated in Chapter 6, with the loss of long wavelength data in two of the four *J-PEX* spectral tracks leading to a reduction in the detection significance of the 243.3 Å photospheric He line. Observations of such features with increased S/N are required in order to achieve unambiguous identification of photospheric material.

In obtaining the highest resolution spectrum ever recorded in the EUV, *J-PEX* has revealed new information about the composition of G191-B2B. These data are complemented by the extremely high resolution UV data from *STIS*, in the form of velocity-resolved features indicating the presence of circumstellar material. Both sets of observations are vital for a comprehensive understanding of this system; neither *J-PEX* or *STIS* alone can supply these data - hence the need for both studies in this work. However, as discussed in section 7.4, *J-PEX* is in its infancy, and the design has the potential for much higher spectral resolution than the $\lambda/\Delta\lambda \approx 4000$ data obtained in flight 36.195. An order of magnitude improvement in *J-PEX* resolution would allow the instrument to match the velocity sensitivity of the E140M *STIS* grating, while the long exposure times possible with a longer duration orbital mission would improve the signal-to-noise ratio in the data. The performance of such an instrument would provide, for the first time, the resolution and effective area required to measure, directly and unambiguously, the structure and composition of white dwarf stars.

7.4 Future work

7.4.1 The continuing development of J-PEX

Low QE has been a widespread but unpredictable problem of MCPs working in the EUV, caused by an insufficient photoelectron yield in the MCP pores. Recent reports suggest that some success has been achieved in realizing high QE (35% – 40%) in the EUV by careful control of the MCP preparation, but these results have proved difficult to reproduce. Efficiency increases of this order promise a $\sim$ 100% increase in spectrometer throughput, and thus a program of research into solving the QE problem is a vital step in the development of spectrometers of this type. Although chemical treatments such as the deposition of photocathodes clearly have a role to play in this work, the central area of concern is the recent drop in bare glass MCP efficiency. This appears to affect the efficiency gains introduced by all subsequent processing, and therefore the enhancement of bare glass QE must be of the highest priority for future work in this area. The nature of this problem is clearly so fundamental that a solution is most likely to be found by working closely with MCP manufacturers.

A further area of concern is the poor performance of MCPs with 6μm pores, and the instabilities experienced when such plates were fitted to the *J-PEX* detector. Although the low QE experienced with these plates now appears to be consistent with efficiency deficits measured for a wide variety of MCP specifications, electrical instabilities brought about by their use in the detector are a separate and equally serious issue. The results of work described in Chapter 4 suggest that these problems arose as a result of breakdowns in the volume of gas trapped in channels

underneath detector components such as contact plates and springs. These problems, and the issue of low QE, made it necessary to replace the 6μm MCPs with larger pore versions, but their use is clearly desirable in order to maximize the spatial resolution of the instrument. Changes to detector design, such as reshaped electrodes which enclose fewer channels, may help to reduce breakdown problems; however, the improved stability brought about by the use of solid edged plates suggests that more success might be found with the 6μm MCPs if they also were of this design. This possibility is one which must be investigated in collaboration with manufacturers of microchannel plates.

In the current detector design, the high voltage power supply unit (PSU) is attached to the rear of the detector body, aft of the signal amplifiers. Heat generated by the power supply unit can therefore only be dissipated into the detector, leading to two undesirable consequences. First, since the contact area between detector and PSU is small, the level of heat dissipation is low, and hence the PSU is subject to an appreciable increase in temperature when power is applied. PSU output voltage drops steadily as temperature increases, limiting the time over which measurements can be taken, and adversely affecting the quality of calibration work which can be carried out. Second, focus studies performed using the calibration facility at NRL revealed position shifts in spectra of up to 60μm over the course of these tests. While the precise cause of the shifts is currently uncertain, mechanical changes in the detector brought about by heating of the structure are suspected. Successful operation at high resolution requires correspondingly high levels of mechanical stability, and the observation of gross shifts over long periods of time suggest the possibility of more subtle shifts being introduced to data during the flight, leading to a serious degradation of resolution.

A possible solution to these issues is offered by relocation of the high voltage supply to one of the two electronics pallets affixed to the interior wall of the forward payload skin. By separating the heat source from the detector structure and optics plate, considerable enhancements in imaging stability and resolution may be achieved. Additionally, the electronics palette will provide a much larger heat sink, and should allow the heat from the HV unit to be dissipated more efficiently. This modification may therefore lead to PSU operation in thermal equilibrium with the electronics palette, providing a more stable supply in the absence of thermally induced voltage drops. These measures require moderate redesigning of the PSU housing and connections, the electronics palette, and the high voltage interface to the MCP detector, but they represent an important step towards realising the full potential of the spectrometer design. Finally, discussions relating to use of the Diffraction Grating Evaluation Facility (DGEF) at NASA Goddard Spaceflight Centre are currently in progress. This facility was designed for calibrating space optics in the VUV, mainly in support of the Hubble Space Telescope development program. The DGEF offers the possibility of comprehensive end-to-end testing of the detector and imaging systems, in vacuum conditions over long periods of time, and is ideal for the study and characterisation of thermal effects on the instrument. Further, the facility is equipped with a parallel beam EUV source, allowing extremely precise measurements of detector resolution without the need for invasive techniques (such as the introduction of pinhole masks directly into the detector), which have been the source of problems in the past. The availability of this facility for such work would represent a significant step towards calibrating the instrument with a precision commensurate with its theoretical capabilities.

Although modifications to components other than the focal plane detector in the *J-PEX* spectrometer lie outside of the scope of this thesis, it is relevant to note that a program of research and development is currently underway, addressing several issues highlighted by the first successful flight. Specifically, a new grating support structure is to be designed, in order to eliminate small distortions believed to be responsible for a degradation in spectral resolution. Improvements in test facilities will also allow more accurate determination of grating spectral and detector spatial resolution. A further aim of the *J-PEX* program is the replacement of existing laminar ion etched gratings with higher efficiency (η) blazed gratings of larger area. Early tests of blazed gratings in the *J-PEX* program produced unexpectedly low efficiencies, and led to the use of laminar optics in flight. However, subsequent changes in the manufacturing process have improved efficiency, and blazed gratings are now being developed for future *J-PEX* missions. The laminar gratings used in flights 36.162 and 36.195 had an area of 456 cm^2 and a groove efficiency of 28.5%; the goal of the current grating research program is the installation of gratings with an area of 518 cm^2, and a groove efficiency of between 54.0 and 75.0%. Including the benefits from restoration of "nominal" MCP QE levels, this program of upgrades will lead to an increase in throughput of up to a factor of 5. Further, instrument resolution will be improved if small pore MCPs can be fitted in the focal plane detector.

7.4.2 High spectral resolution studies of white dwarfs

As has already been noted, the analysis of data from flight 36.195 is ongoing. One of the most outstanding tasks is to modify the cross-correlation algorithms, which currently apply a single stretch factor across the entire wavelength range of each spectrum. The polynomial wavelength solutions applied to the flight data are simply approximations to the incompletely understood problem of non-linear wavelength scales, and there appears to be little prospect of improved data relating to position-dependent image distortion. Therefore, the application of a spline-like scaling vector to each spectral track before co-addition (and possibly during cross-correlation with the *EUVE* data) is likely to improve resolution in the final co-added spectrum.

The helium abundances determined from the *J-PEX* data have been obtained by comparing flight data with a model based on a homogeneous distribution of material. However, recent work indicates that heavy elements are found in a stratified distribution in white dwarf atmospheres (Barstow & Hubeny, 1998, Barstow *et al.*, 1999b, Dreizler & Schuh, 2001, Schuh & Dreizler, 2001). Justification for adopting homogeneous models in the first analysis of the 36.195 spectrum was provided in Chapter 6, but ultimately, stratified models must be incorporated into the work, in order to determine more accurately the interstellar and photospheric He II abundances and, conversely, to test the ability of such models to reproduce these new and more detailed observational data.

G191-B2B and several other hot DAs show distinct circumstellar components to the C IV and other resonance lines, as demonstrated in the work presented in Chapter 5. Although no firm conclusions were drawn from this study, these features may be remnants of the old planetary nebula or evidence of more recent mass loss. Such material may have enhanced the G191-B2B He II column density above that of the LISM, as discussed in section 7.3. Observations of other stars are required to test this proposition, since, in favorable circumstances, the interstellar and circumstellar components can be resolved due to their differing radial velocities.

A significantly greater number of detections of circumstellar features were found in high resolution *STIS* spectra, than in the lower resolution *IUE* data, while the superior throughput leads to improved signal-to-noise ratio in the data. Greater spectral resolving power permits the identification of lines at progressively smaller velocities with respect to the primary photospheric features. This point was graphically demonstrated by the apparently singular nature of the ISM lines in *STIS* E140M data of G191-B2B, which were subsequently found to be composed of *two* components in the E140H data analysed by Sahu *et al.* (1999). Further, higher S/N data should allow the detection of weaker features in stellar spectra. The possibility clearly exists that more circumstellar features await detection in the stars for which only *IUE* data were available, or in stars where data of the resolution of the E140H data is required before multiple components are resolved. This clearly demonstrates the need for high resolution spectroscopic data covering the entire sample of stars. Comprehensive surveys of these features are essential if potentially informative patterns in their distribution are to be identified. The primary goal of future surveys of this type must therefore be to secure consistently high resolution data (preferably from the *STIS* E140H echelle grating, tuned to the wavelength of the C IV resonance doublet) for all stars included in the sample. Increasing the number of objects in the survey will also lead to a more complete picture of the occurrence of these interesting features.

The He II feature discovered in the spectrum of WD 2218+706 during this work is now the subject of much interest (Barstow *et al.*, 2001). As discussed in Chapter 5, the range of possible masses for this star allows for the object to be the product of either post-RGB evolution (in which case, it will be accompanied by a companion object), or AGB evolution, implying that WD 2218+706 is an isolated star, making the presence of helium in its spectrum a unique and important discovery. The detection of any companion object is therefore of great significance, and a proposal has already been accepted to perform infrared photometry of the star. The aim of this proposal is to detect any colour excess in the object due to the presence of an unresolved companion. Following the method described by Holberg *et al.* (1997a), the J, H and K magnitudes of WD 2218+706 will be compared to models produced by Bergeron *et al.* (1995), for a DA white dwarf of similar temperature and gravity. Such observations will allow limits to be placed on the magnitude of any binary companion using the relationship between the observed magnitude (m_o) and the predicted magnitude (m_p) in each band, i.e.

$$m_c = m_p - 2.5 \log \left[10^{0.4(m_p - m_o)} \right]^{-1} . \tag{7.1}$$

These observations should also allow limits to be placed on the spectral type of any companion object, using the J, H, K spectral data presented by Leggett (1992). Should WD 2218+706 subsequently be confirmed as a binary object, then the presence of He in the spectrum may be understood in terms of mass transfer during the common envelope phase of evolution. Alternatively, if the results indicate that this is an isolated object, then the star may represent the first direct detection of photospheric helium in an isolated hot DA white dwarf. If so, WD 2218+706 will provide an important opportunity to improve our understanding of the evolutionary link between the central stars of planetary nebulæ and the white dwarf cooling sequence.

7.5 J-PEX: the future of EUV spectroscopy?

The 36.195 spectrum of G191-B2B presented in Chapter 6 is testimony to the success of the *J-PEX* design in achieving a spectral resolution, in the EUV band, which is unsurpassed by any other currently available instrument. However, the motivating issue of the He content in hot DA atmospheres remains unresolved. The spectrum provides a very strong indication that it is present, but without direct detection of the photospheric absorption lines no definitive statements can be made. It is important to confirm this result for G191-B2B, and to determine its uniqueness, by observing related objects. The proposed improvements in instrument throughput discussed above will increase the available S/N and spectral resolution; two future reflights of the improved instrument are currently under proposal, with Feige 24, REJ 0457-281, and G191-B2B as potential targets. Not only will improvements in the performance of *J-PEX* allow the outstanding issues relating to G191-B2B to be resolved, but they will also permit an expansion of the science goals for the normal-incidence EUV spectrometer program - for example, the complete white dwarf population could be surveyed, allowing a comparison between stars at different stages of evolution to be made. However, rocket flights are limited to short duration observations of a small number of bright targets, and such an ambitious program will only be possible if *J-PEX* can be flown on a long-duration orbital platform, much as early sounding rocket flights led to the presence of the Wide Field Camera onboard *ROSAT* (Barstow, 1983).

The *Astrophysical Plasma Explorer* (NRL, 1997) is a mission proposal based on a long-duration orbiting observatory consisting of four *J-PEX* spectrometers, capable of achieving simultaneously high resolving power (7,600 – 36,000) and offering a large effective area (5 – 20 cm^2). The higher resolution limit corresponds to a velocity resolution of ~ 8 km s^{-1}, which is sufficiently sensitive to begin detecting multiple velocity components in spectral features - the importance of this capability has already been discussed in section 7.3. The individual spectrometers would be fitted with gratings of different ruling densities and a variety of multilayer coatings, to expand the spectral range of the observatory from $\sim$ 100 to $\sim$300 Å. As in the case of the sounding rocket instrument, an optical telescope would be included for accurate aspect reconstruction. The instrument would be suited to platforms such as those used in the NASA SMEX (small explorer) or MIDEX (medium class explorer) programs. Figure 7.1 shows one possible design for the satellite.

In addition to white dwarf research, a wide variety of other fields would benefit from the availability of a *J-PEX* spectrometer on a long duration platform. Spectroscopy is an indispensable tool for measuring the composition, temperature, density, velocity and magnetic field of astrophysical plasmas. EUV wavelengths are useful for studying the origin and composition of the LISM, measuring the ionisation balance of He, and determining the abundances of heavy elements. EUV spectra are also important in the study of accretion processes (using observations of objects such as magnetic and non-magnetic Cataclysmic Variables, or CVs), and for determining the structure and origins of coronal plasmas and flaring activity in active stars. Furthermore, high resolution EUV spectroscopy is important in answering certain cosmological problems, such as determining the abundance of ^{3}He which, along with the D abundance (already estimated from observations of white dwarfs (Sahu *et al.*, 1999)), can place a lower limit on the baryon density of the universe. Such observations would improve our understanding of the relation between stellar evolution and the composition of the galaxy (e.g. Galli *et al.*, 1997, Olive *et al.*, 1995).

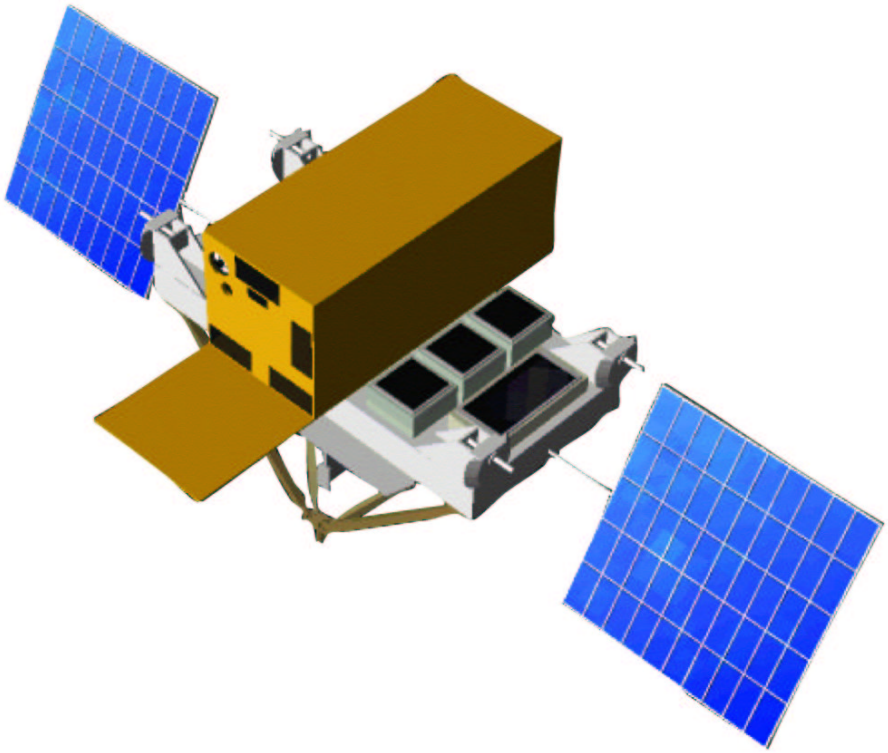

Figure 7.1: An artists impression of the APEX mission, which would carry four spectrometers of the *J-PEX* design.

Missions such as *EUVE*, *Chandra* and *XMM-Newton* have already moved astronomical spectroscopy into the EUV and X-ray wavebands. Future instruments must achieve higher resolution, in order to resolve spectral lines unambiguously and to determine line profiles and Doppler shifts at new levels of precision. MCP photocathodes and multilayer coated optics reach high efficiencies in the EUV waveband, and normal-incidence optics, with potentially large collecting areas, become possible, making the *J-PEX* spectrometer design ideal for studying the EUV sky at unprecedented levels of detail. A facility based on this design could play a central role in studying the physics and evolution of stars and galaxies, and of the interstellar and intergalactic gas. The *J-PEX* sounding rocket program described in this thesis represents the first step in developing a normal incidence, high resolution EUV spectrometry facility - a satellite with the potential to become one of the most important instruments in a new generation of high energy orbiting observatories.

APPENDIX A

COATING PROCEDURES

This appendix consists of material from an in-house manual for MCP coating operations, produced by J.F.Pearson (Leicester University).

In the preparation of X-ray photocathodes for MCP detectors, there are two major problems: (1) defining a suitable coating geometry and (2) protecting unstable materials from water vapour.

In many cases we are trying to coat 0° bias MCPs, i.e. the channels are perpendicular to the front surface. To be effective, the photocathode must be applied to the inside of the channels and penetrate several channel diameters. To achieve a uniform coating around each channel, the MCP must be a 'long' way away from the source and must also be rotated during evaporation. A further complication is that for best results the MCP should be at a temperature of at least 100°C during the evaporation.

All the high yield photocathodes that are presently in use are very sensitive to water vapour. The evaporation material and the finished photocathode must therefore be kept dry. In practice this means that all coating, transfer and assembly operations must be done in a dry nitrogen gas atmosphere. The vacuum chamber must also be let up to dry nitrogen and not laboratory air.

Cleanliness is also important for the future correct operation of a coated MCP, so the number and size of dust particles in the air are monitored when the MCP is being transferred into and out of the coating system (we use a Climate particle monitor).

A.1 Preparation for coating

MCPs are vacuum baked and coated in special stainless steel coating holders. A number of different holders exist for use with differing size and shape of MCPs. The small holders have a number of differing inserts to take varying diameter MCPs.

The holders are cleaned before use by washing in distilled water to remove any traces of CsI and then wiping with

IPA. The holder is then allowed to dry, either naturally or with a light bake in an oven. The correct internal holder and coating mask are then selected.

The MCPs are installed into their holders in a cleanroom or laminar flow cabinet, and then transferred to the vacuum furnace where they are baked out under vacuum at 275-300°C for at least 48 hours.

A.1.1 Calculation of coating angle

The required coating angle depends on the incident angle of the radiation to be detected. This angle must then be set up in the coating system when the MCP is installed, and is defined as the angle, α, (fig A.1) between the nominal centre of the evaporation boat and the centre of the MCP front surface. The coating angle is set up by adjusting the distance, s, between the boat and MCP centres, and is calculated by trigonometry, taking the vertical height, h, to be 762mm (or 1017mm if the AXAF extension tube is on).

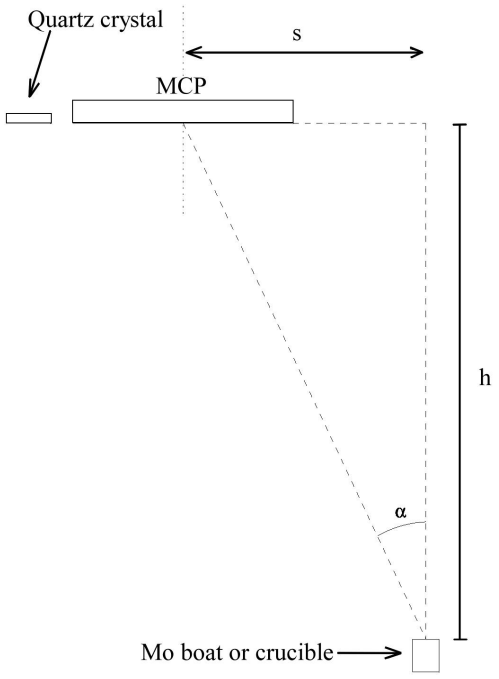

Figure A.1: Coating geometry for MCP photocathode deposition. h is the vertical height between the boat and the MCP surface, s is the horizontal separation between the boat centre and the MCP centre.

In the Leicester vacuum evaporator, two angular ranges are accessible because the boat flange can be inserted in either position A, closest to the tank centre or position B closest to the tank wall (fig A.2). Position A gives a range of 0 to 7.5°, while position B gives a range of 7.5 to 14.7°. Within each range, the angle is adjusted by moving the MCP flange through a linear range of 100mm. The overhead position, i.e. 0° in range A has a linear offset of 1.5mm. The distance between the two boat positions is 100mm.

For example to set a coating angle of 4°:

Horizontal separation s = 762 × tan(4)

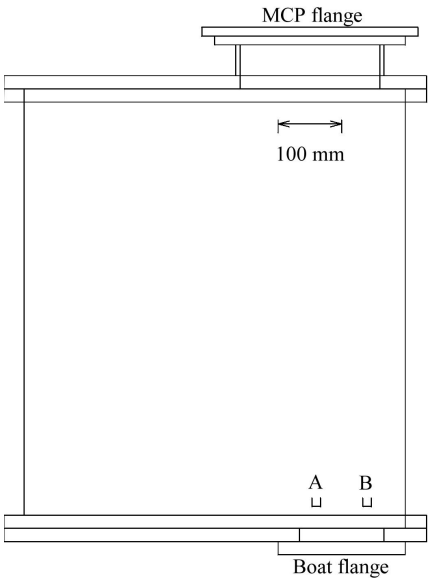

Figure A.2: Schematic showing the two alternative boat positions, A and B, and the range of movement of the MCP centre. Note that the centre of MCP rotation is offset from the centre of the MCP flange by 15mm.

= 53.3mm

Drive reading = Horizontal separation + zero offset

= 53.3 + 1.5

= 54.8 mm

A.1.2 Pre-clean of molybdenum boat

The chamber is pumped down without the MCP but with the empty molybdenum boat in place. When the pressure has dropped below 2×10^{-5} mbar the boat should be cleaned by heating it to a higher temperature than will be used during evaporation. To do this we switch on the auxiliary power circuit and the boat heater panel, gradually increasing the power applied to the boat to 110% of the current required for the evaporation. This value is held for 5 minutes, then both the boat heater panel and the auxiliary power circuit are switched off. The precise currents used will depend on the boat or crucible in use (see Table A.1).

Boat or crucible	Voltage (V)	Current (Amps)
7mm*7mm*40mm Mo boat	10	100
8mm*10mm*40mm Mo boat	10	115
Crucible (alumina oxide)	10	65

Table A.1: Typical currents used for pre-cleaning of boats and crucibles

A.1.3 Loading of boat

The crucible is placed in a nitrogen rich dry bag, from which the transfer of CsI can take place. Once the desired amount of CsI is collected the boat is swiftly returned to the chamber and placed in the basket. At all times the vacuum chamber is purged with nitrogen until the chamber door is sealed.

It is possible to fit extension bars onto the electrical feedthroughs of the boat flange to reduce the distance between the boat and substrate. The reduced distance allows faster coating rates and substantially reduces the amount of raw material required to produce a film of a given thickness, but will produce a larger range of coating angles across the MCP substrate.

A.1.4 CsI pre-heat

In order to remove any residual traces of water vapour the CsI should be slowly heated up after the pressure has fallen below 5×10^{-6} mbar. To do this, we apply an initial boat current as specified in table A.2 and increase it in 5 Amp steps every 4 minutes until a small amount of evaporation is noted on the Edwards FTM4 quartz crystal film thickness monitor. The current at which this happens will vary from one boat to another (typical values are also given in table A.2).

Other alkali halides require similar currents, but MgF_2 requires a much hotter boat; a different design is required to achieve this.

After the boat has been allowed to cool for a few minutes the system is ready to use.

Boat or crucible	Voltage (V)	Initial current (A)	Starting current (A)	Evaporation current (A)
7mm*7mm*40mm Mo boat	10	30	65	65
8mm*10mm*40mm Mo boat	10	60	95	95
Crucible (Alumina oxide)	10	35	60	65

Table A.2: Typical currents for starting pre-heating, first signs of evaporation and normal evaporation of CsI from the available boats and crucibles. All currents in Amps.

A.2 Coating an MCP

The following steps are taken:

1. Load the MCP from the bakeout system to the heater block/mounting flange on the underside of the chamber door.
2. Set up required linear offset to give the desired coating angle.
3. The chamber is then pumped down to pressure better than 5×10^{-6} mbar.

4. The MCP is heated to ∼100°C, the temperature being constantly measured by a thermistor in the mounting flange.

5. The MCP heater is then switched off when the temperature reaches 90°C. If this is not done, residual voltage on the heater may cause a fuse to blow during Gas Glow Discharge cleaning.

6. Gas Glow Discharge clean is activated by opening a leak valve to the chamber and then applying a voltage to the discharge arm. A discharge of about 2 A should be observed. At this point the tank pressure should be approximately 2×10^{-2}mbar. The voltage is constantly monitored to maintain a 2 A discharge current for 10 mins.

7. In order now to stabilize the MCP heater temperature, the heater controller is switched on and set to ∼20% of full power. The system is now ready to begin evaporation.

8. Power is now applied to the boat to begin warming. The boat current is set to 5 A less than is required to begin evaporating the material during CsI pre-heat. While the boat is warming, data is keyed into the FTM4 film thickness monitor. Typical values for a 14000 Å CsI coating are given in table A.3. The density and acoustic impedance are a function of the coating material, with values for some of the common materials being presented in table A.4.

Thickness set point	20000
Tooling factor	100.0
Crystal factor	6.98, 6.97
Frequency	5.997, 5.980

Table A.3: FTM4 typical crystal parameters

Photocathode	CsI	CsBr	MgF_2	CsCl	Al	Au	CuI	KBr	Nichrome
Material density	4.510	4.440	3.140	3.988	2.700	19.30	5.620	2.750	8.370
Acoustic impedance	7.000	7.000	11.40	7.000	8.170	23.18	7.000	7.000	26.71

Table A.4: FTM4 parameters for various coating materials

9. Once the shutter is opened on the FTM4 monitor, the boat current can slowly be increased until evaporation begins, and at this point the motor which rotates the top flange/door and MCP is started; this produces a more even coat. The current is increased by 5 A every 5 mins until the desired coating rate is achieved (ideally 20-40 Å/sec). If the boat current is increased too quickly, thermal lag can produce a very fast evaporation, for which one tends to over-compensate, and hence incur a period of slow or zero evaporation.

10. When the required thickness is reached a boat shutter is rotated into place over the photocathode stream. The system is left to pump overnight, letting the substrate cool.

11. The channel plate is finally removed and installed into its detector body in a glove box or dry bag purged with dry nitrogen.

BIBLIOGRAPHY

Aannestad, P. A. & Sion, E. M. *Astron. J.*, **90**, 1832–1836, September 1985.

Abbott, D. C. *Ap.J.*, **259**, 282–301, August 1982.

Adams, T. F. & Frisch, P. C. *Ap.J.*, **212**, 300–308, February 1977.

Aller, L. H. *Atoms, stars, and nebulae*. Cambridge: Harvard University Press, 1971.

André, J., Sammar, A., Kahn Malek, C., Troussel, P., Bac, S., Barchewitz, R., Pardo, B., Berrouane, H., Moreno, T., Ladan, F. R., Rivoira, R. & Schirmann, D. *Rev. Sci. Instr.*, **63**, 1399–1403, January 1992.

Auer, L. H. & Shipman, H. L. *Ap.J. (Letters)*, **211**, L103–L105, January 1977.

Bannister, N. P., Barstow, M. A., Holberg, J. B. & Bruhweiler, F. C. STIS observations of five hot DA white dwarfs. In Shipman, H. L. & Provencal, J. L., editors, *Proceedings of the 12th European White Dwarf Workshop*, pages 105–110. ASP Conf. Series, 2001.

Barbee, T. W. *Rev. Sci. Instr.*, **60**, 1588–1595, July 1989.

Barbera, M., Collura, A., Dara, A., Leone, M., Powell, F. R., Serio, S., Varisco, S. & Zombeck, M. V. *Exp. Astron.*, **7**, 51–63, 1997.

Barstow, M. A. *A Wide Field Ultrasoft X-ray camera for astronomy*. PhD thesis, University of Leciester, 1983.

Barstow, M. A. ROSAT - an all-sky X-ray and EUV survey of white dwarfs. In *IAU Colloq. 114: White Dwarfs*, pages 156–159, 1989.

Barstow, M. A. *Contemp. Phys.*, **37**(5), 359–374, 1996.

Barstow, M. A., Bannister, N. P., Holberg, J. B., Hubeny, I., Bruhweiler, F. C. & Napiwotzki, R. *Mon. Not. R. Astr. Soc.*, **325**, 1149–1156, August 2001.

Barstow, M. A., Burleigh, M. R., Bannister, N. P., Holberg, J. B. & Hubeny, I. FUSE observations of the hottest DA white dwarfs. In Shipman, H. L. & Provencal, J. L., editors, *Proceedings of the 12th European White Dwarf Workshop*, pages 94–100. ASP Conf. Series, 2001a.

Barstow, M. A., Burleigh, M. R., Bannister, N. P., Holberg, J. B., Hubeny, I., Bruhweiler, F. C. & Napiwotzki, R. Heavy elements in DA white dwarfs. In Shipman, H. & Provencal, J., editors, *Proceedings of the 12th European White Dwarfs Workshop*, pages 128–134. ASP Conf. Series, 2001b.

Barstow, M. A., Dobbie, P. D., Holberg, J. B., Hubeny, I. & Lanz, T. *Mon. Not. R. Astr. Soc.*, **286**, 58–76, March 1997a.

Barstow, M. A., Fleming, T. A., Diamond, C. J., Finley, D. S., Sansom, A. E., Rosen, S. R., Koester, D., Holberg, M. C., Marsh, J. B. & Kidder, K. *Mon. Not. R. Astr. Soc.*, **264**, 16+, September 1993.

Barstow, M. A., Fraser, G. W. & Milward, S. R. *Proc.SPIE*, **597**, 352–361, 1986.

Barstow, M. A., Holberg, J. B., Cruise, A. M. & Penny, A. J. *Mon. Not. R. Astr. Soc.*, **290**, 505–514, September 1997b.

Barstow, M. A., Holberg, J. B., Hubeny, I. & Lanz, T. Heavy elements in white dwarf envelopes. In *ASSL Vol. 214: White dwarfs*, pages 237–243. Kluwer, 1997c.

Barstow, M. A., Holberg, J. B., Hubeny, I., Lanz, T., Bruhweiler, F. C. & Tweedy, R. W. *Mon. Not. R. Astr. Soc.*, **279**, 1120–1136, April 1996.

Barstow, M. A., Holberg, J. B. & Koester, D. *Mon. Not. R. Astr. Soc.*, **268**, L35–+, May 1994a.

Barstow, M. A., Holberg, J. B. & Koester, D. *Mon. Not. R. Astr. Soc.*, **274**, L31–L36, May 1995.

Barstow, M. A., Holberg, J. B., Marsh, M. C., Tweedy, R. W., Burleigh, M. R., Fleming, T. A., Koester, D., Penny, A. J. & Sansom, A. E. *Mon. Not. R. Astr. Soc.*, **271**, 175–182, November 1994b.

Barstow, M. A. & Hubeny, I. *Mon. Not. R. Astr. Soc.*, **299**, 379–388, September 1998.

Barstow, M. A., Hubeny, I. & Holberg, J. B. *Mon. Not. R. Astr. Soc.*, **299**, 520–534, September 1998.

Barstow, M. A., Hubeny, I. & Holberg, J. B. Evidence for the stratification of Fe in the photosphere of G191-B2B. In Solheim, J.-E. & Meištas, E., editors, *ASP Conf. Ser. 169: 11th European Workshop on White Dwarfs*, pages 479+, 1999a.

Barstow, M. A., Hubeny, I. & Holberg, J. B. *Mon. Not. R. Astr. Soc.*, **307**, 884–894, August 1999b.

Barstow, M. A. & Sansom, A. E. *Proc.SPIE*, **1344**, 244–254, November 1990.

Barstow, M. A., Schmitt, J. H. M. M., Clemens, J. C., Pye, J. P., Denby, M., Harris, A. W. & Pankiewicz, G. S. *Mon. Not. R. Astr. Soc.*, **255**, 369–378, April 1992.

Barstow, M. A., Wesemael, F., Holberg, J. B., Buckley, D. A. H., Stobie, R. S., Mittaz, J. P. D., Fontaine, G., Rosen, S. R., Demers, S., Lamontagne, R., Irwin, M. H., Bergeron, P., Kepler, S. O. & Vennes, S. *Mon. Not. R. Astr. Soc.*, **267**, 647+, April 1994c.

Bergeron, P., Wesemael, F. & Beauchamp, A. *Publ. Astron. Soc. Pacific*, **107**, 1047+, November 1995.

Bloecker, T. *Acta Astronomica*, **43**, 305–313, October 1993.

Bohlin, R. C., Colina, L. & Finley, D. S. *Astron. J.*, **110**, 1316+, September 1995.

Bruhweiler, F., Barstow, M., Holberg, J. & Sahu, M. The Unusual C IV Absorption in the Spectrum of the DA White Dwarf G191-B2B. In *American Astronomical Society Meeting*, volume 195, pages 3602+, December 1999.

Bruhweiler, F. C. & Kondo, Y. *Ap.J. (Letters)*, **248**, L123–L127, September 1981.

Bruhweiler, F. C. & Kondo, Y. *Ap.J.*, **259**, 232–243, August 1982.

Buzulutskov, A., Breskin, A. & Chechik, R. *Nucl. Instr. and Meth. (A).*, **366**, 410–412, 1995.

Chandrasekhar, S. *Ap.J.*, **74**, 81+, July 1931.

Chandrasekhar, S. *Mon. Not. R. Astr. Soc.*, **95**, 226+, January 1935.

Chandrasekhar, S. *The mathematical theory of black holes*. Research supported by NSF. Oxford/New York, Clarendon Press/Oxford University Press (International Series of Monographs on Physics. Volume 69), 1983, 663 p., 1983.

Chayer, P., Fontaine, G. & Wesemael, F. *Ap.J. (Supp.)*, **99**, 189+, July 1995a.

Chayer, P., Kruk, J. W., Ake, T. B., Dupree, A. K., Malina, R. F., Siegmund, O. H. W., Sonneborn, G. & Ohl, R. G. *Ap.J. (Letters)*, **538**, L91–L94, July 2000.

Chayer, P., Leblanc, F., Fontaine, G., Wesemael, F., Michaud, G. & Vennes, S. *Ap.J. (Letters)*, **436**, L161–L164, December 1994.

Chayer, P., Vennes, S., Pradhan, A. K., Thejll, P., Beauchamp, A., Fontaine, G. & Wesemael, F. *Ap.J.*, **454**, 429+, November 1995b.

Clemens, J. C., Nather, R. E., Winget, D. E. & 27 co-authors. *Ap.J.*, **391**, 773–783, June 1992.

Cruddace, R., Paresce, F., Bowyer, S. & Lampton, M. *Ap.J.*, **187**, 497–504, February 1974.

Cruddace, R. G., Barstow, M. A., Barbee, Jr. T. W.and Brown, C. M., Culhane, J. L., Doschek, G. A., Fritz, G. G., Kowalski, M. P. & Seely, J. F. A study of the physics and composition of white dwarf atmospheres using high resolution EUV spectroscopy. Technical report, NRL, 1997. NRA 96-OSS-02.

Dahn, C. C., Harrington, R. S., Kallarakal, V. V., Guetter, H. H., Luginbuhl, C. B., Riepe, B. Y., Walker, R. L., Pier, J. R., Vrba, F. J., Monet, D. G. & Ables, H. D. *Astron. J.*, **95**, 237–246, January 1988.

D'Antona, F. & Mazzitelli, I. *An. Rev. Astron. Astrophys.*, **28**, 139–181, 1990.

Dgani, R. & Soker, N. *Ap.J.*, **495**, 337+, March 1998.

Dickey, J. M. & Lockman, F. J. *An. Rev. Astron. Astrophys.*, **28**, 215–261, 1990.

Dobbie, P. D. *EUV observations of opacities along the lines of sight to and in the photospheres of hot hydrogen rich white dwarfs*. PhD thesis, University of Leicester, September 1999.

Dreizler, S. & Schuh, S. Stratified non-LTE model atmospheres for hot white dwarfs. In Shipman, H. L. & Provencal, J. L., editors, *Proceedings of the 12th European White Dwarf Workshop*, pages 69–78. ASP Conf. Series, 2001.

Dreizler, S. & Werner, K. *Astron. Astrophys.*, **314**, 217–232, October 1996.

Dreizler, S. & Wolff, B. *Astron. Astrophys.*, **348**, 189–197, August 1999.

Driebe, T., Schoenberner, D., Bloecker, T. & Herwig, F. *Astron. Astrophys.*, **339**, 123–133, November 1998.

Drilling, J. S. & Schoenberner, D. *Astron. Astrophys.*, **146**, L23–+, May 1985.

Dupree, A. K. *An. Rev. Astron. Astrophys.*, **24**, 377–420, 1986.

Dupree, A. K. & Raymond, J. C. *Ap.J. (Letters)*, **263**, L63–L67, December 1982.

Dupree, A. K. & Raymond, J. C. *Ap.J. (Letters)*, **275**, L71–L75, December 1983.

Dupuis, J., Chayer, P., Vennes, S. ., Christian, D. J. & Kruk, J. W. *Ap.J.*, **537**, 977–992, July 2000.

Emerson, D. *Interpreting astronomical spectra*. Chichester, UK: Wiley, 1996.

Finley, D. S., Koester, D. & Basri, G. *Ap.J.*, **488**, 375+, October 1997.

Fleming, T. A., Liebert, J. & Green, R. F. *Ap.J. (Letters)*, **308**, 176–189, September 1986.

Fowler, R. H. *Mon. Not. R. Astr. Soc.*, **87**, 114+, December 1926.

Fraser, G. W. *Nucl. Instr. and Meth. (A).*, **195**, 523, 1982.

Fraser, G. W. *Nucl. Instr. and Meth. (A).*, **206**, 251, 1983a.

Fraser, G. W. *Nucl. Instr. and Meth. (A).*, **206**, 265, 1983b.

Fraser, G. W. *X-ray detectors in astronomy*. Cambridge Astrophysics series. Cambridge University Press, 1989.

Fraser, G. W., Barstow, M. A., Pearson, J. F., Whiteley, M. J. & M.Lewis. *Nucl. Instr. and Meth. (A).*, **224**, 272, 1984.

Fraser, G. W., Barstow, M. A., Whiteley, M. J. & Wells, A. *Nature*, **300**, 509–511, December 1982.

Frisch, P. C. & York, D. G. *Ap.J. (Letters)*, **271**, L59–L63, August 1983.

Fritz, M. L., Leckenby, H. J. & Sion, E. M. *Astron. J.*, **99**, 908–916, March 1990.

Fruscione, A., Hawkins, I., Jelinsky, P. & Wiercigroch, A. *Ap.J. (Supp.)*, **94**, 127–146, August 1994.

Galli, D., Stanghellini, L., Tosi, M. & Palla, F. *Ap.J.*, **477**, 218+, March 1997.

Golembiewski, C. M., Cruddace, R. G. & Kowalski, M. P. *Proc.SPIE*, **3445**, 197–204, November 1998.

Green, P. J., Ali, B. & Napiwotzki, R. *Ap.J.*, **540**, 992–1004, September 2000.

Greenstein, J. L. *Ap.J.*, **276**, 602–620, January 1984.

Grevesse, N. & Sauval, A. J. *Space Science Reviews*, **85**, 161–174, August 1998.

Gry, C. *Space Science Reviews*, **78**, 239–246, October 1996.

Hambly, N. C., Smartt, S. J. & Hodgkin, S. T. *Ap.J. (Letters)*, **489**, L157–+, November 1997.

Hansen, B. M. S. *Ap.J.*, **520**, 680–695, August 1999.

Hearn, D. R., Richardson, J. A., Bradt, H. V. D., Clark, G. W., Lewin, W. H. G., Mayer, W. F., McClintock, J. E., Primini, F. A. & Rappaport, S. A. *Ap.J. (Letters)*, **203**, L21–L24, January 1976.

Hecht, E. *Optics*. Addison Wesley, 2nd edition, 1987.

Hemphill, R., Edelstein, J. & Rogers, D. *Applied Optics*, **36**(7), 1421–1426, March 1997.

Hernanz, M., Garcia-Berro, E., Isern, J., Mochkovitch, R., Segretain, L. & Chabrier, G. *Ap.J.*, **434**, 652–661, October 1994.

Holberg, J. B., Barstow, M. A., Bruhweiler, F. C. & Collins, J. *Astron. J.*, **111**, 2361+, June 1996.

Holberg, J. B., Barstow, M. A., Bruhweiler, F. C., Hubeny, I. & Green, E. M. *Ap.J.*, **517**, 850–858, June 1999a.

Holberg, J. B., Barstow, M. A., Bruhweiler, F. C. & Sion, E. M. *Ap.J.*, **453**, 313+, November 1995a.

Holberg, J. B., Barstow, M. A. & Green, E. M. *Ap.J. (Letters)*, **474**, L127+, 1997a.

Holberg, J. B., Barstow, M. A., Lanz, T. & Hubeny, I. *Ap.J.*, **484**, 871+, 1997b.

Holberg, J. B., Barstow, M. A. & Sion, E. M. Photospheric and Non-Photospheric Features in the Spectra of Hot White Dwarfs. In *The Third Conference on Faint Blue Stars*, pages 331+, 1997c.

Holberg, J. B., Barstow, M. A. & Sion, E. M. *Ap.J. (Supp.)*, **119**, 207–238, December 1998.

Holberg, J. B., Barstow, M. A. & Sion, E. M. Elemental abundances in hot white dwarfs. In *ASP Conf. Ser. 169: 11th European Workshop on White Dwarfs*, pages 485+, 1999b.

Holberg, J. B., Bruhweiler, F. C. & Andersen, J. *Ap.J.*, **443**, 753–763, April 1995b.

Holberg, J. B., Bruhweiler, F. C., Barstow, M. A. & Dobbie, P. D. *Ap.J.*, **517**, 841–849, June 1999c.

Holberg, J. B., Bruhweiler, F. C., Barstow, M. A. & Dobbie, P. D. Probing the Local ISM with Hot White Dwarfs. In *American Astronomical Society Meeting*, volume 195, pages 7201+, December 1999d.

Hubeny, I., Heap, S. R. & Lanz, T. M. Analysis of the Spectrum of the z=2.73 Galaxy, MS1512-cB58: A Unified Model of the Stellar and Interstellar Contributions. In *American Astronomical Society Meeting*, volume 196, pages 2914+, May 2000.

Iben, I. & MacDonald, J. The Born Again AGB Phenomenon. In *Lecture Notes in Physics Vol. 443: White Dwarfs*, pages 48+, 1995.

Iben, I., J. & Tutukov, A. V. *Ap.J.*, **282**, 615–630, July 1984.

Jelinsky, S. R., Siegmund, O. H. & Mir, J. A. *Proc.SPIE*, **2808**, 617–625, October 1996.

Kahn, S. M., Wesemael, F., Liebert, J., Raymond, J. C., Steiner, J. E. & Shipman, H. L. *Ap.J.*, **278**, 255–265, March 1984.

Keski-Kuha, R. A. M., Thomas, R. J., Gum, J. S. & Condor, C. E. *Applied Optics*, **29**, 4529–4531, November 1990.

Kingsburgh, R. L., Barlow, M. J. & Storey, P. J. *Astron. Astrophys.*, **295**, 75–100, March 1995.

Koester, D. *Ap.J.*, **342**, 999–1002, July 1989.

Kowalski, M. P., Barbee, T. W., Heidemann, K. F., Gursky, H., Rife, J. C., Hunter, W. R., Fritz, G. G. & Cruddace, R. G. *Applied Optics*, **38**, 6487–6493, November 1999.

Kowalski, M. P., Cruddace, R. G., Seely, J. F., Rife, J. C., Hunter, W. R. & Barbee, Jr., T. W. *J. Electron Spect. & Rel. Phenom.*, **80**, 473–476, 1996.

Kowalski, M. P., Fritz, G. G., Cruddace, R. G., Unzicker, A. E. & Swanson, N. *Applied Optics*, **25**, 2440–2446, July 1986.

Kowalski, M. P., Seely, J. F., Goray, L. I., Hunter, W. R. & Rife, J. C. *Applied Optics*, **36**, 8939–8943, December 1997.

Kun, M. *Ap.J. (Supp.)*, **115**, 59+, March 1998.

Labov, S. E. & Bowyer, S. *Ap.J.*, **371**, 810–819, April 1991.

Lallement, R., Ferlet, R., Lagrange, A. M., Lemoine, M. & Vidal-Madjar, A. *Astron. Astrophys.*, **304**, 461+, December 1995.

Lampton, M., Margon, B., Paresce, F., Stern, R. & Bowyer, S. *Ap.J. (Letters)*, **203**, L71–L74, January 1976.

Langill, P. P., Kwok, S. & Hrivnak, B. J. *Publ. Astron. Soc. Pacific*, **106**, 736–744, July 1994.

Lanz, T., Barstow, M. A., Hubeny, I. & Holberg, J. B. *Ap.J.*, **473**, 1089+, December 1996.

Lanz, T. & Hubeny, I. *Ap.J.*, **439**, 905–916, February 1995.

Lapington, J. S. High performance MCP-based imaging detector. In *Proc.SPIE*, volume 2518, 1995.

Lapington, J. S., Breeveld, A. A., Edgar, M. L. & Trow, M. W. *Nucl. Instr. and Meth. (A).*, **310**, 299, 1991.

Lapington, J. S., Sanderson, B., Worth, L. B. C. & Tandy, J. A. *Nucl. Instr. and Meth. (A).*, (In press), 1999.

Lapington, J. S., Sanderson, B. S. & Worth, L. B. *Proc.SPIE*, **3445**, 535–545, November 1998.

Lapington, J. *Nucl. Instr. and Meth. (A).*, **392**, 336–340, 1997.

Lawlor, T. M. & MacDonald, J. The Born Again Phenomena and its Relationship to Hydrogen Deficient Post-AGB Objects. In Shipman, H. & Provencal, J., editors, *Proceedings of the 12th European White Dwarfs Workshop*, pages 20–26. ASP Conf. Series, 2001.

Lees, J. E., Fraser, G. W., Pearce, S. E., Pearson, J. F., Shchemelev, V. N., Pavlov, A. P. & Shulakov, A. S. *Nucl. Instr. and Meth. (A).*, **381**, 453–461, 1996.

Lees, J. E., Fraser, G. W., Willingale, R. & Spragg, J. E. *Nucl. Instr. and Meth. (A).*, **332**, 570–574, 1993.

Lees, J. E. & Pearson, J. F. *Nucl. Instr. and Meth. (A).*, **384**, 410–424, 1997.

Leggett, S. K. *Ap.J. (Supp.)*, **82**, 351–394, September 1992.

Liebert, J., Dahn, C. C. & Monet, D. G. *Ap.J.*, **332**, 891–909, September 1988.

Livio, M. The Progenitors of Type Ia Supernovae. In *Type Ia Supernovae, Theory and Cosmology*, pages 33+, 2000.

MacDonald, J. *Ap.J.*, **394**, 619–627, August 1992.

Mack, J. E., Paresce, F. & Bowyer, S. *Applied Optics*, **15**, 861+, April 1976.

Margon, B., Malina, R., Bowyer, S., Cruddace, R. & Lampton, M. *Ap.J. (Letters)*, **203**, L25–L28, January 1976.

Marsh, M. C. *An EUV selected sample of DA white dwarfs from the ROSAT all sky survey.* PhD thesis, University of Leicester, 1995.

Marsh, M. C., Barstow, M. A., Buckley, D. A., Burleigh, M. R., Holberg, J. B., Koester, D., O'Donoghue, D., Penny, A. J. & Sansom, A. E. *Mon. Not. R. Astr. Soc.*, **287**, 705–721, June 1997a.

Marsh, M. C., Barstow, M. A., Buckley, D. A., Burleigh, M. R., Holberg, J. B., Koester, D., O'Donoghue, D., Penny, A. J. & Sansom, A. E. *Mon. Not. R. Astr. Soc.*, **286**, 369–383, April 1997b.

Martin, A. P. *MCP Optics*. PhD thesis, University of Leicester, Space Research Centre, Dept. Physics & Astronomy, University of Leicester, University Road, Leicester, LE1 7RH, UK., 2000.

Maxted, P. F. L., Marsh, T. R. & North, R. C. *Mon. Not. R. Astr. Soc.*, **317**, L41–L44, September 2000.

Meier, R. R. & Weller, C. S. *J. Geophys. Res.*, **79**, 1575, 1974.

Mestel, L. *Mon. Not. R. Astr. Soc.*, **112**, 583+, 1952.

Mihalas, D. *Stellar atmospheres /2nd edition/*. San Francisco, W. H. Freeman and Co., 1978. 650 p., 1978.

Milward, S. R. *XUV Calibrations and Electron Background Reduction for the ROSAT Wide Field Camera*. PhD thesis, University of Leicester, 1986.

Moore, P. *Astronomers' Stars*, chapter 5, pages 46–57. W. W. Norton & Co., 1989.

Napiwotzki, R. *Astron. Astrophys.*, **322**, 256–265, June 1997.

Napiwotzki, R. *Astron. Astrophys.*, **350**, 101–119, October 1999.

Napiwotzki, R. & Schönberner, D. *Ap.J.*, **301**, 545+, September 1995.

NRL. The Astrophysical Plasma Explorer. Mission Proposal Document NRL Proposal T-062-8, Naval Research Laboratory, E.O.Hulbert Center for Space Research, Code 7620, 4555 Overlook Avenue, SW, Washington DC 20375-5352, USA, 1997.

Olive, K. A., Rood, R. T., Schramm, D. N., Truran, J. & Vangioni-Flam, E. *Ap.J.*, **444**, 680–685, May 1995.

Paerels, F. B. S., Bleeker, J. A. M., Brinkman, A. C. & Heise, J. *Ap.J.*, **329**, 849–854, June 1988.

Paerels, F. B. S. & Heise, J. *Ap.J.*, **339**, 1000–1012, April 1989.

Paresce, F. *Astron. J.*, **89**, 1022–1037, July 1984.

Pearce, S. E., Lees, J. E., Pearson, J. F., Fraser, G. W., Brunton, A. N., Flanagan, K. A., Kenter, A. T., Barbera, M., Dhanak, V., Robinson, A. & Teehan, D. *Proc.SPIE*, **2518**, 322–335, September 1995.

Pearson, J. F. *Advances in soft X-ray performance of Microchannel Plate Detectors.* PhD thesis, University of Leicester, 1984.

Pearson, J. F., Brunton, A. N., Martin, A. P., Fraser, G. W., Lees, J. E., Boutot, J. P., Fairbend, R. & Flyckt, S. O. Characteristics of Photonis 6μm pore microchannel plates. In Flanagan, K. A. & Siegmund, O. H. W., editors, *X-ray, and Gamma-Ray Instrumentation for Astronomy XI*, volume 4140, pages 217–228. Proc.SPIE, 2000.

Pearson, J. F., Lees, J. E., Fraser, G. W., Gringauz, K., Schutte, N. & Roze, Y. *Nucl. Instr. and Meth. (A).*, **325**, 578–583, 1993.

Perlmutter, S., Aldering, G., Goldhaber, G., Knop, R. A., Nugent, P., Castro, P. G., Deustua, S., Fabbro, S., Goobar, A., Groom, D. E., Hook, I. M., Kim, A. G., Kim, M. Y., Lee, J. C., Nunes, N. J., Pain, R., Pennypacker, C. R., Quimby, R., Lidman, C., Ellis, R. S., Irwin, M., McMahon, R. G., Ruiz-Lapuente, P., Walton, N., Schaefer, B., Boyle, B. J., Filippenko, A. V., Matheson, T., Fruchter, A. S., Panagia, N., Newberg, H. J. M., Couch, W. J. & The Supernova Cosmology Project. *Ap.J.*, **517**, 565–586, June 1999.

Pounds, K. A., Allan, D. J., Barber, C. & 54 co-authors. *Mon. Not. R. Astr. Soc.*, **260**, 77–102, January 1993.

Powell, F. R. *Proc.SPIE*, **1140**, 88, October 1989.

Pye, J. P., McGale, P. A., Allan, D. J., Barber, C. R., Bertram, D., Denby, M., Page, C. G., Ricketts, M. J., Stewart, B. C. & West, R. G. *Mon. Not. R. Astr. Soc.*, **274**, 1165–1193, June 1995.

Renzini, A., Bragaglia, A., Ferraro, F. R., Gilmozzi, R., Ortolani, S., Holberg, J. B., Liebert, J., Wesemael, F. & Bohlin, R. C. *Ap.J. (Letters)*, **465**, L23, July 1996.

Ridgeley, A. *Opt. Commun.*, **92**, 177–182, 1992.

Riess, A. G., Filippenko, A. V., Challis, P., Clocchiatti, A., Diercks, A., Garnavich, P. M., Gilliland, R. L., Hogan, C. J., Jha, S., Kirshner, R. P., Leibundgut, B., Phillips, M. M., Reiss, D., Schmidt, B. P., Schommer, R. A., Smith, R. C., Spyromilio, J., Stubbs, C., Suntzeff, N. B. & Tonry, J. *Astron. J.*, **116**, 1009–1038, September 1998.

Rife, J. C., Hunter, W. R., Barbee, T. W. & Cruddace, R. G. *Applied Optics*, **28**, 2984–2986, August 1989.

Rybicki, G. B. & Lightman, A. P. *Radiative processes in astrophysics*. New York, Wiley-Interscience, 1979. 393 p., 1979.

Sahu, M. S., Landsman, W., Bruhweiler, F. C., Gull, T. R., Bowers, C. A., Lindler, D., Feggans, K., Barstow, M. A., Hubeny, I. & Holberg, J. B. *Ap.J. (Letters)*, **523**, L159–L163, October 1999.

Sanderson, B. & Lapington, J. S. *Nucl. Instr. and Meth. (A).*, (In press), 1999.

Sansom, A. E., Barstow, M. A., Holberg, J. B. & Kidder, K. M. *Mon. Not. R. Astr. Soc.*, **256**, 1–7, May 1992.

Schuh, S. & Dreizler, S. Application of stratified non-LTE model atmospheres to hot DA white dwarfs. In Shipman, H. L. & Provencal, J. L., editors, *Proceedings of the 12th European White Dwarf Workshop*, pages 79–84. ASP Conf. Series, 2001.

Seely, J. F., Kowalski, M. P., Cruddace, R. G., Rife, J. C., Barbee, T. W. & Hunter, W. R. *Applied Optics*, **34**, 6453–6458, October 1995.

Segretain, L., Chabrier, G., Hernanz, M., Garcia-Berro, E., Isern, J. & Mochkovitch, R. *Ap.J.*, **434**, 641–651, October 1994.

Shaviv, G. & Kovetz, A. *Astron. Astrophys.*, **51**, 383–391, September 1976.

Shipman, H. L. *Ap.J. (Letters)*, **206**, L67–L69, May 1976.

Siegmund, O. H., Gummin, M. A., Ravinett, T., Jelinsky, S. R. & Edgar, M. L. *Proc.SPIE*, **2808**, 98–106, October 1996.

Siegmund, O. H. W., Everman, D. E., Vallerga, J. V. & Lampton, M. *Applied Optics*, **27**, 1568–1573, April 1988.

Siegmund, O. H. W., Lampton, M., Bixler, J., Bowyer, S. & Malina, R. F. *IEEE Transactions on Nuclear Science*, **33**, 724–727, February 1986a.

Siegmund, O. H. W., Vallerga, J. & Jelinsky, P. *Proc.SPIE*, **689**, 40–48, 1986b.

Sion, E. M., Greenstein, J. L., Landstreet, J. D., Liebert, J., Shipman, H. L. & Wegner, G. A. *Ap.J.*, **269**, 253–257, June 1983.

Sion, E. M., Holberg, J. B., Barstow, M. A. & Scheible, M. P. *Astron. J.*, **113**, 364+, January 1997.

Sion, E. M., Liebert, J. & Wesemael, F. *Ap.J.*, **292**, 477–483, May 1985.

Sion, E. M., Schaefer, K. G., Bond, H. E., Saffer, R. A. & Cheng, F. H. *Ap.J. (Letters)*, **496**, L29–+, March 1998.

Struve, O. *Mon. Not. R. Astr. Soc.*, **26**, 268+, November 1865.

Taylor, R. C., Hettrick, M. C. & Malina, R. F. *Rev. Sci. Instr.*, **54**, 171–176, February 1983.

Thomas, R. J., Keski-Kuha, R. A. M., Neupert, W. M., Condor, C. E. & Gum, J. S. *Applied Optics*, **30**, 2245–2251, June 1991.

Thonnard, S. E., Osterman, S. N., McCoy, R. P., Williams, J. Z., Dymond, K. F., Ferragut, N. J., Doerner, M. A. & Parker, S. E. *Proc.SPIE*, **2282**, 98–106, September 1994.

Tweedy, R. W. & Kwitter, K. B. *Ap.J. (Letters)*, **433**, L93–L96, October 1994.

Tweedy, R. W. & Napiwotzki, R. *Astron. J.*, **108**, 978–983, September 1994.

Vennes, S. *Astron. Astrophys.*, **354**, 995–998, February 2000.

Vennes, S. . & Lanz, T. *Ap.J.*, **553**, 399–404, May 2001.

Vennes, S., Chayer, P., Hurwitz, M. & Bowyer, S. *Ap.J.*, **468**, 898+, September 1996.

Vennes, S., Pelletier, C., Fontaine, G. & Wesemael, F. *Ap.J.*, **331**, 876–897, August 1988.

Vennes, S., Thejll, P. & Shipman, H. L. Abundances of trace heavy elements in hot DA white dwarfs. In *White Dwarfs*, pages 235+, 1991.

Vennes, S. & Thorstensen, J. R. *Astron. J.*, **108**, 1881–1892, November 1994.

Walpole, R. E. & Myers, R. H. *Probability and statistics for engineers and scientists*. MacMillan, fourth edition, 1989.

Weidemann, V. *Astron. Astrophys.*, **188**, 74–84, December 1987.

Weinberger, R. *Astron. Astrophys. (Supp.)*, **78**, 301–324, May 1989.

Weller, C. S. Near-earth ultraviolet environment. In *Ultraviolet and vacuum ultraviolet systems; Proceedings of the Meeting, Washington, DC, April 21, 22, 1981. (A83-13954 03-35) Bellingham, WA, SPIE - The International Society for Optical Engineering, 1981, p. 216-222.*, pages 216–222, 1981.

Weller, C. S. & Meier, R. R. *J. Geophys. Res.*, **79**, 1572, 1974.

Werner, K. *Astron. Astrophys.*, **251**, 147–160, November 1991.

Werner, K., Dreizler, S., Heber, U., Rauch, T., Fleming, T. A., Sion, E. M. & Vauclair, G. *Astron. Astrophys.*, **307**, 860–868, March 1996.

Wesemael, F., Henry, R. B. C. & Shipman, H. L. *Ap.J.*, **287**, 868–873, December 1984.

Whiteley, M. J., Pearson, J. F., Fraser, G. W. & Barstow, M. A. *Nucl. Instr. and Meth. (A).*, **224**, 287, 1984.

Winget, D. E., Hansen, C. J., Liebert, J., Van Horn, H. M., Fontaine, G., Nather, R. E., Kepler, S. O. & Lamb, D. Q. *Ap.J. (Letters)*, **315**, L77–L81, April 1987.

Wolff, B., Jordan, S., Koester, D. & Reimers, D. *Astron. Astrophys.*, **361**, 629–640, September 2000.

Wolff, B., Koester, D., Dreizler, S. & Haas, S. *Astron. Astrophys.*, **329**, 1045–1058, January 1998.

Wood, M. A. Theoretical white dwarf luminosity functions: DA models. In *Lecture Notes in Physics Vol. 443: White Dwarfs*, pages 41+, 1995.

INDEX